



# Polish Maritime Research

Special Issue S1 (86) 2015  
Vol. 22

ADDRESS OF PUBLISHER  
& EDITOR'S OFFICE:

GDAŃSK UNIVERSITY  
OF TECHNOLOGY

Faculty of Ocean Engineering  
& Ship Technology  
G. Narutowicza 11/12  
80-233 Gdańsk, POLAND

tel.: +48 58 347 13 66  
fax: +48 58 341 13 66

## Marine Processes Studies and Marine Engineering

### CONTENS

#### EDITORIAL STAFF:

Jacek Rudnicki  
| Editor in Chief  
Przemysław Wierzchowski  
| Scientific Editor  
Jan Michalski  
| Editor for review matters  
Aleksander Kniat  
| Editor for international  
relations  
Kazimierz Kempa  
| Technical Editor  
Piotr Bzura  
| Managing Editor

Price:  
single issue: 25 zł

Prices for abroad  
single issue:  
- in Europe EURO 15  
- overseas USD 20

WEB:  
[www.bg.pg.gda.pl/pmr/pmr.php](http://www.bg.pg.gda.pl/pmr/pmr.php)

ISSN 1233-2585

- 4 **Wenlong Yao, Yuan Liu, Honghai Sun, Guichen Zhang, Jundong Zhang, Mingshun Zhou, Ming Sun, Dezhi Jiang**  
*OPTIMAL CONTROL STRATEGY FOR MARINE SSP PODDED PROPULSION MOTOR BASED ON STRONG TRACKING-EPF*
- 10 **Zengqiang Hana, Chuanying Wanga, Hengyin Zhub,**  
*RESEARCH ON DEEP JOINTS AND LOBE EXTENSION BASED ON DIGITAL BOREHOLE CAMERA TECHNOLOGY*
- 15 **Shaopeng Luana, Xiyong Hou, Yetang Wang**  
*ASSESSING THE ACCURACY OF SRTM DEM AND ASTER GDEM DATASETS FOR THE COASTAL ZONE OF SHANDONG PROVINCE, EASTERN CHINA*
- 21 **Li Zhi-Fu, Shi YuYun, Ren HuiLong, Li Hui, Muhammad Aqeel Ashraf**  
*SIMULATION OF IRREGULAR WAVES IN A NUMERICAL WAVE TANK*
- 26 **Li Chunhui, Pan Xishan, Ke Jie, Dong Xiaotian**  
*COMPARISON OF 2D AND 3D MODELS OF SALINITY NUMERICAL SIMULATION*
- 30 **Dashan Dong, Jin Li, Yuanyuan Teng**  
*ANTI-SEISMIC DEVICE DESIGN FOR CONTAINER CRANE AND ITS ELASTIC-PLASTIC TIME HISTORY ANALYSIS*
- 35 **Zhao Jie, Zhou Tongling, Wang Gui-xuan**  
*NUMERICAL ANALYSIS OF CONSOLIDATION SETTLEMENT AND CREEP DEFORMATION OF ARTIFICIAL ISLAND REVETMENT STRUCTURE IN A LARGE-SCALE MARINE RECLAMATION LAND PROJECT*
- 43 **Lili Yu, Junhua Li, Chaojian Shi**  
*MODELING OF ACOUSTIC FIELD FOR A PARAMETRIC FOCUSING SOURCE USING THE SPHEROIDAL BEAM EQUATION*
- 48 **JunHua Li, YanTing Fan**  
*HYDRAULIC ANALYSIS OF LEAKAGE FROM SUBMARINE PIPE NETWORK*
- 56 **Xiuling Li, Juan Wang, Min Luo**  
*PSEUDO-STATIC EXPERIMENT AND ANALYSIS ON SEISMIC BEHAVIOR OF THE RC COLUMNS STRENGTHENED BY GHPFRCC*

ADDRESS OF PUBLISHER  
& EDITOR'S OFFICE:

GDAŃSK UNIVERSITY  
OF TECHNOLOGY

Faculty of Ocean Engineering  
& Ship Technology  
G. Narutowicza 11/12  
80-233 Gdańsk, POLAND

tel.: +48 58 347 13 66

fax: +48 58 341 13 66

- 61 **Hongbo Zhao, Qinghe Zhang, Mingxiao Xie**  
*NUMERICAL MODELING OF HYDRODYNAMIC AND SEDIMENT SILTATION  
DUE TO TYPHOON IN ESTUARY CHANNEL REGULATION*
- 67 **Rui Deng, Wenyang Duan, Shan Ma, Yong Ma**  
*NUMERICAL RESEARCH OF THE VISCOUS EFFECT OF THE BILGE KEEL ON  
THE DAMPING MOMENT*
- 75 **Miao Chen, Duanfeng Han**  
*MULTI-GRID MODEL FOR CROWD'S EVACUATION IN SHIPS BASED ON  
CELLULAR AUTOMATA*
- 82 **Ning Zhao, Zhen Han**  
*A SIMULATION MODEL OF SEAWATER VERTICAL TEMPERATURE BY USING  
BACK-PROPAGATION NEURAL NETWORK*
- 89 **Jian LI, Shanxiong CHEN, Lingfa JIANG**  
*DYNAMIC STRENGTH AND ACCUMULATED PLASTIC STRAIN DEVELOPMENT  
LAWS AND MODELS OF THE REMOLDED RED CLAY UNDER LONG-TERM  
CYCLIC LOADS: LABORATORY TEST RESULTS*
- 95 **B. Zhanga, Z. Wangac, T.Wangb, H.J. Yua**  
*DESIGN METHOD OF WINCH DRIVEN BY CONTACTLESS MAGNETIC  
COUPLING UNDER DEEPWATER*
- 100 **Chunguan Zhang, Jingguo Chen, Mingyi Song,  
Jinkuan Wang, Bingqiang Yuan**  
*STRUCTURAL INTERPRETATION OF THE QINGDONG AREA IN BOHAI BAY  
BASIN FROM SHIPBORNE GRAVITY DATA*
- 106 **Hongtao Gao, Biao Li**  
*ESTABLISHMENT OF MOTION MODEL FOR WAVE CAPTURE BUOY AND  
RESEARCH ON HYDRODYNAMIC PERFORMANCE OF FLOATING-TYPE WAVE  
ENERGY CONVERTER*
- 112 **Ming Lv, Haiqiang Liu, Xin Nie, Muhammad Aqeel Ashraf**  
*CHARACTERISTIC STUDIES OF MICRON ZINC PARTICLE HYDROLYSIS IN A  
FIXED BED REACTOR*
- 121 **Lihui Wang, Le Yu, Yanhua Zhu**  
*CONSTRUCTION METHOD OF THE TOPOGRAPHICAL FEATURES MODEL  
FOR UNDERWATER TERRAIN NAVIGATION*
- 126 **Jiaqing Du, Shouji Du, Shuilong Shen, Zhenyu Yina**  
*NUMERICAL INVESTIGATION OF THE UNDRAINED COMPRESSION AND  
PULL-OUT CAPACITY OF SUCTION FOUNDATIONS IN CLAY*
- 136 **Chuang Cai, Xinyong Cai, Yi Li**  
*MODEL TESTS FOR SHALLOW-WATER SHIP MANEUVERABILITY IN THREE  
GORGES RESERVOIR*
- 141 **Mi Zhou, Wancheng Yuan, Yue Zhang**  
*SEISMIC MATERIAL PROPERTIES OF REINFORCED CONCRETE AND STEEL  
CASING COMPOSITE CONCRETE IN ELEVATED PILE-GROUP FOUNDATION*
- 149 **Xinghui Yin, Linan Liu, Xiaomeng Zhao, Muhammad Aqeel Ashraf**  
*IMAGE FUSION FOR TRAVEL TIME TOMOGRAPHY INVERSION*
- 157 **QI Duo, FENG Jinfu, LI Yongli, LIU An, HU  
Junhua, XU Hu, Muhammad Aqeel Ashraf**  
*STABILITY CONTROL OF PROPELLER AUTONOMOUS UNDERWATER VEHICLE  
BASED ON COMBINED SECTIONS METHOD*
- 163 **Chao MI, Zhiwei ZHANG, Xin HE, Youfang HUANG, Weijian MI**  
*TWO-STAGE CLASSIFICATION APPROACH FOR HUMAN DETECTION IN  
CAMERA VIDEO IN BULK PORTS*

## Editorial

POLISH MARITIME RESEARCH is a scientific journal of worldwide circulation. The journal appears as a quarterly four times a year. The first issue of it was published in September 1994. Its main aim is to present original, innovative scientific ideas and Research & Development achievements in the field of :

### **Engineering, Computing & Technology, Mechanical Engineering,**

which could find applications in the broad domain of maritime economy. Hence there are published papers which concern methods of the designing, manufacturing and operating processes of such technical objects and devices as : ships, port equipment, ocean engineering units, underwater vehicles and equipment as well as harbour facilities, with accounting for marine environment protection.

The Editors of POLISH MARITIME RESEARCH make also efforts to present problems dealing with education of engineers and scientific and teaching personnel. As a rule, the basic papers are supplemented by information on conferences , important scientific events as well as cooperation in carrying out international scientific research projects.

### Scientific Board

**Chairman : Prof. JERZY GIRTLER - Gdańsk University of Technology, Poland**

**Vice-chairman : Prof. ANTONI JANKOWSKI - Institute of Aeronautics, Poland**

**Vice-chairman : Prof. MIROŚLAW L. WYSZYŃSKI - University of Birmingham, United Kingdom**

<b>Dr POUL ANDERSEN</b> Technical University of Denmark Denmark	<b>Prof. WOLFGANG FRICKE</b> Technical University Hamburg- Harburg Germany	<b>Prof. YASUHIKO OHTA</b> Nagoya Institute of Technology Japan
<b>Dr MEHMET ATLAR</b> University of Newcastle United Kingdom	<b>Prof. STANISŁAW GUCMA</b> Maritime University of Szczecin Poland	<b>Dr YOSHIO SATO</b> National Traffic Safety and Environment Laboratory Japan
<b>Prof. GÖRAN BARK</b> Chalmers University of Technology Sweden	<b>Prof. ANTONI ISKRA</b> Poznań University of Technology Poland	<b>Prof. KLAUS SCHIER</b> University of Applied Sciences Germany
<b>Prof. SERGEY BARSUKOV</b> Army Institute of Odessa Ukraine	<b>Prof. JAN KICIŃSKI</b> Institute of Fluid-Flow Machinery of PASci Poland	<b>Prof. FREDERICK STERN</b> University of Iowa, IA, USA
<b>Prof. MUSTAFA BAYHAN</b> Süleyman Demirel University Turkey	<b>Prof. ZYGMUNT KITOWSKI</b> Naval University Poland	<b>Prof. JÓZEF SZALA</b> Bydgoszcz University of Technology and Agriculture Poland
<b>Prof. VINCENZO CRUPI</b> University of Messina, Italy	<b>Prof. JAN KULCZYK</b> Wrocław University of Technology Poland	<b>Prof. TADEUSZ SZELANGIEWICZ</b> Technical University of Szczecin Poland
<b>Prof. MAREK DZIDA</b> Gdańsk University of Technology Poland	<b>Prof. NICOS LADOMMATOS</b> University College London United Kingdom	<b>Prof. WITALIJ SZCZAGIN</b> State Technical University of Kaliningrad Russia
<b>Prof. ODD M. FALTINSEN</b> Norwegian University of Science and Technology Norway	<b>Prof. JÓZEF LISOWSKI</b> Gdynia Maritime University Poland	<b>Prof. BORIS TIKHOMIROV</b> State Marine University of St. Petersburg Russia
<b>Prof. PATRICK V. FARRELL</b> University of Wisconsin Madison, WI USA	<b>Prof. JERZY MATUSIAK</b> Helsinki University of Technology Finland	<b>Prof. DRACOS VASSALOS</b> University of Glasgow and Strathclyde United Kingdom
	<b>Prof. EUGEN NEGRUS</b> University of Bucharest Romania	

## OPTIMAL CONTROL STRATEGY FOR MARINE SSP PODDED PROPULSION MOTOR BASED ON STRONG TRACKING-EPF

Wenlong Yao<sup>a,b</sup>

Yuan Liu<sup>c</sup>,

Honghai Sun<sup>c</sup>,

Guichen Zhang<sup>d</sup>,

Jundong Zhang<sup>b</sup>,

Mingshun Zhou<sup>a</sup>,

Ming Sun<sup>a</sup>,

Dezhi Jiang<sup>a</sup>,

a) Dept. of Marine Engineering, Qingdao Ocean Shipping Mariners College,  
Qingdao, China

b) College of Marine Engineering, Dalian Maritime University, Dalian, China

c) Dept. of Naval Architecture & Ocean Engineering, Qingdao Ocean  
Shipping Mariners College, Qingdao, China

d) School of Shipbuilding Engineering, Journal of Harbin Engineering  
University, Harbin, China

### ABSTRACT

*Aiming at the non-linearity of state equation and observation equation of SSP (Siemen Schottel Propulsor) propulsion motor, an improved particle filter algorithm based on strong tracking extent Kalman filter (ST-EKF) was presented, and it was imported into the marine SSP propulsion motor control system. The strong tracking filter was used to update particles in the new algorithm and produce importance densities. As a result, the problems of particle degeneracy and sample impoverishment were ameliorated, the propulsion motor states and the rotor resistance were estimated simultaneously using strong track filter (STF), and the tracking ability of marine SSP propulsion motor control system was improved. Simulation result shown that the improved EPF algorithm was not only improving the prediction accuracy of the motor states and the rotor resistance, but also it can satisfy the requirement of navigation in harbor. It had the better accuracy than EPF algorithm.*

**Keywords:** Marine electric propulsion, EPF, ST-EKF, SSP podded propulsion, Propulsion motor

### INTRODUCTION

Marine podded propulsion is the new type of marine electrical propulsion system which has the advantages of simple structure, reliable operation and convenient maintenance, etc. But, the propulsion motor is more sensitive to load variation and external disturbance, such as thrust ripple, the cogging effect and nonlinear factors which have great influence to the end effect on tracking precision due to the marine podded propulsion system has no intermediate bearing and other transmission mechanism [3]. At present, the research of the propulsion motor control mainly focused on the areas of integral backstepping control [13], direct torque control [5], feedback linearization control [1], the sliding mode control [16], decoupling control [6], hybrid control method [2] and vector control [11] and so on, they have in common is that in view of the torque and flux linkage for independent control, so

as to realize the linearization of the propulsion motor control.

In addition to utilize the advanced control method for the SSP propulsion motor speed sensorless control system, the accuracy of motor parameters is also the main factor which influence the control performance. However, the SSP propulsion motor in the process of running, parameters will be changed with the conditions and sea condition which shows the time-varying, when the fixed parameter model are utilized for calculating, the errors will be introduced inevitably, and the control performance will be degraded [15]. Therefore, the online identification of motor parameter has become the popular research, the motor parameters can be obtained by utilizing the constraints to simplify the model structure and reduce the measuring variables among the researches. Also the motor parameters can be identified by utilizing the

model reference adaptive [4], observer estimation [7], artificial intelligence algorithm [8].

In addition, it is the key to the control system design for the marine electric propulsion system that the problems of the unknown rough sea conditions as well as the speed estimation in extremely low speed and zero speed [17]. Therefore, it need to be able to estimate the motor speed, at the same time, load torque, rotor flux motor parameter and the speed of the near zero for the parameters estimation method of the SSP control system. In paper [5], the direct torque control of permanent magnet synchronous motors without speed sensor is achieved through precisely estimating the stator flux linkage and rot or speed, and indirectly, the torque by means of the extended Kalman filter. Retaining the advantages of direct torque control method in rapid torque response and strong robustness, the system has significantly reduced ripples of flux linkage and torque. Besides, the effects of motor parameter variations and load disturbance are reduced.

Extended Kalman filter (EKF) is a novel filtering method of the nonlinear systems. However the traditional EKF method due to the partial linearization to transfer function and the measure function, can not adapt the serious non-linear situation; Moreover, derivate matrix of nonlinear function can not be carried out by utilizing the partial derivative [10], so its divergence has aroused much attention. The particle filter is an algorithm based on Monte Carlo methods. Its theory can be used in any non-linear and non-Gaussian state space models. R. V. Merwe brings forward the UPF (Unscented Particle Filter, UPF) algorithm [9] in which UKF (Unscented Kalman Filter, UKF) [12] was used to get more popular proposal distribution function so that the covariance of importance weights was reduced in the year of 2000. However, the EPF algorithm is realized by first order local linearization to the system equations based on Taylor series, the proposal distribution have bigger truncation errors, it results in the decrease of filtering precision, but it has the advantage of the relatively small amount of calculation. The UPF algorithm is realized by utilizing the UKF to get the importance of the particle filter function, although the accuracy can markedly be improved, but it has the disadvantages of too big amount of calculation and poor real-time performance.

The strong tracking extended Kalman particle filter algorithm (ST-EPF) is proposed in this article. The ST-EKF algorithm are utilized to update the particles in this algorithm. It is easy to cause the deviation of estimation even the phenomenon such as divergence, poor robustness, especially when it will lose the ability to mutation status tracking during it reaches steady state because of the controller word length and memory restrictions of the traditional EPF algorithm. The particle samples are processed by the ST-EKF algorithm in the ST-EPF algorithm, and the importance density are generated, the particle degradation and sample impoverishment problem can be relieved, their ability to mutation status tracking can also be improved and it can satisfy the mobility performance of the marine podded propulsion control system better.

## THE PARTICLE FILTER BASED ON ST-EKF

### PRINCIPLE OF ST-EKF

Time update equations

$$P_{k+1,k} = \Phi_{k+1,k} P_k \Phi_{k+1,k}^T + Q_k \quad (1)$$

Measurement updates equations:

$$K_{k+1} = P_{k+1,k} H_{k+1}^T [H_{k+1} P_{k+1,k} H_{k+1}^T + R_{k+1}]^{-1} \quad (2)$$

$$P_{k+1} = [I - K_{k+1} H_{k+1}] P_{k+1,k} \quad (3)$$

The time-varying fading factor  $\lambda_{k+1}$  are introduced by the orthogonality principle in strong tracking filtering, the prediction error covariance  $P_{k+1,k}$  are adjusted, the gain matrix  $K_{k+1}$  are controlled real-time, it makes the residual sequence of different time everywhere maintain orthogonality of orthogonal or approximate, the ability of the filter to track state changes is improved, it has a strong robustness and anti-interference ability, and the computational complexity is moderate. The equation (3) was simlified to the following form:

$$P_{k+1,k} = LMD(k+1) \Phi_{k+1,k} P_k \Phi_{k+1,k}^T + Q_k \quad (4)$$

Where,  $LMD(k+1) = diag[\lambda_{k+1}^1, \lambda_{k+1}^2, \dots, \lambda_{k+1}^n]$  is the time-varying fading matrix,  $\lambda_{k+1}^{(i)} \geq 1, i = 1, 2, \dots, n$  is the time-varying fading factor  $K_{k+1} = P_{k+1,k} H_{k+1}^T [H_{k+1} P_{k+1,k} H_{k+1}^T + R_{k+1}]^{-1}$ . It is determined by orthogonal principle. To simplify the simulation which can be obtained by the method of literature, in the subprime:

$$\lambda_{k+1}^{(i)} = \begin{cases} \lambda_{k+1}, & \lambda_{k+1} > 1 \\ 1, & \lambda_{k+1} \leq 1 \end{cases} \quad (5)$$

$$\lambda_{k+1} = tr[N_{k+1}] / tr[M_{k+1}] \quad (6)$$

$$N_{k+1} = V_{k+1} - \beta R_k - H_k Q_k H_k^T \quad (7)$$

$$M_{k+1} = \Phi_k P_{k/k} \Phi_k^T H_k^T H_k \quad (8)$$

Where,  $tr(\bullet)$  is the sum of the diagonal matrix,  $N_{k+1}$  and  $M_{k+1}$  are derived for the approximate orthogonal residual at different times, they have no specific physical meaning.  $V_{k+1}$  is the output sequence of the mean square error matrix, it is calculated as follows:

$$V_{k+1} = \begin{cases} \gamma_1 \gamma_1^T, & k = 0 \\ [\rho V_k + \gamma_{k+1} \gamma_{k+1}^T] / (1 + \rho), & k \geq 1 \end{cases} \quad (9)$$

Where,  $0 < \rho \leq 1$  is the residual sequence of forgetting factor,  $\beta \geq 1$  is the selected weakening factor.

### THE IMPROVED PARTICLE FILTER ALGORITHM

(1) Initialize with(  $k = 0$ ):

Draw the states  $x_0^{(i)}$ ,  $p(x_0)$ , assign the particle a weight

$$w_0^{(i)} = 1/N \quad i = 1, 2 \dots N \quad (10)$$

$$\bar{x}_0^{(i)} = W \left[ x_0^{(i)} \right] \quad (11)$$

$$P_0^{(i)} = E \left[ \left( x_0^{(i)} - \bar{x}_0^{(i)} \right) \left( x_0^{(i)} - \bar{x}_0^{(i)} \right)^T \right] \quad (12)$$

Where:  $w_0$  is the initial weights of support points,  $\bar{x}_0$  is the initial value of the fixed state estimation,  $P_0$  is the initial value of matrix square-root of the state covariance.

(2) Importance Sampling ( $k = 1, 2, \dots$ ):

We can get  $\bar{x}_k^{(i)}$ ,  $P_k^{(i)}$  by using the ST-EKF algorithm for each particle  $x_{k-1}^{(i)}$ :

$$x_{k,k-1}^{(i)} = f(\bar{x}_{k-1}^{(i)}) \quad (13)$$

$$P_{k,k-1}^{(i)} = \lambda_k^{(i)} \Phi_k^{(i)} P_{k-1}^{(i)} \Phi_k^{(iT)} + Q_k^{(i)} \quad (14)$$

$$K_k^{(i)} = P_{k,k-1}^{(i)} H_k^{(iT)} \left( H_k^{(i)} P_{k,k-1}^{(i)} H_k^{(iT)} + R_k^{(i)} \right)^{-1} \quad (15)$$

$$\bar{x}_k^{(i)} = \bar{x}_{k,k-1}^{(i)} + K_k \left( z_k - h(x_{k,k-1}^{(i)}) \right) \quad (16)$$

$$\bar{P}_k^{(i)} = [I - K_k H_k^{(i)}] P_{k,k-1}^{(i)} \quad (17)$$

Where:  $z_k$  is the observed vectors that are dealt with by the ST-EKF,  $Q$  is the covariance matrix of the system noise series,  $R$  is the covariance matrix of the observed noise series which is dealt with by the ST-EKF.

We get proposal distribution function:

$$q \left( x_k^{(i)} \mid x_{0:k-1}^{(i)}, z_{1:k} \right) = N \left( \bar{x}_k^{(i)}, P_k^{(i)} \right) \quad (18)$$

The proposal distribution function makes use of the new observations, the sampling precision of particle was improved. We can get the new particles  $\{x_k^{(i)}\}_{i=1}^N$  drawn from  $x_k^{(i)} \boxtimes q \left( x_k^{(i)} \mid x_{0:k-1}^{(i)}, z_{1:k} \right)$

(3) Update and normalize the weights

Update:

$$w_k^{(i)} = w_{k-1}^{(i)} \frac{p(z_k / x_k^{(i)}) p(x_k^{(i)} / x_{k-1}^{(i)})}{q \left( x_k^{(i)} \mid x_{0:k-1}^{(i)}, z_{1:k} \right)} \quad (19)$$

Normalize the weights

$$\tilde{w}_k^{(i)} = w_k^{(i)} / \sum_{j=1}^N w_k^{(j)} \quad (20)$$

(4) Resample

Resampling generates a new particle set by sampling from  $\{\bar{x}_k^{(i)}, i = 1, 2 \dots N\}$ , with  $j, \Pr \{x_k^{(i)} = \bar{x}_k^{(j)}\} = w_k^{(j)}$ . Here  $j$  is the particle index after resampling.

The weight are reseted:  $w_k^{(i)} = 1/N$ .

(5) Update state

$$x(k/k) = \frac{i}{N} \sum_{i=1}^N x_k^{(i)} \quad (21)$$

It can be obtained from the step (2),  $\bar{x}_k^{(i)}$  and  $P_k^{(i)}$  are respectively mean and covariance through the calculation of ST-EKF. These handled observation vectors of particles reflect new prior with smaller covariance than former so that we can get more popular proposal distribution function, the covariance of importance weights has been reduced.

## MODEL ANALYSIS OF MARINE SSP PROPULSION MOTOR CONTROL SYSTEM

The semi-submersible vessel „Kangshengkou” full electric propulsion system of Cosco is to be the research objection, the hardware of the control system was composed by the Siemens Simotion D, Sinamics, the upper computer and so on, the software of the control system contains Winccflexible, Step7, Scout and Matlab. This research was established in the basis of hardware-in-loop simulation of the SSP propulsion system which was based on the formal work [14], problem description is as follows:

Electromagnetic torque of the SSP propulsion is

$$T_e = \frac{3p}{2} \frac{\psi_r^2}{R_r} \omega_s^* \quad (22)$$

Where  $T_e$  is electromagnetic torque,  $P$  is the number of magnetic poles,  $R_r$  is the rotor resistance,  $\psi_r$  is the rotor flux valid values,  $\frac{d\theta}{dt} = \omega$  is the given slip angular frequency,  $\omega_s^*$  is the setting slip angular frequency. The rotor flux is the setting value actually (Li et al., 2011),  $T_e$  is proportional to the  $T_L = \text{sgn}(\omega) \frac{K_T}{4\pi^2} \rho D^5 \omega^2$ .

The friction torque of SSP propulsion system  $T_f$  is

$$T_f = \text{sign}(\omega) T_s + k_\omega \omega \quad (23)$$

Where  $\omega = 2\pi n/60$ ,  $n$  is propeller speed,  $T_s$  is the static friction torque,  $k_\omega$  is the linear friction coefficient.

The motion equation of the SSP propulsion system is

$$\frac{d\omega}{dt} = \frac{1}{J} (T_e - F\omega - T_L) \quad (24)$$

$$\frac{d\theta}{dt} = \omega \quad (25)$$

Where  $J$  is SSP moment of inertia,  $T_m$  is the load torque.

The dynamic model of SSP propulsion system is

$$T_p = K_T (J) \cdot \rho D^5 n |n| \quad (26)$$

$$F_c = K_F (J) \cdot \rho D^4 n |n| \cdot (1 - \tau) \quad (27)$$

$$P_p = 2\pi n T_p = K_T (J) \cdot 2\pi \rho D^5 n^3 \quad (28)$$

Where  $T_c(i_a, i_b, i_c, \theta) = P \frac{\partial W_m(\psi, \theta)}{\partial \theta}$ ,  $i_a$  is thrust deduction coefficient,  $i_b$  is wake fraction, the value can be obtained

by ship's manual,  $T_p$  is propeller torque,  $F_e$  is propeller effective thrust,  $\rho$  is density of water,  $D$  is propeller diameter,  $K_T(J)$  is torque coefficient of dimensionless,  $K_F(J)$  is the thrust coefficient of dimensionless,  $K_T(J)$  and  $K_F(J)$  are the function of  $J$ , they can be obtained by the propeller working characteristic curve. During stable sailing in the sea, the ratio of propeller is a constant value, it shows that propeller will work on the speed ratio of the characteristic curve.

## SIMULATION AND RESULTS

The marine SSP propulsion motor control system was established under the Matlab/Simulink environment, the propeller model was realized by utilizing the S-function. The simulation parameter of propulsion motor was based on "Kangshengkou", as follows: power rating = 4700 kW, rated voltage = 660V, rated speed = 155 r/min, rotor permanent magnet flux linkage = 4.55 Wb, rated torque = 1185 KN-m, stator resistance = 1.632 m, number of motor pole = 8, inductance of d axis = 0.25 mH, inductance of q axis = 0.47 mH.

When ship navigation in harbor at 130 r/min, it needs to manoeuvre the vehicle frequently, the simulation analysis was carried out on this working condition. The simulation time is 1 s, the initial speed is 130 r/min, at the beginning of the simulation, the motor load torque is 240 KN-m, at the time of 0.5 s the speed was changed to 110 r/min. At the same time the sea condition suddenly changes, which at the beginning, the motor load torque is 240 KN-m, at the time of 0.36 s propeller load torque changes to 220 KN-m. The simulation results about the control method of SSP propulsion motor based on vector control with EPF and ST-EPF composite algorithm are shown as Figure 1- Figure 6.

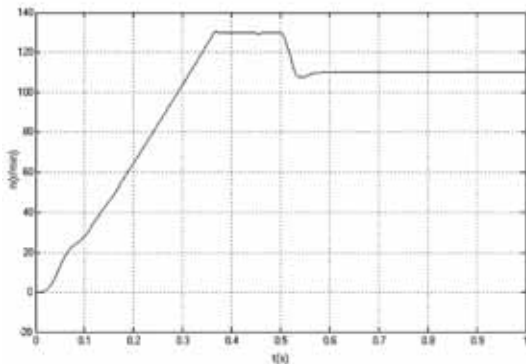


Fig. 1. Speed curve based on EPF

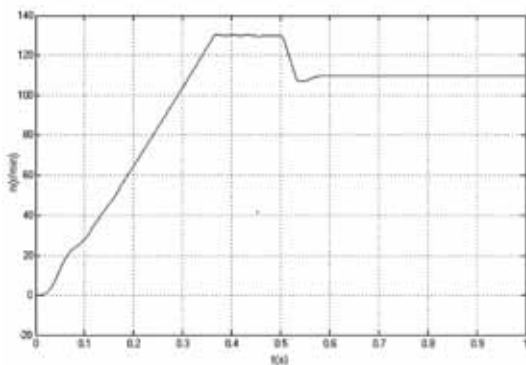


Fig. 2. Speed curve based on ST-EPF

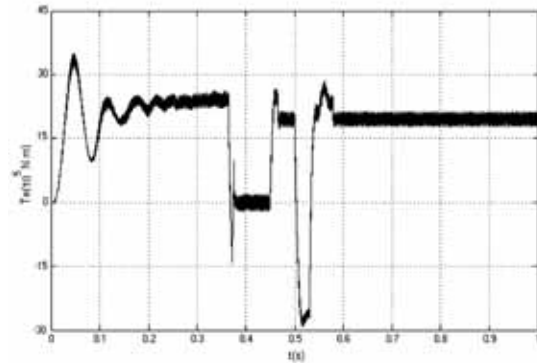


Fig. 3. Torque curve based on EPF

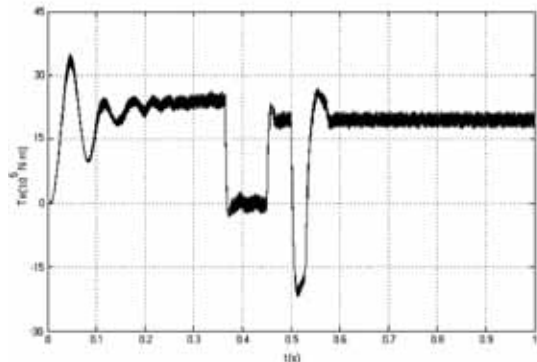


Fig. 4. Torque curve based on ST-EPF

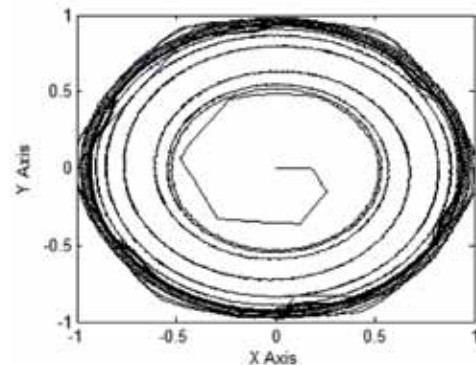


Fig. 5. Stator flux based on EPF

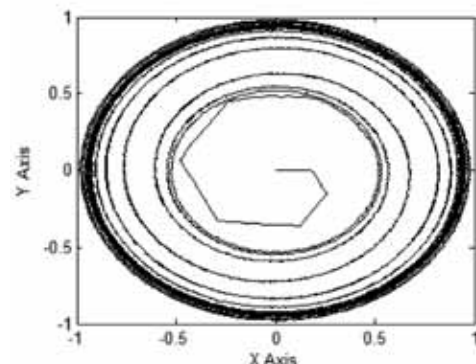


Fig. 6. Stator flux based on ST-EPF

The simulation results show that: When ship navigation in harbor and with the rough sea, under the two control modes, speed up smoothly, and the speed changes slightly after the torque of the propeller load changes but back then. The system reaches the given speed 130 r/min after 0.36 s and propeller

load changes in 0.36 s, the controller, torque and current have a corresponding response by the ST-EPF. It can be shown that the SSP propulsion system based on ST-EPF composite control has the lower speed fluctuation, smaller steady state operating static error and better dynamic response ability than which based on EPF.

## CONCLUSIONS

In this paper the ST-EPF control algorithm was introduced into the sensorless vector control of marine propulsion motor control system, the orthogonality principle was introduced to the tracking process of control system, the gain matrix was controlled real-time, the track state mutation ability of the filter was improved. The simulation results show that the ST-EPF observer for the control system has good robustness, especially to the changes of the system parameter, the adaptability of measurement noise and system noise are superior to the EPF observer, the EPF observer error problem of poor robustness of the model was better solved, the marine podded propulsion motor flux and speed can be estimated accurately.

## ACKNOWLEDGMENTS

This work is supported by Shinan District Science and Technology Development Funds of Qingdao City under Grant 2012-5-004-ZH and 2012-5-005-ZH, the Shandong Province Higher Educational Science and Technology Program under Grant J13LN72, National Natural Science Foundation (NNSF) of China under Grant 51179102, Ministry of industry and information Technology of China branch project under Grant 201301188, Science and Technology Program of COSCO under Grant 2012-1-H-004 and 2014-1-H-005.

## REFERENCES

1. Angelo C, Bossio G, Garcia G, et al.,2006. Speed control of PMSMs with interconnection an damping assignment or feedback linearization comments about their performance. *Industrial Electronics*. Montreal, 2182-2187.
2. Cetin E, Oguz U,2008. A hybrid controller for the speed of a permanent magnet synchronous motor drive [J]. *Control Engineering Practice*,16, 260-270.
3. Islam M F, Veitch B, Liu P, et al., 2010. Gap Effect on Performance of Podded Propulsors in Straight-Ahead and Azimuthing Conditions. *Marine Technology*, 47,47-58.
4. Ji Feng,Fu Lijun,Ye Zhihao,2011. Study on Vector Control for Vessel Electric Propulsion. *Journal of wuhan university of science and technology*,35,361-364
5. LI Bingqiang, LIN Hui,2011. Direct Control of Current Vector for Surface-mounted Permanent Magnet Synchronous Motor. *Proceedings of the CSEE*,31,288-294
6. LI Liang-liang, HE Yong, YE Hai-xiang, 2011. Simulation of Permanent Magnet Synchronous Motor Vector Control Based on ITAE Optimization. *Electric Machines & Control Application*,38, 31-45
7. Li Zhongbing,Zhang Huanren,2011. Extended Kalman Filter Enhanced Ship Electrical Propulsion System, *Navigation of China*, 34, 45-50
8. Lu Wenbin Yao Wenxi Lü Zhengyu,2013. Speed Sensorless Vector Control with Improved Closed-Loop Flux Observer for Induction Machines. *Transactions of China Electro Technical Society*,28, 148-153.
9. R.V.Merwe,A.Douvet,N.De.Freitas et al,2000. The unscented particle filter. *Technical Report CUED/F@INPENG/ TR380:Cambridge University Engi -neering Department*.
10. Sui Shu-lin,Yao Wen-long,2008. Spacecraft of autonomous optical navigation Based on wavelet-UPF. *Systems Engineering and Elctronics*. 8,1519-1522
11. Suman Maiti, Chandan Chakraborty, Sabyasachi Sengupta, 2009. Simulation studies on model reference adaptive controller based speed estimation technique for the vector controlled permanent magnet synchronous motor drive. *Simulation Modelling Practice and Theory*,7, 585-596.
12. Van Dyke M C, Schwartz J L , Hall C D,2004. Unscented Kalman filtering for spacecraft attitude state and parameter estimation. [http://www.Space-flight.org/AAS\\_meetings/2004\\_winter/w2004-program.pdf](http://www.Space-flight.org/AAS_meetings/2004_winter/w2004-program.pdf), 2004-03-10.
13. WANG Li-peng, ZHANG Hua-guang,LIU Xiu-chong,2012. Integral backstepping controller in the sensorless vector-control system for permanent magnet synchronous motor. *Control Theory & Applications*, 29,199-204
14. Wenlong Yao, Yuan Liu ,Jundong Zhang, Sun Ming, Zhang Gui-chen and Wei shao,2013. Design of Vector Control based on MFAC for SSP Podded Propulsion, *Proc. of the Int. Conf. on Robotics and Biomimetics (ROBIO 2013)*, 12,2418-2423
15. Wenlong Yao, Jundong Zhang,Ronghu Chi, Zhang Gui-chen. Model-free adaptive vector control of ship podded SSP propulsion motor, *Journal of Traffic and Transportation Engineering*, 2014,14(6): 59-66.
16. YU Ming, CONG Shuang, XU Juan,2008. Design of nonlinear motor adaptive fuzzy sliding mode controller based on GA, *Journal of System Simulation*. 20, 3141-3145.

17. ZHANG Guichen, MA Jie, 2010. Study and Application of Podded Electric Propulsion System Based on SIMOTION. Ship Building of China, 51,45-50.

### CONTACT WITH AUTHOR

Wenlong Yao  
yaowenlong@dlmu.edu.cn  
tel:+86 532 85752355  
fax:+86 532 85752355

Mingshun Zhou  
Ming Sun  
Dezhi Jiang

Dept. of Marine Engineering,  
Qingdao Ocean Shipping Mariners College  
Qingdao, China

Wenlong Yao  
Jundong Zhang

College of Marine Engineering  
Dalian Maritime University  
Dalian, China

Yuan Liu  
Honghai Sun

Dept. of Naval Architecture & Ocean Engineering  
Qingdao Ocean Shipping Mariners College  
Qingdao, China

Guichen Zhangd

School of Shipbuilding Engineering  
Journal of Harbin Engineering University  
Harbin, China

# RESEARCH ON DEEP JOINTS AND LODGE EXTENSION BASED ON DIGITAL BOREHOLE CAMERA TECHNOLOGY

Zengqiang Han<sup>a</sup>,  
Chuanying Wang<sup>a</sup>,  
Hengyin Zhu<sup>b</sup>,

- a) State Key Laboratory of Geomechanics and Geotechnical Engineering,  
Institute of Rock and Soil Mechanics, Chinese Academy of Sciences  
b) Geological Party of Anhui Bureau of Geology and Mineral Exploration,  
Luan, China

## ABSTRACT

*Structure characteristics of rock and orebody in deep borehole are obtained by borehole camera technology. By investigating on the joints and fissures in Shapinggou molybdenum mine, the dominant orientation of joint fissure in surrounding rock and orebody were statistically analyzed. Applying the theory of metallogeny and geostatistics, the relationship between joint fissure and lode's extension direction is explored. The results indicate that joints in the orebody of ZK61 borehole have only one dominant orientation  $SE126^{\circ}\angle 68^{\circ}$ ; however, the dominant orientations of joints in surrounding rock were  $SE118^{\circ}\angle 73^{\circ}$ ,  $SW225^{\circ}\angle 70^{\circ}$  and  $SE122^{\circ}\angle 65^{\circ}$ ,  $NE79^{\circ}\angle 63^{\circ}$ . Then a preliminary conclusion showed that the lode's extension direction is specific and it is influenced by joints of surrounding rock. Results of other boreholes are generally agree well with the ZK61, suggesting the analysis reliably reflects the lode's extension properties and the conclusion presents important references for deep ore prospecting.*

**Keywords:** digital borehole camera, deep ore prospecting, dominant orientation, lode's extension direction

## INTRODUCTION

There are a large number of joints exist in deep orebody such as flow banding, interbed, fracture, bedding, etc, and the orientation of these joints is closely related to the extension direction of ore-lode. It has important significance for deep ore prospecting to investigate the development of mine of jointed rock and explore the relationship between deep rock-ore joints and the extension of deep ore-lodes. Through the joints exploration of Shapinggou Molybdenum Mine based on borehole camera technology, dominant occurrences of rock-ore joints are calculated and the relationship between joints dominant occurrence and extension direction of ore-lodes is analyzed. This research provides the basis for arrangement of holes in the next step prospecting and ore reserves estimation.

### JOINT ACQUISITION AND STATISTICAL ANALYSIS

### DIGITAL BOREHOLE CAMERA TECHNOLOGY

Digital borehole camera technology (DBCT) is a new exploration technology which can directly observe the internal of the borehole based on the optics theory. Borehole wall images can be quickly obtained and joints parameter information can be accessed by calculating. Based on this technology, Digital Panoramic Borehole Camera System (DPBCS) as shown in Fig.1 was successfully developed by Institute of Rock and Soil Mechanics, Chinese Academy of Sciences in 1998[4,5]. Electronic technology, video technology, digital technology and computer technology are used in this system which records and analyzes a situ video of borehole wall from a panoramic perspective. Through the direct research on the borehole wall, we can accurately detect joints within the borehole and reflect within the borehole strata occurrence in detail avoiding the influence of low core drilling rate and disturbance. The application of this technology can reflect the actual situation of drilling than in core drilling and resolve the accuracy and completeness of drilling engineering geology information collection [6, 7].



Fig. 1. Digital panoramic borehole camera system

The key of digital borehole camera system is the breakthrough in panoramic and digital technology. The panoramic technology can realize 360° three-dimensional displays of borehole walls which included azimuth information and can form flat panoramic image. Digital technology can digitalize videos to images and restore the real borehole wall, namely the digital image of borehole wall. The imaging principle of digital borehole camera technology is analyzed in Fig.2.

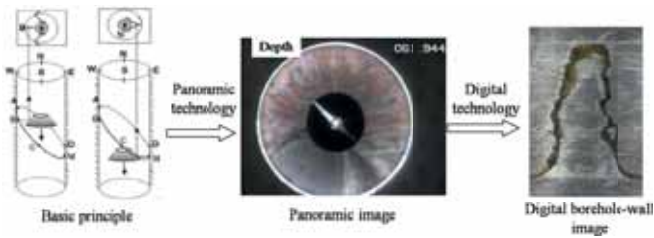


Fig. 2. Sketch of system imaging principle

By using video image analysis system as shown in Fig.3 to process the borehole wall video obtained through field testing, the planar image of borehole wall and virtual borehole core image are obtained.

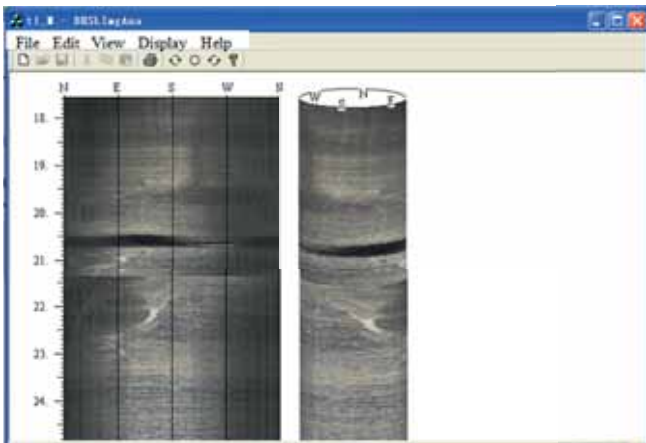


Fig. 3. Analysis software of the system

The planar image presents a complete two-dimensional expanded view of inner borehole wall, which vertically sections the inner wall in the north direction. From the image, joint information, including the orientation, color of orebody, fracture width, filling and borehole damage, etc. is obtained. Due to this article research the extension of deep ore-lodes based on joints occurrence, the calculation principle of joints are introduced. As shown in Fig.4, assuming that the joint in the borehole is a 3D plane and completely cut the borehole [3, 6].

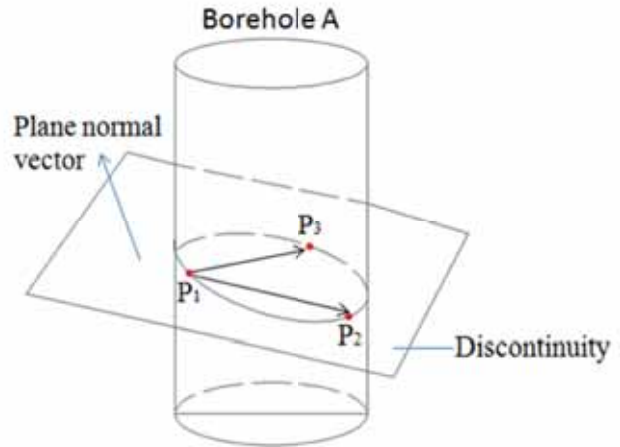


Fig. 4. Sketch of calculating discontinuity occurrence

The method to calculate fracture orientation is introduced by taking three non-collinear points P1, P2 and P3 on the planar fracture as shown in Fig.4. Thus, vectors  $\vec{V}_1$  and  $\vec{V}_2$  on this plane can be obtained as:

$$\vec{V}_1 = \overrightarrow{P_1 P_2}, \quad \vec{V}_2 = \overrightarrow{P_1 P_3} \quad (1)$$

The normal vector  $\vec{N}$  of the plane can be expressed as:

$$\vec{N} = \vec{V}_1 \times \vec{V}_2 \quad (2)$$

In order to express unit normal vector, the above function can be transformed into:

$$\vec{N}_u = \frac{\vec{N}}{|\vec{N}|} \quad (3)$$

If the Z-component of unit normal vector  $\vec{N}_u$  is less than zero, the opposite vector  $\vec{N}_0 = \{X_0, Y_0, Z_0\}$  is taken which satisfies:

$$\vec{N}_0 = -\vec{N}_u \quad (4)$$

Thus, the dip angle  $\beta$  of the fracture can be deduced through the following function as:

$$\beta = \cos^{-1} Z_0 \quad (5)$$

Assuming that vector  $\vec{N}_p = \{X_p, Y_p\}$  is the projection of  $\vec{N}_0$  on the XY plane, then the dip azimuth  $\alpha$  of the fracture can be obtained through the following formula:

$$\alpha = \begin{cases} 90^\circ - \tan^{-1} Y_p / X_p & \text{when } X_p > 0 \\ 90^\circ & \text{and } Y_p > 0 \\ 270^\circ - \tan^{-1} Y_p / X_p & \text{when } X_p < 0 \\ 270^\circ & \text{and } X_p < 0 \end{cases} \quad (6)$$

Through the calculation principle of structural plane, DBCT resolve the problem which traditional core drilling cannot calculate joint orientation improving the accuracy of the angle calculation.

## ANALYSIS OF BOREHOLE IMAGE

Located in the southwest of Jinzhai County, Anhui Province, Shapingou Molybdenum Mine is China's largest existing proven porphyry molybdenum deposit. It is classified as an ultra-large type with 500,000 tons of Molybdenum reserve according to preliminary estimate. The mining area locates at the east section of Qinling-Dabie Mountain Molybdenum metallogenic belt, and Northeast to the intersection of North-West-West Tongbai-Mozitan Deep Fault and the secondary Yinshan-Sihe Fault of North-East Shangma Fault. Magmatic activities are frequent in the region. Acid-intermediate alkaline magmatic rock in Late Yanshanian is largely distributed [10]. Most of the overlying strata are eroded, exposing breccias and various brecciform geological bodies in the center. There are various types of magmatic rocks, ranging from ultra basic, acid to alkaline rocks. Rock types include explosion breccias, quartz syenite, biotite syenite, medium and fine-grained monzogranite and plagioclase amphibolite. They provide favorable conditions for the formation of molybdenum ores.

Borehole ZK61 is 1201.9 m deep, and there are visible molybdenum ores with thickness of 689 m at the depth range of 512 - 1201 m. Due to limits of casing pipe and water quality in the bottom of the borehole, the actual borehole camera prospecting range is 104 - 880 m. Through the borehole wall image based on borehole camera technology and rock core image, main rock color of borehole ZK61 is gray white while the main types of rock consist of quartz syenite, biotite syenite, medium and fine-grained monzogranite and plagioclase amphibolite. Main ore body color is taupe as shown in Fig. 5.

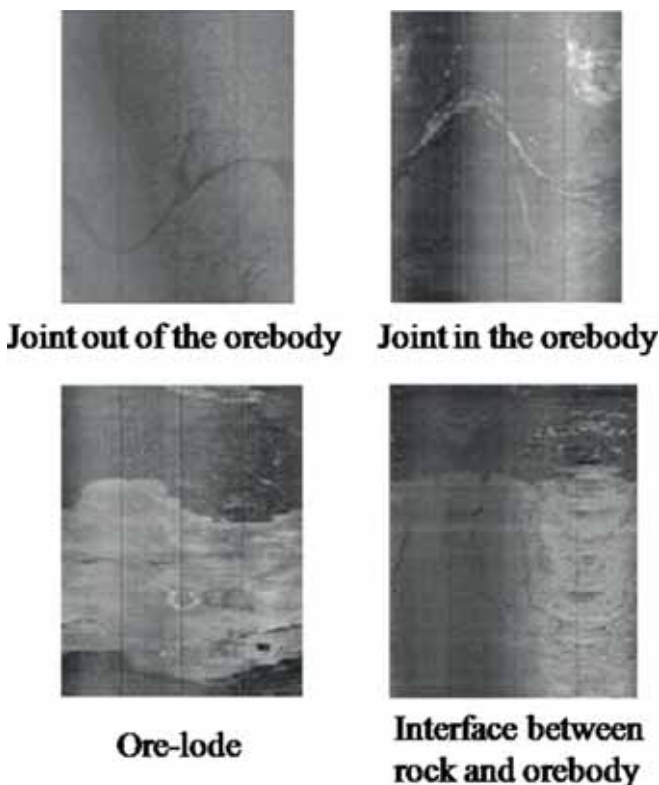


Fig. 5. Different discontinuities in borehole ZK61

## STATISTICAL ANALYSIS OF JOINTS IN BOREHOLE

Parameters including occurrence, depth and width in more than 741 joints are calculated based on digital borehole camera technology in order to fully reflect geological features of rock-ore in deep borehole. Due to the large number of joints and great differences in genetic type, formation period and distribution region, Advisable statistical method is used in this research for the statistics of joints [1, 2]. The results are as follows:

(1) Statistical analysis of the occurrence data is implemented to calculate the dominant occurrence with the assumption that joints causes of formation and distribution region are ignored. The results show that the dominant occurrences are  $N78^{\circ}E\angle55^{\circ}$ ,  $S61^{\circ}E\angle57^{\circ}$ ,  $S3^{\circ}E\angle61^{\circ}$ ,  $N72^{\circ}W\angle43^{\circ}$ .

(2) According to the respective statistical analysis of joints in area outside of orebody and area within orebody, it shows: orientation distribution for joints outside of the orebody is relatively scattered, and there is no prominent dominant orientation; dominant orientation within the orebody is  $S58^{\circ}E\angle23^{\circ}$  and  $S57^{\circ}E\angle51^{\circ}$ .

(3) For the typical geological interfaces between orebody and rock, specialized statistical analysis is needed to carry out. The result shows that:

- I) distribution of joints outside of orebody is dispersed with no obvious dominant occurrence;
- II) distribution of joints in orebody is more concentrated;
- III) Occurrence of several larger width joints is similar.

## ANALYSIS OF ORE-LODES EXTENSION

### CORRELATION ANALYSIS ON JOINTS OCCURRENCE AND ORE-LODES EXTENSION

Orebody is natural aggregates of mineral with a variety of different forms, occurrence and scales which embeds in the crust or the surface of the earth. Its geometry figure is decided by the mineralization and the ore controlling geological factors such as strata, rock and tectonic. Ore-lode is tabular orebody formed in all kinds of rock joints that its occurrence is similar with joints in the rock and orebody. In terms of prediction and prospecting, the distribution and characteristics of potential orebody can be deduced based on the research of joints and ore-lodes. These are "interface mineralization theory" about deposit mineralization [9, 11].

The interfaces in "interface mineralization theory" are geological surfaces as shown in Fig. 6 including: 1) the physical and chemical conditions exchange interface of the ore fluid; 2) joints of ore-forming structures; 3) interlayer gliding surface; 4) intrusive contact surface; 5) conversion surface of siliceous and calcareous rock; 6) transition surface of basic and ultra basic rock; 7) sediment interface; 8) sedimentary discontinuity.

There is transport process of minerals in most deposits metallogeny process and most deposits show a certain pattern. The interfaces and mutation belts which are significant different in physicochemical properties are often the physical

and chemical barriers of ore fluid migration on the road and these are the emplacement of the deep orebody. This theory makes it possible to analyze the extension of deep pre-lodes. Combined with the deposit mainly vertical change type as shown in Fig.6, this research can provide accurate basic data analysis for prediction of extension direction of ore-lodes based on shape and occurrence information of ore-joints.

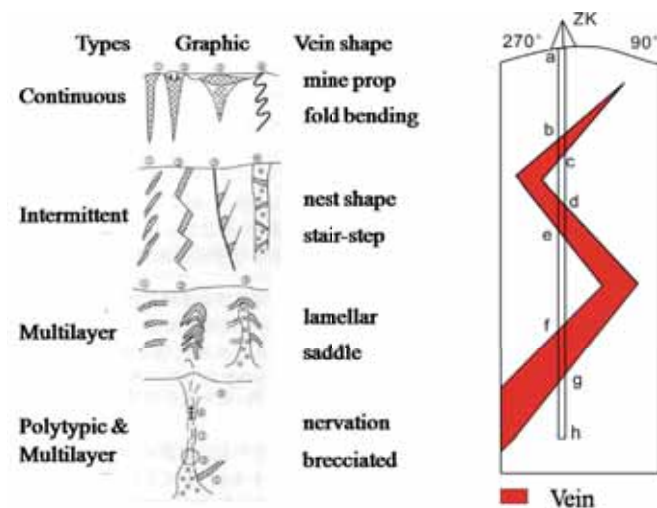


Fig. 6. The main change types of deposit and sketch of drilling cutting through the vein

## ANALYSIS OF DEEP ORE-LODES EXTENSION DIRECTION

Statistical results of rock-ore joints in Shapinggou Molybdenum Mine are shown in Tab. 1. The dominant occurrences of joints in rock stay the same as joints in ore body: orientation distribution concentrates in 105~139° and dip angle distribution concentrates in 55~78°. The dominant occurrences of several rock-ore interface are 118°∠67°, 115°∠63°, 129°∠61°.

Tab. 1. Comparison of different discontinuities

Types of Joints	Depth	Dominant Orientation
In rock	387.2~511.8	none
In orebody	512.5~1201.9	114~139° ∠65~73°
Interface	583.5	118° ∠67°
	622.3	115° ∠63°
	637.2	129° ∠61°

In conclusion, the dominant occurrences of joints in borehole ZK61 show some regularity that orientation and dip angle are in a certain range. Based on interface mineralization theory, this regularity can reveal the extension of deep ore-lodes in certain. The dominant occurrences of joints in rock are close to joints in ore body regardless of regional distribution and output form, so we can analyze the extension of ore-lodes especially large ore-lodes. The result in this article will provide the basis for guiding drilling borehole position and mineral reserves evaluation.

## CONCLUSION

Through the investigation of borehole mine jointed rock mass, the different packet structure distribution is obtained

and it provides basic data for the correct evaluation of the extension direction of vein.

According to interface of metallogenic theory and based on dominant occurrence of different packet discontinuities in rock and ore body, a conclusion is verified that dominant occurrence in and out of ore body stays the same as dominant occurrence in the whole borehole. Analysis of the relationship between the joint fissure advantage occurrence and extension direction of vein is developed and the results have the important guiding significance for the next deep prospecting.

## ACKNOWLEDGMENTS

This study is subsidized by National Natural Science Foundation of China (41402278) and by Strategic Research Program of the Chinese Academy of Sciences (XDB10030200).

## REFERENCES

1. CHEN Jian-ping, SHI Bing-feng, WANG Qing. Study of the dominant orientations of random fractures of fractured rock masses[J]. Chinese Journal of Rock Mechanics and Engineering, 2005, 24(12): 241-245.
2. JIANG Jian-ping, ZHANG Yang-song, LUO Guo-yu, et al. The application of preferred plane theory to geotechnical engineering practice [J]. Journal of Hydraulic Engineering. 2001, 16(8): 90-96.
3. John Kemeny, Randy Post. Estimating three-dimensional rock discontinuity orientation from digital images of fracture traces [J]. Computers & Geosciences, 2003, 9: 65-77.
4. PRENSKY S E. Advances in borehole imaging technology and application[C]//Borehole Imaging: Applications and Case Histories. London: Geological Society, 1999: 1-43.
5. WANG Chuan-ying, LAW KTIM. Review of borehole camera technology[J]. Chinese Journal of Rock Mechanics and Engineering, 2005, 24(19): 3440-3448. TR-07-56, Vicksburg, Mississippi: US Army Engineer Research and Development Center, 168p.
6. WANG Chuan-ying, ZHONG Sheng, SUN Wei-chun. Study of connectivity of discontinuities of borehole based on digital borehole images[J]. Chinese Journal of Rock Mechanics and Engineering, 2009, 28(12): 2405-2410.
7. WANG Chuan-ying, GE Xiu-run, BAI Shi-wei. The digital panoramic borehole camera system and its application[J]. Rock and Soil Mechanics, 2001, 22(4): 523-526.
8. WANG Jin-liang, LI Jun-ping, LI Yong-feng, et al. The current research situation and suggestions of deep exploration for crisis mines[J]. Conservation and Utilization of Mineral Resources, 2010, 4(2): 45-49.

9. ZHANG Shou-ting; ZHAO Peng-da; CHEN Jian-ping, et al. Multitarget minerals prediction and assessment and their significance[J]. Journal of Chengdu University of Technology, 2003, 30(5): 441-446.
10. ZHANG Huai-dong, SHI Dong-fang, Hao Yue-jin, et al. Geological features of the Shapinggou porphyry molybdenum ore deposit, Jinzhai country, Anhui province [J]. Geology of Anhui, 2010, 20(2): 104-108.
11. Zhao Peng-da. Quantitative mineral prediction and deep mineral exploration[J]. Earth Science Frontiers, 2007, 14(5): 1-10.

## CONTACT WITH AUTHOR

Zengqiang Han

Chuanying Wang

State Key Laboratory of Geomechanics and  
Geotechnical Engineering  
Institute of Rock and Soil Mechanics  
Chinese Academy of Sciences  
Wuhan Hubei  
430071 China

tel: +86 027 87197362,

fax:+86 027 87197362

e-mail: zqhan@whrsm.ac.cn

Hengyin Zhub

No.313 Geological Party of Anhui Bureau of Geology  
and Mineral Exploration  
Luan  
China

# ASSESSING THE ACCURACY OF SRTM DEM AND ASTER GDEM DATASETS FOR THE COASTAL ZONE OF SHANDONG PROVINCE, EASTERN CHINA

Shaopeng Luana<sup>c, d</sup>

Xiyong Hou<sup>a</sup>

Yetang Wang<sup>b</sup>

- a) Yantai Institute of Coastal Zone Research, Chinese Academy of Sciences, Yantai, China
- b) College of Population, Resources and Environment, Shandong Normal University, Jinan, China
- c) University of Chinese Academy of Sciences, Beijing, China
- d) Geomatics Center of Yantai City

## ABSTRACT

*This study assessed the performance of recently released 3 arc second SRTM DEM version 4.1 by CSI-CGIAR and 1 arc second ASTER GDEM version 1 and version 2 by METI-NASA in comparison with ground control points from 1:50000 digital line graphs for the coastal zone of Shandong Province, Eastern China. The vertical accuracy of SRTM DEM is 13.74 m root mean square error (RMSE), and GDEM version 1 reaches 24.11 m RMSE. Version 2 of ASTER GDEM shows better performance than version 1 and SRTM DEM with a RMSE of 12.12 m. A strong correlation of the magnitude of elevation error with slope and elevation is identified, with larger error magnitudes in the steeper slopes and higher elevations. Taking into account slope and elevation has the potential to considerably improve the accuracy of the SRTM DEM and GDEM version 1 products. However, this improvement for GDEM version 2 can be negligible due to their limited explanatory power for the DEM elevation errors.*

**Keywords:** Elevation errors, SRTM DEM, ASTER DEM

## INTRODUCTION

Chinese coastal zones are vulnerable to coastal flooding resulting from future sea-level rise due to the rapid developments of densely populated deltas and large growing cities [13]. The threats are becoming potentially strong because of the predicted sea level rise of over 1m in this century [16]. A high resolution DEM can three-dimensionally represent beach erosion, flooding, and natural and man-made features on the coastal zones. This will enable us to better understand the associated vulnerability and risks and determine our responses to the risks. A high precise DEM is also required for hydrological studies [1, 11, 28], glacial mass loss assessment [14], orthorectification of satellite images [27], vegetation cover studies [18], and spatial dataset construction (e.g., gridded surface temperature and stable isotopic composition over Antarctica) [25, 26]. In general, DEM data sets can be created by means of ground survey, photogrammetric techniques, radar altimetry, radar interferometry, and stereoscopic pairs. Among them, Spaceborne Interferometric SAR (InSAR) and

stereoscopic pair from Earth Observation Satellites are two promising technologies for obtaining elevation information at a global or regional scale.

In February 2000, the Shuttle Radar Topography Mission (SRTM) spearheaded by the National Geospatial-Intelligence Agency (NGA), NASA, the Italian Space Agency (ASI) and the German Aerospace Center (DLR) provides the first spatially continuous elevation information covering more than 80% of the Earth's land [15]. The SRTM data has a spatial resolution of 3 arc second (approximately 90m) which is available for the Earth land between latitudes 57oS and 60oN, and 1 arc second (approximately 30m) only for the United States. Despite global coverage of SRTM data, considerable voids occur in water-body and some steep mountainous regions due to the incorrect radar reflection, and excessive atmospheric interference coherence [10]. The voids impede the utilization of the SRTM data for certain applications, for instance, for hydrological modeling. Many attempts have been made to fill the data gaps by spatial

filters, iterative hole filling, and interpolation techniques developed by the Consortium for Spatial Information of the Consultative Group for International Agricultural Research (CSI-CGIAR) [9], since the first release of SRTM data set in 2004. The latest refined SRTM DEM (version 4.1) by CSI-CGIAR is available at no charge for any users at: <http://srtm.csi.cgiar.org/>. While many validations of this product have been performed at global and regional scales due to its great potential use [5, 7, 19], more regional evaluations would give more benefits to global users due to the various SRTM elevation biases from one region to another.

Recently, much attention has been paid to the release in July 2009 and October 2011 of the Global Digital Elevation Models (GDEM) generated from Advanced Spaceborne Thermal Emission and Reflection Radiometer (ASTER) stereo images by the Ministry of Economy, Trade, and Industry (METI) of Japan and the United States National Aeronautics and Space Administration (NASA) due to their free and widespread accessibility. Compared to the SRTM DEM, ASTER GDEM has a higher spatial resolution (about 30 m), and a wider land surface coverage (83°N-83°S), especially covering some high latitude and steep mountainous regions beyond the coverage of SRTM. ASTER GDEM is therefore expected to be one of the best sources of global topographic data for various scientific applications. At a global scale, the elevation accuracy of version 1 of ASTER GDEM is estimated at 95% confidence as 20 meters by a comparison of ASTER GDEM with other reliable datasets [2]. Moreover, the version 2 greatly improved its accuracy upon version 1. Despite of much improvement of ASTER DEM, at local scale, it is still important to perform a case-by-case verification of the precision of GDEM data for understanding the potential and limitations in its application in a specific region.

Our main objective is to evaluate the quality of SRTM DEM (version 4.1) and ASTER GDEM version 1 and version 2 in terms of vertical accuracy in the coastal zone of Shandong Province, China using ground control points from 1:50000 topographic maps.

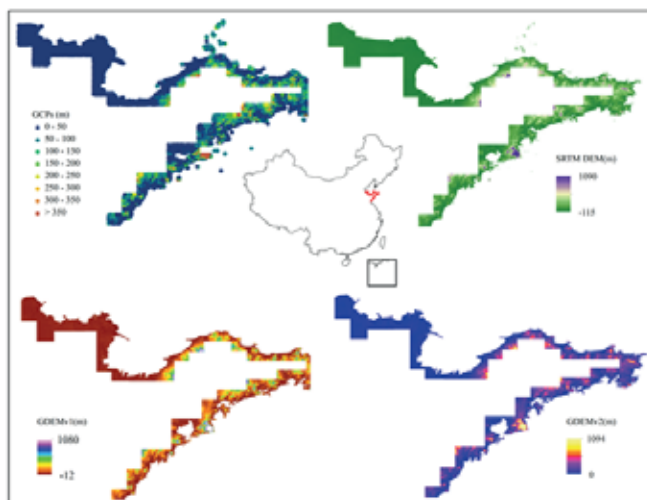


Fig. 1. Location of study area, ground control points (GCPs) from 1:50000 digital line graphs, SRTM DEM, ASTER GDEM version 1 and ASTER DEM version 2

## STUDY AREA

Our study focuses in the coastal zone of Shandong Province, located at the East China seaboard and lower reach of the Yellow River (Fig. 1). It faces the Bohai Sea in the north, and the Yellow Sea in the east. With a total length of 3024 km, coastline of Shandong Province accounts for one sixth of total length in China. The relief varies from the Yellow River delta plain in the northwest, and coastal plain in the southeast, to hilly regions along the eastern peninsula. The elevations range from 0 (in some areas a few metres below mean sea level) to more than 800m above sea level.

## DATA AND METHODS

The version 4.1 SRTM DEM is the latest version post-processed by CSI-CGIAR. The data set improves significantly on the original versions by filling voids based on the new interpolation algorithms and better additional DEMs [8, 9]. In addition, in this data set, the high resolution shoreline information generated by the US Geological Survey [23] was used to distinguish land and ocean regions. The SRTM DEMs are provided in 5°×5° tiles with both Arc-Info ASCII format and GeoTiff.

ASTER GDEM version 1 (GDEMv1) was generated from VNIR Band 3N of all the existing ASTER images during 1999-2008. The data are available for easy download as 1°×1° tiles at 1 arc-second (30 m) resolution with geographic lat/long coordinates. A quality assessment file is included in each 1°×1° tile to demonstrate the number of images used for the elevation generation at each pixel and the location if elevation anomalies have been corrected. Preliminary validation of GDEMv1 showed the vertical accuracy with a root mean square error (RMSE) of 10-25 m [2]. However, GDEMv1 contains some significant anomalies resulting from cloud, artifacts associated with irregular stack boundaries such as pits, bumps and mole runs, and water masking issues [2]. A new version of the ASTER GDEM (GDEMv2) with the same grid and tile structure as GDEMv1 was released in mid-October, 2011 by the joint of NASA and METI. The voids and artifacts in GDEMv2 greatly declined, even eliminated in some regions by the improvement in spatial coverage using 260000 additional scenes, spatial resolution based on a smaller correlation kernel, and water masking [3].

To explore the difference in SRTM DEM and GDEM, 13244 ground control points (GCPs) were collected from elevation point layer of 1:50000 digital line graphs (DLGs) derived from vertical aerial photographs. The horizontal accuracy of GCP was estimated to be less than 25 m and vertical accuracy less than 2.5 m [20]. The GCP elevation data were initially referenced to the 1985 Yellow Sea Datum, and horizontally georeferenced to the Xi'an 1980 reference system, while the datum of SRTM DEM and GDEM is WGS 1984 with EGM96. The GCP locations were converted to WGS 1984 reference system using a seven seven-parameter spatial transform model. The error of coordinate conversion was less than 0.02 m [24]. A vertical transformation between 1985 Yellow Sea Datum and EGM96 are not required due to their negligible difference

(a few centimeters in East China, [29, 30]) for SRTM and GDEM accuracy assessment.

Vertical accuracies of SRTM DEM and GDEM were assessed by comparing the difference between the GCP elevation and the corresponding DEM value. Since the GCPs are not directly in accord with a DEM point location, for every control point location, the corresponding DEM elevation was extracted through the bilinear interpolation. Positive differences mean the interpolated DEM elevation was below the GCP elevation. Negative errors represent the locations where the DEM elevation was above GCP elevation. Three dimension spatial analysis tools available at the commercial software ArcGIS version 9.3 were applied to calculate the slope and slope aspect of SRTM DEM and GDEM at the location of each GCP. The extracted slope aspect were classified to one category with a value of -1 for flat terra and 8 categories with a width of 45° (i.e., North, Northeast, East, Southeast, South, Southwest, West and Northwest). Summary statistics of SRTM DEM and GDEM errors are expressed by the standard deviation, mean absolute error and root mean square error. We also quantified the relationship between the errors and topographic variables such as altitude, slope, and aspect using the software SPSS 13.

## RESULTS

### ACCURACY OF SRTM DEM, GDEMv1, AND GDEMv2

Fig. 2 shows frequency distribution of SRTM DEM, GDEMv1, and GDEMv2 errors determined from a comparison to GCP elevations from 1:50000 scale topographic maps. Table 1 quantifies the accuracy of the SRTM DEM, GDEMv1 and GDEMv2 for the coast zones of Shandong Province. The errors of SRTM DEM, GDEMv1 and GDEMv2 ASTER exhibit similar frequency distribution patterns with the more number of positive errors than the negative (Fig. 2). However, the errors of SRTM DEM and GDEMv2 are more concentrated at near medium values than those of GDEMv1. Furthermore, the range of GDEMv1 error with a maximum of 169 m, and a minimum of -49 m is broader than other two DEMs. The basic statistics for these difference shows that the mean SRTM DEM elevations are about 7.1 m lower than GCP elevations, ASTER GDEMv1 are about 12.3 m lower, and GDEMv2 are around 3.8 m lower, implying a general underestimation of topographic elevation by the SRTM DEM, GDEMv1 and GDEMv2 (Fig. 2 and Table 1).

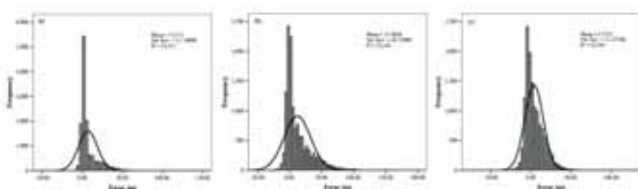


Fig. 2. Error distribution histogram of (a) SRTM DEM; (b) GDEMv1; (c) GDEMv2

The accuracy of SRTM DEM as determined using our benchmarks is 11.75 m standard deviation, and 13.74 m RMSE. GDEMv1 presents relative large residual errors with a standard

deviation of 20.72 m and an RMSE of 24.11 m. Compared to the GDEM version 1, the accuracy of version 2 (GDEMv2) greatly improved with 11.52 m standard deviation and 12.12 m RMSE. Linear regression of the relationships between GCP elevations and SRTM DEM, GDEMv1 and GDEMv2 yields very high determination coefficients of 0.991, 0.966 and 0.988, respectively (not shown), and thus there are significant correlations between GCP elevations and the three DEMs. All the slopes of the regression lines slightly below 1 probably show that the three DEMs tend to increasingly underestimate GCP elevation with increasing elevation.

Tab. 1. Statistical analysis of the deviation of SRTM DEM, ASTER GDEM version 1 and version 2 from GCP data

Comparison	Mean	Standard deviation	RMSE	Minimum	Maximum
GCPs-SRTM	7.11	11.75	13.74	-30	150
GCPs-GDEMv1	12.31	20.72	24.11	-49	166
GCPs-GDEMv2	3.76	11.53	12.12	-69	109

### RELATIONSHIP OF ELEVATION ERROR WITH ELEVATION IN DEMS, SLOPE AND ASPECT

Plots of the elevation errors vs. elevations in the three DEMs and slope angle indicate strong positive correlations between the magnitudes of elevation error and both elevation and slope angle (Fig. 3). To estimate the strength of the relationships, we calculated the goodness of linear fit ( $R^2$ , the coefficient of determination), which gives the amount of the variation in one variable that can be accounted for by another variable. The slope angle explained 70.2% of the SRTM DEM elevation error variance. 59.2% of the variation of elevation error magnitudes can be accounted for by elevation in SRTM DEM. For GDEMv1, the slope angle and elevation account for 64.8% and 44.6% of the variation in elevation error magnitudes, respectively. However, the slope angle and elevation has little explanatory power for the GDEMv2 elevation errors. A multiple regression model based on the variables used to predict the elevation errors in the three DEMs are expressed as follows:

$$\text{elevation error} = \alpha \text{slope} + \beta \text{elevation} + \epsilon. \quad (1)$$

Where  $\alpha$  and  $\beta$  are model coefficients, and  $\epsilon$  is residual. The overall adjusted  $R$ -squared is 0.723 for SRTM DEM elevation error model, 0.673 for GDEMv1 error model, only 0.348 for GDEMv2 elevation error model.

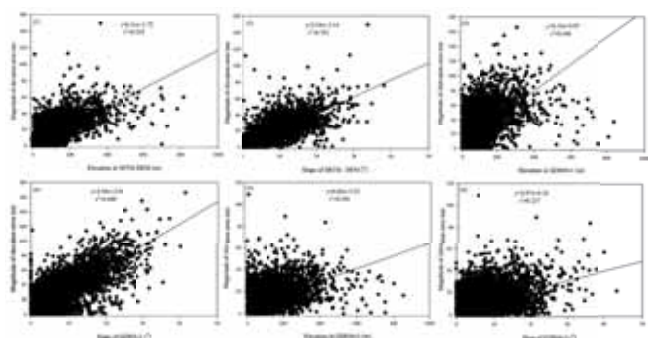


Fig.3. Plots showing relationship between the elevation error magnitudes of SRTM DEM, GDEMv1 and GDEMv2 and slope angle and elevation

Although there is no significant correlation between elevation error and slope aspect, elevation accuracy of SRTM and GDEMv1 varies greatly at different direction classes (Fig. 4). SRTM DEM has the best elevation accuracy in the East with a RMSE of about 6.5 m, standard deviation of 6 m and mean absolute error (MAE) of about 3.5 m, and worst accuracy in the West with about 18 m RMSE, 14 m standard deviation and 12 m MAE. For GDEMv1, the values of RMSE are approximately 14 m in the South and Southeast, increases for West and East, and reaches the maximum of approximately 40 m for the North. The mean absolute error and standard deviation exhibit a similar pattern. Similar elevation error in each direction for GDEMv2 shows the aspects do not significantly affect the elevation accuracy of GDEMv2 (Fig.4).

Variance in elevation error explained by slope is strongly linked with magnitude of elevation errors in aspect category: the larger the error in the class aspect is, the more variance in elevation error accounted for by slope is (Fig.4). For instance, the variance of SRTM elevation error explained by slope angle reaches 76.4% in the Northwest, corresponding to the maximum error in the aspect.

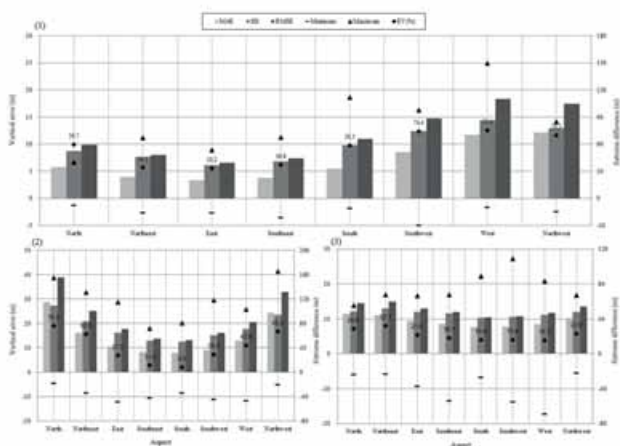


Fig. 4. Basic statistics of the vertical accuracy of the SRTMDEM version 4.1, ASTER GDEM version 1 and ASTER GDEM version 2 across all aspects (MAE: mean absolute error; SD: standard deviation, RMSE: and EV: explained variance by slope)

## DISCUSSION

SRTM DEM and ASTER GDEMv1 and GDEMv2 closely correspond to GCP elevation from 1:50000 scale topographic maps. However, there is still a negative bias in the SRTM DEM and ASTER GDEM elevations with respect to the GCPs. The difference between the Yellow Sea Datum and WGS84-EGM96 heights may at least partly contribute to the phenomenon.

While officially stated vertical accuracy of SRTM DEM is  $\pm 16$  m at 90% confidence, global accuracy varies over different regions [17, 21]. The accuracy of SRTM DEM in Eurasia is 16.09 m standard deviation in comparison with satellite radar altimetry [4]. Based on GCPs, vertical errors are estimated to be about 6 m in the Western Australia [7], 8.5 m (at 90% confidence) for North America [8, 23]. Centimeter-accurate real-time kinematic GPS (RTK-GPS) surveying indicated SRTM DEM elevation error in North Greece is 6.4 m [9], 7.58

m in Phuket (USA) [5], and 4.07m in Catskillsa (Thailand) [5]. This study yields elevation errors in SRTM DEM for coastal zones of Shandong Province with a standard deviation of 11.75 m by the comparison of GCP elevation and bilinear interpolation of DEM.

There are artifacts and residual anomalies in the ASTER GDEMv1, and thus it is regarded as “experimental” or “research grade.” In the GCP comparisons, GDEMv1 showed the lowest accuracy with RMSE values of about 24 m. However, this still agrees with the above mentioned accuracy range of GDEMv1 elevations (10-25 m RMSE, ASTER Validation Team, 2009). GDEMv2 greatly improved its accuracy with a RMSE of 12.12 m on the version 1, in accord with the validation by the joint effort between Japan and the United States [3].

The accuracy of the three DEMs decreased as surface slope became steeper, and the elevation became higher, agreeing with the previous studies that surface relief play an important role in the DEM accuracy [5, 19, 22, 30]. The impact of surface slope appears to be much more profound than the contribution of elevation for the accuracy of SRTM DEM and GDEMv1 because of large errors occurring at low elevations with considerable slopes. However, elevation explains more variance of GDEMv2 error than slope despite of their limited explanatory power (Fig. 3). Slope and elevation data derived from the SRTM DEM and GDEMv1 can better predict the elevation errors in the two DEMs. A multiple regression model based on the variables explained 72.3 % and 67.3% of the total variation in SRTM error and GDEMv1 error, respectively.

## CONCLUSION

This study evaluated the quality of SRTM DEM, ASTER GDEMv1 and GDEMv2 and their accuracy as a function of slope and elevation. GDEMv2 generally proved to be more accurate than SRTM DEM and GDEM. Incorporating slope and elevation into a multiple regression model will substantially improve the accuracy of SRTM DEM and GDEM. Due to the higher resolution, fewer voids and higher accuracy than SRTM DEM, GDEM version 2 would be widely used in coastal environment studies.

## ACKNOWLEDGMENTS

Funding this study was from CAS “Strategic Priority Research Program-Climate Change: Carbon Budget and Relevant Issues” (XDA05130703), China Academy of Sciences Key deployment project (KZZD-EW-14), and Shandong province High School Science & Technology Project (J11LE12).

## REFERENCES

1. Andersson, J.O. Nyberg, L., Using official map data on topography, wetlands and vegetation cover for prediction of stream water chemistry in boreal headwater catchments, Hydrology and Earth System Science, Vol.13, pp. 537–549, 2009.

2. ASTER GDEM Validation Team, ASTER global DEM validation summary report. METI & NASA, 28pp, 2009.
3. ASTER GDEM Validation Team, ASTER global DEM validation summary report. METI & NASA, 25pp, 2011
4. Berry, P. A. M., Garlick, J. D., Smith, R. G., Near-global validation of the SRTM DEM using satellite radar altimetry, *Remote Sensing of Environment*, Vol. 106, pp. 17–27, 2007.
5. Gorokhovich, Y., Voustantiouk, A., Accuracy assessment of the processed SRTM-based elevation data by CGIAR using field data from USA and Thailand and its relation to the terrain characteristics, *Remote Sensing of Environment*, Vol. 104, pp. 409–415, 2006.
6. Guo, H., Jiao, W., Yang, Y., Liu, G., Systematic error of the 1985 National Height Datum, *Geomatics and Information Science of Wuhan University*, Vol. 29, pp.715–719, 2004.
7. Hirt, C., Filmer, M. S., Featherstone, W. E., Comparison and validation of the recent freely available ASTER-GDEM ver1, SRTM ver4.1 and GEODATA DEM-9S ver3 digital elevation models over Australia, *Australia Journal of Earth Sciences*, Vol. 57, pp. 337–347, 2010.
8. Jarvis, A., Reuter, H. I., Neson, A., Guevara, E., Hole-filled SRTM for the globe Version 4, Available from the CGIAR-SXI SRTM 90m database: <http://srtm.csi.cgiar.org>, 2008.
9. Jarvis, A., Rubiano, J., Nelson, A., Farrow, A., Mulligan, M., Practical use of SRTM data in the tropics – Comparisons with digital elevation models generated from cartographic data, Working Document No. 198. Cali, International Centre for Tropical Agriculture (CIAT): 32 pp, 2004.
10. Kääb, A., Combination of SRTM3 and repeat ASTER data for deriving alpine glacier flow velocities in the Bhutan Himalaya, *Remote Sensing of Environment*, Vol. 94, pp. 463–474, 2005.
11. Lin, S., Jing, C., Chaplot, V., Yu, X., Zhang, Z., Moore, N., Wu, J., Effect of DEM resolution on SWAT outputs of runoff, sediment and nutrients, *Hydrology and Earth System Science Discussion*, Vol. 7, pp. 4411–4435, 2010.
12. Mouratidis, A., Briole, P., Katsambalos, K., SRTM 3" DEM (versions 1, 2, 3, 4) validation by means of extensive kinematic GPS measurements: a case study from North Greece, *International Journal of Remote Sensing*, Vol. 31, pp. 6205–6222, 2010.
13. Nicholls, R. J., Cazenave, A., Sea-level rise and its impact on coastal zones, *Science*, Vol. 328, pp.1517–1519, 2010.
14. Peduzzi, P., Herold, C., Silverio, W., Assessing high altitude glacier thickness, volume and area changes using field, GIS and remote sensing techniques: the case of Nevado Coropuna (Peru), *The Cryosphere*, Vol. 4, pp. 313–323, 2010.
15. Rabus, B., Eineder, M., Roth, A., Bamler, R., The shuttle radar topography mission—a new class of digital elevation models acquired by spaceborne radar, *ISPRS Journal of Photogrammetry and Remote Sensing*, Vol. 57, pp. 241–262, 2003.
16. Rahmstorf S., A new view on sea level rise, *Nature Reports: Climate Change*, Vol. 4, pp. 44–45, 2010.
17. Rodriguez, E., Morris, C. S., Belz, J. E., Chapin, E. C., Martin, J. M., Daffer, W., Hensley S., An assessment of the SRTM topographic products, Technical Report JPL D-31639. Pasadena, California: Jet Propulsion Laboratory 143 pp, 2005.
18. Sharma, B. D., Clevers, J., De Graaf, R., Chapagain, N. R., Assessing the land cover situation in Surkhang, Upper Mustang, Nepal, using an ASTER image, *Him. J. Sci.*, Vol. 1, pp. 93-98, 2003.
19. Shortridge, A., Messina, J., Spatial structure and landscape associations of SRTM error, *Remote Sensing Environment*, Vol. 115, pp.1576–1587, 2011.
20. State Bureau of Technical Supervision: Specifications for aerophotogrammetric office operation of 1:25000, 1:50000, 1:100000 topographic maps, Beijing: Standards Press of China, 2008.
21. Suna, G., Ranson, K. J., Kharukc, V. I., Kovacs, K., Validation of surface height from shuttle radar topography mission using shuttle laser altimeter, *Remote Sensing Environment*, Vol. 88, pp. 401–411, 2003.
22. Toutin T., Impact of terrain slope and aspect on radargrammetric DEM accuracy, *ISPRS Journal of Photogrammetry and Remote Sensing*, Vol. 57, pp. 228–240, 2002.
23. US Geological Survey, SRTM Water Body Data Set, Web document. <http://edc.usgs.gov/products/elevation/swbd.html> (accessed 28.July 2009), 2003.
24. [24] Wang, J. X., Wang, J., Lu, C. P., Problem of coordinate transformation between WGS-84 and BEIJING 54, *Journal of Geodesy and Geodynamics*, Vol. 23, pp. 70–73, 2003. (In Chinese)
25. Wang, Y., Hou, S., Masson-Delmotte, V., Jouzel, J., A generate additive model for the spatial distribution of stable isotopic composition in Antarctic surface snow, *Chemical Geology*, Vol. 271, pp.133–141, 2010.

26. Wang, Y., Hou, S., Spatial distribution of 10m firn temperature in the Antarctic Ice Sheet, *Science in China: Earth Science*, Vol. 54, pp. 655–666, 2011.
27. Wang, Y, Hou, S., Liu, Y., Glacier change in the Karlik Mountain, Eastern Tien Shan during 1971/72-2001/02 using remote sensing data and GIS technology, *Annals of Glaciology*, Vol. 50, pp.39–45, 2009.
28. Wechsler, S. P., Uncertainties associated with digital elevation models for hydrologic applications: a review, *Hydrology and Earth System Science*, Vol. 11, pp.1481–1500, 2007.
29. Zhai, Z., Wei, Z., Wu, F., Ren, H., Computation of vertical deviation of Chinese height datum from geoid by using EGM 2008 model, *Journal of Geodesy and Geodynamics*, Vol. 31, pp.116–118, 2011. (In Chinese)
30. Zhao, S., Cheng, W., Zhou, C., Chen, X., Zhang, S., Zhou, Z., Liu, H., and Chai, H., Accuracy assessment of the ASTER GDEM and SRTM3 DEM: an example in the Loess Plateau and North China Plain of China, *International Journal of Remote Sensing*, Vol. 32, pp. 8081–8093, 2011.

## CONTACT WITH AUTHOR

Shaopeng Luan

Xiyong Hou

Yantai Institute of Coastal Zone Research  
Chinese Academy of Sciences  
Yantai  
264003 China

Yetang Wang

College of Population,  
Resources and Environment,  
Shandong Normal University,  
Jinan,  
250014, China

tel.: +86 531 86180646

fax.: +86 531 86180646

e-mail: wangyetang@163.com

Shaopeng Luan

University of Chinese Academy of Sciences,  
Beijing  
100049 China

Shaopeng Luan

Geomatics Center of Yantai City

# SIMULATION OF IRREGULAR WAVES IN A NUMERICAL WAVE TANK

Li Zhi-Fu<sup>a</sup>

Shi YuYun

Ren HuiLong<sup>a</sup>

Li Hui

Muhammad Aqeel Ashraf<sup>b, c</sup>

a) College of Shipbuilding Engineering, Harbin Engineering University, Harbin Heilongjiang, China

b) Department of Geology, Faculty of Science, University of Malaya, Kuala Lumpur, Malaysia

c) Faculty of Science & Natural Resources, Universiti Malaysia Sabah, 88400 Kota Kinabalu, Sabah, Malaysia

## ABSTRACT

*The time domain boundary element method was utilized to simulate the propagation of the irregular waves in a numerical wave tank. The problem was solved in a time-marching scheme, upon the irregular waves being fed through the inflow boundary, in which the theoretical solution was obtained from the wave energy spectrum. The open boundary condition was modeled by the multi transmitting formula (MTF), in which the phase velocity was calculated according to the Sommerfeld's condition. The velocity potential and wave elevation were directly obtained by integrating the free surface condition twice, with respect to time. The accuracy of the developed numerical scheme was verified by simulating the propagation of irregular waves. The numerical results show good agreements with the analytical solutions, which prove that the proposed scheme is a promising way to the simulation of wave-body interactions.*

**Keywords:** open boundary condition, Multi transmitting formula, Irregular waves, Boundary element method, Numerical wave tank

## INTRODUCTION

The Rankine panel method is a main way to simulate the interactions between floating structures and waves. The method has many merits in the simulation of nonlinear problems [1], ship motions with forward problems [5], varying bottom of ocean floor simulation [8] and hydroelasticity response of marine vessels [4].

However, if the Rankine panel method is utilized, it's necessary to truncate the computation domain into finite to save computer cost. And then the non-reflection boundary condition is needed to guarantee the accurate of the simulation. The Sommerfeld-Orlanski's condition have been widely used by researchers [6, 7], but it cannot give a good result for irregular waves simulation. Marching with linear solutions method is used by Liu [10, 11], but the computation cost is huge. The piston-like active wave absorber is also used in common [2, 3], but it is hard to be applied in 3D problems. Another frequently used method is the artificial beach [9], but some panels will be wasted. In addition to the above, the multi-transmitting formula method is also widely used by researchers [14, 15], but the phase velocity has to be set before the simulation, which is a limitation to the simulation of irregular waves.

The aim of this paper are, therefore, (1) to develop a numerical scheme to simulate the propagation of irregular waves in a numerical wave tank, (2) to find an efficient non-reflection open boundary condition for the Rankine panel method. The accuracy of the numerical scheme is verified by the comparison of analytical solutions with the numerical ones.

## MATHEMATICAL FORMULATION

The Cartesian coordinate system is adopted to describe the fluid motions, with its origin in the undisturbed free surface, x-axis positive to the wave propagation, and z-axis positive in the opposite direction of gravity, shown in Fig.1. The fluid is assumed to be ideal, incompressible, its motion is irrotational, and the surface tension is ignored. Then the velocity field can be described by the velocity potential.

$$\mathbf{V}(\bar{X}) = \left( \frac{\partial \phi}{\partial x}, \frac{\partial \phi}{\partial y}, \frac{\partial \phi}{\partial z} \right) \quad (1)$$

Due to the mass conservation, the fluid should satisfy the Laplace equation in the whole fluid domain.

$$\nabla^2 \phi = 0 \quad (2)$$

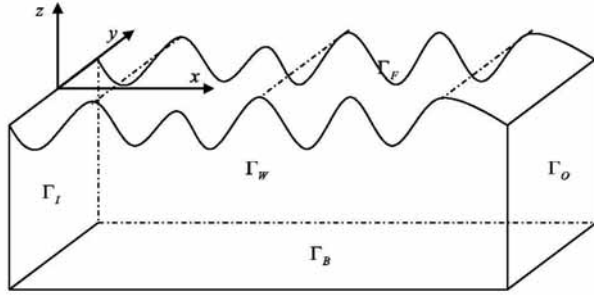


Fig.1. Coordinates system and computation domain

The kinematic boundary condition specifies that the free surface moves with the fluid particles, and the free surface kinematic boundary condition can be written as

$$\frac{\partial \zeta}{\partial t} + \frac{\partial \phi}{\partial x} \frac{\partial \zeta}{\partial x} + \frac{\partial \phi}{\partial y} \frac{\partial \zeta}{\partial y} - \frac{\partial \phi}{\partial z} = 0, \text{ on } \Gamma_F \quad (3)$$

The fluid pressure for the irrotational flow is determined by the Bernoulli's equation, and assuming the pressure on the free surface is constant, then the dynamic free surface condition can be obtained,

$$\frac{\partial \phi}{\partial t} + \frac{1}{2} \nabla \phi \cdot \nabla \phi + g \zeta = 0, \text{ on } \Gamma_F \quad (4)$$

The linear free surface conditions can be obtained from Eqn.(3) and Eqn.(4) by using a perturbation procedure. The kinematic and dynamic conditions are,

$$\frac{\partial \zeta}{\partial t} - \frac{\partial \phi}{\partial z} = 0, \text{ on } z = 0 \quad (5)$$

and

$$\frac{\partial \phi}{\partial t} + g \zeta = 0, \text{ on } z = 0 \quad (6)$$

By substituting (5) into (6) we can get

$$\frac{\partial^2 \phi}{\partial t^2} + g \frac{\partial \phi}{\partial z} = 0, \text{ on } z = 0 \quad (7)$$

Integrating (7) twice with respect to time, and using the trapezoidal numerical integral method as well as the initial conditions. Then at each time step, the velocity potential on the free surface can be written as

$$\phi(p, (n+1) \cdot \Delta t) = \phi(p, n \cdot \Delta t) - g \cdot \Delta t^2 \cdot \sum_{i=1}^n \frac{\partial \phi(p, i \cdot \Delta t)}{\partial z} \quad (8)$$

By using the same method, we can obtain the wave elevation in the time marching scheme.

On the lateral boundary, the rigid wall condition will be used, for the simulated waves are unidirectional,

$$\frac{\partial \phi}{\partial y} = 0, \text{ on } z = 0 \quad (9)$$

and the non-penetrating condition at the bottom boundary is

$$\frac{\partial \phi}{\partial z} = 0, \text{ on } \Gamma_B \quad (10)$$

To enclose the problem, the fluid domain should be truncated at some distance from the region of interest. Then an artificial boundary should be adopted, as will be described in the following sections.

$$\phi = \phi_{MTF}, \text{ on } \Gamma_O \quad (11)$$

## OPEN BOUNDARY CONDITION

Open boundary modeling is of great importance in the simulation of irregular waves in the time domain. Various approaches have been developed to accommodate the elliptical problem. In this research, the MTF was combined with the Sommerfeld's condition, in which the Sommerfeld's condition is used to evaluate the wave phase velocity, and for the short waves the damping zone method will be distributed near the open boundary, but with a very short damping length ( $\lambda_{\min}$ ).

The MTF for the non-reflecting boundary conditions was first proposed by Liao [10], via a direct simulation of one way wave propagation using a space-time extrapolation by an artificial wave speed. According to the theory of Liao, for the N-order MTF, the velocity potential on the open boundary can be written as

$$\phi((p+1)\Delta t, 0) = \sum_{j=1}^N (-1)^{j+1} C_j^N \cdot \phi((p+1-j)\Delta t, -j \cdot c_a \cdot \Delta t) \quad (12)$$

where  $C_j^n$  is the binominal coefficients

$$C_j^n = \frac{n!}{(n-j)! j!} \quad (13)$$

The Sommerfeld's radiation condition [13] is known as follows:

$$\frac{\partial \phi}{\partial t} + c \frac{\partial \phi}{\partial n} = 0, \text{ on } \Gamma_O \quad (14)$$

Combination of the dynamic free surface condition (6) and the Sommerfeld's condition (14) yields

$$c = \frac{g \zeta}{\phi_n} \quad (15)$$

Therefore, the artificial phase velocity can be calculated in the time marching scheme according to (15). In this paper, the 2-order MTF approximation formula will be used.

$$\phi(t + \Delta t, x) = 2\phi(t, x - c_a \cdot \Delta t) - \phi(t - \Delta t, x - 2c_a \cdot \Delta t) \quad (16)$$

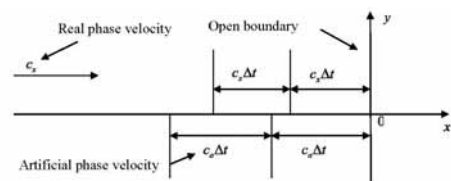


Fig.2. Sketch of multi-transmitting formula

## NUMERICAL METHODS

Various numerical approaches can be used to solve this initial boundary value problem mentioned above, among which the boundary element method has been widely used. The direct boundary integral equation to solve the prescribed boundary problem is derived using the Green's second identity.

$$2\pi\varphi(p, t + \Delta t) = \iint_S [G(p, q) \frac{\partial}{\partial n_q} \varphi(q, t + \Delta t) - \varphi(q, t + \Delta t) \frac{\partial}{\partial n_q} G(p, q)] ds_q \quad (17)$$

Two symmetry planes are utilized to model the half domain and exclude the bottom boundary. The resulting Green function is

$$G(p, q) = \frac{1}{R_1} + \frac{1}{R_2} + \frac{1}{R_3} + \frac{1}{R_4} \quad (18)$$

Where  $p(x, y, z)$  is the field point and  $q(\xi, \eta, \zeta)$  is the source point, and

$$R_1 = \sqrt{(x - \xi)^2 + (y - \eta)^2 + (z - \zeta)^2} \quad (19)$$

$$R_2 = \sqrt{(x - \xi)^2 + (y + \eta)^2 + (z - \zeta)^2} \quad (20)$$

$$R_3 = \sqrt{(x - \xi)^2 + (y + \eta)^2 + (z + \zeta + 2d)^2} \quad (21)$$

$$R_4 = \sqrt{(x - \xi)^2 + (y - \eta)^2 + (z + \zeta + 2d)^2} \quad (22)$$

## 4. EXPERIMENT RESULTS

### SIMULATION OF REGULAR WAVES

Before the simulation of irregular waves, it's necessary to verify the numerical schemes, by simulating the propagation of the regular waves. For the regular wave simulation, the boundary value problem was solved in the time marching scheme. The total simulation time was , and the time step was , and six panels for each wavelength. The range of wavelength is from to . The velocity potential time history of the partial record point was compared with the theoretical input waves, shown in Fig.3. The numerical results are in good agreement with the analytical ones, which indicates that the present model of the open boundary works well for the non-reflection condition.

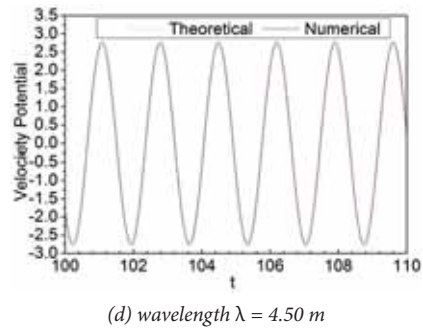
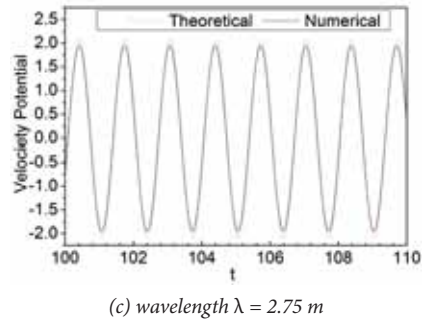
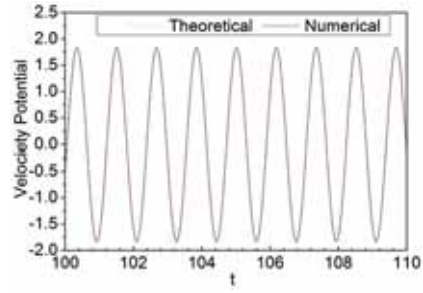
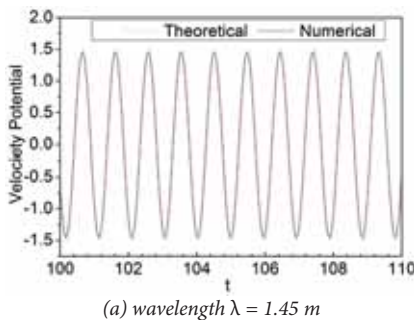
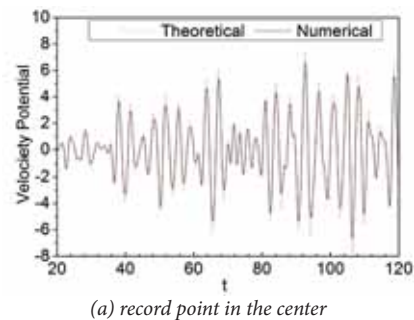
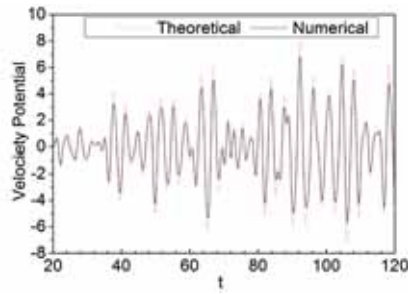


Fig.3. Time history of the simulated regular waves at the middle point

### SIMULATION OF IRREGULAR WAVES

The dimensions of the numerical wave tank was 10 m x 2 m x 2 m, six elements were distributed for one wavelength, and the time increment was set for  $T / 40$ , , The total simulation time was 200 s. The theoretical solutions were obtained from the wave energy spectrum, with the wave frequency domain 0.5 rad/s ~ 4.5 rad/s. The full records of the wave velocity potential were measured at the longitudinal tank center, which were compared with the theoretical waves. And the values of simulated waves agree fairly well with the theoretical solutions, shown in Fig.4.





(b) record point near  $\Gamma_1$

Fig.4. Time history of the simulated irregular waves

## CONCLUSIONS

In the present work, a time domain numerical program was implemented to the simulation of irregular wave propagations, and the boundary value problem was solved in the time marching procedure.

The non-reflection open boundary condition was modeled by the MTF, which can let the wave pass totally if the artificial phase velocity is similar to the real phase velocity. Through the combination of the Sommerfeld's condition with the kinematic free surface condition, the formula used to evaluate the phase velocity was derived. And then the wave simulation results were compared with the theoretical ones, including regular waves and irregular waves, respectively. The wave simulation results show excellent agreement with the theoretical values. After a series of numerical experiments, it has proven that the proposed non-reflection open boundary model can be applied to the simulation of wave-body interactions.

Further study may be done to predict the linear or nonlinear wave-body interactions using the proposed non-reflection open boundary condition.

## ACKNOWLEDGMENT

The authors gratefully acknowledge the financial support provided by the National Natural Science Foundation of China (Grant No. 51079034), and by the National Basic Research Program of China (Grant No. 2011CB013703).

## REFERENCE

- Bai, W. and R.E. Taylor, Higher-order boundary element simulation of fully nonlinear wave radiation by oscillating vertical cylinders. *Applied Ocean Research*, 2006. 28(4): p. 247-265.
- Brandini, C. and S. Grilli, Modeling of freak wave generation in a 3D-NWT. 2001.
- Clément, A., Coupling of two absorbing boundary conditions for 2D time-domain simulations of free surface gravity waves. *Journal of Computational Physics*, 1996. 126(1): p. 139-151.
- Das, S. and K.F. Cheung, Hydroelasticity of marine vessels advancing in a seaway. *Journal of Fluids and Structures*, 2012. 34(0): p. 271-290.
- He, G. and M. Kashiwagi, A time-domain higher-order boundary element method for 3D forward-speed radiation and diffraction problems. *Journal of Marine Science and Technology*, 2013. 19(2): p. 228-244.
- Isaacson, M. and K.F. Cheung, Second order wave diffraction around two-dimensional bodies by time-domain method. *Applied Ocean Research*, 1991. 13(4): p. 175-186.
- Jagannathan, S., Non-linear free surface flows and an application of the Orlandi boundary condition. *International journal for numerical methods in fluids*, 1988. 8(9): p. 1051-1070.
- Kim, T. and Y. Kim, Numerical analysis on floating-body motion responses in arbitrary bathymetry. *Ocean Engineering*, 2013. 62: p. 123-139.
- Kim, Y., D.C. Kring, and P.D. Sclavounos, Linear and nonlinear interactions of surface waves with bodies by a three-dimensional Rankine panel method. *Applied Ocean Research*, 1997. 19(5-6): p. 235-249.
- Liao, Z.-P., Extrapolation non-reflecting boundary conditions. *Wave Motion*, 1996. 24(2): p. 117-138.
- Liu, S.K. and A.D. Papanikolaou, Time-domain hybrid method for simulating large amplitude motions of ships advancing in waves. *International Journal of Naval Architecture and Ocean Engineering*, 2011. 3(1): p. 72-79.
- Liu, S.K., A. Papanikolaou, and G. Zaraphonitis, Prediction of added resistance of ships in waves. *Ocean Engineering*, 2011. 38(4): p. 641-650.
- Orlandi, I., A simple boundary condition for unbounded hyperbolic flows. *Journal of computational physics*, 1976. 21(3): p. 251-269.
- Xu, G. and W.-y. Duan, Time-domain simulation for water wave radiation by floating structures (Part A). *Journal of Marine Science and Application*, 2008. 7: p. 226-235.
- Zhang, W.D.T., Non-reflecting simulation for fully-nonlinear irregular wave radiation. 24th International Workshop on Water Waves and Floating Bodies, 2009.

## CONTACT WITH AUTHOR

Li Zhi-Fu  
lizhifu@hrbeu.edu.cn

Ren HuiLong

College of Shipbuilding Engineering  
Harbin Engineering University  
Harbin Heilongjiang  
150001 China

Shi YuYun  
Li Hui,

Muhammad Aqeel Ashraf

Department of Geology  
Faculty of Science  
University of Malaya  
50603 Kuala Lumpur  
Malaysia

# COMPARISON OF 2D AND 3D MODELS OF SALINITY NUMERICAL SIMULATION

Li Chunhui<sup>a,b</sup>,

Pan Xishan<sup>c</sup>,

Ke Jie<sup>a,b</sup>,

Dong Xiaotian<sup>a,b</sup>,

a) Key Laboratory of Coastal Disaster and Defense, Ministry of Education,

Hohai University, Nanjing, China

b) Environment Marine Laboratory, Hohai University, Nanjing, China

c) Tidal Flat Research Center of Jiangsu Province, Nanjing, China

## ABSTRACT

*For the study of the effect of 2D and 3D mathematical model in salinity simulation, with Liuheng island strong brine discharge of seawater desalination project as an example, using 2D and 3D salinity mathematical models of Liuheng island to simulate coastal hydrodynamic environment and salinity distribution before and after the concentrated brine discharge, and analyzed the results. Finally got the applicable scope of the two models, it has an important significance in the study of similar problems.*

**Keywords:** 2D model, 3D model, salty, strong brine, numerical simulation

## INTRODUCTION

Mathematical models and other quantitative methods have been used to research the impact of brine on the water environment and salinity distribution, and this area have made some achievements Domestic and foreign [1-8]. By means of numerical experiments, Luo Feng and Li Ruijie have studied the effect of different hydrologic meteorological environmental factors on saltwater intrusion in the Yangtze river estuary. Anton, Al-Barwani have established mathematical model using 2D convection diffusion equation, and they discussed the influence of Oman discharged coastal brine on tidal oscillation flow. Wang Xiaomeng, Liu Xuehai have set up jiaozhou bay salinity diffusion model, and they handle the planning seawater desalination as input conditions, simulating and calculating salinity distribution and variation of jiaozhou bay, etc. Nowadays, salinity diffusion studies adopt 2D and 3D model simulation mostly. 2D model is simplified by 3D model, with characteristic of fast, convenient processing, furthermore 3D model can draw conclusions of vertical variation of flow and salinity. It is complicated not only because three space coordinates of moving elements should be considered, but some difficulties on equation solving encountered, and cost more simulation time. So, a comparative studies of 2D and 3D simulation can help us to select model effectively, but also is of significance in the study of similar problems.

Based on fully collecting hydrological terrain information in islands nearby, a case study in Liuheng island seawater desalination project has established 3D and 2D salinity mathematical model in connection with tide and salinity simulation near the discharge. In line with actual engineering design and through comparison and analysis, impact on hydrology characteristics and the influence of salinity distribution is calculated, and the salinity increment is analysed.

2. Three-dimensional numerical simulation of flow and salinity in Liuheng sea area

Simulation area is shown in figure 1, mesh dissection is shown in figure 2, 3D simulation of vertical evenly divided into 6 layers, simulation time is from 00:00 on January 11, 2013 to 23:00 on January 19, 2013. Model is verified by the synchronous observations of January 2013, the tide validation is shown in figure 3 (—' is calculated value, , ' for the measured values, the abscissa represents time (h), ordinate represents the water level (m)). Velocity and salinity selection is illustrated by the S1 station on spring tide, the measured values and calculated values of surface, 0.6 layer and the underlying surface velocity is compared, as shown in figure 4 ~ 6 (figure , —' for the calculated value, , ' for the measured values, the abscissa represents time (h), ordinate represents the velocity (m/s)/flow direction (°)/salinity (ppt). By the figure, the tide level calculation values

are in good agreement with the measured data, the calculated results of the velocity, flow direction, salinity of each layer is coincided basically with the measured data, the established model can well reflect the tidal current, salinity distribution characteristics of the Liuheng island sea areas nearby.

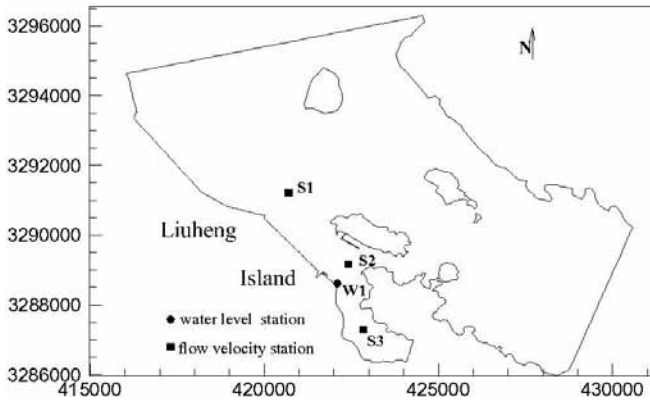


Fig. 1. The small scale calculation area and the field stations distribution

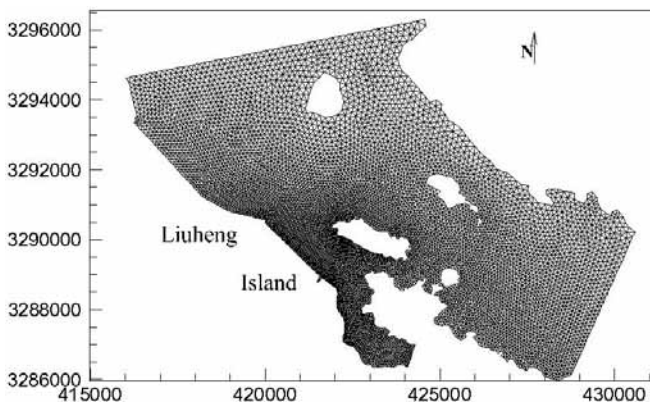


Fig. 2. The grid of the calculation area

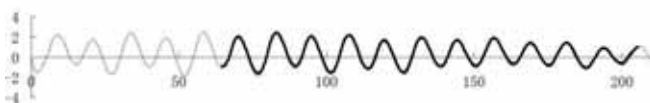


Fig. 3. Comparison of water level from field data with the calculation values

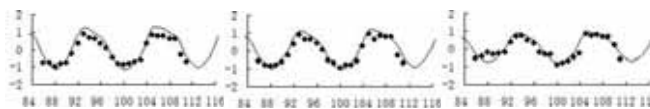


Fig. 4. Comparison of flow velocity from field data with the calculation values (surface, middle and bottom layers)

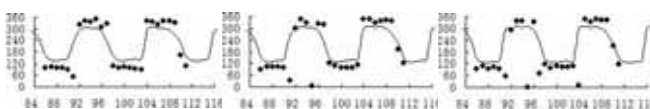


Fig. 5. Comparison of flow direction from field data with the calculation values (surface, middle and bottom layers)

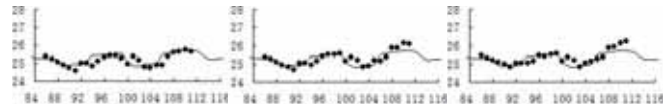


Fig. 6. Comparison of salinity from field data with the calculation values (surface, middle and bottom layers)

## TWO-DIMENSIONAL TIDAL CURRENT AND SALINITY NUMERICAL SIMULATION

2D simulation area and the parameters is adopted from 3D numerical simulation, the tidal level verification is shown in figure 7. Flow velocity, direction and salinity selection is illustrated with S1 station during the spring tide. By the figure 8, the tide level calculation values are in good agreement with the measured data, the calculated results of velocity, direction and salinity of each layer is coincided basically with the measured data, the established model can well reflect the Liuheng island tidal current, salinity distribution characteristics.

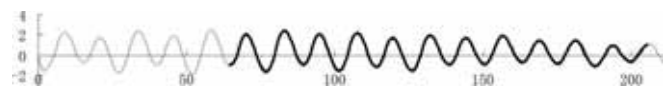


Fig. 7. Comparison of water level from field data with the calculation values

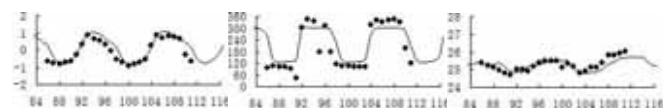


Fig. 8. Comparison of flow velocity, flow direction, salinity from field data with the calculation values

## 4. COMPARISON OF 2D AND 3D CALCULATED RESULT BEFORE BRINE DISPOSAL

The comparison of average vertical salinity values of 2D and 3D at the stations of S1, S2, S3 are given in the Fig.9(,—' is 2D value, ,-' is 3D values, the abscissa represents time (h), ordinate represents the salinity (ppt)). Table 1 presents the difference between the 2D simulated values and 3D average vertical values(3D minus 2D). As can be seen from the figure and table, the difference of the two salinity values from different method is very small, and values are basically the same.

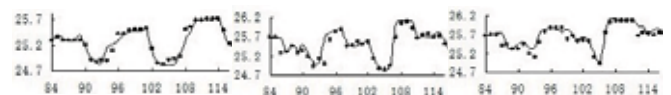


Fig. 9. Comparison of 2D simulated values and 3D average vertical values

Tab. 1. Difference between the 2D simulated values and 3D average vertical values(ppt)

S1	S2	S3
0.009261	-0.07604	-0.07767

## COMPARISON OF 2D AND 3D CALCULATED RESULT AFTER BRINE DISPOSAL

Water withdrawal and displacement as shown in Table 2, Water intake and outfall location shown in Figure 10. After verification the 2D and 3D salinity mathematical model with the measured data, set the water intake and outfall as the source and sink in model to predict the impact of brine disposal on the surrounding environment and the salinity distribution.

Tab. 2. The design discharge of the water intake and outfall

	Location	Discharge (kt/h)	salinity (ppt)	Location (From the bottom) (m)
intake	29°42'48.50"N, 122°11'39.59"E	56	—	1
outfall	29°43'0.45"N, 122°11'22.77"E	30	48	0.3

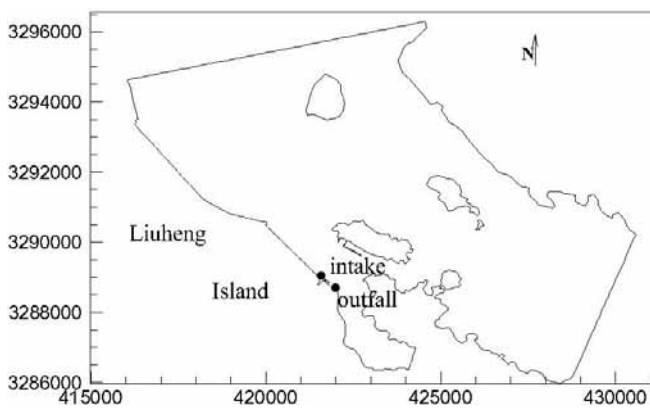


Fig. 10. The location of the water intake and outfall

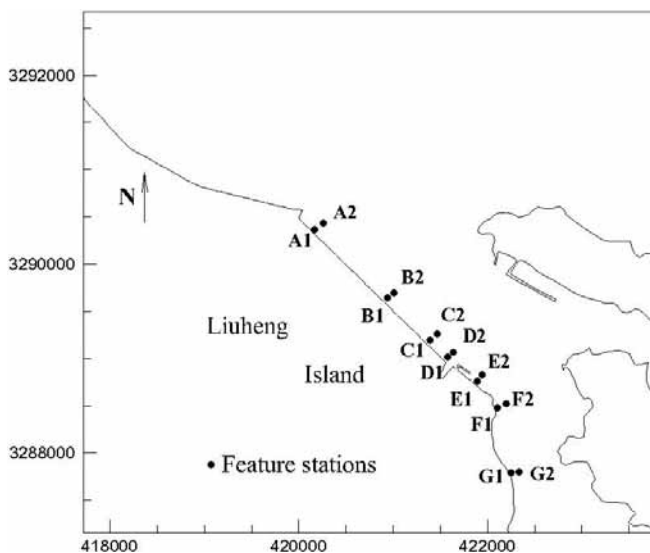


Fig. 11. The location of feature stations

As can be seen from Figure 12, salinity has significant incremental vertical stratification after the brine disposal, the largest increment at the bottom, and the least at the surface. These are because the outfall located at the bottom, the density of brine disposal is larger than the sea water, the higher concentration of salt water outward diffusion in the bottom, resulted that the increment of the salinity in the bottom is greater than the upper.

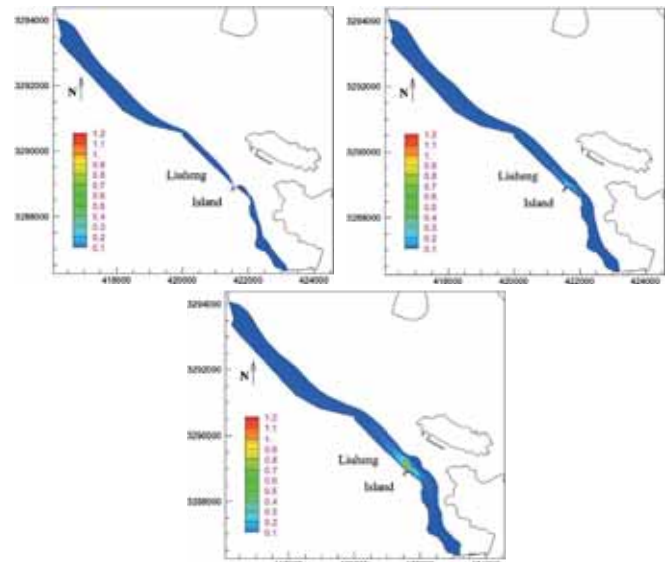


Fig. 12. The incremental displacements of the spring tide (surface, middle and bottom layers)

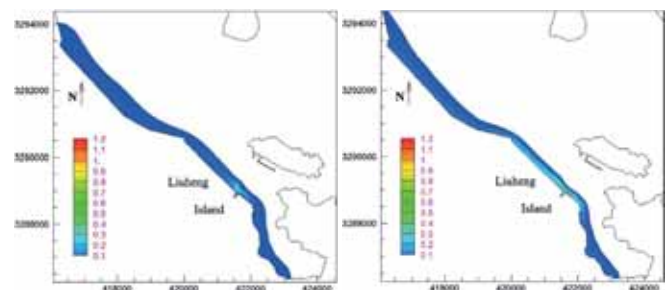


Fig. 13. The incremental displacements of the spring tide (3D average vertical and 2D)

As can be seen from Fig 13, the brine disposal range of the 3D and 2D calculated results are basically the same, and the difference is that, the greater increment in 3D model is concentrated in the outfall, and the increment scope of 2D is larger than 3D model. These are because in the 3D model, the brine diffusion with the bottom water, but the velocity in the bottom is less than the average velocity (2D model results), so that the increment of 3D model is more concentrated than 2D model.

In order to better reflect the difference between the 2D and 3D calculated results after the brine disposal project, 14 feature points are set around the outfall to analysis the salinity calculation results, points distribution in figure 11. Table 3 presents the difference at the feature points between the 2D simulated values and 3D average vertical values (3D minus 2D).

Tab. 3. Difference between the 2D simulated values and 3D average vertical values (ppt)

feature station	difference	feature station	difference
A1	-0.263283	A2	-0.154693
B1	-0.28877	B2	-0.147945
C1	-0.378092	C2	-0.101155
D1	-0.399361	D2	-0.078855
E1	-0.297576	E2	-0.116532
F1	-0.238772	F2	-0.136838
G1	-0.161838	G2	-0.134843

As can be seen from Tab 3, the results at A1-G1 points near the shore have a larger difference, the values of 2D are obviously greater than 3D results. And the point closer outfall, the difference is greater. The points far away from the shore, the difference of calculated results at A2-D2 points is small, further evidence that brine diffusion at the 3D simulation is more slowly than 2D, reflected that the influence of the vertical velocity variation on the simulation of brine diffusion.

## CONCLUSION

For the study of the effect of 2D and 3D mathematical model in salinity simulation, with Liuheng island strong brine discharge of seawater desalination project as an example, using 2D and 3D salinity mathematical models of Liuheng island to simulate coastal hydrodynamic environment and salinity distribution before and after the concentrated brine discharge. Results show that before the concentrated brine discharge (natural conditions), the simulation results of the two models are almost the same. For the 2D model is simple to set up and has the characteristics of short calculation time, it is recommended to use 2D model to simulate the natural waters salinity; After concentrated brine discharge, 2D and 3D simulation results appeared larger differences, this is mainly due to the strong brine has the characteristics of large density, concentrated in the underlying diffusion, for this kind of apparent salinity stratification is need to use 3D model for research. From the spread of the concentrated brine discharge after scale, 2D and 3D results have not much difference. If only need to study the influence area of strong brine, using 2D model for research is also desirable.

## REFERENCE

1. AL-BARWANI H H, ANTON Purnama. Re-assessing the impact of desalination plants brine discharges on eroding beaches. *Desalination*, 2007(204):94-101.
2. Anton Purama, AL-Barwani H H, AL-Lawatia M. Modeling dispersion of brine waste discharges from a coastal desalination plant. *Desalination*, 2003(155):41-47.
3. Anton Purnama, H.H.AL-Barwani. Spreading of brine waste discharges into the Gulf of Oman. *Desalination*. 2006(195):26-31.
4. Luo Feng, Li Ruijie. Influence of hydrometeorological variation on saltwater intrusion in Changjiang River Estuary. *Journal of Marine Sciences*, 2011,3(29):9-17.
5. MALFEITO J J, DIAZ-CANEJA J. Brine discharge from the Javea desalination plant. *Desalination*, 2005(185):87-94.
6. Rachel Einav, Fredi Lokiec. Environmental aspects of a desalination plant in Ashkelon. *Desalination*. 2003(156):79-85.

7. TSIOURTIS N X, Desalination and the environment. *Desalination*, 2001(141): 223-235.
8. Wang Xiaomeng, Liu Xuehai. The effect of brine discharged from desalination plant on the distribution of the salinity in the Jiaozhou Bay .*Acta Oceanologica Sinica*, 2009,1(31):44-51.

## CONTACT WITH AUTHOR

Li Chunhui  
lichunhui35@126.com

Ke Jie  
kj36170909@163.com

Dong Xiaotian  
do.ng.xt@163.com

Key Laboratory of Coastal Disaster and Defense\  
Ministry of Education  
Hohai University  
Nanjing 210098  
China

Environment Marine Laboratory, Hohai University  
Nanjing  
China

tel: 18512547902, fax: 025-83786997

Pan Xishan  
xspan@nhri.cn

Tidal Flat Research Center of Jiangsu Province  
Nanjing  
China

# ANTI-SEISMIC DEVICE DESIGN FOR CONTAINER CRANE AND ITS ELASTIC-PLASTIC TIME HISTORY ANALYSIS

Dashan Dong,

Jin Li,

Yuanyuan Teng,

School of Logistical Engineering, Shanghai Maritime University, Shanghai

## ABSTRACT

*Quayside container crane is a kind of large dimension steel structure, which is the major equipment used for lifting container at modern ports. With the aim to ensure the safety and reliability of the crane under seismic loads, an anti-seismic device is designed. To validate the efficiency and reliability of the anti-seismic device, elastic-plastic time history analysis under rare seismic intensity is carried out. And the results of elastic-plastic time history analysis when the crane installed anti-seismic device and uninstalled the device are compared.*

**Keywords:** quayside container crane, time history analysis, energy design method, anti-seismic device

## INTRODUCTION

Quayside container crane is the main equipment used for lifting containers at modern harbors. However, most major ports are built in the seismic belts. In order to avoid damage to the crane under the earthquake, a frictional anti-seismic device is designed for the container crane.[4-5]

In this paper, an anti-seismic device is designed for the quayside container crane, and the efficiency of the device is validated by the time-history analysis and model simulation. In order to ensure the accuracy of the analysis, the seismic waves are provided by the local Seismological Bureau in Los Angeles, where is also the J481 crane located.

## COMMON ANTI-SEISMIC MEASURES FOR QUAYSIDE CONTAINER CRANES

Anti-seismic design is widely used in high buildings and important buildings. There are lots of anti-seismic methods, such as the TMD, TLD or use the seismic isolation devices to reduce the damage to the structure. Because of the complexity of the container crane, it's hard to use a TMD or TLD device on the structure. According to the crane's characteristics, some commonly used anti-seismic design methods are the following:

1) Elastic leg-lift design to lift the legs under the earthquake. Leg-lift has eliminated the constraints between the crane and the ground, thus prevented the transfer and increase of the lateral loads, and limited the transfer of the acceleration of earthquake.

2) Plastic frame design to adapt to the deformation that occurred during the earthquake. If the deformations of legs are beyond the capacity, crane collapse occurs.

3) Seismic isolation device design. Fig.1 shows a seismic isolation device use the dampers and springs as isolation components. Besides, seismic isolation devices can also use the friction pairs as isolation and energy components.

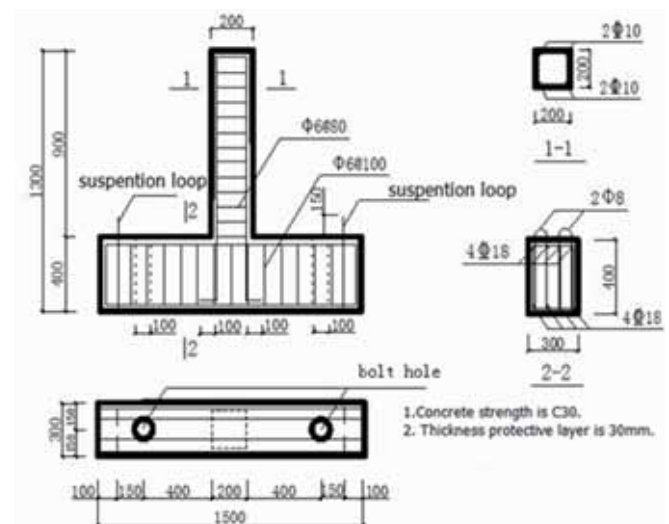


Fig. 1. Seismic isolation device's Schematic diagram

## ANTI-SEISMIC DEVICE DESIGN

### WORKING PRINCIPLES

In this paper the frictional anti-seismic device uses several slotted bolted connections as the main structure, which is referred to as SBCs. Fig.2 shows the slotted bolted connection.

Compared with other types of anti-seismic device, SBCs has the following advantages:

- 1) It not only can be used for general bracing in single frame structure but also to connect the beam-column joints. And it just needs to make minor changes to the original standard structure without affecting the original design functions.
- 2) SBCs are easy to construct, and the materials are not special. It has obvious economic benefits.
- 3) SBCs can maintain a stable and high efficiency energy consumption under multiple cycles.
- 4) Before slipping the anti-seismic device works as a general support to increase the lateral stiffness and reduce the structural deformation. When slipping the structural stiffness has changed, while the stress is always kept in a controlled elastic stage[2].

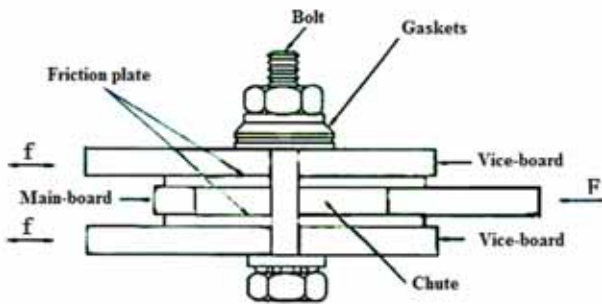


Fig. 2. The slotted bolted connection

## ENERGY METHOD

### ENERGY DEMAND OF ANTI-SEISMIC DEVICE

For the structure without the anti-seismic device, part of the seismic energy input to the structure stored in the form of elastic deformation energy and kinetic energy. Another part of energy is consumed by non-elastic deformation generated by the structure itself (Formula 1).

For the structure with the anti-seismic device, not only have the same energy consumption form as general structure, but also the additional energy consumption device will absorb and consume most of the seismic input energy (Formula 2).

If the structure is not destroyed in the earthquake, the energy consumption and seismic input energy should keep a balance.

For the structure without the anti-seismic device:

$$E_I = E_K + E_D + E_L + E_H \quad (1)$$

For the structure with the anti-seismic device:

$$E_I' = E_K' + E_D' + E_L' + E_H' + E_M \quad (2)$$

### ENERGY DISSIPATION CAPABILITY

The energy dissipation capacity is closely related with the displacement of the frictional anti-seismic device.[3] It can be calculated by hysteresis curves and its approximate expression is:

$$E_M = n\varphi m E_{Mi} \cos \theta \quad (3)$$

The recovery force model of anti-seismic device can be seen as the ideal rigid-plastic model. So the energy consumed by one anti-seismic device in one cycle is:

$$E_{Mi} = 4F_y d_0 \cos \theta \quad (4)$$

### CHUTE DISTANCE SETTING

The chute distance setting is one of the most important steps about frictional anti-seismic device's design. If the chute design distance is too long, it will affect the structure stiffness even lead to structural damage. While if the chute distance is too short, the anti-seismic device needs a larger one-way trip to dissipate the energy. That will collide with the chute ends and make additional dynamic impact to the structure.

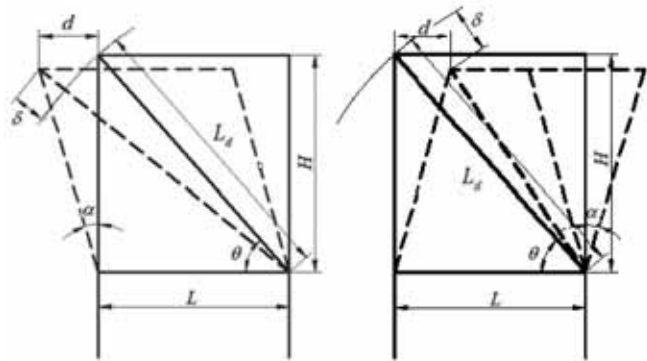


Fig. 3. Deformation of Structural with anti-seismic device

Tab. 1. The relationship of the structural damage and the displacement angle between layers

Basic good	Minor damage	Moderate damage	Severe damage	Collapse
1/500	1/500 ~ 1/250	1/250 ~ 1/125	1/125 ~ 1/50	1/50

To ensure the structure does not collapse that (Tab.1):

$$\tan \alpha = \frac{d}{H} \leq \tan \left( \frac{1}{50} \right) \quad (5)$$

Where,  $\alpha$  is the displacement angle between layers.

From Fig. 3 we can get, when the frictional anti-seismic device in a stretched state the maximum offset is:

$$\delta_{\max} = \sqrt{H^2 + (L + 0.02H)^2} - L_d \quad (6)$$

When the frictional anti-seismic device in a compressed state the maximum offset is:

$$\delta_{\max} = L_d - \sqrt{H^2 + (L - 0.02H)^2} \quad (7)$$

So the design chute distance can't exceed the minimum offset value either when the frictional anti-seismic device is in a stretched or compressed state. According to dimensions of the crane specifically designed for Port of Los Angeles, the chute length is .

### SLIDING FORCE CALCULATION

J481 quayside container crane is designed for Port of Los Angeles of the United States. According to tender requirements,

various structure calculations under different loads and situation has done with ANSYS. Results show that the largest load in diagonal brace is 202 ton.

When apply 0.3g earthquake vibration amplitude in the direction of trolley runs, the largest load in diagonal brace is 259 ton. Since the condition considered is the toughest, the actual force is generally less than the calculated force. Therefore, we set the sliding force of the anti-seismic device is 212ton. So when the local vibration amplitude comes to 0.3g, the anti-seismic device working.

According to the design methods above, the anti-seismic device is shown in Fig.4.

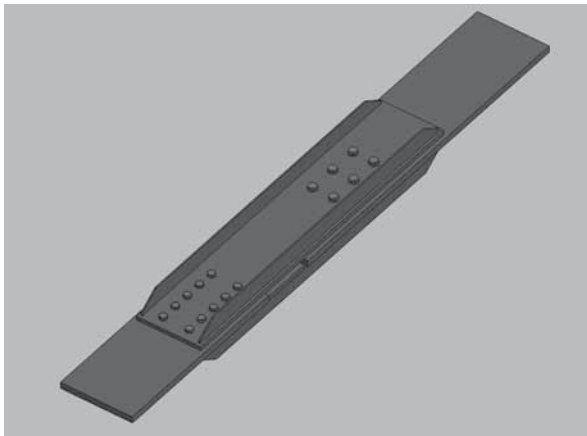


Fig. 4. One piece of anti-seismic device

### INSTALLATION LOCATIONS

According to the basic design principles, experience and the purposes that SBCs only can be applied to the single bracing support or beam bottom support, we can determine the layout locations of the frictional anti-seismic devices. Fig.5 shows the examples of anti-seismic devices' installation on single bracing support container crane.



Fig. 5. Examples of anti-seismic devices' installation on single bracing support container crane

### SELECTION OF THE SEISMIC WAVE

In this paper, a time-history analysis of J481 quayside container crane is presented respectively under the occasional level seismic wave (CLE).

Since the provided seismic waves recorded a long time, most of the time it makes a tiny vibration on the structure. It is very necessary to intercept some parts of the seismic waves to analysis. We intercept the acceleration which is bigger than 0.1g of the CLE seismic wave. Input the selected seismic wave data to do the time-history calculation based on the ANSYS.

Belong to the analysis results by the seven CLE waves, the 2th and 4th make the greatest impact on the structure, which is named as CLE-2 and CLE-4. In the following presentation we take CLE-4 (FP direction) as an example. The time-history curves as shown in Fig.6.

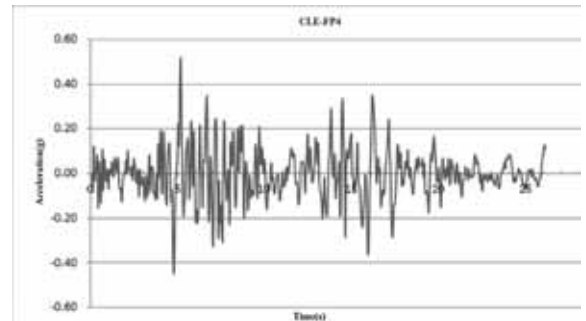


Fig. 6. Time-history curves under CLE-4

## TRADITIONAL CRANE SYSTEM DYNAMIC TIME-HISTORY RESULT

Apply the seismic loads on the J481 container crane, and then do the time-history analysis. [6] The results show the structure's response under vary seismic waves. The analysis results under CLE-4 seismic wave as shown in Fig.7~9.

Under the occasional level seismic waves (CLE-2 and CLE-4) crane's maximum stress over the entire time is larger than the structure's yield limit, and crane is in the elastic-plastic stage. The maximum displacement at the joint is bigger than the maximum allowable displacement. So the crane without anti-seismic device doesn't meet the anti-seismic requirements under occasional earthquake.

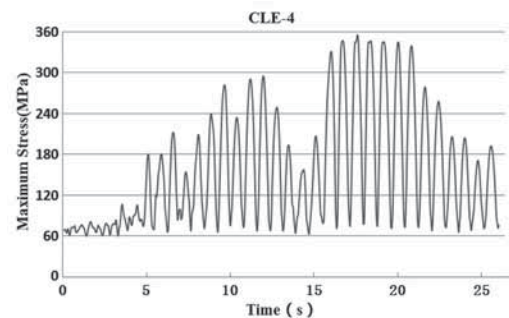


Fig. 7. The structure's maximum stress-time history curves under CLE-4 seismic wave without anti-seismic device

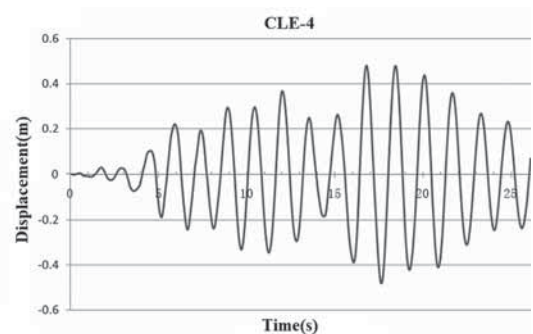


Fig. 8. The maximum displacement of the joint at the balance beam under CLE-4 without anti-seismic device

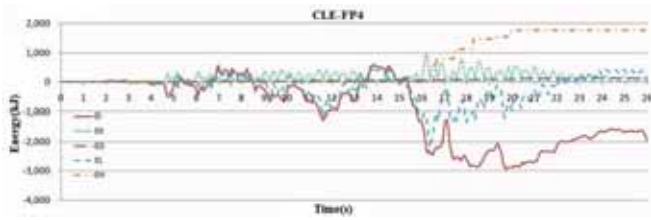


Fig. 9. The various energy sub-charts when the structure under CLE-4 seismic waves without anti-seismic device

## TIME-HISTORY ANALYSIS OF STRUCTURE WITH ANTI-SEISMIC DEVICE[7]

Under the occasional level seismic waves (CLE-2 and CLE-4), J481 container crane which is installed with the anti-seismic device is always in the elastic stage, and avoid the damage caused by plastic deformation. It can be seen that the device makes a great effect. Specific results can be found in Fig. 10 to 13. Take CLE-4 as an example.

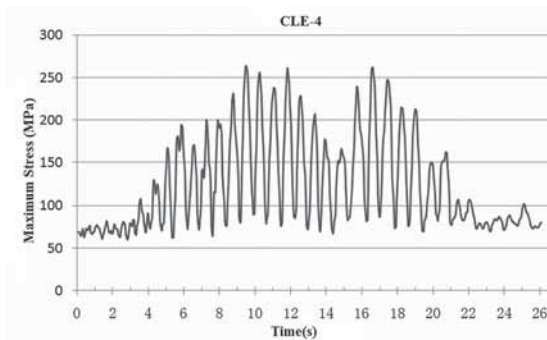


Fig. 10. Maximum stress-time history curves under the CLE-4 with anti-seismic device

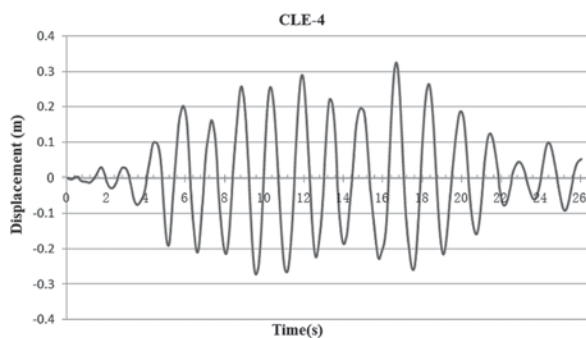


Fig. 11. The maximum displacement of the joint at the balance beam under CLE-4 with anti-seismic device

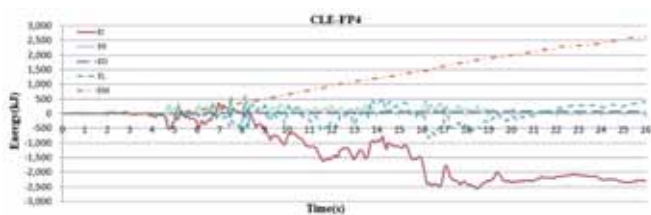


Fig. 12. Various energy sub-charts of structure with anti-seismic device under CLE-4 with anti-seismic device

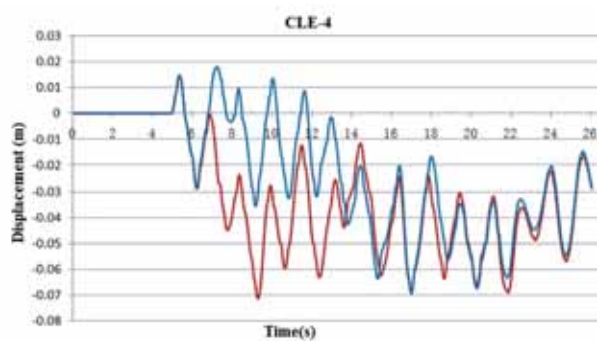


Fig. 13. Displacement-Time history curves of anti-seismic device under CLE-4

## DYNAMIC TIME-HISTORY ANALYSIS OF ANTI-SEISMIC DEVICE

Under the occasional level seismic waves and considerate the thermal expansion of frictional damper[1], the transient simulation can provide the load-displacement-time history curves, hysteresis curve and energy consumption of the device, which is shown in Fig.14 to 16.[3]

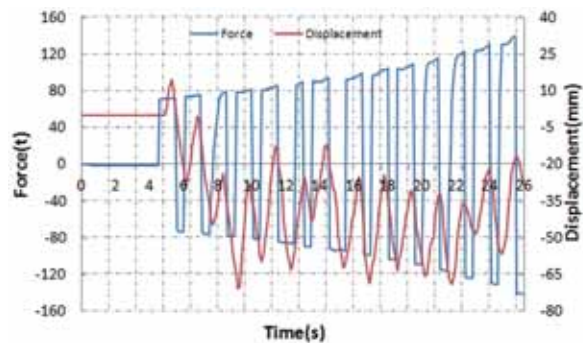


Fig. 14. The force-displacement-time history curves of anti-seismic device under CLE-4

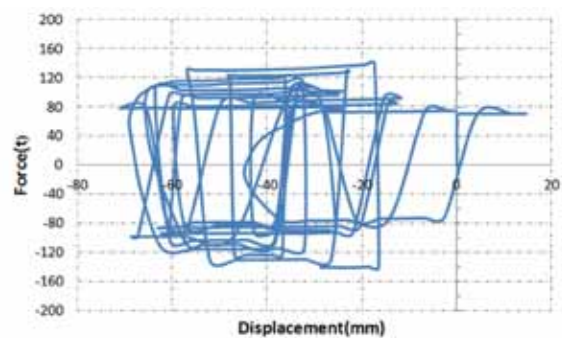


Fig. 15. Hysteresis curve of anti-seismic device under CLE-4

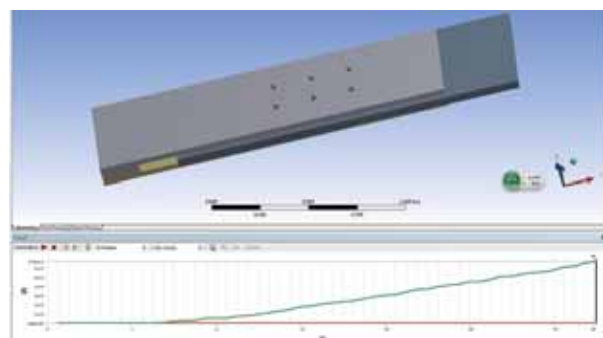


Fig. 16. Energy consumption of anti-seismic device under CLE-4

Under the CLE-2 seismic wave, according to the simulate model's energy consumption and formula 3, the total energy consumption is 1163.76 kJ. The energy consumption based on the energy sub-item time-history analysis is 1290 kJ. The calculation error is within 9.78%. Similarly, the calculation error is within 1% when under the CLE-4.

The analysis above proves that the anti-seismic device can effectively consume energy under the strong earthquakes.

## CONCLUSIONS

In this article, we build the normal, anti-seismic device element model of crane and calculate the dynamic response acceleration by the time-history analysis. According to the research, we can get some conclusion as following:

- 1) The anti-seismic device based on SBCs can effectively consume energy under the strong earthquakes.
- 2) Energy method is suitable for quayside container crane's seismic response analysis. Its accuracy is verified by the energy calculated by the method of simulation and hysteresis curves of time-history analysis.
- 3) The impact to energy consumption caused by thermal expansion in the frictional anti-seismic device cannot be ignored.

## REFERENCE

1. AA Yevtushenko, P Grzes, The FEM-modeling of the frictional heating phenomenon in the pad/disc tribo system, Numerical Heat Transfer, Part A, 2010
2. Grigorian C E and Popov E P, Slotted Bolted Connections for Energy Dissipation, Proc. of Seminar on Seismic Isolation, Passive Energy Dissipation and Active Control, Vol.2. San Francisco, USA, 1993
3. I Lopez, JM Busturia, H Nijmeijer, Energy dissipation of a friction damper, Journal of sound and vibration, 2004
4. KW Min, JY Seong, J Kim, Simple design procedure of a friction damper for reducing seismic responses of a single-story structure, Engineering Structures, 2010
5. Lee SK, Park JH, Moon BW, Min KW, Lee SH, Kim JK. Design of a bracing-friction damper system for seismic retrofitting. Smart Struct Syst 2008;4(5):685-96.
6. Zheng Pei, Zhang Qing, Qin Xian Rong. Earthquake Response Behavior of Quayside Container Cranes. Journal of Wu Han University of Technology. 2010. Vol.21.3.:70-74
7. Zheng Pei, Zhang Qing. Analysis of anti-seismic behavior of large-scale container cranes. Engineering Journal of Wu Han University. 2010. Vol.43. :116-12

## CONTACT WITH AUTHOR

Dashan Dong

Jin Li  
email: hellolijin1209@163.com  
tel.: 86-15800307906

Yuanyuan Teng

School of Logistical Engineering  
Shanghai Maritime University  
201306 Shanghai

# NUMERICAL ANALYSIS OF CONSOLIDATION SETTLEMENT AND CREEP DEFORMATION OF ARTIFICIAL ISLAND REVETMENT STRUCTURE IN A LARGE-SCALE MARINE RECLAMATION LAND PROJECT

Zhao Jie, Ph. D

Zhou Tongling, Ms. C.

Wang Gui-xuan, Prof.

Dalian University R & D Center of the Civil Engineering Technology  
Dalian, China

## ABSTRACT

*In order to analyze the influential factors of soft foundation settlement in a marine reclamation land project, the consolidation settlement and pore pressure dissipation of the entire area are numerically simulated using Soft-Soil-Creep Model, in which the PLAXIS finite element software for professional geotechnical engineering is applied and empirical data of Japanese Kansai's airport project are used. Moreover, the figures of settlement and pore pressure results in the different basic period are drawn, and the corresponding analysis conclusions are obtained based on the comparison among the results from the computational parameters of depth. In addition, the influence rules of various parameters on settlement results is concluded through running the parameter sensitivity analysis in Soft-Soil-Creep Model, and the experience and conclusions can be for reference in the design and construction of similar large-scale marine reclamation land project. Also the empirical value method of the creep index has not been applied widely. Further research needs to be done.*

**Keywords:** marine reclamation land; Soft-Soil-Creep model; consolidation settlement; pore pressure; micro-structure; numerical analysis.

## INTRODUCTION

Plentiful soft soil layers that water content is higher are distributed in Chinese coastal areas, such as soft soil sedimentary of coastal facies in Tianjin, Dalian, Qingdao and so on. The soft soil is mainly made up of fine-grained soil whose major kind is muddy soil. In terms of the engineering properties of soft soil, it has high water content, low strength, low coefficient of permeability and obvious rheological property. It is the most common to the rheological phenomenon of soft soil, which is the primary soil in the construction of marine reclamation land project. Microstructure of marine sedimentary soft soil is complex, and its engineering properties have a very close relationship with certain types of microstructure. Therefore, the long-term influence of microstructure of soft soil, consolidation and soft soil creep must be taken comprehensive consideration.

Soil microstructure means size of soil particles, shape, surface characteristics, the link way and the arrangement between the particles in the soil and so on. Under the external environmental influence, a variety of soil exhibited features reflect on change of all its intrinsic microstructure, so microstructure of soil plays an important role in the changing of the soil nature.

From the 1920s, Terzaghi pointed out that micro-structural necessity of the soil needed to be considered when the geological nature of the clay is in the evaluation, which linked marine sedimentary soft soil to engineering properties of soil. From then on, a new study field of soil microstructure was founded. It is And Casagrande proposed a composite model containing silt and clay by Terzaghi's model, which described sensitive characteristics of soil structure of marine sediments. So the relationship between micro-structural characteristics and mechanical properties of soil is systematic studied. And the essential factors affecting the deformation and force of the micro-structural itself characteristics are revealed, which are important for mechanism analysis of consolidation settlement, permeability and shear deformation.

Foundation settlement usually includes the initial settlement and the post-construction settlement (primary consolidation settlement and secondary consolidation settlement). Terzaghi Consolidation Theory assumed that the total normal stress does not change along with time in the process of consolidation, thus consolidation settlement can be only approximately figured up. However, Biot Equation

[1, 2] can calculate both initial consolidation settlement and consolidation settlement and horizontal displacement. However, the secondary consolidation settlement is not taken into account in the above the two theories, which leads to be larger different from actual settlement value. In fact, for most soft soil, secondary consolidation deformation has a large proportion of the total deformation, so the part of soil deformation cannot be neglected. Therefore, most scholars proposed consolidation theories considered rheological property, which made calculation of settlement value consider secondary settlement.

In twentieth century 30's, Bingham put forward material rheological theory, which marked appearance of rheological subject. Subsequently our country scholar Chen Zongji put rheological theory into the use of consolidation theory, and built consolidation theory considering rheology and deduced consolidation equation as well as the solution of equation based on it [4]. Based on the spread of study of soft soil settlement problem of finite method, Folque presented a consolidation model of unsaturated soil considering rheological question and got the solution of constitutive equation of model [5,8]. Tang Bin et al [9] adopted finite producer to analyze consolidation of soft soil foundation based on rheological characters; Mamoru Mimura et al [6] studied number one runway of Kansai International Airport and contrasted local actual monitoring value with finite numerical calculation value of consolidation settlement post construction. The two results are almost similar. In this paper, Consolidation settlement and creep analysis calculation are proceeded to marine reclamation land project using Soft-Soil-Creep Model as well as plane finite method, in which the PLAXIS finite element software for professional geotechnical engineering is applied and empirical data of Japanese Kansai's airport project are used. Then the sensitivity analysis is carried out for some factors which affect soil consolidation and creep. Furthermore, the corresponding analysis conclusions are obtained which can be for reference in the design and construction of similar large-scale marine reclamation land project.

## BASIC PRINCIPLE OF CONSOLIDATION

Excess pore pressure of soil gradually dissipates, internal water content slowly outflows, and effective stress gradually increases. Such a phenomenon is called soil consolidation. In project practice, soft soil not only produces consolidation settlement before excess pore water pressure absolutely dissipates, even though consolidation has finished (excess pore water pressure completely dissipated) and certain settlement deformation still exists in the soft soil. Therefore, the whole soil settlement should be considered the combined effect of soft soil creep and settlement.

Basic consolidation equation [3] in the PLAXIS was obtained by Biot Theory. Darcy Law is adopted in the seepage problems, which was based on small strain theory and presumed that soil skeleton was of elasticity deformation. Based on Terzaghi Principle, stress of soil was divided into effective stress and pore pressure:

$$\sigma = \sigma' + m(P_{steady} + P_{excess}) \quad (1)$$

Where  $\sigma = (\sigma_{xx} \ \sigma_{yy} \ \sigma_{zz} \ \sigma_{xy} \ \sigma_{yz} \ \sigma_{zx})^T$ ;  $m = (1 \ 1 \ 1 \ 0 \ 0 \ 0)^T$ , and  $m$  includes the vectors of unit normal stress and zero shear stress component. And  $\sigma, \sigma', P_{excess}, P_{steady}$  represent respectively total stress vector, effective stress, excess pore pressure, the final steady-state solution in consolidation. Also, the constitutive equation can be expressed in the form of increment.  $\sigma \ \& \ ', \ \varepsilon \ \& \ ,$  represent respectively the increment of effective stress and increment of strain. So the constitutive equation can be written as

$$\sigma \ \& \ ' = M \ \varepsilon \ \& \quad (2)$$

$$\varepsilon = (\varepsilon_{xx} \ \varepsilon_{yy} \ \varepsilon_{zz} \ \gamma_{xy} \ \gamma_{yz} \ \gamma_{zx})^T \quad (3)$$

Where,  $M$  is the material stiffness matrix.

## SOFT-SOIL-CREEP MODEL

The Soft-Soil-Creep model is applied to simulate the consolidation settlement of foundation and the secondary consolidation settlement of the total area in the numerical calculation. Neher and Vermeer et al [10] proposed the Soft-Soil-Creep model, which is a three-dimensional creep model expanded by one-dimensional creep model based on standard 24h load test. The main parameters contain natural severe  $\gamma$ , saturation severe  $\gamma_{sat}$ , horizontal permeability coefficient  $k_h$ , vertical permeability coefficient  $k_v$ , cohesion force  $c$ , internal friction angle  $\varphi$ , dilation angle  $\psi$ , fixed compression index  $\lambda^*$ , modified swelling index  $\kappa^*$ , fixed creep index  $\mu^*$ .

Buisman first put forward the following equation of creep equation under constant effective stress:

$$\varepsilon = \varepsilon_c - C_B \log \left[ \frac{t_c + t'}{t_c} \right] \quad (4)$$

Subsequently, Butterfield proposed a new style as follow.

$$\varepsilon = \varepsilon_c - C \ln \left[ \frac{\tau_c + t'}{\tau_c} \right] \quad (5)$$

where  $\varepsilon_c$  is the total strain when primary consolidation finished, and  $t_c$  is the time that primary consolidation finishes. Moreover substitution of  $\tau_c$  in the sixth equation into  $t_c$  in the fifth equation,  $t' = t - t_c$  can be obtained which is the time of effective creep. In summary, combining with scholars' research results of creep model, such as Jianhua Yin et al,  $\varepsilon_c$  can be expressed with the following style:

$$\varepsilon_c = \varepsilon_c^e + \varepsilon_c^c = -A \ln \left[ \frac{\sigma'}{\sigma_0'} \right] - B \ln \left[ \frac{\sigma_{pc}}{\sigma_{p0}} \right] \quad (6)$$

$$\varepsilon_c = \varepsilon_c^e + \varepsilon_c^c = -A \ln \left[ \frac{\sigma'}{\sigma_0'} \right] - B \ln \left[ \frac{\sigma_{pc}}{\sigma_{p0}} \right] - C \ln \left[ \frac{\tau_c + t'}{\tau_c} \right] \quad (7)$$

where  $\sigma_0', \sigma', \sigma_p^0, \sigma_p^c, \sigma_p$  represent respectively the initial effective stress before load, the effective stress of final load, the preloading consolidation stress before loading, final

consolidation stress, and the preloading consolidation stress.

$$\frac{\tau}{\tau_c} = \left[ \frac{\sigma'}{\sigma_{pc}} \right]^{\frac{B}{C}} \quad (8)$$

At last, creep equation can be obtained as follow:

$$\dot{\varepsilon} = \dot{\varepsilon}^e + \dot{\varepsilon}^c = -A \frac{\dot{\sigma}'}{\sigma'} - \frac{C}{\tau} \left[ \frac{\sigma'}{\sigma_p} \right]^{\frac{B}{C}} \quad (9)$$

Where:

$$A = \frac{C_r}{(1+e_0)\ln 10} \quad (10)$$

$$B = \frac{C_c C_r}{(1+e_0)\ln 10} \quad (11)$$

$$C = \frac{C_\alpha}{(1+e_0)\ln 10} \quad (12)$$

Basic stiffness parameters and the meaning as follow:

1. fixed compression index

$$\mu^* = \frac{C_\alpha}{(1+e_0)\ln 10} \quad (13)$$

where  $C_c = \frac{e_1 - e_2}{\lg p_2 - \lg p_1}$  represents the compression index.

2. modified swelling index

$$\kappa^* = \frac{3(1-\nu_{ur})}{(1+\nu_{ur})} A = \frac{3(1-\nu_{ur})}{(1+\nu_{ur})\ln 10} \frac{C_r}{(1+e_0)} \quad (14)$$

where  $C_r$  represents swelling index,  $\nu_{ur}$  represents unloading - reloading Poisson's ratio;

3. fixed creep index

$$\mu^* = \frac{C_\alpha}{(1+e_0)\ln 10} \quad (15)$$

where  $C_\alpha$  represents creep index.

## ANALYSIS OF PRACTICAL PROJECT

### PROJECT SITUATION

Field area of marine reclamation land project of Airport Industrial Park was 21 km<sup>2</sup>. After field of project formed, the elevation of top ground was 3.1 meters. Rectangular artificial island was reclaimed. And its length was 6621.1 meters and the width was 3328.3 meters. Moreover the formation of artificial islands revetment and land of Airport Industrial Park includes dredging, water rubble mound, underwater explosive ramming, overland advance backfilling and so on. Also, stratum structure of the site consists of marine sediment, sediments of alternative sea and river and continental sediment,

which is 50 ~ 80 meters of covering. Among them, marine sedimentary layers contain silt, silt clay, silt clay, silt sand, belonging to plastic flow - soft plastic state and local more fine sand. And sediments of alternative sea and river sediment includes clay and silt clay, belonging to plastic - hard plastic state and local folders fine sand. And continental sedimentary layers include clay, silt clay, belonging to hard plastic state, a strong bedrock weathered rock is primary in basic rock. The revetment structure is only taken as the examples in this paper (Fig.7), settlement and excess pore pressure distribution law of different positions were analyzed.

## THE MICROSTRUCTURE ANALYSIS OF SOIL

In the paper, the scanning electron microscopy method was used in the analysis way of soil microstructure, with the vacuum freeze-drying method for sample preparation. Therefore, the instrument specification of scanning electron microscope was 20 kv and its magnification is 10,000 times. For field area, representative soil samples were tested and studied. Scanning electron micrographs were obtained under certain magnification (Fig.1~6). The relationship between microstructural characteristics and mechanical properties of soil was systematic studied.

Tab. 1. soil sample depth of microstructure analysis

number	sample name	sample depth
①	silt	3.0 m -3.5m
②	mucky silt clay	9.0 m -9.5m
③	silt clay	29.1 m -29.3 m
④	silt clay	33.1 m -33.3 m
⑤	Silt clay	47.1 m -47.3 m
⑥	clay	17.1 m -17.3 m

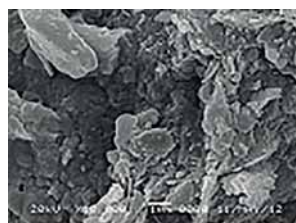


Fig. 1. SEM figure of soil sample①

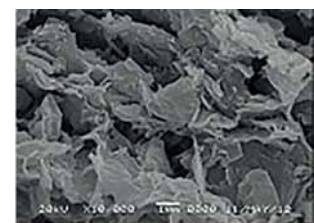


Fig. 2. SEM figure of soil sample②

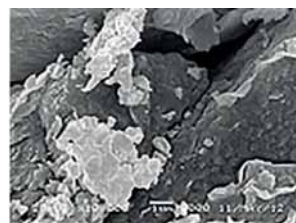


Fig. 3. SEM figure of soil sample③

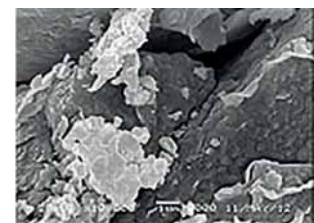


Fig. 4. SEM figure of soil sample④



Fig. 5. SEM figure of soil sample⑤

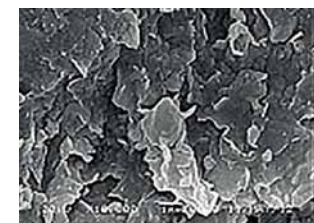


Fig. 6. SEM figure of soil sample⑥

It can be seen from above figures:

1. Soil sample 1 is gray-black in the whole. In the view of high-power electron micrograph, the soil sample takes the flocculation as the skeleton, which connected together to the flocculation by the clay chain. The porosity is mainly intergranular pore, but some large pore exists in it, which indicate that the intensity of the silt is low. However compressibility and rheology sensitivity of the silt is high.
2. Soil sample 2 presents pewter above side, however the other sides are black. Also, the middle of soil sample exist fracture. In the view of high-power electron micrograph, a soil sample also is flocculent link structure taking the flocculation as the skeleton. The porosity is mainly in-terparticle pore. Compared with the silt, the pore reduces and the pore size is small, which indicates that the intensity of the soil sample is low.
3. The soil sample 3 shows pale brown, layering and intermediate mixed with partial sand whose strength is higher by identified. From a high-power electron micrograph, soil samples see tablets or powder set for the skeleton. Certain distance between the particles exists. The distance of particle is connected with clay chains that are formed with clay tablets or clay domain, which forms soil structure of large pores between the particles.
4. Soil sample 4 shows yellow sand in the whole, the soil sample is coarser than the former soil sample and its hardness is higher. soil samples stacked together by clay particles to be clay domain, and then clay domains aggregate together into regular or irregular aggregates that further aggregated together to form a larger group of clay (block) .
5. Soil sample 5 shows yellow sand in the whole, which is the most coarse and the highest hardness in all soil samples by identified; in the view of high-power electron micrograph, the soil sample is the same with soil sample 5.

6. Soil sample 6 shows cyan, the whole show stone gray. In the view of high-power electron micrograph, the soil samples also sets clay tablets or powder form sheet for the skeleton, clay tab-lets to face-face contact based, and the porosity is relatively small, belonging to marine sedimen-tary soil of low compressibility.

## CALCULATION PARAMETERS AND MODEL

PLAXIS, the software of finite element analysis in geotechnical engineering, was used for calculation. The 2D subsidence analysis model was established, in which second-order six-node tri-angular elements were used. The maximum height of model is 80 meters and the width is 425 me-ters. East revetment was divided into 3,280 elements and 6,677 nodes. However, west revetment was divided into 3,018 elements and 6,153 nodes as Fig.8. As kinds of soil in engineering are var-ious, the paper lists some typical calculation parameters of soil used in calculating (Tab.2), where bedrock, sand and backfilling stone using Mohr-Coulomb model and the entire clay use SSC mod-el.

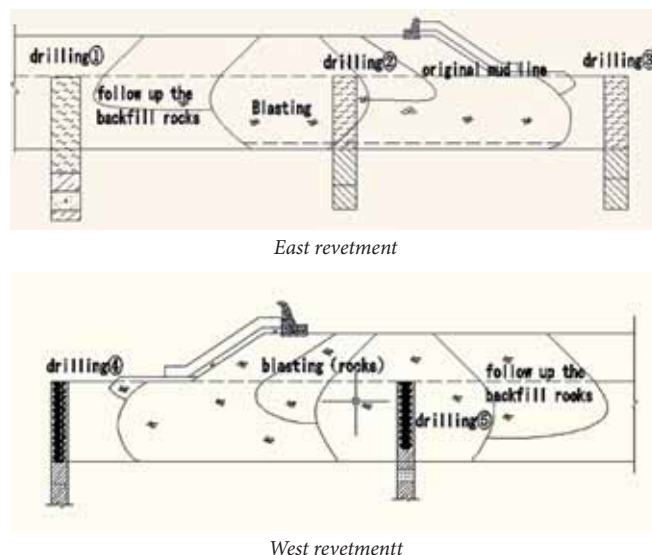


Fig.7. cross-section drawn of typical revetment structure

Tab.2. Typical physical and mechanical parameters of soil

Soil name	Soil constitutive model	Stauration bulk density $\gamma$ /(kN/m <sup>3</sup> )	Void ratio e	Cohesion C/(kPa)	Internal friction angle $\Phi$ /( $^{\circ}$ )	Permeability Coefficient k/(m/d)	Compression index $\lambda$	Swelling index $\kappa$	Creep index $\mu$	Poisson's ratio $\nu$	Stiffness E/(MPa)
Clay	SSC	16.6	1.64	13.1	12.4	0.00025	0.105	0.021	0.0042	-	-
Silt clay	SSC	19.0	0.91	38.8	13.7	0.00023	0.052	0.0105	0.0021	-	-
Silt	SSC	19.6	0.78	41.8	17.6	0.00019	0.046	0.0093	0.0019	-	-
Fine	M-C	19.0	-	0.0	27.0	2	-	-	-	0.35	50
Rock	M-C	20.0	-	0.0	38.0	8	-	-	-	0.28	150
Strong weathered rock	M-C	20.5	-	0.0	38.0	8	-	-	-	0.3	180

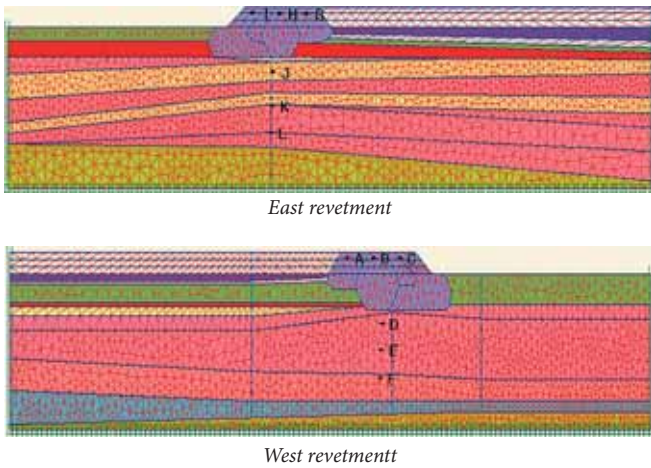


Fig.8. finite elements model of revetment

### ANALYSIS OF CALCULATION RESULTS

The results of above calculation are as shown in Tab.3 and Fig.9. And we can see residual settlement laws of different basic period after the completion as follow: with time going by, the settlement of east and west revetment gradually increases. After the completion 100a, the maximum settlement in the area of east revetment is 0.638 meters and west revetment is 0.586 meters. Therefore, the reason for the difference settlement value between east revetment and west revetment is that physical and mechanical properties of soil under revetment are different. The soil under east revetment is thin silt clay, but the soil of west revetment is thick silt clay. After adopting the Rubble, a small amount of silt still exists. So the settlement of west revetment is slightly superior to settlement of east revetment.

Tab.3. residual settlement after construction in the different reference period

sectional position	settlement in (m)			
	5 years	10years	20years	100yea
west revetment	0.183	0.295	0.389	0.638
east revetment	0.151	0.256	0.343	0.586

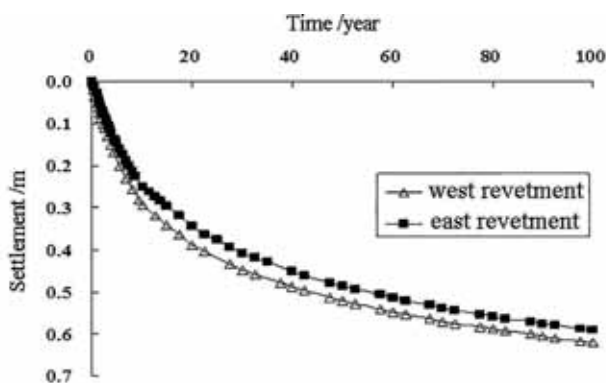


Fig.9. the comparison of settlement trend of revetment after construction

Through comparing the dissipation of pore water pressure at depth of 25 m, 35m and 45 m, it can be seen that excess pore water pressure of deep foundation slow dissipates and the area still will be slow sinking, but the trend

becomes slow. Moreover, the model adopts one-way drainage, and left, under, right boundary is not drained. Because of the path of seepage is from bottom to top, so one of crucial main factors of dissipated speed of pore pressure is the length of the seepage path. Also another influential factor is the permeability coefficient (Sand permeability coefficient is 2 ~ 7 m/d, permeability coefficient of backfill rock is 8 m/d): closed to area of sand and rock, pore pressure dissipation obviously speeds up. According to Geological Survey Report, besides sand layer, permeability coefficient of soil is  $10e^{-3} \sim 10e^{-4}$  m/d, so the speed of soil dissipation at the same depth of soil is approximate. Besides, a special case appears in the revetment. As filling area is large and the filling follows the rocks, coefficient of permeability is much larger than mucky soil before filling, which accelerates drainage, leading to dissipate fast at pore water pressure of revetment.

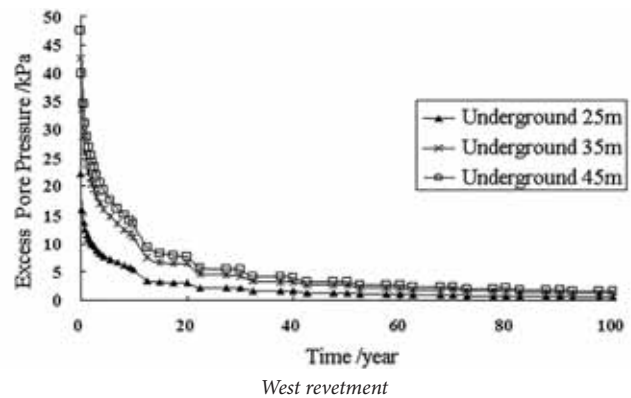
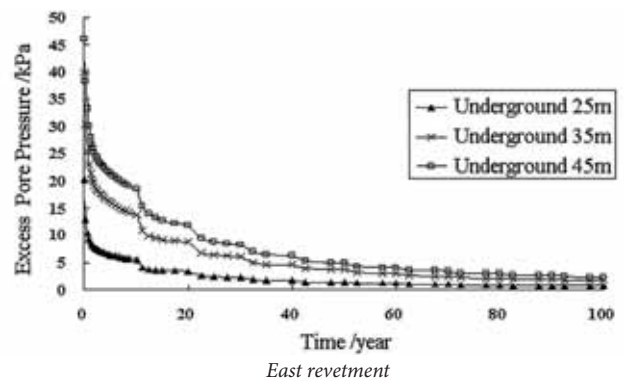


Fig.10. The dissipation of excess pore water pressure

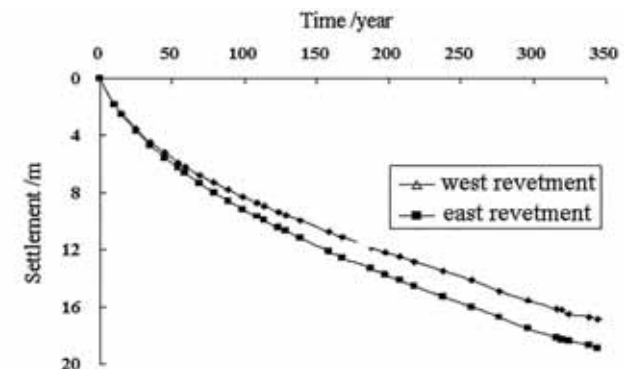


Fig. 11. The comparison of after construction settlement of east revetment

According to the above results of table and figures, it can be concluded that excess pore water pressure of the area of revetment dissipates faster. After the completion 100a, excess pore water pressure in shallow soil layer is tend to zero, and the consolidation settlement of soil finished in the main, but the deep soil still exists some excess pore water pressure without dissipation, excess pore water pressure without dissipated has a about 8% proportion of the total excess pore water pressure.

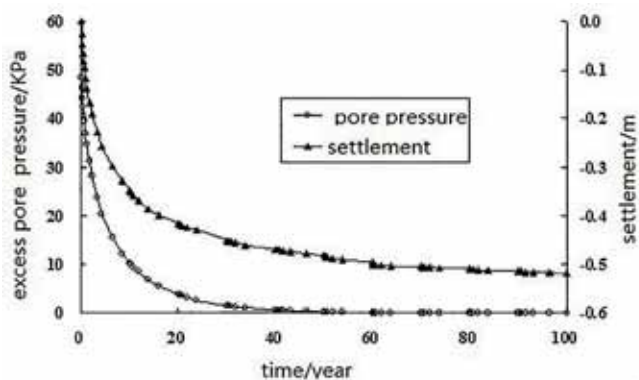
Now, existing measured data is settlement value of east revetment from August 19, 2011 year to August 5, 2012 year. To verify the accuracy of the numerical simulation analysis results, the settlement after the completion of east revetment filling 346 d was done through the numerical simulation. As fig.11 showed that actual measured settlement is 16.2 cm, but the value of numerical simulation is 18.9 cm. Therefore, we can know that the result of numerical simulation is approximate to actual measured value, which is more conservative.

### THE SENSITIVITY ANALYSIS

To accurately choose geotechnical model is a premise for geotechnical soil mechanics doing quantitative and qualitative analysis. Constitutive model and the parameters have an effect on the rationality of soil settlement analysis. Considering discrete type of geotechnical soil parameters, for the settlement numerical analysis of marine reclamation land project, the sensitivity analysis was done, which the change of main soil mechanics parameters had an effect on settlement.

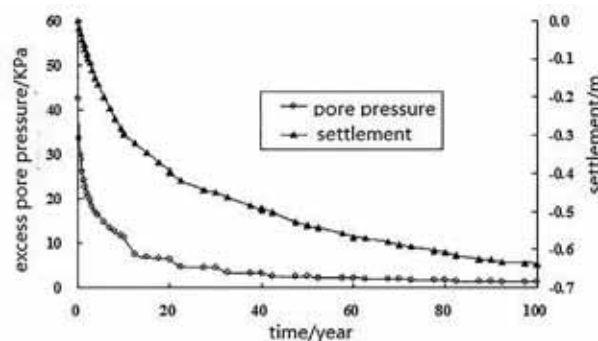
### THE INFLUENCE OF MODEL SELECTION

Soft soil model is a model of Cam-Clay, which especially is applied to primary compression of clay soil of normal consolidation, which can't explain rheological phenomenon (main performance is creep and stress relaxation). However, certain creep existed in the soil and the secondary compression some extent followed with primary compression. SSC model is just applied to the solution of soil rheological problem. Therefore, comparing the settlement result of SS model with SSC model, we can see that creep characteristics of soil had an effect on the final settlement (Fig.12).



a) Result of SS model

Fig.12. The comparison of SS model and SSC model settlement curve



b) Result of SSC model

Fig.12. The comparison of SS model and SSC model settlement curve

As Fig. 12. showed that primary consolidation had mainly finished when pore pressure slope tended to zero. And from now to hundred years after construction, the growth of SS model settlement is small, also the curve are very smooth. While the increase of SSC model settlement is very obvious, also the trend of increase will last hundred years, but the slope of curve become small, at last the settlement is tend to be steady at some time.

Tab.4 the comparison of settlement results of two creep model

location	model	S <sub>1</sub> /m	S/m	S <sub>2</sub> /m
east bank	SSC	0.492	0.586	0.094
	SS	0.501	0.518	0.017
west bank	SSC	0.539	0.638	0.099
	SS	0.512	0.525	0.013

Notes: S<sub>1</sub> is the settlement that excess pore water pressure tends to zero, S is the total settlement of hundred years after construction, and S<sub>2</sub> is the settlement of creep.

As Tab. 4 showed that the settlement of east revetment creep had a 16 % proportion of the settlement after construction based on the result of SSC model, but west revetment occupied 15.5 %, which indicated when excess pore water pressure tended to zero, creep deformation still existed after primary consolidation had mainly finished, which corresponds to objective theory. However, for SS model, without the error of finite element calculation, there wasn't creep deformation after excess pore water pressure dissipated, which doesn't correspond to objective theory. Thus it is sure that the SSC model is rational to calculate creep deformation of soft soil.

### THE INFLUENCE OF CREEP INDEX

The numerical analysis of two dimensional settlement referred to the experiential data from Japanese Kansai airport [7]. Creep index was taken 1/25 of compression index. In order to analyze influence of creep index on residual settlement, the sensitivity analysis of creep index was done. In the case of modified creep index taking 1/20, 1/25, 1/30 of modified compression index, Fig.13 shows that settlement of west revetment changes in the different reference period. As can be seen, the final residual settlement decreases along with the decrease of the creep index, and the curves become slow.

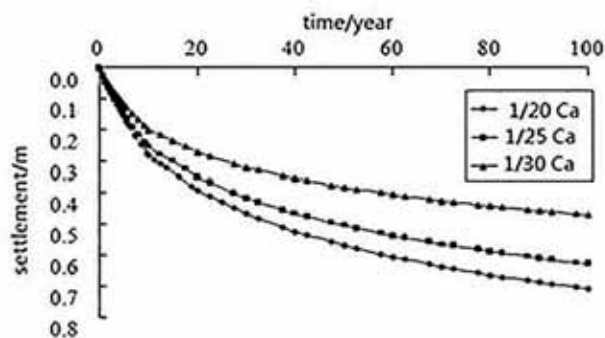


Fig. 13. alteration of modified creep index impact on residual settlement

Tab.5. OCR effect on residual settlement

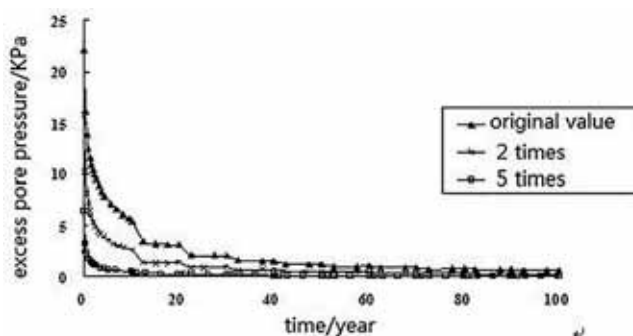
OCR value	settlement of different base period(m)				
	location	5 years	10 years	20 years	100 years
original value	West bank	0.183	0.295	0.389	0.638
	east bank	0.151	0.256	0.343	0.586
+25%	west bank	0.135	0.224	0.313	0.583
	east bank	0.120	0.205	0.280	0.491
+50%	west bank	0.122	0.194	0.265	0.483
	east bank	0.106	0.172	0.231	0.389

## THE INFLUENCE OF OVER CONSOLIDATION RATION

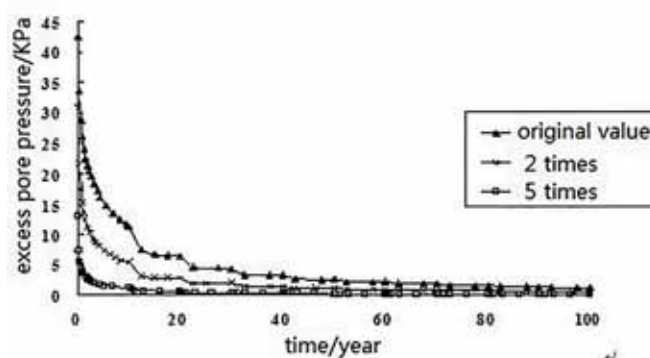
Only the OCR value was changed to analyze the effect on settlement trends and final result. Under other conditions constant, the OCR value respectively increased by 25 %, so the re-sults were obtained in Tab. 5. We can see that the greater the OCR value, the shorter the steady time of settlement, the smaller the final settlement became.

## THE INFLUENCE OF PERMEABILITY COEFFICIENT

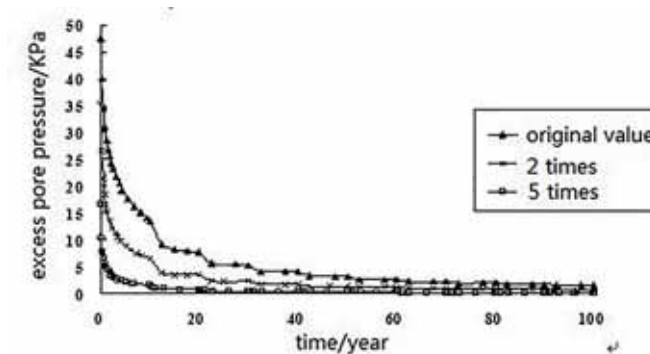
Only the permeability coefficient of soil was changed to analyze the influence on the speed of pore pressure dissipation as well as the final settlement. Under other conditions constant, the soil permeability coefficient was expanded to 2 times and 5 times of the original value. Thus the in-fluence of permeability coefficient was obtained in Fig. 14 and tab. 6



a) excess pore pressure at underground 25m



b) excess pore pressure at underground 35m



c) excess pore pressure at underground 45m

Fig.14.The comparison of permeability coefficient expanded to the original 2times and 5times

Tab.6 permeability coefficient effect on settlement

permeably coefficient	Settlement of different base period (m)				
	location	5years	10s	20s	50s
1time	West bank	0.183	0.295	0.389	0.514
2 times	West bank	0.209	0.325	0.436	0.519
5 times	West bank	0.296	0.412	0.501	0.522

Fig.14 and Tab. 6 showed that the greater permeability coefficient, the faster pore pressure dis-sipation, while the shorter the steady time of settlement. Although the final settlement value slightly increased, the difference is small.

## CONCLUSION

1. The microstructure of soil samples 1, 2 showed flocculent link structure, and some lager voids are found between the basic elements, an unconsolidated flexible framework is constructed. While, there is no connection between elements, which leads to the voids are instability, so they intend to be unstable and low strength under the compression forces. The microstructure type of the deeper silt clay is the clay matrix structure, and its skeleton particles are mainly connected with clay-based, so it's easy to see that the strength of the clay and the silt clay is stronger than the silt and the silt clay. Macro colors of silt clay at

three different depths show a decreasing trend with the incremental depth. Comparison of the three SEM figures, we can see that the voids decreased gradually with increasing the density and structural. Therefore, the strength of three became stronger gradually.

2. The largest settlement in the area of revetment is about 0.6 ~ 0.7m after 100 years of completion of Land reclamation project. From the analysis of the charts of consolidation degree and excess pore water pressure dissipation, after the completed 100a, the deep inside soil still exists a small amount of pore water pressure without dissipation, and the field area will slowly be sinking, however, the trend will become gradually slow.
3. Based on Soft-Soil-Creep model of PLAXIS and its finite element program, trends of settlement of soft ground can be depicted accurately and the creep can be also predicted more accurately. It can provide the basis for the settlement that is set aside to make sure the reclamation ground elevation after construction meets the design requirements.
4. The results of sensitivity analysis of calculation parameters indicate that the greater the OCR value, the shorter the steady time of settlement, while the final settlement became small with it. The greater the permeability coefficient, the faster pore pressure dissipation, and the shorter the steady time of settlement. Although the final settlement value slightly increased, the difference is small.
5. The modified creep index takes 1/25 of compression index in the settlement of numerical analysis which refers to the empirical data of Japanese Kansai Airport engineering ( $C_a / C_c = 0.04 \pm 0.01$ ). In order to promote the use of the determination method for the key parameters of creep, more extensive research must be carried out in related fields.

## REFERENCE

1. Biot M A. General solutions of the equations of elasticity and consolidation for a porous material. *Journal of Applied Mechanics*, 1956, 23:91-96.
2. Biot M A. General theory of three-dimensional consolidation. *Journal of Applied Physics*, 1941, 12: 155-164.
3. Brinkgreve R B J. *Plaxis version 8 scientific manual*. Netherlands: A.A.Balkema Publishers, 2002.
4. Chen Zongji. The consolidation and sub-time effect of unidirectional problems. *Civil Engineering Journal*. 1958(1): 1-10.
5. Chen Wensu. *The settlement of soft soil creep numerical simulation*. Tianjin: Tianjin Univesity, 2004.

6. Mimura, M., Jeon, B.G. Numerical assessment for the behavior of the Pleistocene marine foundations due to completion of the 1st phase island of Kansai international airport. *Soils and Foundations*, 2011, 51(6):1115-1128.
7. Mimura, M., Jeon, B.G. Interactive Behavior of the Pleistocene Reclaimed Foundations due to the Completion of the adjacent Reclamation. *Annuals of Disas. Prev. Res. Inst., Kyoto Univ.*, No.54B, 2011
8. [8] Sun Junzhu. *Rheological and geotechnical engineering application*. Beijing: China Building Industry Press, 1999.
9. Tang Bin, Chen Xiaoping, Zhang Wei. Consider the rheological properties of soft Consolidation finite element analysis. *Rock and Soil Mechanics*, 2004, 25(4): 583-586.
10. VERMEER P A, NEHER H P. A soft soil model that accounts for creep//Beyond 2000 in *Computational Geotechnics-10 Years of PLAXIS International*. Netherlands: A. A. Balkema Publishers, 1999.
11. Yin J H., Graham J. Viscous-elastic-plastic modeling of one-Dimensional time-dependent behavior of clays. *Canadian Geotechnical Journal*, 1989, 29: 199-209.

## CONTACT WITH AUTHOR

Zhao Jie  
zhaojie\_gd@163.com

Zhou Tongling  
Wang Gui-xuan

Dalian University R & D Center  
of the Civil Engineering Technology  
116622, Dalian  
China

# MODELING OF ACOUSTIC FIELD FOR A PARAMETRIC FOCUSING SOURCE USING THE SPHEROIDAL BEAM EQUATION

Lili Yu<sup>a</sup>

Junhua Li<sup>b</sup>

Chaojian Shi<sup>a</sup>

a) Department of Navigation Technology, Shanghai Maritime University,  
Shanghai, China

b) College of Ocean Science and Engineering, Shanghai Maritime University,  
Shanghai, China

## ABSTRACT

*A theoretical model of acoustic field for a parametric focusing source on concave spherical surface is proposed. In this model, the source boundary conditions of the Spheroidal Beam Equation (SBE) for difference frequency wave excitation were studied. Propagation curves and beam patterns for difference frequency component of the acoustic field are compared with those obtained for Khokhlov-Zabolotskaya-Kuznetsov (KZK) model. The results demonstrate that the focused parametric model of SBE is good valid for a large aperture angle in the strongly focused acoustic field. It is also investigated that high directivity and good focal ability with the decreasing of downshift ratio and the increasing of half-aperture angle for the focused parametric model of SBE.*

**Keywords:** parametric focusing source, difference frequency wave, SBE, acoustic field

## INTRODUCTION

Since the difference frequency waves generated by parametric array have low frequency, high directivity and resolution, and good penetrative performance, parametric array is applied for underwater detection [2, 6]. There is a great significance for distinguishing seabed properties and detecting buried object [1, 5]. The experimental results for the near field of a parametric planar source have been published in Ref.5, which have carried out computations of the near field on the basis of the Khokhlov-Zabolotskaya-Kuznetsov (KZK) equation, and favorable agreement between the theoretical and experimental results was obtained [9]. The nonlinear behavior of a bounded sound beam generated by a parametric planar source in the far-field region of the source was also studied in Ref.6, which have introduced a coordinate transform in order to accommodate the spherical spreading of the acoustic field [4]. However, these works were generally used to describe nonlinear interactions of a parametric planar sound source. Although effects of focusing on the parametric interaction between two focused beams generated by monochromatic sources was investigated with KZK equation, this model is more suitable for a weak focused ultrasound beam because that it derived under the paraxial approximation and the upper limit of the applicability is about for the half aperture angle [3].

Later, the spheroidal beam equation (SBE) proposed by Kamakura et al. [10] used the oblate spheroidal coordinate system for theoretical prediction on strongly focused ultrasound beams with a circular aperture; the upper limit of the half aperture angle is up to 40°. Moreover, SBE can be easily extended to the analysis of nonlinear harmonic generation with high frequencies in finite amplitude sound beams [8]. However, SBE is generally used to describe sound propagation for geometrical self-focusing source with a single-frequency wave excitation. Currently, there are few reported results referring to SBE application in nonlinear interactions for difference frequency waves generated by parametric focusing source.

In this paper, we study some boundary conditions for difference frequency waves on a strongly focusing source using SBE. A strongly focusing source radiates a difference frequency sound wave, and some modifications are made to allow a boundary condition with two prescribed frequencies. In this case, two sinusoidal waves at the source are assumed to be just adjacent harmonics. The fundamental component corresponds to difference frequency sound. The numerical results are compared with results obtained in weakly focused amplitude sound beams, where KZK model have been used. Then, the propagation curve and beam patterns of difference frequency wave for SBE are investigated by

varying parameters such as downshift ratio and half-aperture angle.

## THEORY AND METHODS

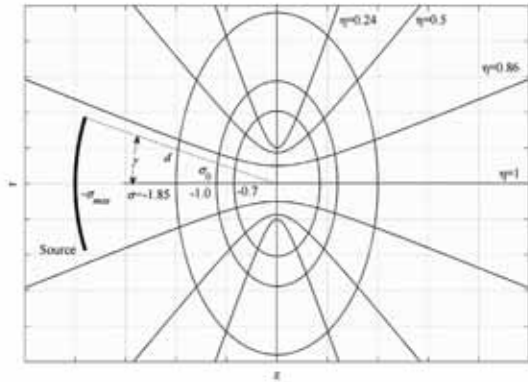


Fig.1. Oblate spheroidal coordinate system

To explain sound propagation with a large aperture angle, we apply SBE in an oblate spheroidal coordinate system [10] (Fig. 1). The focused ultrasound field is divided into two regions, i.e.,  $\sigma < \sigma_0$  and  $\sigma \geq \sigma_0$ , where  $\sigma_0$  denotes a specific transition location. The former division near the source is a spherical wave region, and the latter division near the focus is a plane wave region. The SBE model to describe the spheroidal and planar waves in two regions are expressed as follows respectively [10]:

$$\frac{\partial^2 \bar{p}}{\partial \tau_s \partial \sigma} + \frac{1}{2} \frac{\sin 2\theta}{\sigma(1+\sigma^2)} \frac{\partial^2 \bar{p}}{\partial \tau_s \partial \theta} + \frac{\varepsilon \sqrt{\sigma^2 + \sin^2 \theta}}{\sigma(1+\sigma^2)} \times \left( \frac{\partial^2 \bar{p}}{\partial \theta^2} + \cot \theta \frac{\partial \bar{p}}{\partial \theta} \right) + \frac{E}{\sigma} \frac{\partial \bar{p}}{\partial \tau_s} = -\frac{\sqrt{\sigma^2 + \sin^2 \theta}}{\sigma} \left( \alpha b \frac{\partial^3 \bar{p}}{\partial \tau_s^3} + \frac{b}{2l_D} \frac{\partial^2 \bar{p}^2}{\partial \tau_s^2} \right) E \quad (\sigma < \sigma_0 < 0) \quad (1)$$

$$\frac{\partial^2 \bar{p}}{\partial \tau_p \partial \sigma} - \frac{\sigma}{1+\sigma^2} \sin \theta \frac{\partial^2 \bar{p}}{\partial \tau_p \partial \theta} - \frac{\varepsilon(2-\cos \theta)}{1+\sigma^2} \times \left( \frac{\partial^2 \bar{p}}{\partial \theta^2} + \cot \theta \frac{\partial \bar{p}}{\partial \theta} \right) = \left( \alpha b \frac{\partial^3 \bar{p}}{\partial \tau_p^3} + \frac{b}{2l_D} \frac{\partial^2 \bar{p}^2}{\partial \tau_p^2} \right) E \quad (\sigma \geq \sigma_0, \sigma_0 < 0) \quad (2)$$

$$\left\{ \begin{aligned} & \frac{\partial g_n}{\partial \sigma} + \frac{1}{2} \frac{\sin(2\theta)}{\sigma(1+\sigma^2)} \frac{\partial g_n}{\partial \theta} + \frac{\varepsilon \sqrt{\sigma^2 + \sin^2 \theta}}{n \cdot \sigma(1+\sigma^2)} \left( \frac{\partial^2 h_n}{\partial \theta^2} + \cot \theta \frac{\partial h_n}{\partial \theta} \right) + \frac{E}{\sigma} g_n = \\ & = -\frac{\sqrt{\sigma^2 + \sin^2 \theta}}{\sigma} \left\{ -\alpha \cdot b \cdot n^2 g_n + \frac{b}{2l_D} n \left[ \frac{1}{2} \sum_{p=1}^{n-1} (g_p g_{n-p} - h_p h_{n-p}) - \sum_{p=n+1}^{\infty} (g_{p-n} g_p + h_{p-n} h_p) \right] \right\} E \\ & \frac{\partial h_n}{\partial \sigma} + \frac{1}{2} \frac{\sin(2\theta)}{\sigma(1+\sigma^2)} \frac{\partial h_n}{\partial \theta} - \frac{\varepsilon \sqrt{\sigma^2 + \sin^2 \theta}}{n \cdot \sigma(1+\sigma^2)} \left( \frac{\partial^2 g_n}{\partial \theta^2} + \cot \theta \frac{\partial g_n}{\partial \theta} \right) + \frac{E}{\sigma} h_n = \\ & = -\frac{\sqrt{\sigma^2 + \sin^2 \theta}}{\sigma} \left\{ -\alpha \cdot b \cdot n^2 h_n + \frac{b}{2l_D} n \left[ \frac{1}{2} \sum_{p=1}^{n-1} (h_p g_{n-p} + g_p h_{n-p}) + \sum_{p=n+1}^{\infty} (h_{p-n} g_p - g_{p-n} h_p) \right] \right\} E \end{aligned} \right. \quad (\sigma < \sigma_0 < 0) \quad (4)$$

where the variables  $(\sigma, \eta)$  in the oblate spheroidal coordinate are related to the cylindrical coordinate  $(r, z)$  through the relationships of  $r = b\sqrt{(1+\sigma^2)(1-\eta^2)}$  and  $z = b\sigma\eta$ , in which  $b$  is the half inter-focal length. The angle variable  $\Theta$  is related to  $\eta$  as  $\eta = \cos\Theta$  and  $\gamma$  is the half-aperture angle. The coefficient  $\varepsilon$  is set at  $1/2 kb$  and  $E$  is a function of  $\sigma$  and  $\Theta$ ;  $\tau_s$  is the spherically retarded time near the source;  $\tau_p$  is the retarded time for planar waves near the focus;  $\bar{p} = p/p_0$  is the normalized sound pressure with  $p_0$  as the initial amplitude of sound pressure on the surface of the source;  $\alpha$  is the sound attenuation coefficient;  $l_D$  is shock formation distance for a planar wave, which is related to the nonlinear coefficient  $\beta$  of the medium. If  $\beta = 0$ , the SBE model can be used to predict linear fields.

In the frequency domain, the solutions of Eq. (1) and Eq. (2) are represented by the following Fourier series expansions, respectively [10],

$$\bar{p} = \begin{cases} \sum_{n=1}^{\infty} [g_n^{(s)} \sin(n\tau_s) + h_n^{(s)} \cos(n\tau_s)] & (\sigma < \sigma_0 < 0) \\ \sum_{n=1}^{\infty} [g_n^{(p)} \sin(n\tau_p) + h_n^{(p)} \cos(n\tau_p)] & (\sigma \geq \sigma_0, \sigma_0 < 0) \end{cases} \quad (3)$$

where  $g_n^{(s)}$ ,  $h_n^{(s)}$ ,  $g_n^{(p)}$  and  $h_n^{(p)}$  are amplitude components of the  $n$ -th harmonic and are functions of the spatial variables  $\sigma$  and  $\Theta$ .

Substituting Eq. (3) to in Eqs. (1) and (2), we obtain the following two set of coupled nonlinear partial differential equations in the amplitudes of the various Fourier components.

$$\left\{ \begin{aligned} & \frac{\partial g_n}{\partial \sigma} - \frac{\sigma \sin \theta}{(1+\sigma^2)} \frac{\partial g_n}{\partial \theta} - \frac{\varepsilon(2-\cos \theta)}{n \cdot (1+\sigma^2)} \left( \frac{\partial^2 h_n}{\partial \theta^2} + \cot \theta \frac{\partial h_n}{\partial \theta} \right) = \\ & = \left\{ -\alpha \cdot b \cdot n^2 g_n + \frac{b}{2l_D} n \left[ \frac{1}{2} \sum_{p=1}^{n-1} (g_p g_{n-p} - h_p h_{n-p}) - \sum_{p=n+1}^{\infty} (g_{p-n} g_p + h_{p-n} h_p) \right] \right\} E \quad (\sigma \geq \sigma_0, \sigma_0 < 0) \\ & \frac{\partial h_n}{\partial \sigma} - \frac{\sigma \sin \theta}{(1+\sigma^2)} \frac{\partial h_n}{\partial \theta} + \frac{\varepsilon(2-\cos \theta)}{n \cdot (1+\sigma^2)} \left( \frac{\partial^2 g_n}{\partial \theta^2} + \cot \theta \frac{\partial g_n}{\partial \theta} \right) = \\ & = \left\{ -\alpha \cdot b \cdot n^2 g_n + \frac{b}{2l_D} n \left[ \frac{1}{2} \sum_{p=1}^{n-1} (h_p g_{n-p} + g_p h_{n-p}) + \sum_{p=n+1}^{\infty} (h_{p-n} g_p - g_{p-n} h_p) \right] \right\} E \end{aligned} \right. \quad (5)$$

It is practicable to obtain the solution of the n-th harmonic component using an implicit backward finite difference method.

Now let the source be excited simultaneously at the two frequencies  $f_1$  and  $f_2$ . We impose periodicity in the boundary conditions on the source, and the two frequencies must therefore be commensurable. This means that there exist  $f$  such that

$$f_1 = N_1 f \quad \text{and} \quad f_2 = N_2 f \quad (6)$$

where  $N_1$  and  $N_2$  are integers greater than unity. Let  $f$  denote the largest possible frequency that satisfies these conditions. We refer to  $f$  as the basic frequency and to  $f_- = |f_1 - f_2|$  as the difference frequency. Also, the center frequency  $f_m = (f_1 + f_2)/f$  and the downshift ratio  $f_m/f_-$  are introduced.

Consequently, boundary conditions at the source in the SBE system yield the following relation:

$$\bar{p}|_{\sigma=-\sigma_{\max}} = U_1(\theta) \sin(N_1 \tau_s + \phi) + U_2(\theta) \sin(N_2 \tau_s) \quad (7)$$

where  $U_1(\theta)$  and  $U_2(\theta)$  are the pressure distribution function on the surface of the source, both  $N_1$  and  $N_2$  are integer greater than unity, and  $\phi$  is the initial phase. The value of initial phase does not play an important role in the parametric amplification under the condition of  $N_1 \geq 3$  and  $N_2 \geq 3$ , which the difference frequency is essentially independent of the variation of  $\phi$  [9]. Therefore, the zero phase of  $\phi$  is used for the sake of convenience.

Thus, the initial values of  $g_n^{(s)}$  and  $h_n^{(s)}$  at  $\sigma = -\sigma_{\max}$  are given through the boundary condition of Eq. (7):

$$\left\{ \begin{aligned} & g_{N_1}^{(s)} = U_1(\theta) \cos \phi \\ & h_{N_1}^{(s)} = 0 \\ & g_{N_2}^{(s)} = U_2(\theta) \\ & h_{N_2}^{(s)} = U_1(\theta) \sin \phi \\ & g_n^{(s)} = h_n^{(s)} = 0, \quad n \neq N_1, N_2 \end{aligned} \right. \quad (8)$$

In this section we present numerical results for the acoustic field from a strongly focusing source with uniform amplitude distribution described by

$$U_1(\theta) = U_2(\theta) = \begin{cases} 1 & (0 \leq \theta \leq \gamma) \\ 0 & (\text{others}) \end{cases} \quad (9)$$

Then, the pressure amplitudes at  $\sigma = -\sigma_{\max}$  are obtained by  $\sqrt{g_n^{(s)^2} + h_n^{(s)^2}}$ .

## NUMERICAL EXAMPLES

To examine the validity of SBE for parametric focusing source with a concave spherical source, the effects of focusing are carried out for the primary, difference and sum frequency waves with  $f_m/f_- = 5.5$ ,  $p_0 = 100$  Kpa,  $d = 10$  cm,  $\gamma = 30^\circ$ . In addition, degassed water, with sound velocity  $c_0 = 1500$  m/s, density  $\rho_0 = 1000$  kg/m<sup>3</sup>, nonlinear coefficient  $\beta = 3.5$ , and attenuation coefficient  $\alpha = 0.0253$  Np/m at 1 MHz with frequency dependence  $f^2$ , is used as the propagation medium in the simulation. Since it is not easy to solve the SBE equation analytically, numerical computation is performed by means of an implicit backward finite difference method. For ensuring reasonable accuracy, we establish 600 grid points from 0 to  $\Pi/2$  on the  $\Theta$  axis, and thus the step size of  $\Theta$  is  $2.618 \times 10^{-3}$  rad. The transition location is numerically determined to be a reasonable choice for  $\sigma_0 = -1.0$  [7].

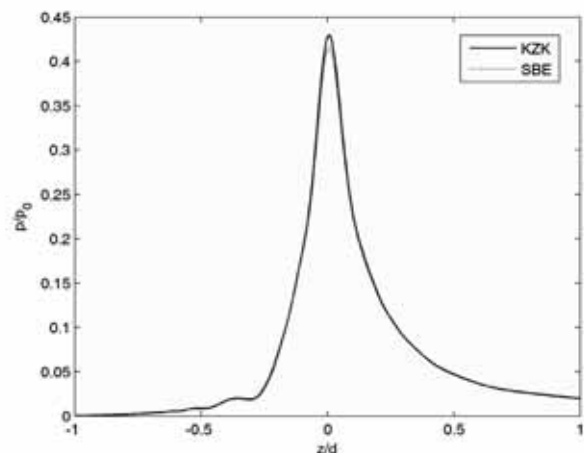


Fig. 2a. On-axis Comparison of pressure amplitude between the SBE model and KZK model for difference frequency wave

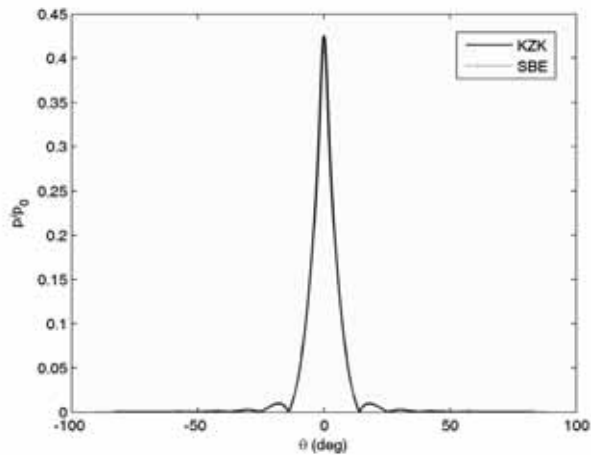


Fig. 2b. Beam patterns in the focal plane Comparison of pressure amplitude between the SBE model and KZK model for difference frequency wave

An interesting comparison is shown in Fig. 2 for the SBE and KZK solutions with the difference frequency wave. It can be found that the pressure amplitude from SBE is slightly smaller than that from KZK model in the focal region and the maximum deviation is less than 3%, but both models are in good agreement in the axial distribution and beam patterns. Moreover, previous studies [3] validated effectiveness of KZK model for a parametric focusing source. Consequently, the focused parametric model of SBE is also good valid for a parametric focusing source on a concave spherical surface with a large aperture angle in the acoustic field.

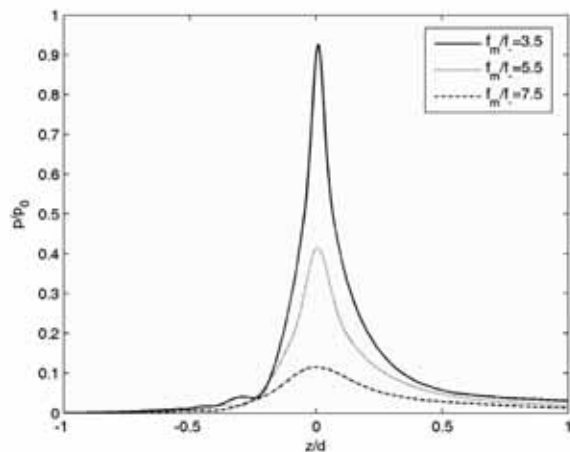


Fig. 3a. On-axis Comparison of pressure amplitude for difference frequency wave using SBE model with three different of downshift ratios

For three different of downshift ratios (e.g.  $f_m/f_- = 3.5, 5.5,$  and  $7.5$ ), the corresponding propagation curves and beam patterns for the difference frequency wave are shown in Fig.3. With the downshift ratio  $f_m/f_-$  increasing, the pressure amplitude along the axis is gradually decreasing, while the angle of -3 dB beam width is evidently broadening in the focal region. Also, the pressure amplitude varies very slowly whether along the axis or across the axis. This means that the increasing of downshift ratio  $f_m/f_-$  weakens the efficiency of difference frequency generation.

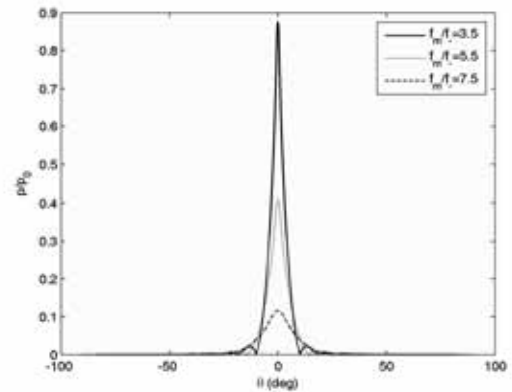


Fig. 3b. Beam patterns in the focal plane Comparison of pressure amplitude for difference frequency wave using SBE model with three different of downshift ratios

Figure 4 shows propagation curve and beam patterns for the difference wave with three different of half-aperture angles (e.g.  $\gamma = 20^\circ, 30^\circ,$  and  $40^\circ$ ) and a fixed downshift ratio  $f_m/f_- = 5.5$ . The larger the half-aperture angle  $\gamma$ , the higher is the pressure amplitude along the axis, and the shorter is the angle of -3 dB beam width in the focal region.

From Figs.3 and 4, it can be implemented by decreasing of the downshift ratio  $f_m/f_-$  and increasing of the half-aperture angle  $\gamma$  for high directivity and resolution, good focused ability and penetrative performance.

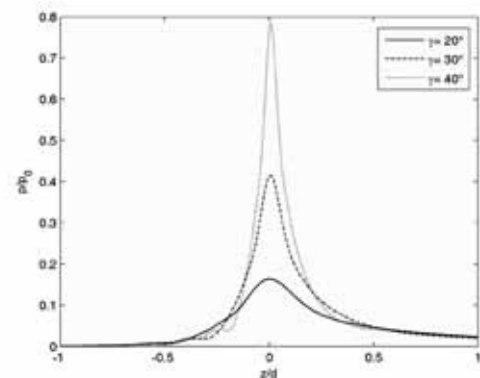


Fig. 4a. On-axis Comparison of pressure amplitude for difference frequency wave using SBE model with three different of half-aperture angle

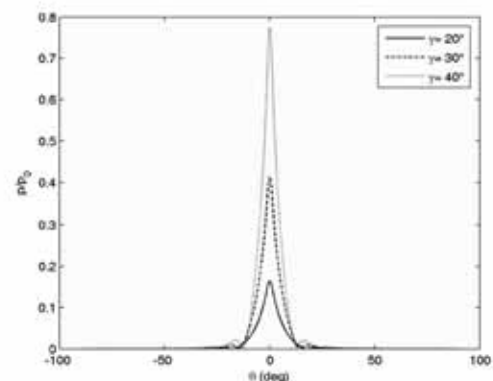


Fig. 4b. Beam patterns in the focal plane Comparison of pressure amplitude for difference frequency wave using SBE model with three different of half-aperture angle

## CONCLUSION

In conclusion, this study proposes source boundary conditions using SBE for a focused parametric source on a concave spherical source. The pilot study of parametric effects by SBE model is implemented, numerical results of which are good agree with that of KZK model. The simulations show that the difference frequency radiation is effectively focused, in that the -3 dB beam width became quite narrow in the focal plane. In addition, with decreasing the downshift ratio and increasing the half-aperture angle, it can be obtained that high directivity and resolution, good focused ability and penetrative performance. It is really benefit to distinguishing seabed properties and detecting buried object. Compared with KZK model, a focused parametric model of SBE lays a theoretical basis for the study of parametric effects under high frequencies and large aperture angles.

## ACKNOWLEDGMENTS

The authors thank Prof. Tomoo Kamakura, the university of Electro-Communication, Japan, for his useful help in solving the SBE programming.

This paper was supported by the National Natural Science Foundation of China under Grant No. 51209133, Program for Innovative Research Team in Shanghai Maritime University, Shanghai Municipal Education Commission First-class Disciplines Project and Innovation Project of Shanghai Graduate Education (No. 20131129).

## REFERENCES

1. D Boulinguez, A Quinquis, 3-D underwater object recognition. *IEEE Journal of Oceanic Engineering*, 2002, 27(4), 814-829.
2. E Kozaczka, G Grelowska, S Kozaczka, and W Szymczak, Detection of Objects Buried in the Sea Bottom with the Use of Parametric Echosounder. *Archives of Acoustics*, 2013, 38(1), 99-104.
3. J. Naze Tjøtta, S. Tjøtta and E.H. Vefring, Effects of focusing on the nonlinear interaction between two collinear finite amplitude sound beams, *J.Acoust.Soc.Am.* 1991, 89 (3), 1017-1027.
4. J. Naze Tjøtta, S. Tjøtta, and E.H. Vefring, Propagation and interaction of two collinear finite amplitude sound beams, *J.Acoust.Soc.Am.* 1990, 88 (6), 2859-2869.
5. J. Wunderlich, S. Müller, High-resolution sub-bottom profiling using parametric acoustics. *International Ocean Systems*, 2003, 7(4), 6-11.
6. P.J. Westervelt, Parametric Acoustic Array. *J.Acoust.Soc. Am.* 1963, 35(4), 535-537.
7. R.M. Xia, W.D. Shou, G.P. Chen and M.D. Zhang, The further study of the spheroidal beam equation for focused finite-amplitude sound beams, *J.Comput. Acoust.* 2003, 11 (1), 47-53.
8. S.Y. Qian, T. Kamakura and M. Akiyama, Simulation of sound field in a tissue medium generated by a concave spherically annular transducer, *Ultrasonics*, 2006, 44 (1), 271-274.
9. T. Kamakura, N. Hamada, K. Aoki, and Y. Kumamoto, Nonlinearly generated spectral components in the nearfield of a directive sound source. *J.Acoust.Soc.Am.* 1989, 85 (6), 2331-2337.
10. T. Kamakura, T. Ishiwata and K. Matsuda, Model equation for stringly focused finite-amplitude sound beams, *J.Acoust.Soc.Am.* 2000, 107 (6), 3035-3046.

## CONTACT WITH AUTHOR

Lili Yu  
llyu@shmtu.edu.cn

Chaojian Shi

Department of Navigation Technology  
Shanghai Maritime University  
200136 Shanghai  
China

Junhua Li

College of Ocean Science and Engineering  
Shanghai Maritime University  
200136 Shanghai  
China

# HYDRAULIC ANALYSIS OF LEAKAGE FROM SUBMARINE PIPE NETWORK

JunHua Li

YanTing Fan

School of Ocean Science and Engineering, Shanghai Maritime University  
Shanghai, China

## ABSTRACT

*The leakage from submarine pipe network is investigated by a numerical model in this paper. A whole event including of the steady flow before the leakage, the transient flow during the leakage and the steady flow after the leakage is considered in the model. The numerical results of the discharge and the head compare with the theoretical solution under the condition of steady flow. Good agreement is obtained. The numerical results of the discharge and the head show that the discharge and the head in each pipe changes suddenly after the leakage occurring. The abrupt trend of the discharge in each pipe is not same completely. Some change upwards, while others downwards. However, the abrupt trend of the head is always downward. The effects of leakage discharge on the transient flow are also investigated. It is founded that the larger the leakage discharge, the more obvious the abrupt trend of the discharge and the head before or after the leakage is.*

**Keywords:** submarine pipe network, leakage, transient flow

## INTRODUCTION

Submarine pipe networks are used as the important conveyance system all around the world. Unfortunately, the corrosion of the pipe, the interaction between wave current and networks and the mismanagement have led to leaking accidents in the submarine pipe networks. The leakage from submarine pipe networks will not only cause immense waste of resources and serious economic losses, but also severe pollution to the marine environment. Therefore, it is necessary to further the study of the leakage from submarine pipeline networks.

The submarine pipe network goes through from the initial state of no leaking to the leaking state and to the stable state after the leaking at last. Meanwhile, current in the pipes goes through from the initial steady state to the transient flow state and to the stable transient state at last. Therefore, these three states are not only mutual independent changing process but also mutual successive. In consequence, the flow process before and after the leakage should be studied as a successive changing process.

Previous researchers adopted steady flow model [6] and unsteady flow model [5, 7] to carry on researches about the inverse problem of network leakage respectively. Until now, there are less study that takes the before-leak state, transient leak state and stable leak state as a whole successive process. The reason may be that the previous networks put much emphasis on the maximum pressure caused by transient flow which results from equipment operations (like the sudden stop of pump or the start/stop of valve). The simulation before, in and after the

process of leakage is important to the design, maintenance, operation and leak detection. Therefore, the point of this study is taking the state before the leakage, during the leakage and the stable leak state as a whole successive changing process of flow for simulation. The content includes the simulation of the whole process of the steady flow, the transient flow and the stable transient flow, the leakage influence towards the pressure and the discharge as well as the leakage magnitude influence towards the transient flow during the leakage.

## THE TRANSIENT FLOW MODEL OF PIPE NETWORKS

### THE GOVERNING EQUATION

The hydraulic parameters of the flow in the pipe change with time when the leakage occurs, which called the hydraulic transient. The property of hydraulic transient in the networks can be simulated by using transient flow model.

Assumed that the network is under a regular state before the leakage and there is no operation of equipments. At the moment, the flow of the network is in the stable state. After the stabilization of the leakage, the flow will also be under the condition of steady flow. So the steady flow model is used to stimulate before and after the leakage. Betâmio and Koelle [2] suggested that transient flow model can also be used to stimulate the steady flow state of the network. Therefore, this paper uses the transient flow model to stimulate the hydraulic behaviour before or after the leakage or during the leakage occurs.

Assumed that the full pipe flow is in the network, in which liquid column separation won't occur. The pipe wall is made of linear elastic material. The frictional loss under the unsteady state equals to the one in the steady state. With all conditions above, the transient flow equation of one-dimensional network [8] can be expressed as:

$$\frac{\partial H}{\partial t} + \frac{a^2}{gA} \frac{\partial Q}{\partial x} = 0 \quad (1)$$

$$\frac{\partial H}{\partial x} + \frac{1}{gA} \frac{\partial Q}{\partial t} + \frac{fQ|Q|}{2gDA^2} = 0 \quad (2)$$

When the leakage occurs in the network, the outflow equation of the leaking orifice is written as:

$$Q_L = C_d A_L \sqrt{2g(H_L - z_L)} \quad (3)$$

Where: x is the distance along with the pipe; t is the time; Q is the discharge; H is the piezometric head; D is the inner diameter of pipe; A is the cross sectional area of pipe; a is the water hammer wavespeed; g is the acceleration of gravity; f is the Darcy-Weisbach coefficient of friction resistance; QL is the discharge of leakage; Cd is the coefficient of leaking flux; AL is the area of leakage; HL is the piezometric head in the pipe where leakage occurs; zL is the potential head where the leakage occurs.

## SOLUTIONS

The transient flow equations are a group of quasi-linear hyperbolic partial differential equations, which including the continuity equation and the momentum equation. It only can be solved by numerical method. At present, method of characteristics (MOC) is most common to solve the transient flow in the networks [8]. The equations are discretized by the method of characteristics. The specific process of discretization is seen in document 1 or 8. The equations after discretization are written as:

$$(H_P - H_A) + \frac{a}{gA} (Q_P - Q_A) + \frac{f\Delta x Q_A^2}{2gDA^2} = 0 \quad \frac{dx}{dt} = C^+ \quad (4)$$

$$(H_P - H_B) - \frac{a}{gA} (Q_P - Q_B) - \frac{f\Delta x Q_B^2}{2gDA^2} = 0 \quad \frac{dx}{dt} = C^- \quad (5)$$

Where the subscript P is present point at present time step, the subscript A is the previous point at previous time step; the subscript B is the latter point at the previous time step; Δx is space intervals, C+ and C- is the characteristic line and the inverse characteristic line respectively.

There are four unknown for each section in the pipe networks: upstream flux, upstream head, downstream flux and downstream head. These four unknowns are not solved by those two equations mentioned above. It still needs two compatible equations, which include equations of the mass

conservation and the equivalence of head at the nodes. These two compatible equations are not used on the boundary. As a result, the flux, the head or the relation between flux and head are given. The simultaneous equations (discrete equations, compatible equations and boundary conditions) are shown as the form of matrix:

$$[M]\{v\} = \{R\} \quad (6)$$

Where [M] is the coefficient matrix of unknown variables, {v} is an unknown vector of the discharges and the heads at present time step, {R} is a vector independent on unknown variables.

## THE STEADY FLOW MODEL IN PIPE NETWORKS

The initial hydraulic parameters (velocity and head) are given to solve the transient flow model. In some pipe systems, the maximal pressure under the condition of transient flow is quite sensitive to the velocity under the initial condition [4]. Therefore, it is significant to give reasonable flow velocity and pressure under the initial steady flow condition for the calculation of transient flow.

With regard to an operational pipe network, the flux in each pipe and the head in the node are obtained by the solution of the steady flow model in pipe networks according to the boundary conditions and topology structure of the network. The following steady flow model is used to solve the flux and the head in the initial condition.

## CONTINUITY EQUATION AT THE NODE

$$\sum_{n=1}^j Q_{in} + Q_{iq} = 0 \quad i = 1, 2, \dots, M \quad (7)$$

Where M is the number of nodes, i is number of the pipe connected with the node i; Qiq is the external flux at the node i. It sets that the flux into the node is positive and the flux out the node is negative.

## ENERGY EQUATION

$$|H_i^k - H_j^k| = |\bar{R} Q_k^2| \quad k = 1, 2, \dots, L \quad (8)$$

Where L is the number of pipes, k is the number of pipe connecting between node i and node j,  $\bar{R} = \frac{8\lambda l_k}{\pi^2 d_k^5 g}$ .

Hardy-Cross Method and Newton-Raphson Iterative Method are used as the solutions to the equations mentioned above. Hardy-Cross Method is available for loop pipe network (if none-loop pipe network, forming loop network by virtual pipes). Newton-Raphson Iterative Method is used in this paper.

## APPLICATION

It is simulated the process of leakage in the pipe network shown in Fig.1. This pipe network was introduced by Pudar and Liggett originally [6], and then by Liggett and Chen [5]. The lengths of the pipes in this pipe network are given in the figure. The pipe diameter is 254mm. The thickness of pipe is 1.6mm. Node 1 and node 4 are boundary nodes. Node 1 is connected with the tank, with 30m head constantly. Node 4 is the outflow node, with 0.01 m<sup>2</sup>/s quantity of flux.

### THE CONDITION OF STEADY FLOW

To verify the program, calculate the pipe network under the condition of steady flow firstly. Tab.1 shows the flux in each pipe. The results compare with the theory solutions by taking node 3 as an example. The pipes connecting with node 3 are pipe 2, pipe 3, pipe 10 and pipe 11 as shown Fig.1. Suppose that the discharge into node 3 is positive, and outflow is negative. Plus all the discharge at node 3 and get: . Similarly, the sum of node 2, 4, 5, 6 is 0.0, -0.001, 0.0, 0.0, 0.0 respectively. The results above are approximate to the theory solution of the accumulative sum of node flux being 0 in the condition of steady flow.

Tab.1. The velocity and discharge in each pipe under the condition of steady flow

Pipe No.	Upstream node	Downstream node	Pipe length (m)	Velocity (m/s)	Discharge (m <sup>3</sup> /s)
1	1	2	1066.8	0.92	0.047
2	1	3	762	1.05	0.054
3	3	2	762	0.30	0.015
4	2	5	1066.8	0.21	0.011
5	2	4	762	1.01	0.051
6	5	4	762	0.96	0.048
7	6	5	762	0.15	0.007
8	7	6	762	0.15	0.007
9	7	5	1066.8	0.18	0.009
10	3	7	762	0.33	0.016
11	3	5	762	0.41	0.021

Tab.2 shows the head at each node in pipe network under the condition of steady flow. The numerical results compare with the solutions of Darcy-Weisbach Equation. The coefficient of friction resistance is obtained by Swamee-Jain Equation. It is known from the table that the head differences of pipe between two nodes are basically agreement with the solution of Darcy-Weisbach Equation.

Tab.2. The head at the nodes

Pipe No.	Head at upstream node	Head at downstream node	Head difference (m)	Velocity (m/s)	f	$h_f = f \frac{l V^2}{d 2g}$
1	30.00	27.17	2.83	0.92	0.0155	2.81
2	30.00	27.44	2.56	1.05	0.0151	2.54
3	27.44	27.17	0.27	0.30	0.0195	0.27
4	27.17	26.96	0.21	0.21	0.0210	0.20
5	27.17	24.78	2.39	1.01	0.0152	2.37
6	26.96	24.78	2.18	0.96	0.0154	2.17
7	27.04	26.96	0.08	0.15	0.0228	0.08
8	27.12	27.04	0.08	0.15	0.0228	0.08
9	27.12	26.96	0.16	0.18	0.0218	0.15
10	27.44	27.12	0.32	0.33	0.0191	0.32
11	27.44	26.96	0.48	0.41	0.0182	0.47

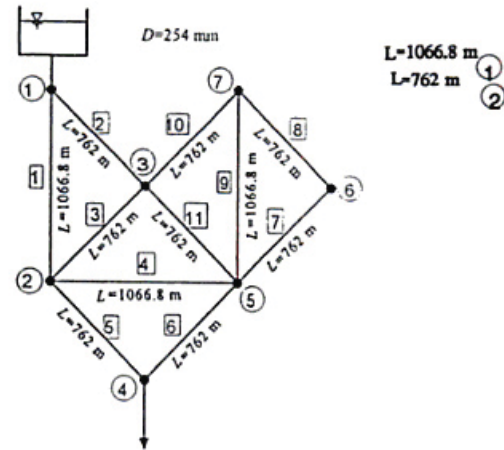


Fig. 1 The process of leakage in the pipe network

### THE CONDITION OF LEAKAGE

#### LEAKAGE AT NODE 5

The number is maximum pipes at node 5 as shown in Fig.1. If leakage occurs at node 5, the variation of the flux or head in all pipes is quite sensitive to the leakage from other nodes. In consideration of this aspect, the leaking at node 5 is considered firstly.

##### (1) The condition of a sudden leakage

Simulation of the transient flow resulted from the leakage at node 5. The total length of time is 578s. From 0s-110s, there is no leaking in steady flow. At 111st s, the leakage occurred at node 5, with 41-mm diameter leaking orifice, 61 pipe sections, 57 nodes and 0.115s time step.

Fig.2 shows the downstream discharge variation with time in 11 pipes. From the figures, it is obtained that the downstream flux in pipe 6 (namely the flux of node 4) remain steady under the condition of steady flow and suddenly decrease after the leakage compared with the one in the steady state. After a period of time, the discharge became steady again. However, the abrupt trends of downstream discharges in other pipes are opposite to the one in pipe 6 after the leakage occurs.

Fig.3 gives the node 2-7 head variation with the time respectively. As shown in the figures, the heads of all nodes are constant before the leakage occurred. When the leakage occurred, the head changed suddenly until steady. The head after the leakage is less than the one in initial steady flow.

With regard to the leakage sensitivity of flux and head, the figures show clearly that the flux in the pipes is more sensitive to the leakage than the head.

Fig.4 gives the partial enlarged drawing of the head variation with time at node 4 when the transient flow occurred. As shown in the figure, the head waved periodically in transient flow. The period and the peak amplitude of waves decrease gradually. The peak amplitude of head is 1.3 times of the one in the condition of steady flow. The minimum value of head is 1.5 times of the one under the condition of steady.

##### (2) The condition of a slow leakage

Besides the speed of leak slows down, other conditions remain the same. The leak occurs from the 111st s, with the

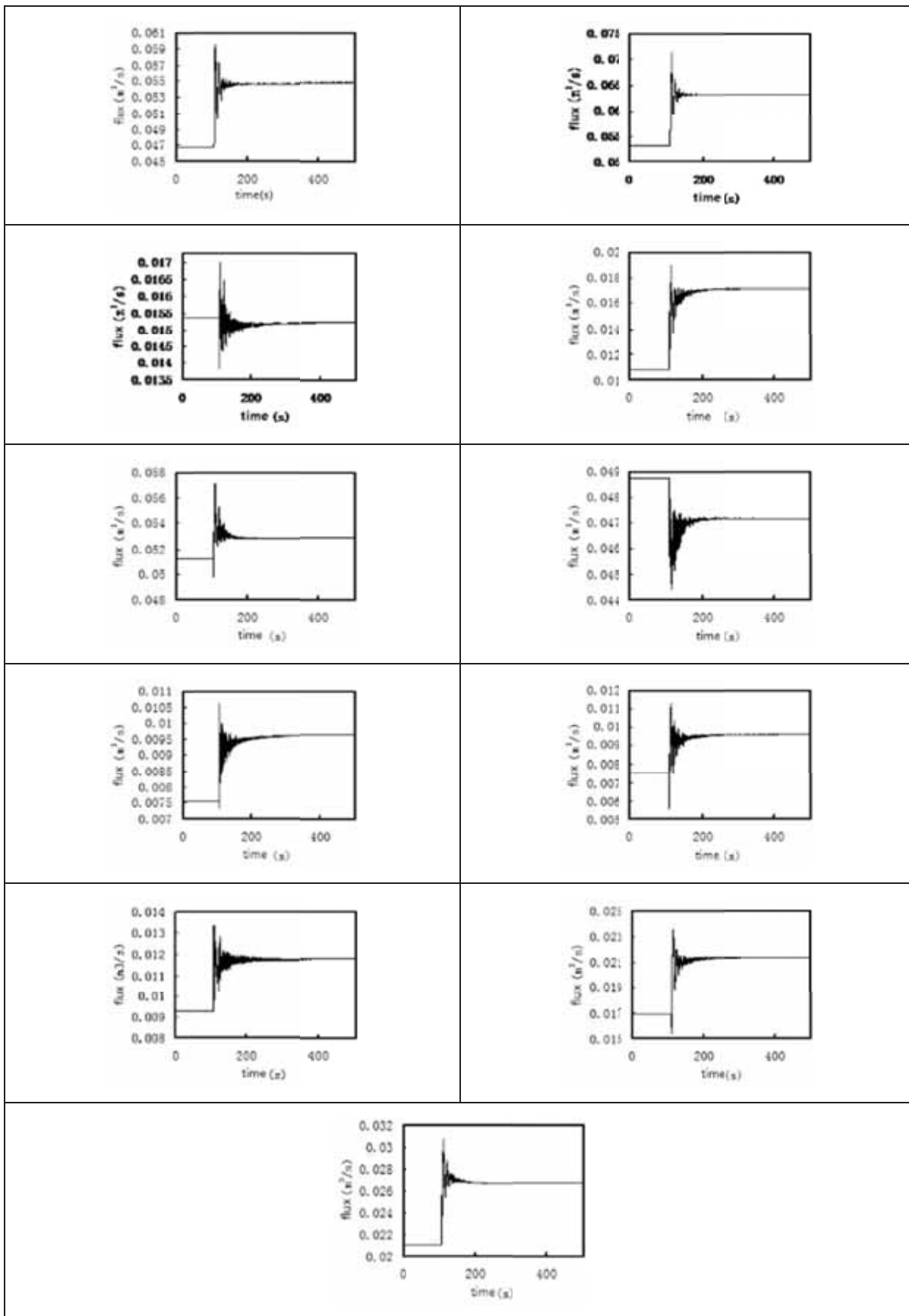


Fig. 2 The downstream discharge variation with time in 11 pipes

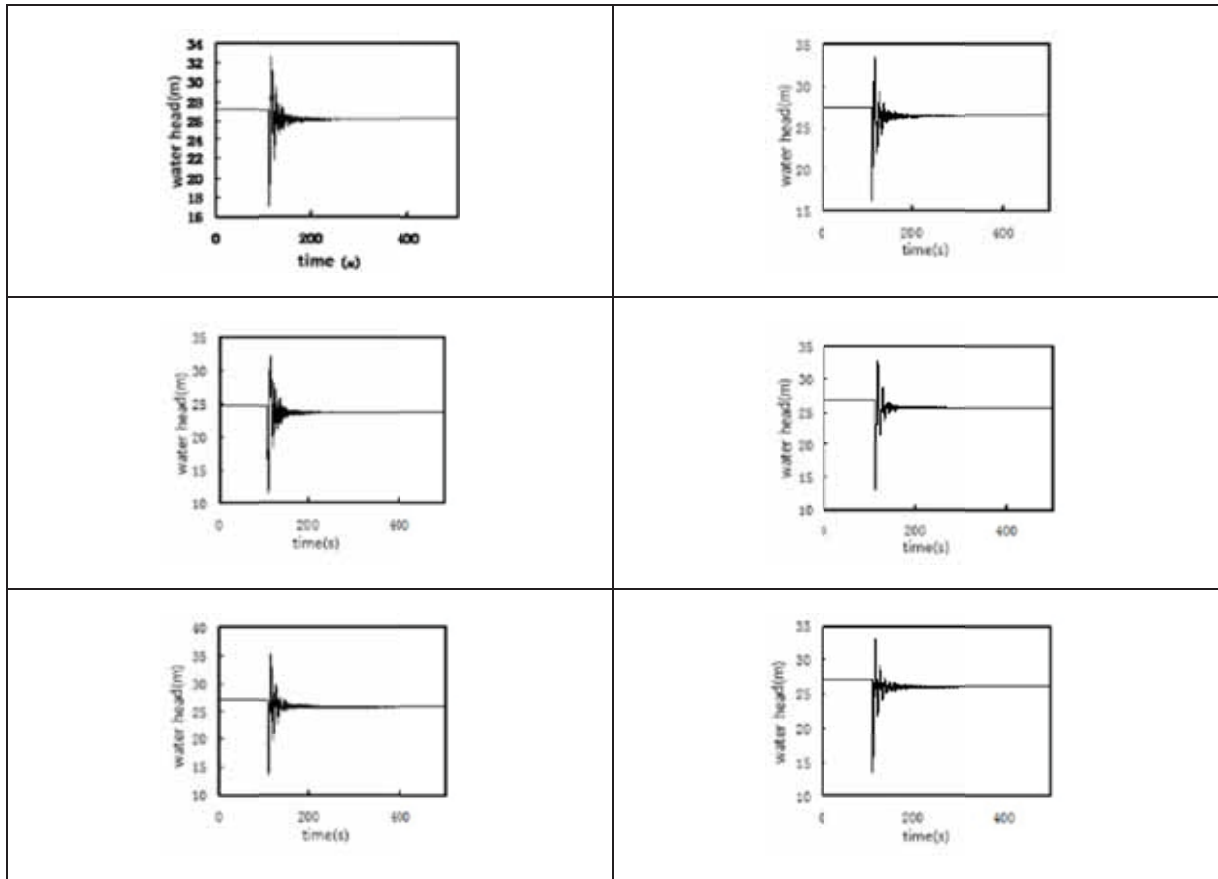


Fig. 3 The node 2-7 head variation with the time respectively

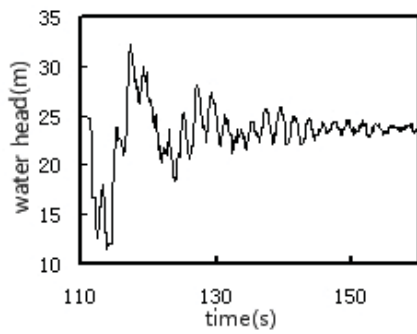


Fig. 4 The partial enlarged drawing of the head variation with time at node 4

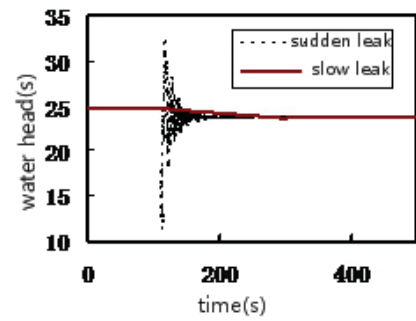


Fig. 5 The head variation with the time at the node 4

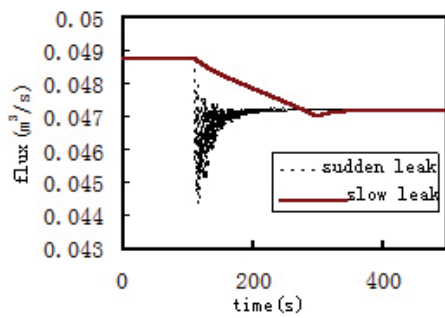


Fig. 6 The downstream discharge variation with time in the pipe 6

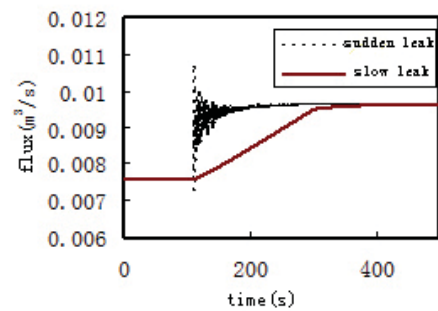


Fig. 7 The downstream discharge variation with time in the pipe 7

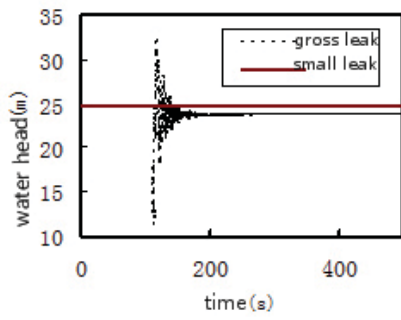


Fig. 8 The head variation with time at node 6 with the diameter 41mm and 15mm respectively

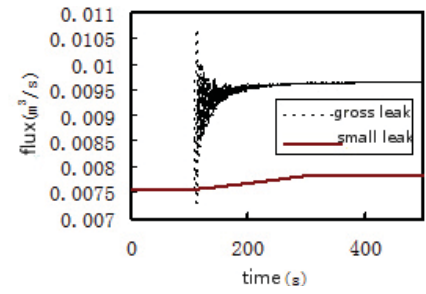
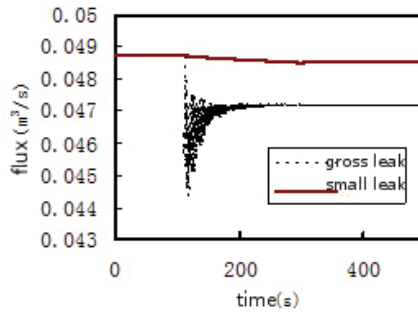


Fig. 9 The flux variation with time under the condition of the leakage diameter 41mm and 15mm respectively

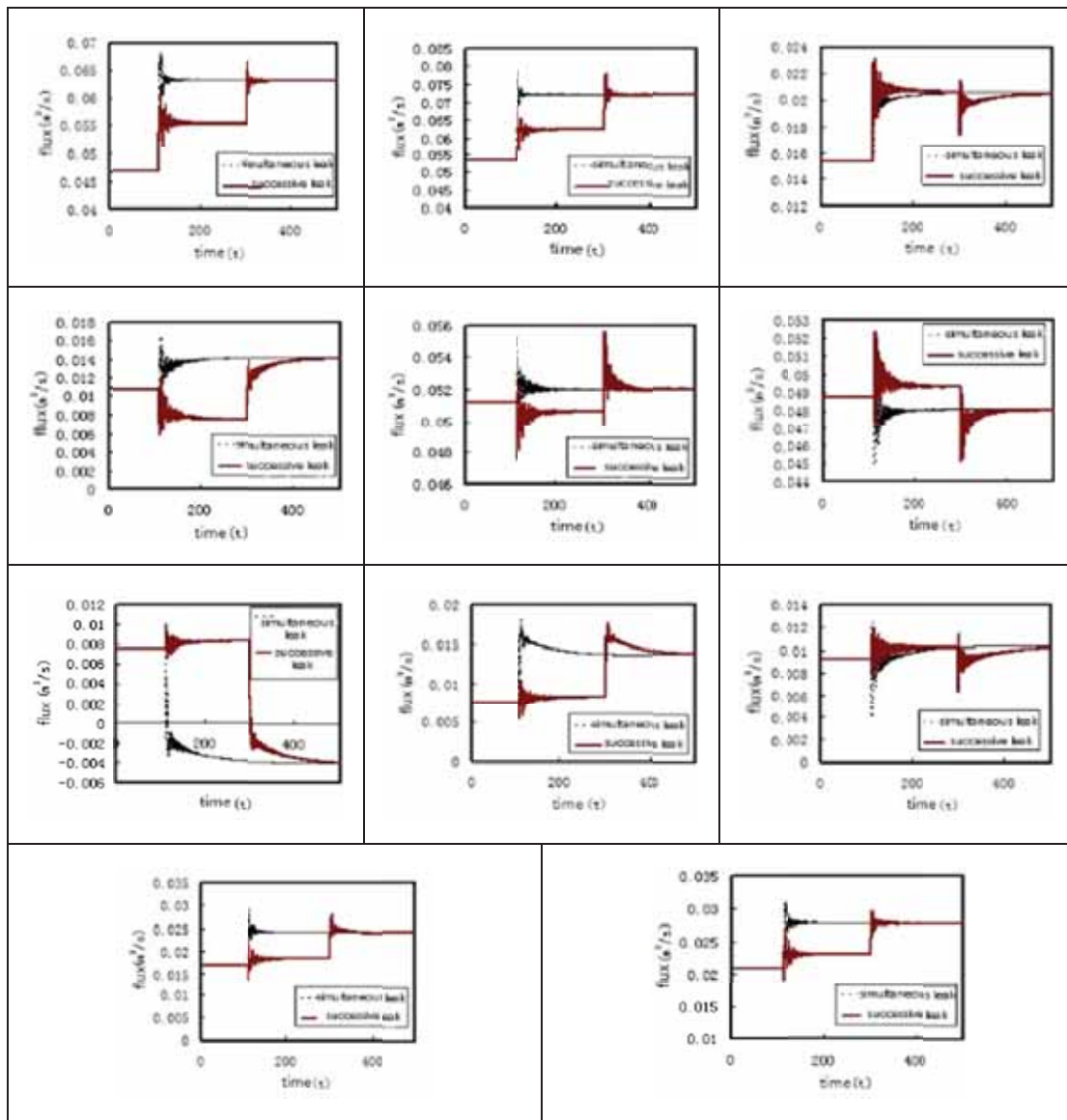


Fig. 10 The variation of downstream flux in the pipes and head at nodes with time under the condition of simultaneous and successive leakage respectively

diameter of leaking orifice increased from 0 gradually to 41mm at the 300th s.

The result also shows that the change law of flux and head in each pipe under the condition of the slow leakage is same as the one of a sudden leakage. However, the fluctuation range in transient flow is various tremendously.

Fig.5 gives the head variation with the time at the node 4 under the condition of sudden and slow leakage respectively. As shown in the figure, the head is slightly fluctuated during the slow leakage. There is no obvious peak and trough. So the slow leakage does not cause tremendous hammer pressure.

Fig.6 and Fig.7 gives the downstream discharge variation with time in the pipe 6 and 7 respectively. It is also shown in the figure that the changing regulation is similar to the one of the head. Namely the flux fluctuation is not obvious when a slow leakage occurs.

### (3) Different diameters of leakage

Suppose that the diameter of leakage is 15mm. The other condition is same as the condition of sudden leakage. Fig.8 shows the head variation with time at node 6 with the diameter 41mm and 15mm respectively. Fig.9 gives the flux variation with time under the condition of the leakage diameter 41mm and 15mm respectively. These figures show clearly that the head, the flux and the intensity of fluctuation under the condition of the small leak are all less than the ones under the condition of the large leak.

## LEAKAGE AT OTHER NODES

All the examples above analyze the flux and the head

Tab 3. The abrupt trend of downstream flux when leakage occurs at different nodes

Leaking position Pipe No.	Node 2	Node 3	Node 5	Node 6	Node 7
1	increase	increase	increase	increase	increase
2	increase	increase	increase	increase	increase
3	increase	decrease	decrease	decrease	decrease
4	decrease	increase	increase	increase	increase
5	decrease	increase	increase	increase	increase
6	increase	decrease	decrease	decrease	decrease
7	increase	decrease	increase	decrease	decrease
8	increase	decrease	increase	increase	decrease
9	increase	decrease	increase	decrease	decrease
10	increase	decrease	increase	increase	increase
11	increase	decrease	increase	increase	increase

Tab.4. The abrupt trend of the head when leakage occurs at different nodes

Leaking position Pipe No.	Node 2	Node 3	Node 5	Node 6	Node 7
2	decrease	decrease	decrease	decrease	decrease
3	decrease	decrease	decrease	decrease	decrease
4	decrease	decrease	decrease	decrease	decrease
5	decrease	decrease	decrease	decrease	decrease
6	decrease	decrease	decrease	decrease	decrease
7	decrease	decrease	decrease	decrease	decrease

variation when a leakage occurs at node 5. How change the flux and the head when the leakage occurs at other nodes? Is it the same as the one when a leakage occurred at node 5? In consideration of this aspect, it is investigated the condition that the leakage occurs at other node except node 5. The time length and the leakage condition are same as those of the sudden leakage at node 5.

Tab.3 and Tab.4 show the changing trend of the downstream flux in all pipes and the head at all nodes before and after the leakage occurs at other nodes. Table 3 points out that the combined changing laws of downstream flux in all pipes under the condition of the leakage at different node are different. Meanwhile, there is no repeatability in the combined changing forms. From Table 4, it is pointed out that no matter which nodes there is leakage, the node head is less than the one in steady flow without leakage.

## MULTI-NODES LEAKAGE

The leakage in the pipe network may be occurred at multiple nodes. Multi-node leakages may occur simultaneously, or occur successively. Thus, it is investigated the condition that the leakage occurs at two nodes simultaneously and occurs successively. The leaked positions are chosen at node 2 and node 6. The leakage condition is same as that of a sudden leakage at node 5. The leakage began at node 2 firstly and then at node 6 after leaking for 190s under the condition of the successive leakage. The total time of leakage still is 578s.

Fig.10 show the variation of downstream flux in the pipes and head at nodes with time under the condition of simultaneous and successive leakage respectively. From the view, the flux goes up and down compared with the steady flow without leakage, while the head declines. In comparison with simultaneous leakages, the changing trend of the head and flux before and after the leakage is the same. Moreover, the flux and head exists the periodical abrupt changes in the process of leakage.

## CONCLUSIONS

The transient flow model is employed for simulating the leakage in pipe network. The whole event including of the steady flow before the leakage, the transient flow during the leakage and the steady flow after the leakage is considered in the model. The numerical results are validated against the theoretical solution under the condition of steady flow. The following conclusions are obtained:

(1) When the leakage occurs in the pipes, the flux and the head change suddenly and fluctuate, in comparison with those before the leakage. The abrupt trend of the flux in each pipe is not same completely. Some is upwards, while others downwards. However, the abrupt trend of the head is always downwards.

(2) The fluctuation strength of the flux and the head under the condition of the leakage is related with the magnitude and speed of the leakage. As it leaks more and faster, the fluctuating

range of the head and the flux is bigger.

(3) When the leakages occur in different position, the combination law of abrupt trend of the flux is different. The abrupt trend of the head is downward no matter where the position of the leakage.

(4) When the leakages occur successively, the abrupt change of the flux and the water head are all stepped.

### ACKNOWLEDGMENTS

This paper was supported by the National Natural Science Foundation of China under Grant No.51209133, the Foundation of Shanghai Maritime University (No.20121051), Program for Innovative Team in Shanghai Maritime University, Shanghai Municipal Education Commission First-class Disciplines Project and Innovation Project of Shanghai Graduate Education (No. 20131129).

### REFERENCES

1. Axworthy,D.(1997) Water distribution network modelling from steady state to waterhammer. Ph.D. thesis, Dept. of Civil Engineering,Univ of Toronto,Toronto.
2. Betamio de.Almeida.A and Koeile.E.(1992).Fluid transients in pipe networks.Computational Mechanics Publications.Southampton.C.K.
3. Cheong,L.C.(1991).Unaccounted for water and economics of leak detection.8th Int.Water Supply Congress and Exhibition.Water Supply:The review journal of the Int. Water Supply.
4. Karney B.W.. and McInnis.D.(1990). Transient analysis of water distribution system. J. Of -4 WW4,82(7).62-70.
5. Ligget J.A. and Chen,L.C.(1994).Inverse transient analysis in pipe network.J Hyd.Eng.120(8),p934-955.
6. Pudar,R.S. And Liggett,J.A.(1991).Leaks in pipe networks.J of Hyd.Eng. 118(7),1992,p 1031-1046.
7. Vitkovsky,J.P. Simpson,A.R.,and Lambert,M.F.(2000). Leak detection and calibration using transients and genetic algorithms,J. Water Resour. Plann. Manage.126(4),p262-265.
8. Wylie E.B. and Streerer V.L.(1993).Fluid transients in systems.Prentice-Hall Englewood Cliffs,N.J.

### CONTACT WITH AUTHOR

JunHua Li  
Lzj912@163.com

YanTing Fan

School of Ocean Science and Engineering,  
Shanghai Maritime University  
Shanghai 200136  
China

## PSEUDO-STATIC EXPERIMENT AND ANALYSIS ON SEISMIC BEHAVIOR OF THE RC COLUMNS STRENGTHENED BY GHPFRCC

Xiuling Li\*,  
Juan Wang\*,  
Min Luo<sup>b</sup>,

a) School of Civil Engineering, Shandong Jianzhu University  
Jinan Shandong, China

b) Sichuan Engineering Technical College  
Deyang Sichuan, China

### ABSTRACT

*Green high performance fiber reinforced cementitious composites (GHPFRCC) are a new class of sustainable cementitious composites, employing a high volume of fly ash to replace cement. In addition to increasing the sustainability of the construction environment, GHPFRCC exhibits a high tensile ductility and multiple cracking behaviors in the strain-hardening state. These materials can effectively improve the structural energy dissipation capacity and structural durability. In this study, the optimum mixture ratio of GHPFRCC is presented established using an orthogonal experiment for a specific engineering application. The described GHPFRCC sustains the mechanical performance of concrete and is employed as the outer cladding to strengthen concrete columns. The finite element analysis of the material was based on the software ABAQUS and pseudo static experiments were conducted to exhibit retrofitting of GHPFRCC applied in the rehabilitation of seismic-damaged concrete columns. The computed and experimental results showed that GHPFRCC, while incorporating high volume fly ash, can retain significant multiple cracking behaviors. The energy dissipation capacity of the GHPFRCC reinforced concrete (RC) column is better than the comparable unreinforced column.*

**Keywords:** Green high performance fiber reinforced cementitious composites (GHPFRCC), pseudo-static test, reinforced concrete (RC) column, strengthen, seismic performance

### INTRODUCTION

Global earthquake disasters have occurred with increasing frequency in recent years, such as Wenchuan earthquake in China, which caused great casualties and property losses [2]. The seismic damage of reinforced concrete frame columns during an earthquake may cause fatal impact to the structure. To avoid the collapse of a frame structure during an earthquake, improving the seismic performance of the frame column is crucial. Methods for effectively strengthening earthquake-damaged reinforced concrete (RC) columns have become an important problem in the civil engineering field [8, 9].

A promising approach for improving the seismic performance of concrete columns is to employ concrete materials utilizing reinforcing materials such as steel fibers [13], carbon fiber reinforced polymers (CFRP) [1, 15], etc. Among these, green high performance fiber reinforced cementitious composites (GHPFRCC) are a new type of environment-friendly of cement-based composites with attractive characteristics for use in civil applications. These new materials exhibit including extremely remarkable pseudo strain hardening behavior,

saturated multiple cracking, ultra-high toughness, and are environmentally sustainable [3, 7]. Therefore, GHPFRCC is becoming a preferable repair material to strengthen the mechanical performance of reinforced concrete structures.

In this study, we intended to test the feasibility of seismic damaged concrete columns strengthened by GHPFRCC using a computer simulation and laboratory experiments, the aim of which is to provide a solution to the problem of retrofitting earthquake-damaged concrete structures. The optimum mixing ratio of the GHPFRCC was designed using an orthogonal experiment method and two columns were strengthened by enwrapping different thickness of this designed GHPFRCC [6]. The finite element models of the two retrofitted columns and the unwrapped column were fabricated built and the P- $\Delta$  curves were calculated. Finally, laboratory experiments on the three specimens were conducted using a low frequency cyclic load. Both the calculations and experiment results indicated that GHPFRCC is effective in increasing the seismic energy dissipation capacity of the RC columns.

## MATERIAL PARAMETERS OF GHPFRCC

The GHPFRCC material is comprised of water, fine sand, polyvinyl alcohol (PVA) fibers, cement, fly ash and a water reducing agent. And the mechanical properties of these materials are as follows [5].

The mesh number of the fine sand (from Qingdao) was 106-180 and the effective particle size was 151  $\mu\text{m}$ , the density was 2660  $\text{kg/m}^3$ , crushed-rate was 0.34, wear rate 0.40, silt content 0.06, solubility in hydrochloric acid 0.24, content of  $\text{SO}_2 \leq 98.96\%$ .

PVA fibers (Kuraray Co. Ltd., Rec15, Japan) were used as the reinforcing fibers in GHPFRCC. The mechanical and geometrical properties were as follows: length 12 mm, diameter 39  $\mu\text{m}$ , tensile strength 1620 MPa, elongation 7%, Young's modulus 42.8 GPa, and density 1.3  $\text{g/mm}^3$ .

Ordinary Portland cement (type P.O. 42.5 R, Shandong Shanshui Cement Group Ltd.) was used and the density was 3100  $\text{kg/m}^3$ ; initial setting time was 170 mins, final setting time was 200mins, the specific surface area was 350  $\text{kg/m}^2$ , the content of  $\text{SO}_3 \leq 2\%$ , content of  $\text{MgO} \leq 4.5\%$ , the compressive and flexural strength of the 28d cure of the concrete was 51 MPa and 9.5 MPa, respectively.

The density of the fly ash (Grade I, Shandong Zoucheng Power Plant) was 2200  $\text{kg/m}^3$ , and the water demand was 91%, material loss on ignition was 2.8%, moisture content  $\leq 2\%$ , the amount retained on a 45  $\mu\text{m}$  sieve was 9%.

The water reducing agent was obtained from the Shandong Huadi Construction Technology Company. It was a polycarboxylate water reducing agent and its solid content was 25%, Alkali content 0.01%, the pH value of the material 7.0.

Tap water was used throughout the study.

In previous studies, the mechanical properties of GHPFRCC such as compressive strength, tensile stress-strain, bending strength-deflection were analyzed with respect to variations in mixing ratios and the optimal value was determined [10], shown as Tab. 1. The mechanics performance results of GHPFRCC with this optimum mixture ratio are shown in Tab. 2.

Tab. 1. Optimum mixture of the GHPFRCC

Water Binder Ratio	Sand Binder Ratio	PVA Fiber/%	Fly Ash/%	Water Reducing Agent /%
0.24	0.46	1.70	60	0.10

Tab. 2. Test results for GHPFRCC with Optimum Mixture Ratio

Compressive Strength	Tensile Strength	Bending Strength	Elasticity Modulus	Poisson's Ratio
42.15 MPa	3.02 MPa	14.5 MPa	$2.91 \times 10^4$ MPa	0.23

## FINITE ELEMENT ANALYSIS BASED ON ABAQUS

Three concrete columns were used to simulate the seismic performance subjected by the low-frequency cyclic load. Among these sample, column A was a pure C30 concrete control column, column B was wrapped with a 25 mm thickness of

GHPFRCC, column C was wrapped with a 35 mm thickness of GHPFRCC and the three columns had the same section size and steel reinforcements. The concrete geometry size and reinforcement diagram are shown in Fig. 1.

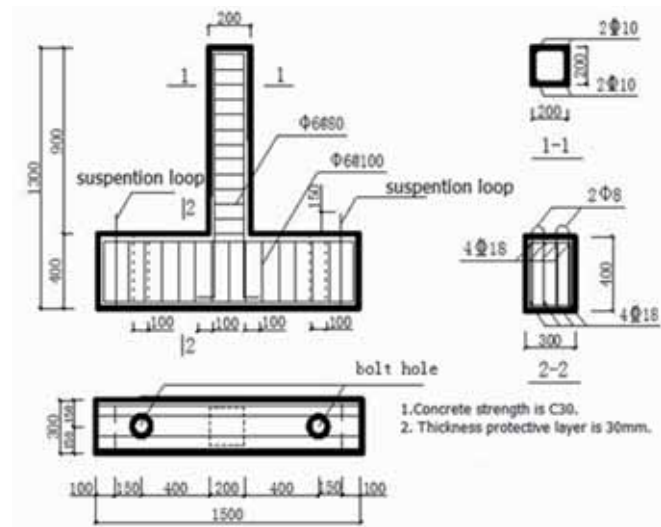


Fig. 1. Reinforced concrete column

The finite element software ABAQUS was used to analyze the seismic behavior of the three columns. Basic assumptions were as follows:

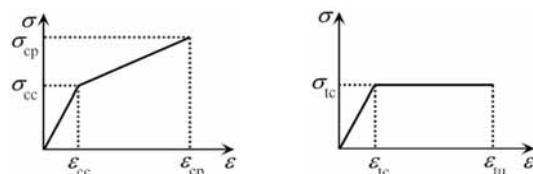
- (1) The bond-slip problems between GHPFRCC and concrete were not considered;
- (2) The bond-slip problem between steel bar and concrete were not considered;
- (3) Rebar was considered as the ideal elastic-plastic material;
- (4) The nonlinear material problems of concrete were considered in the simulation analysis.

### 2.1 Finite element model

ABAQUS provides three concrete constitutive models [14]: concrete smeared cracking, damaged concrete plasticity and concrete cracking model. The damaged concrete plasticity model was selected.

The concrete constitutive relationship was chosen from appendix C of "Code for the design of concrete structures" (GB50010-2010) [12] and the bilinear ideal elastic-plastic model was used for the reinforcements.

GHPFRCC has a tensile strain capacity of up to 6% and exhibits a pseudo-strain hardening behavior accompanied by multiple cracking. The tensile and compressive constitutive relationship of GHPFRCC is shown as Fig. 2(a), (b), respectively [4].



(a) Tensile stress-strain curve (b) Compressive stress-strain curve

Fig. 2. GHPFRCC constitutive relations

The compressive stress  $\sigma_c$  and tensile stress  $\sigma_t$  of GHPFRCC can be calculated using Equation (1) and Equation (2).

$$\sigma_t = \begin{cases} \frac{\varepsilon}{\varepsilon_{tc}} \sigma_{tc} & 0 < \varepsilon < \varepsilon_{tc} \\ \sigma_{tc} & \varepsilon \geq \varepsilon_{tc} \end{cases} \quad (1)$$

$$\sigma_c = \begin{cases} \frac{\varepsilon}{\varepsilon_{cc}} \sigma_{cc} & 0 < \varepsilon \leq \varepsilon_{cc} \\ \sigma_{cc} + \frac{\varepsilon - \varepsilon_{cc}}{\varepsilon_{cp} - \varepsilon_{cc}} (\sigma_{cp} - \sigma_{cc}) & \varepsilon_{cc} < \varepsilon \leq \varepsilon_{cp} \end{cases} \quad (2)$$

The embedded element was used to simulate the bond between rebar and concrete. GHPFRCC has a favorable bond behavior with concrete and steel reinforcements. The tie connection method was adopted between the concrete and GHPFRCC, as well as between the cushion block and column and the column and transverse beam.

The vertical concentrated force at the top of column was exerted by the Ramp curve of ABAQUS and the force was 120 kN (axial compression ratio is 0.15). The horizontal load was imposed through the set load amplitude curves under displacement control. The six degrees of freedom of the transverse beam at the bottom of column were all restrained, i.e.  $U1=U2=U3=UR1=UR2=UR3=0$ .

During the mesh generation, the Hex element was adopted for concrete and the GHPFRCC element shape and C3D8R for the element type. T3D2 element was selected for reinforcement.

### 2.2 Calculated results and analysis

Stress nephograms of the three columns are shown in Fig. 3(a), (b), (c), respectively. The load-displacement skeleton curves obtained from the data processing are shown in Fig. 4(a), (b), (c), respectively.

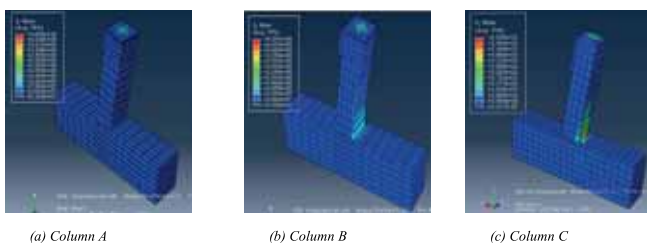


Fig. 3. Stress nephogram of analysis results

The simulation results show that the maximum horizontally bearing capacity of column A was 76 kN, the ultimate displacement was 22 mm; for column B, the maximum bearing capacity was 98.4 kN with a displacement of 53.1mm, and for column C, the maximum bearing capacity was 101.5 kN with a displacement of 63.4mm.

As can be seen, reinforced concrete columns strengthened by GHPFRCC have good ductility and energy-absorbing ability

and the effects improve with the increase of the wrapped thickness of the GHPFRCC.

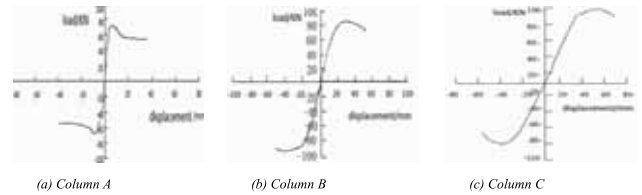


Fig. 4. P-Δ skeleton curves of analysis results

## EXPERIMENTAL WORK

Three reinforced concrete columns were considered and the strengthening schemes are shown in Tab. 3. The reinforcement diagram is shown in Fig. 1. HRB400 and HPB300 are chosen for steel reinforcements and stirrups, respectively. The ready-mixed concrete with grade C30 was adopted.

Tab. 3. Strengthening Schemes

No.	Height (mm)	Section size(mm <sup>2</sup> )	Strengthening methods	Section size after strengthened(mm <sup>2</sup> )
column A	900	200×200	--	200×200
column B	900	150×150	Outsourced 25mm thick GHPFRCC	200×200
column C	900	130×130	Outsourced 35mm thick GHPFRCC	200×200

Strain gauges were adhered to the steel reinforcements prior to concrete pouring. The control column A was cast at the same time and column B and C adopted secondary casting. Initially columns B and C were cast according to the size shown in Tab. 3 and then wrapped with different thickness of GHPFRCC after 28 days' of humid preservation curing. The wrapped thickness of GHPFRCC was 25 mm and 35 mm for column B and C, respectively. In order to obtain good bonding performance between GHPFRCC and the concrete, it was necessary to polish the concrete surface prior to the second pouring of GHPFRCC.

The pseudo-static experiment was conducted with the MTS system. In order to observe the experimental phenomenon more clearly, the concrete column surface was whitewashed with 5 cm × 5 cm grids before the test. To ensure a smooth surface, a layer of mortar was cast on top of the column.

Displacement at top of column was measured using a laser range finder and strain was recorded using the Shanghai Zhubang Cekong system. The hysteresis curve was automatically extracted from the MTS. The loading process controlled by the sample deformation and the initial deformation step was 1 mm with 1mm deformation increments, and the system was cycled twice for each deformation magnitude (see Fig. 5).

When the bearing capacity dropped to 85% of the maximum load and not less than the yield load, the columns would fail and the test would be terminated [3]. The experimental apparatus is shown Fig. 6.



Fig. 5. Loading system



Fig. 6. Test apparatus

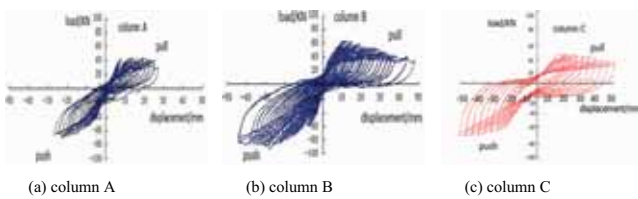


Fig. 7. Hysteresis curves of test results

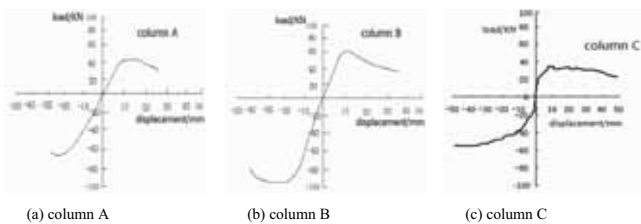


Fig. 8. P-Δ skeleton curves of test results

## RESULTS AND DISCUSSION

Columns A, B, C were tested using a low frequency cyclic loading test and the load-deformation hysteresis curves collected by the MTS are shown in Fig. 7. The P-Δ skeleton curves were obtained by connecting the hysteresis curve peak at each loading level the first cycle (see Fig. 8).

For the control column A, the bearing load increases slightly after cracks appeared at the bottom side of the column. With the increase of the controlled deformation, the concrete at the bottom of column began to be crushed and the maximum crack width reached 5mm. The appearance of two main penetrating

cracks at the bottom of the column leads to the failure of column A. For column B, wrapped with 25mm of GHPFRCC, there are no main penetrating cracks, but many transverse fine cracks and the maximum crack width was less than 0.1 mm. For column C, wrapped with 35mm of GHPFRCC, there are fewer cracks than column B, but the cracks appeared early at the bottom of the column and the GHPFRCC detached from the crossbeam.

In terms of bearing capacity, the maximum load of column A was 69.19 kN, and the maximum value of column B was 92.06 kN, which increased by approximately 31% in comparison to the control column A.

The maximum displacement of column A, B and C was 26mm, 46mm, and 49mm, respectively.

The surrounding area of the hysteresis curve of the columns strengthened by GHPFRCC was larger than the control column and it means that the energy dissipation capability improved. Even at the plastic stage, the GHPFRCC can still absorb large amounts of energy after steel reinforcements yield and this demonstrated good ductility.

As can be seen from Fig. 7 and Fig. 8, the load, unload forces of the three columns are not symmetric (generally the load is greater than the unload), the main reasons are as follows. The construction of the material may be subpar leading to a deviation between the specimen and the base of the test system. It was difficult to adjust the height of MTS actuator to be the same as that of the column, so that the actuator is not completely level, resulting in the deviation between load and unload.

## CONCLUSIONS

(1) There was a significant difference between the simulation and experimental results where the test values were less than the simulation values for both sample displacement and ultimate bearing capacity. There was friction between the tackle and the top of the counterforce frame, which influenced the horizontal load which is the main reason for the aforementioned result.

(2) The hysteresis curve of the column strengthened using GHPFRCC is plump, which means that GHPFRCC can effectively improve the bearing capacity and deformation capacity of column, but work is need to improve the retrofitting construction technology.

(3) Strain at the column surface before and after reinforcement is nearly the same and the deformation between GHPFRCC and concrete is coordinated.

## ACKNOWLEDGEMENT

This work was financially supported by the National Natural Science Foundation of China (Grant Nos. 51278290 and 51108253), the Science and Technology Planning Project of Housing and Urban-Rural Development Ministry (Grant No. 2012-K2-11), Program for Scientific Research Innovation Team in Colleges and Universities of Shandong Province, and Educational Commission of Shandong Province (Grant No. J11LE09), and the Ministry of Education Innovation Team (Grant No. IRT13075).

## REFERENCES

1. Haddad, R. H., AL-Mekhlafy, N., and Ashteyat, A. M., Repair of heat-damaged reinforced concrete slabs using fibrous composite materials, *Construction and Building Materials*, Vol. 25, no. 3, pp. 1213-1221, 2011.
2. Li, H. N., Li, X. L., Experiment and analysis of torsional seismic responses for asymmetric structures with semi-active control by MR dampers, *Smart Materials and Structures*, Vol. 18, no. 7, pp. 1-10, 2009.
3. Li, V. C., Tailoring ECC for Special Attributes: A Review, *International Journal of Concrete Structures and Materials*, Vol. 6, no. 3, pp. 135-144, 2011.
4. Li, X. L., Luo, M., Study on the reinforced concrete column strengthened by GHPFRCC with high volume of fly ash, *Applied Mechanics and Materials*, Vols.99-100, pp. 213-219, 2011.
5. Li, X. L., Luo, M., and Wang, J., Experimental research on the flexural toughness of green high performance fiber reinforced cementitious composites (GHPFRCC), *Materials Research Innovations*, Vol. 18, no. S2, pp. 43-47, 2014.
6. Li, X. L., Luo, M., and Wang, J., Orthogonal design and performance of green high performance fiber reinforced cementitious composites, *Concrete*, no. 12, pp. 8-13, 2013. (in Chinese)
7. Li, X. L., Wang, J., Compressive Strength and Poisson's Ratio of green high performance fiber reinforced cementitious composites, *Concrete*, no. 4, pp. 70-73, 2014. (in Chinese)
8. Liang, X. W., Kang, L., Deng, M. K. , and Dang, Z., Experimental investigation on seismic behavior of columns with fiber-reinforced concrete in potential plastic region, *Journal of Building Structure*, Vol. 35, no. 2, pp. 63-70, 2014. (in Chinese)
9. Lu, Y., Comparative study of seismic behavior of multistory reinforced concrete framed structures, *Journal of Structure Engineering*, Vol. 128, no. 2, pp. 169-178, 2002
10. Luo, M., Experimental study on the columns reinforced by green high performance fiber reinforced cementitious composites, Jinan: Shandong Jianzhu University, 2013. (in Chinese)
11. Ministry of Construction of the People's Republic of China, JGJ 101-96, Specification of testing methods for earthquake resistant building, Beijing: China Architecture Industry Press, 1997.
12. Ministry of Housing and Urban-Rural Development of the People's Republic of China, GB50010-2010, Code for design of concrete structures, Beijing: China Architecture Industry Press, 2011.
13. Wang, J., Li, H., Chen, X., and Jia, Y. M., Experimental Study on the Seismic Performance of RC Frame with the Steel Fiber RPC Permanent Pillar, *Journal of Shenyang Jianzhu University (Natural Science)*, Vol. 30, no. 2, pp. 220-226, 2014.
14. Wang, Y. Z., Fu, C. G., Structural engineering analysis and example explanation of ABAQUS, Beijing: China building industry press, 2010. (in Chinese)
15. Yu, Y. D., Liu, Y., Zhang, K., and Zheng, Z. K., Study on the ultimate compressive stress of rectangular concrete columns with CFRP sheets under secondary eccentric loading, *Journal of Qingdao Technological University*, Vol. 35, no. 1, pp. 13-17, 2014. (in Chinese)

## CONTACT WITH AUTHOR

Xiuling Lia  
dlutiem@163.com

Juan Wang

School of Civil Engineering,  
Shandong Jianzhu University  
Jinan Shandong,  
250101 P. R. China

Tel: 86-0531-86361922, Fax: 86-0531-86361386

Min Luob

Sichuan Engineering Technical College  
Deyang Sichuan  
618000 P. R. China

# NUMERICAL MODELING OF HYDRODYNAMIC AND SEDIMENT SILTATION DUE TO TYPHOON IN ESTUARY CHANNEL REGULATION

Hongbo Zhao<sup>a, b</sup>

Qinghe Zhang<sup>a</sup>

Mingxiao Xie<sup>b</sup>

a) School of Civil Engineering, Tianjin University, Tianjin, China

b) Tianjin Research Institute for Water Transport Engineering

Key Laboratory of Engineering Sediment of Ministry of Transport  
Tianjin, China

## ABSTRACT

*Oujiang Estuary is a complex tidal estuary with many channels and shoals in the East China Sea, which was affected by typhoon frequently. The navigation channel of Wenzhou Port is located in the north branch of Oujiang Estuary, which happened serious sediment siltation in many times due to typhoon impact. The regulation is considered to decrease siltation of the channel and protect shoals as well. According to the site survey data, the mathematic model is established and validated, which simulates the hydrodynamic, sediment transport and channel siltation due to typhoon in Oujiang Estuary. The channel regulation scenario is studied by the model simulation after analysis of the siltation character. It indicates that the high concentration sediment from shoals north of channel is main sediment source caused siltation in the channel, which can be prevented into the channel by the regulation scenario and decrease siltation efficiently.*

**Keywords:** Oujiang Estuary, numerical model, channel regulation, sediment siltation, typhoon

## INTRODUCTION

There are over 3 times typhoon influenced seriously and 1.4 times typhoon landed directly in average annually in east sea areas of Zhejiang Province, China, according to the statistics. During typhoon attacking, storm surge and wave is generated driven by strong wind, which enhances the water turbulence. The sediment on of nearshore area and estuary is suspended and transported by strong wave and storm surge, which may cause serious siltation in harbor and navigation channel. Sudden siltation due to typhoon in Yangtze Estuary navigation channels had affect the operation and development of Shanghai International Shipping Center, which caused the siltation thickness about 0.3 ~ 0.7 m in each typhoon [6]. Oujiang Estuary is a very complex tidal estuary with many channels and shoals in the East China Sea, which was affected by typhoon frequently. The navigation channel of Wenzhou Port is located in the north branch of Oujiang Estuary, which happened serious sediment siltation in many times due to typhoon impact. Therefore, it is important and necessary to study the hydrodynamics and sediment siltation of the channel due to typhoon, which is not only helpful to learn mechanism of siltation but also provide the basis for the channel regulation. Numerical model can be used to simulate the typhoon, wind wave, current and sediment siltation. A set of models will be

established to study the sediment siltation due to typhoon in estuary channel regulation in this paper.

## NATURAL CONDITIONS AND SILTATION

Oujiang is a strong tidal estuary that tides can reach up to 78 km upstream from its mouth, with a river basin of  $1.8 \times 10^4$  km<sup>2</sup>. According to measured data, the average total amount of fresh water discharge is 470 m<sup>3</sup>/s, and the suspend load transport amount is about  $2.051 \times 10^6$  t annually. Oujiang Estuary is divide North branch and South branch by Lingkun island and Niyu island. The average water diversion ratios of the South Branch and the North Branch of the Oujiang River are 21% and 79% during flood, and 26% and 74% during ebb [3]. Oujiang estuary is dominated by semidiurnal tides with average tidal range of over 4 m and the maximum tidal range of over 7 m. Tidal currents in the estuary belong to shallow water semidiurnal tidal currents. The maximum current velocity in the north channel is about 2.0 ~ 3.0 m/s. The sediment concentration is high near the estuary and the shoals where the maximum vertically averaged concentration measured were all over 1.0 kg/m<sup>3</sup>. The sediment concentration impact of typhoon is higher than normal hydrodynamic conditions. The average median

size  $d_{50}$  of suspended load in the Oujiang Estuary is range from  $6 \times 10^{-6}$  m to  $8 \times 10^{-6}$  m.

The navigation channel of Wenzhou Port is located in the north branch of Oujiang estuary (Fig.1), which already caused serious sediment siltation near Sanjiaosha shoals while typhoon affected. According to the measured data in 2005, the siltation thickness is above 0.4 m averagely in the channel near the shoals due to typhoon Haitang. The mean siltation thickness is 1.1 m and 1.2 m influenced by typhoon Matsa and typhoon Talim respectively [7]. The depth change measured in the channel near shoals is shown in Fig. 2.

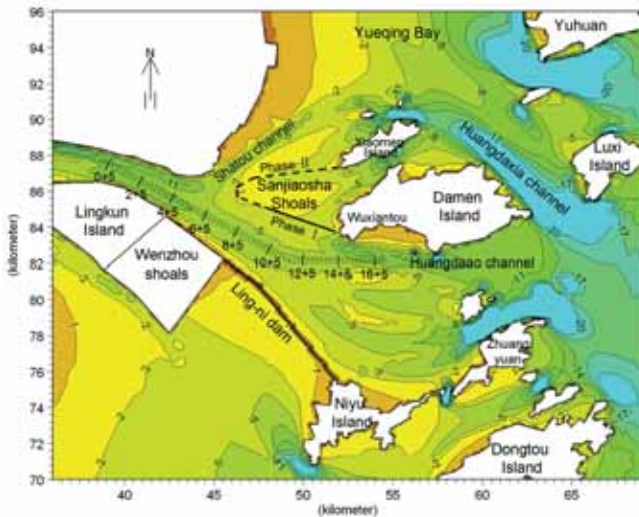


Fig. 1. Sketch of Oujiang Estuary and layout of the channel regulation

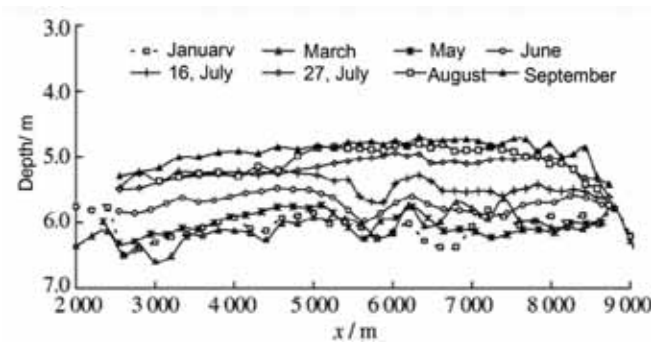


Fig. 2. The depth measured along the channel near Sanjiaosha shoals in 2005

The hydrodynamic and sediment conditions of Oujiang Estuary are very complex, and the typhoon is important hydrodynamic factor of sudden serious siltation in channel. The sediment suspended and transported under storm wave from Sanjiaosha shoals is the main sediment source caused serious siltation in the channel. In order to reduce the channel siltation, the regulation is considered in north of channel shown in Fig. 1, and the channel is deepened to -7 m (refer to theoretical sea level datum, the same below). The regulation dam level is +3.7 m for Scenario 2a and +6.8 m for Scenario 2b.

The numerical models are established to study the effect of reduced siltation due to typhoon in different regulation scenario.

## MODEL DESCRIPTION

Based on characteristic of hydrodynamics and sediment of Oujiang Estuary, the typhoon wind model, hydrodynamic and sediment transport model is considered that will be applied to simulate the storm wave and surge, current, sediment transport and sudden siltation in the channel due to typhoon. The numerical model composition is shown in Fig.3.

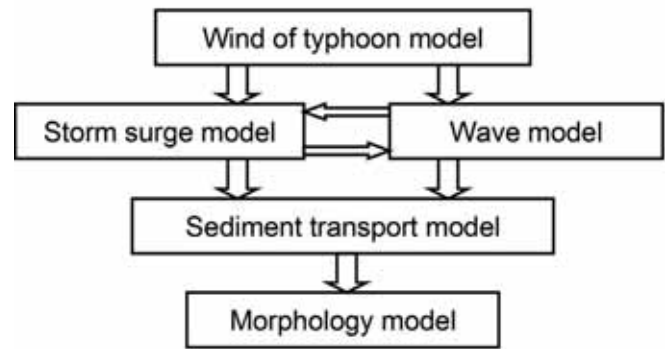


Fig. 3. Composition of the numerical model

## WIND OF TYPHOON MODEL

Parametric wind models are frequently used for the wind forcing recent years. The advantages of parametric models are their convenience of use and the fact that it can reproduce the atmospheric pressure and wind distribution characteristic of tropical cyclone [2]. The models can be used to study the sensitivity of surge to changes of track, central atmospheric pressure, radius of maximum wind velocity, and other parameters.

The model equations of atmospheric pressure field due to typhoon are as follows:

$$P(r) = P_{\infty} - \frac{P_{\infty} - P_0}{\sqrt{1 + 2(r/R)^2}} \quad (0 \leq r \leq 2R) \quad (1)$$

$$P(r) = P_{\infty} - \frac{P_{\infty} - P_0}{1 + r/R} \quad (2R \leq r < \infty) \quad (2)$$

where  $P_{(r)}$  is atmospheric pressure at the calculating point,  $P_0$  is atmospheric pressure at the center of typhoon,  $p_{\infty}$  is the peripheral atmospheric pressure,  $R$  is radius of maximum wind velocity,  $r$  is the distance from the calculating point to the center of typhoon.

The model equations of wind due to typhoon are as follows [5]:

$$W_x = C_1 V_{dx} \exp\left(-\frac{\pi}{4} \cdot \frac{|r-R|}{R}\right) - C_2 \left\{ -\frac{f}{2} + \sqrt{\frac{f^2}{4} + \frac{2\Delta P}{\rho_a R^2} [1 + 2(\frac{r}{R})^2]^{\frac{3}{2}}} \right\} \cdot [(x-x_0) \sin \theta + (y-y_0) \cos \theta] \quad (3)$$

$$W_y = C_1 V_{dy} \exp\left(-\frac{\pi}{4} \cdot \frac{|r-R|}{R}\right) + C_2 \left\{ -\frac{f}{2} + \sqrt{\frac{f^2}{4} + \frac{2\Delta P}{\rho_a R^2} [1 + 2(\frac{r}{R})^2]^{\frac{3}{2}}} \right\} \cdot [(x-x_0) \cos \theta - (y-y_0) \sin \theta] \quad (4)$$

$$(2R \leq r < \infty)$$

$$W_x = C_1 V_{dx} \exp\left(-\frac{\pi}{4} \frac{|r-R|}{R}\right) - C_2 \left\{ -\frac{f}{2} + \sqrt{\frac{f^2}{4} + \frac{\Delta P}{\rho_a R^2} \left[1 + \frac{r}{R}\right]^{-2}} \right\} \cdot [(x-x_0)\sin\theta + (y-y_0)\cos\theta] \quad (5)$$

$$W_y = C_1 V_{dy} \exp\left(-\frac{\pi}{4} \frac{|r-R|}{R}\right) + C_2 \left\{ -\frac{f}{2} + \sqrt{\frac{f^2}{4} + \frac{\Delta P}{\rho_a R^2} \left[1 + \frac{r}{R}\right]^{-2}} \right\} \cdot [(x-x_0)\cos\theta - (y-y_0)\sin\theta] \quad (6)$$

where  $W_x$ ,  $W_y$  is wind velocity in x, y direction at the calculating point,  $C_1$ ,  $C_2$  is empirical constant ( $C_1 = 0.1$ ,  $C_2 = 0.8$ ),  $V_{dx}$ ,  $V_{dy}$  is the movement velocity of typhoon in x, y direction,  $f$  is the Coriolis force parameter,  $x_0$ ,  $y_0$  is the coordinate of the center of typhoon,  $\theta$  is the flow angle ( $\theta = 20^\circ$ ),  $\rho_a$  is atmospheric density,  $\Delta p = p_\infty - p_0$ .

The atmospheric pressure at the center of typhoon ( $p_0$ ) and the radius of maximum wind velocity ( $R$ ) observed by an aerial survey from  $28^\circ\text{N}$  to  $31^\circ\text{N}$  in the northwestern Pacific was extracted to construct the following approximate relationship [4]:

$$R = R_k - 0.4(P_0 - 900) + 0.01(P_0 - 900)^2 \quad (7)$$

in which,  $R_k$  is an experimental constant. The recommended value is 40, and it can be adjusted according to the validated precision of the atmospheric pressure and wind velocity measured.

## WAVE MODEL

It is very important to simulate wave process for describing sediment movement. The SWAN wave model is typically designed for wave simulations in the near-shore region and applied in many coastal engineering recent years. The SWAN model is a third generation spectral model, suitable for the simulation of wind generated waves from the nearshore to the surf-zone. The spectrum that is considered in SWAN is the action density spectrum rather than the energy density spectrum. In the SWAN wave model, the evolution of the wave spectrum and time is described by the spectral action balance equation, which for Cartesian coordinates is:

$$\frac{\partial}{\partial t} N + \frac{\partial}{\partial x} C_x N + \frac{\partial}{\partial y} C_y N + \frac{\partial}{\partial \sigma} C_\sigma N + \frac{\partial}{\partial \theta} C_\theta N = \frac{S}{\sigma} \quad (8)$$

The first term in the left-hand side of this equation represents the local rate of change of action density in time; the second and third terms represent propagation of action in geographical space (with propagation velocities  $C_x$  and  $C_y$  in x and y space). The fourth term represents a shifting of the relative frequency due to variations in depths and currents (with propagation velocity  $C_\sigma$  in  $\sigma$  space). The fifth term represents depth-induced and current-induced refraction and propagation in directional space (with propagation velocity  $C_\theta$  in  $\theta$  space). The term  $S = S(\sigma, \theta)$  at the right hand side of the action balance equation is the source term in terms of energy density, representing the effects of generation, dissipation and nonlinear wave-wave interaction. This term consists of linear and exponential growth

by wind, dissipation due to white capping, bottom friction, depth-induced wave breaking and energy transfer due to quadruplet and triad wave-wave interaction.

## STORM SURGE MODEL

To simulate the storm surge, the Advanced Circulation Model (ADCIRC) is adopted, which can simulate tide and current over an unstructured grid. It can also be used for simulation the storm surge driven by wind and wave in coastal waters; forecasting hurricane storm surge and flooding. It can also take into account of influence of wave radiation stress that is important to current and sediment movement. The governing equation of is described as follows:

$$\frac{\partial \zeta}{\partial t} + \frac{\partial UH}{\partial x} + \frac{\partial VH}{\partial y} = 0 \quad (9)$$

$$\frac{\partial U}{\partial t} + U \frac{\partial U}{\partial x} + V \frac{\partial U}{\partial y} - fV = -\frac{\partial}{\partial x} \left[ \frac{p_\zeta}{\rho_0} + g\zeta - g(\eta + \gamma) \right] + \frac{\tau_{sx}}{\rho_0 H} - \frac{\tau_{bx}}{\rho_0 H} + D_x - B_x \quad (10)$$

$$\frac{\partial V}{\partial t} + U \frac{\partial V}{\partial x} + V \frac{\partial V}{\partial y} - fU = -\frac{\partial}{\partial y} \left[ \frac{p_\zeta}{\rho_0} + g\zeta - g(\eta + \gamma) \right] + \frac{\tau_{sy}}{\rho_0 H} - \frac{\tau_{by}}{\rho_0 H} + D_y - B_y \quad (11)$$

where,  $U$  and  $V$  are depth-averaged velocities in the x, y directions,  $\zeta$  is free surface departure from the geoid,  $p_s$  is total water column thickness,  $f$  is the Coriolis force parameter,  $p_\zeta$  is atmospheric pressure of water surface,  $\rho_0$  is water density,  $\tau_{sx}$  and  $\tau_{sy}$  is the imposed surface stress,  $\tau_{bx}$  and  $\tau_{by}$  is the bottom stress,  $D_x$  and  $D_y$  are momentum dispersions,  $B_x$  and  $B_y$  are vertically integrated baroclinic pressure gradient,  $(\eta + \gamma)$  is Newtonian equilibrium tide potential.

## SEDIMENT TRANSPORT MODEL

Sediment transport is adopted sediment carrying capacity model to simulate, which has been successfully in many sediment transport prediction with good results for both cohesive sediments and non-cohesive sediments in coastal area in China [1]. The suspended sediment transport equation can be written as:

$$\frac{\partial(hS)}{\partial t} + \frac{\partial(huS)}{\partial x} + \frac{\partial(hvS)}{\partial y} + \alpha\omega(S - S_s) = 0 \quad (12)$$

In which,  $h$  is water depth,  $S$  is the depth-averaged sediment concentration,  $S_s$  is the sediment carrying capacity for the combined waves and current,  $u$  and  $v$  are the current velocity along x and y directions, respectively,  $\alpha$  is the deposition probability,  $\omega$  is the settling velocity,  $S_s$  is the sediment carrying capacity, which can be applied to combined wave and current situations. It is expressed as

$$S_* = S_{*C} + S_{*W} \quad (13)$$

In which  $S_c$  and  $S_w$  are the sediment carrying capacities due current and waves, repetitively.

The carrying capacity of pure current can be expressed as follows:

$$S_c = \alpha \frac{\gamma_s V^3}{(\gamma_s - \gamma) c^2 h \omega} \quad (14)$$

In which  $\alpha$  is a dimensionless coefficient to be determined by experimental or in-situ data,  $V$  is the current velocity.

The carrying capacity of waves can be expressed as following:

$$S_w = \beta_1 \frac{\gamma_s}{\gamma_s - \gamma} \frac{f_w H_{rms}^3}{T^3 g^2 h \omega \sinh^3(kh)} + \beta_2 \frac{\gamma_s}{\gamma_s - \gamma} \frac{D_{B2}}{gh\omega} \quad (15)$$

where  $f_w$  is the friction factor,  $H_{rms}$  is the root-mean-square wave height,  $T$  is the wave period,  $k$  is the wave number,  $D_{B2}$  is wave energy dissipation,  $\beta_1$  is dimensionless coefficient,  $\beta_2$  is dimensionless coefficient in breaking wave condition.

## MORPHOLOGY MODEL

The seabed change caused by suspended sediment equation can be expressed as follows:

$$\gamma_0 \frac{\partial \eta_s}{\partial t} = \alpha \omega (S - S_*) \quad (16)$$

where  $\eta_s$  is the seabed elevation induced by suspended sediment,  $\gamma_0$  is the dry density of suspended sediment,  $\alpha$  is the deposition probability, which can be adjusted according to the data measured.

The seabed change caused by bed load sediment equation can be expressed as follows:

$$\gamma_b \frac{\partial \eta_b}{\partial t} + \frac{\partial q_x}{\partial x} + \frac{\partial q_y}{\partial y} = 0 \quad (17)$$

where  $\eta_b$  is the seabed elevation induced by bed load sediment,  $\gamma_b$  is the dry density of bed load sediment,  $q_x$  and  $q_y$  is the components of  $q_b$  in x and y directions.  $q_b$  is the bed load transport quantity that can be calculated by the following formula.

$$q_b = \frac{k_2}{C_0^2} \frac{\gamma_s}{\gamma_s - \gamma} m \frac{|\vec{V} + \vec{V}_w|^{3/2}}{\omega_b} \quad (18)$$

The total erosion and deposition thickness is  $\eta_s + \eta_b$ .

There are a few important parameters in the model as follows. Manning roughness coefficient  $\eta$  is 0.01; the dry density of suspended sediment  $\gamma_0$  is 720 kg/m<sup>3</sup>; the settling velocity  $\omega$  is 0.0004 m/s; the sediment carrying capacity,  $\beta_c$ ,  $\beta_1$  and  $\beta_2$  is 0.0069, 0.3, and  $5 \times 10^{-7}$  respectively.

In the process of numerical model above, the wind field is calculated by the Typhoon wind model, and the storm surge and wave field are computed by the ADCIRC and SWAN respectively according to typhoon wind field. The two models take into account of interaction of currents and waves through coupling calculations. The ADCIRC computes the water levels and current velocity field for SWAN, and SWAN feedbacks the radiation stress to ADCIRC. The all factors from results of ADCIRC and SWAN provides to the Sediment transport model for simulation of sediment field. At last, the change of seabed is obtained by the Morphology model.

## MODEL VALIDATION

### COMPUTATION DOMAIN AND MODEL GRID

Typhoon is large scale simulation, but sediment is regional area. The numerical model will adopt the nest method to simulate the hydrodynamic and sediment accurately. The typhoon wind model and wave model adopts the square grid and space step is 5 km, which contains part of South China Sea, Eastern China sea, Yellow sea and Bohai Sea. In the Oujiang Estuary sea areas, the nested grid space step is 100 m. The storm surge model and sediment transport model is established used finite element that the maximum space step is 1500 m and the minimum is 30 m (Fig. 4). The west boundary reaches Meiao, and the east boundary reaches -30 m contour. The north boundary reaches the Yueqing Bay, and the south boundary reaches north of Aojiang Estuary.

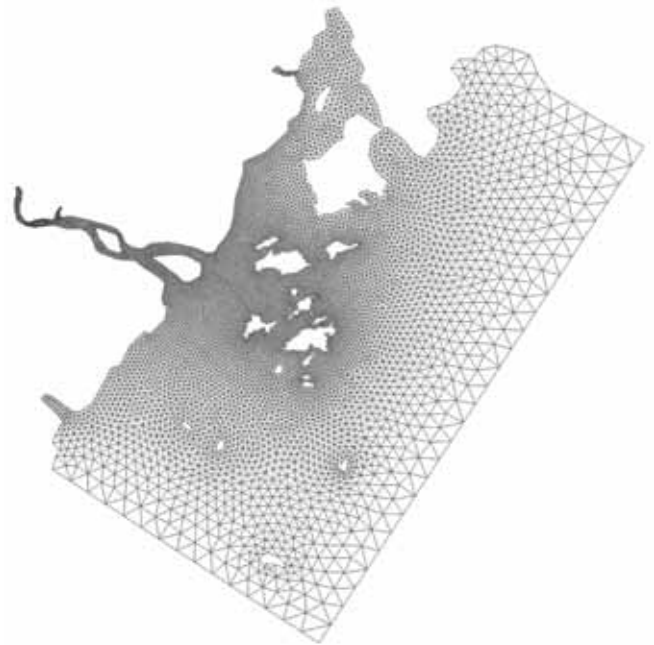


Fig. 4. Grid of regional model

### MODEL VERIFICATION

The typhoon No. 0505 (Haitang) landed at Lianjiang on July 19, 2005, and weakened to a tropical storm as it moved in Nanping, Fujian province. The lowest pressure center is 975 hpa and the maximum wind speed is 32 m/s. The typhoon path of No.0505 is shown in Tab.1. The discharge of Oujiang River is 4950 m<sup>3</sup>/s measured in the period of typhoon. The siltation thickness is above 0.4 m averagely in the channel near the Sanjiaosha shoals due to the typhoon.

According to the data of typhoon No.0505, center pressure, the typhoon wind and wave is simulated (Fig.6). The storm surge is simulated using the data of typhoon wind and wave, which tide open boundary is provided by China Tide Model. The sediment transport and siltation is simulated with the hydrodynamic results above. The validation results of wind

speed, wave height, storm surge and siltation thickness in the channel of Oujiang Estuary due to No. 0505 typhoon are shown in Fig.7 ~ Fig.9.

Tab. 1. The track of typhoon No.0505

Time (UTC)	Latitude (°)	Longitude (°)	Pressure (hPa)
2005 7 17 0:00	21.5	125.8	920
2005 7 17 6:00	22.3	125.0	930
2005 7 17 12:00	23.1	124.0	935
2005 7 17 18:00	23.7	123.1	940
2005 7 18 0:00	23.8	121.8	950
2005 7 18 6:00	24.0	121.5	960
2005 7 18 12:00	24.5	121.2	970
2005 7 18 18:00	24.8	120.6	975
2005 7 19 0:00	25.0	120.4	980
2005 7 19 6:00	25.6	120.1	980

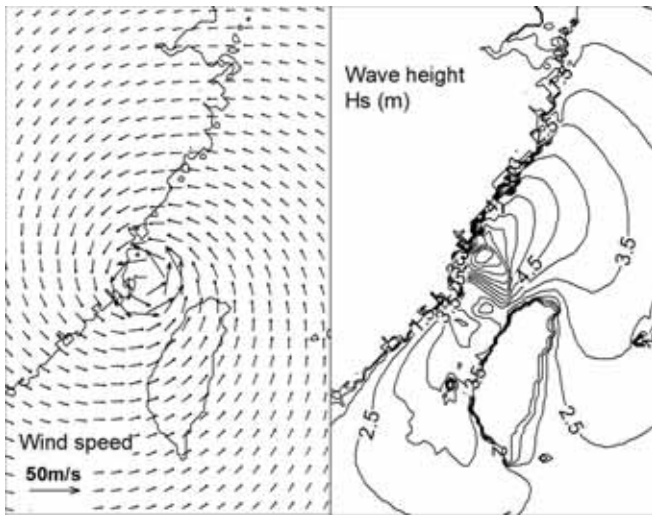


Fig. 6. Wind and wave field of No. 0505 typhoon landing

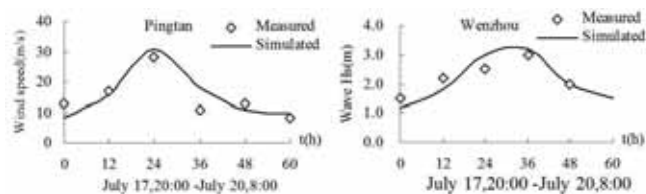


Fig. 7. Validation of wind and wave of No. 0505 typhoon

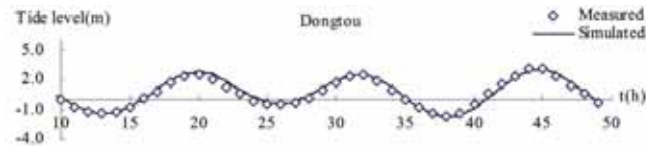


Fig. 8. Validation of storm surge of No. 0505 typhoon

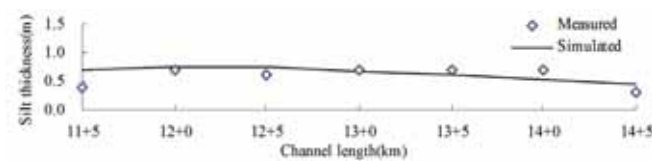


Fig. 8. Validation of storm surge of No. 0505 typhoon

The validation results indicate that the wind speed, storm surge and siltation are in good agreement with the data measured. Moreover, the numerical model also validates the wind speed, storm surge of typhoon No. 9417, No. 9608, and No. 0216. The numerical models can be used to simulate and study on the regulation of channel further.

## ANALYSIS OF MODEL RESULTS

The model simulation result show that the sediment concentration is high that is above  $5\text{kg/m}^3$  in the Oujiang estuary within the typhoon No. 0505 landing. The sediment concentration of Wenzhou navigation channel is affected by the sediment transported from Sanjiaosha shoals that is little influence to the north area. Thus, the regulation to reduce the sediment from Sanjiaosha shoals into the channel should be considered.

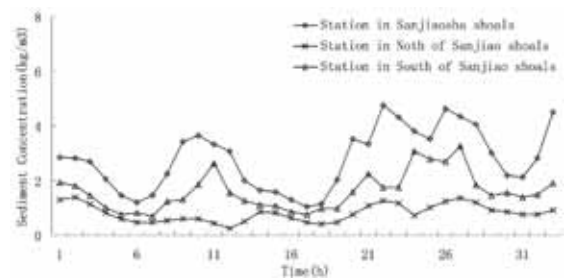


Fig. 10. The sediment concentration in different stations near the Sanjiao shoals due to typhoon No. 0505

The regulation scenarios including dam level of +3.7 m and +6.8 m is simulated respectively using the numerical model above. According to the results of storm current, sediment concentration and the siltation, the sediment concentration in the Sanjiaosha shoals area is  $3 \sim 5\text{kg/m}^3$  and the high concentration sediment is transported into the channel by ebb tidal current. In the regulation scenarios, the high concentration sediment from Sanjiaosha shoals north of channel is prevented into the channel by the regulation dam, which reduces the siltation in channel near the shoals. Figure 11 indicates the current field in flood tide and ebb tide of Scenario 2b.

The effect of reduced siltation with regulation is different in the two scenarios, and the siltation volume is decreased with the increase of regulation dam height. Comparing with the channel siltation due to typhoon No. 0505 before regulation, the siltation thickness from 5+5 km to 15+5 km along the channel near Sanjiaosha shoals of the Scenario 2a (the dam top level +3.7 m) is reduced 26%, and that of Scenario 2b (the dam top level +6.8 m) is reduced 47%. The siltation thickness along the channel in different Scenario is shown in Figure 12.

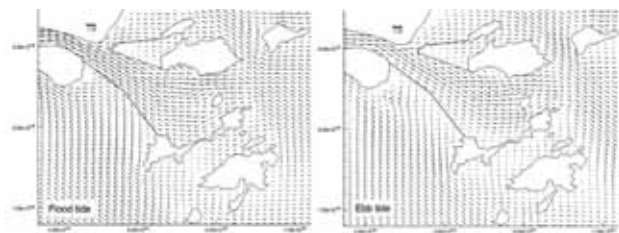


Fig. 11. The flood and ebb tidal current field due to typhoon No.0505 in Scenario 2b

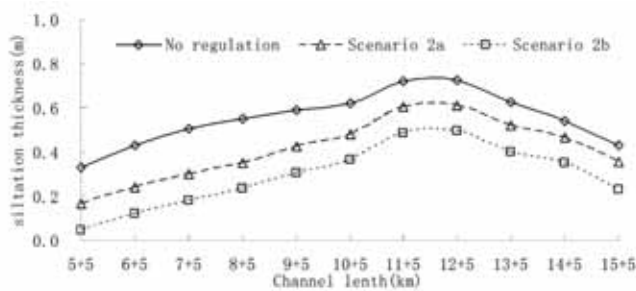


Fig. 12. The siltation thickness due to typhoon No.0505 along channel in different scenarios

## CONCLUSIONS

Based on lots of measured data, the numerical models including typhoon wind model, wave model, storm model and sediment model are established and validated. The simulated results are in good agreement with the data measured. It shows that the high concentration sediment from Sanjiaosha shoals north of channel is main sediment source caused siltation in the channel. The regulation scenarios have good effect to decrease the channel siltation due to typhoon.

## ACKNOWLEDGEMENTS

This study is subsidized by National High Technology Research and Development Program 863 of China (2012AA112509) and Central Public Welfare Research Institutes for Basic Research Funds (TKS130106).

## REFERENCES

1. Dou G. R., Dong F. W., Dou X. B., Sediment transport capacity of tidal currents and waves Chinese Bulletin of Science, Vol. 40, no.13, pp. 1096–1101, 1995.
2. Fujita T., Pressure distribution in typhoon. Geophy Mag, Vol. 23, pp. 437-452, 1952.
3. LI M. G., The effect of reclamation in areas between islands in a complex tidal estuary on the hydrodynamic sediment environment. Journal of Hydrodynamics, Vol. 22, no.3, pp. 338-350, 2010.
4. NOAA, Meteorological criteria for standard project hurricane and probable maximum hurricane wind fields, Gulf and East Coasts of the United States, National Oceanic and Atmospheric Administration, 1979.
5. Ueno T., Non-Linear numerical studies on tides and surges in the central part of Seto Inland Sea. Oceanographical Mag, Vol. 16, no.2, pp. 53-124, 1964.
6. ZHAO D. Z., LIU J, WU H. L., Preliminary analysis of typhoon-induced sudden sedimentation in navigation channel in Yangtze Estuary over last decade. Journal of Sediment Research, Vol. 4, no.2, pp. 54-60, 2012.

7. ZUO L. Q., Further study on back silting and regulation of mouth bar in Oujiang estuary. Hydro-science and engineering, Vol. 3, pp. 6-13, 2012.

## CONTACT WITH AUTHOR

Hongbo Zhao  
thskzhaohongbo@163.com

Qinghe Zhang

School of Civil Engineering, Tianjin University  
300072 Tianjin  
China

Hongbo Zhao

Mingxiao Xie

Tianjin Research Institute  
for Water Transport Engineering,  
Key Laboratory of Engineering Sediment  
of Ministry of Transport,  
300456 Tianjin  
China

# NUMERICAL RESEARCH OF THE VISCOUS EFFECT OF THE BILGE KEEL ON THE DAMPING MOMENT

Rui Deng,

Wenyang Duan,

Shan Ma,

Yong Ma,

Shipbuilding Engineering College of Harbin Engineering University

Harbin, China

## ABSTRACT

*Bilge keels are effective passive devices in mitigating the rolling motion, and the usage of them covers almost all the sea going vessels. This paper focuses on the viscous effect of the bilge keel, ignored the effect of the free surface and the effect of the ship hull, for the general viscous characteristic of the bilge keel. In order to investigate the viscous effect of the bilge keel on the total damping moment, a special 2 dimensional numerical model, which includes a submerged cylinder with and without bilge keels, is designed for the simulation of forced rolling. Three important factors such as bilge keels width, rolling periods, as well as maximal rolling angles are taken into account, and the viscous flow field around the cylinder is simulated by some codes based on the viscous method in different conditions, in which the three factors are coupled. Verification and validation based on the ITTC method are performed for the cylinder without bilge keels in the conditions of different rolling periods and maximal rolling angles. The primary calculation of damping moment induced by the cylinder with 0mm, 4mm, and 10mm width bilge keels shows some interesting results, and a systematic analysis is conducted. The analysis of the damping moment components suggests there is phase difference between the damping moment induced by the cylinder and the bilge keels, and when the bilge keels width reaches a special size, the total damping moment is mitigated. The calculation of the damping moments induced by the cylinder with some larger bilge keels are also performed, and the results suggest that, the damping moment induced by the bilge keels is increased rapidly and becomes the dominant part in the total damping moment while the width of the bilge keels are increased, but the damping moment induced by the cylinder is not changed significantly. Some illustration of the vortices formation and shedding is included, which is the mechanism of the damping moment caused by the bilge keels. The present work shows an interesting problem, and it is useful for the bilge keel design.*

**Keywords:** calculation model, viscous code, phase difference, damping moment, bilge keel

## INTRODUCTION

Ships are susceptible to rolling motion especially subjected to beam sea, and the performance of seagoing surface vessels is affected by limiting the effectiveness of the crew, damaging cargo, and limiting the operation of on-board equipment. The rolling motion can be considered as linear motion while the maximal rolling angle is not large, and the problem can be analyzed by related theories. But, another motion defined as nonlinear motion which can not be investigated by the theories when the maximal rolling angle is quite large, is much more important and attracts the researchers since the damage it caused. Prediction of the nonlinear rolling motion is one of the most difficult things since it deals with a motion similar to a spring-mass damper system, poorly damped by ship generated waves, in addition to the action of waves from the seas. Compared with the other motions of the vessels, viscous effect contributes obviously in nonlinear rolling motion, and

the motion can not be calculated accurately by the traditional potential theory. Because of the complexity of the viscous flow, nonlinear rolling motion is researched mainly by model test and empirical formula for a long time. Parametric excitation for rolling motion is used in 1861 by Froude [6], and it is still under using by the researchers. Later, in 1977, Ikeda et al. [8] developed an empirical method to predict the roll damping according to a series of model experiments. Both these potential theories appeared weakly in the application until 1998, Yeung et al. [34] proposed a composite roll moment equation to address separately the wave damping and the viscous damping related to flow separations, and the viscous effect captured the attention of the researchers. In 2001, Chakrabarti [1] further decomposed the roll damping coefficient for a ship hull form to the skin friction of the hull, eddy shedding from the hull, free surface waves, lift effect damping, and bilge keel damping.

Meanwhile, some results of roll predictions in time domain based on potential flow [14][19] showed partially dependent on empirical roll damping data which was limited to the pertinence relation of frequency and ship form. In addition to the numerical calculation results, Kwang et al. [13] in 2004 measured the velocity field in the vicinity of the structure by particle image velocimetry (PIV), and elucidated that the viscous damping (also called the eddy making damping) in a vortical flow affected the rolling motion of a blunt body. For this reason, numerical methods are in urgent [33] need for simulations of viscous flow and larger amplitude motions of surface ships. An unsteady Reynolds-averaged Navier-Stokes method which is based on an extension of CFDShip-IOWA (a general-purpose code for computational ship hydrodynamics) was developed by Robert V. Wilson(2006) [21] to predict ship motions with larger amplitude and non-slender geometry, in comparison to traditional linearized methods. Since then, a new way to investigate the nonlinear rolling motion is implemented, in which viscous method takes an important part. LUO Min-li(2011) [15] simulated the single-degree-of-freedom forced motion of a ship section and computes added mass and damping coefficient of sway, heave, rolling and sway to roll mode Based on CFD RANS method. Pablo M. Carrica [18] simulated the fully appended ONR Tumblehome model DTMB 5613 with the ship hydrodynamics code CFDShip-Iowa v4.5 and validated against experiments of an auto-piloted, self propelled model ship. DTMB5512 model's roll damping motions at different initial roll angles were simulated based on CFD by YANG Bo [32], and vessel's roll damping coefficients are calculated through the simulation results. A RANS based CFD solver with VOF modeling of free surface was employed to investigate the forced rolling motion of an intact ship, sloshing of water in tank and forced rolling motion of a damage ship by Qiuxin Gao [20] in 2012. YANG Chun-lei [33] simulated free decay and forced rolling at various forward speeds and amplitudes for a 3-D ship hull and predicted ship roll damping, in which a RANS solver was employed and a dynamic mesh technique was adopted and discussed in detail. The latest contribution of the researchers shows that viscous effect is an important part in the prediction of the nonlinear rolling motion, and the numerical model which takes the viscous flow into account is fit for describing the motion.

Bilge keels, which are longitudinal appendages, are effective passive devices in mitigating the motion [24-27], and the application is extended to many types of vessels. H.H. Chun [7] (2001) investigated the roll damping characteristics of three models of a 3-ton class fishing vessel representing the bare hull and hull with bilge keels by the free roll decay tests in calm water and also in uniform head waves in a towing tank, suggested that the bilge keel contribute significantly to the increment of the roll damping for zero speed even for small fishing vessels. Latter, different methods were adopted to discover the damping mechanism. Multiple time scales was applied by M. Eissa [15] (2003) to construct a second-order uniform expansion of the non-linear rolling response of a ship in regular beam seas, and found that the damping moment consisted of the linear term associated with radiation and viscous damping and a cubic term due to frictional resistance

and eddies behind bilge keels and hard bilge corners. Kinnas et al. [11][12] used a finite volume based Navier–Stokes solver to study vertical flows around bilge keels, and pointed out that the primary damping mechanism arising from a bilge keel was the formation and shedding of vortices. Discrete vortex method was also an important method developed by Vaidhyanathan [29] and Yeung et al. [35]. And based on desingularized blob vortices, which is applicable to free surface flows in the roll damping calculation of vessels with bilge keels and showed similar results. Then, some researchers investigated the effect [4][17] of the bilge keels and the hydrodynamic force [2][5] of the vessels with bilge keels, including the hydrodynamic flow [3]. Generally, the design of bilge keel width for conventional vessels is a balance between appendage resistance and roll reduction, and the effect of the bilge keels width is rare discussed, except for some special conditions [22]. Only Krish P. Thiagarajan [28] performed an experimental study involving a range of bilge keel widths from 0% to 20% of half beam of a FPSO with rectangular geometry in 2010. Both free decay and forced oscillation tests were conducted on the range of geometries at different amplitudes and frequencies. The results were analyzed by potential method and the analysis shows that, for given amplitude of rolling motion, the damping coefficient increases with increasing bilge keel size up to a certain point and then declines. The influence of the surface wave induced by the geometry was included in the damping moment measured in the experiment, and the effect of the viscous flow was ignored by the potential method which was used to analyse the result, so it is necessary to take these two problems into account in order to present a clear relationship between the bilge keel width and the viscous damping moment. But an important question presented by Krish P. Thiagarajan is whether there is a point of diminishing marginal returns for damping due to a larger bilge keel. In this paper, examines of the effect of bilge keel size through numerical simulation are conducted involving a range of bilge keel widths from 0% to 10% of half beam of a cylinder, and the cylinder is submerged in the water. The calculation is performed based on the viscous theory, no surface wave is induced by the rolling motion, and the damping moments are analysed directly without any potential method. The results show that there is minimal damping moment for the geometry with bilge keels while the bilge keel gets a special width, and the total damping moment is increased while the bilge keel size is increased and larger than the special one.

## MATHEMATICAL MODEL

In order to avoid the influence of the surface wave induced by the motion of the geometry, a cylinder submerged in the water deep from the surface is used, and the model can be simplified as 2-D if the effect of the tip is ignored. In this way, the free surface is not necessary to simulate, also no need to take the buoyancy and gravity into account. The diameter of the two dimensional cylinder is defined as  $d$ , and the width of the bilge keel is defined as  $b$ . In the present paper, 1.0 m, the angle between bilge keels equals to  $\theta$  degrees, and  $\theta$  is variable in the different conditions. In the condition that cylinder without bilges, equals to 0, and the numerical model is shown in Fig.1.

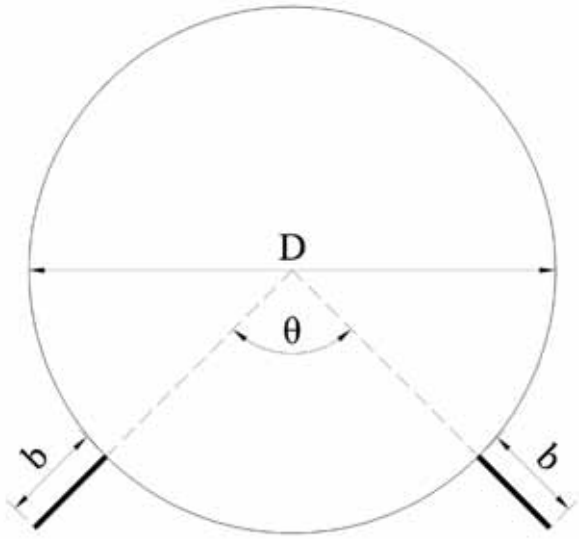


Fig. 1. Cylinder and the bilge keels

The rolling axis is the centre of the cylinder, and the function of the forced rolling motion is:

$$\varphi = \alpha \cos(\omega t + \alpha_0) \quad (1)$$

where  $\varphi$  is rolling angle,  $\alpha$  is the maximal rolling angle,  $\omega$  is rolling frequency,  $t$  is time, and  $\alpha_0$  is phase angle. The cylinder is defined at the equilibrium position which means  $\varphi = 0$  when  $t = 0$ , so  $\alpha_0$  is  $\pi/2$  in equation (1). The relationship between rolling frequency  $\omega$  and rolling period  $T$  is:

$$T = \frac{2\pi}{\omega} \quad (2)$$

Taken as incompressible viscous fluid, the flow field should satisfy the equations of continuity:

$$\frac{\partial u_i}{\partial x_i} = 0 \quad (i = 1, 2) \quad (3)$$

The unsteady incompressible RANS are:

$$\frac{\partial u_i}{\partial t} + \frac{\partial}{\partial x_j} (u_i u_j) = -\frac{\partial P}{\partial x_i} + \frac{\partial}{\partial x_j} \left( \mu \frac{\partial u_i}{\partial x_j} - \overline{u_i u_j} \right) \quad (4)$$

$(i, j = 1, 2)$

The turbulence model in the present simulations is the classical 2-equation eddy viscosity model,  $k-\omega$  Shear Stress Transport (SST) model, and the equations of which are presented as follows:

$$\frac{\partial k}{\partial t} + u_j \frac{\partial k}{\partial x_j} = \frac{\partial}{\partial x_j} \left[ \left( \nu + \frac{\nu_t}{\sigma_k} \right) \frac{\partial k}{\partial x_j} \right] + \nu_t \left[ \left( \frac{\partial \overline{u_i}}{\partial x_j} + \frac{\partial \overline{u_j}}{\partial x_i} \right) \frac{\partial \overline{u_i}}{\partial x_j} \right] - \beta^* f_{\beta} k \omega \quad (5)$$

$(i, j = 1, 2)$

$$\frac{\partial \omega}{\partial t} + u_j \frac{\partial \omega}{\partial x_j} = \frac{\partial}{\partial x_j} \left[ \left( \nu + \frac{\nu_t}{\sigma_\omega} \right) \frac{\partial \omega}{\partial x_j} \right] + \alpha \left[ \left( \frac{\partial \overline{u_i}}{\partial x_j} + \frac{\partial \overline{u_j}}{\partial x_i} \right) \frac{\partial \overline{u_i}}{\partial x_j} \right] - \beta \omega^2 + D_\omega \quad (6)$$

$(i, j = 1, 2)$

The calculation method of the parameters can be found in the related theories.

The equations are coupled through the Pressure Implicit Split Operator (PISO) algorithm. For spatial discretization, a second order up-wind difference scheme and a central difference scheme are applied. The damping force is obtained by the integration of the pressure on the cylinder and bilge keels. The damping moment of the cylinder is defined as the damping force times  $D/2$ , and the damping moment of the bilge keels is defined as an integral of the damping force along the bilge keels.

## VERIFICATION AND VALIDATION

For the simulation of the forced rolling motion of the 2-D cylinder under water with bilge keels, it is quite hard to perform experiment, but some mathematical methods can be used to verify and validate the calculation. The verification and validation (V&V) procedures, which is introduced and demonstrated by Wilson and Stern [23][30-31], and suggested by the ITTC [9][10] can be used to estimate the numerical and modelling errors along with uncertainties of the unsteady forced rolling motion simulations. Numerical uncertainty  $U_{SN}$  is decomposed into contributions from iteration number, grid size, time step, and other parameters. The uncertainties caused by iteration number, grid size, time step, and other parameters are defined as  $U_I$ ,  $U_G$ ,  $U_T$  and  $U_P$  respectively. Simulation error  $\delta_{SN}$  also can be caused by the factors above, and those simulation errors are defined as  $\delta_I$ ,  $\delta_G$ ,  $\delta_T$  and  $\delta_P$ . In the present work, the time step is fixed while discussing the grid errors, and the iterative errors are considered to be negligible in comparison to those due to grid, so the uncertainties  $U_{SN}$  and simulation errors  $\delta_{SN}$  are given by

$$U_{SN}^2 = U_I^2 + U_G^2 + U_T^2 + U_P^2 \approx U_G^2 \quad (6)$$

$$\delta_{SN} = \delta_I + \delta_G + \delta_T + \delta_P \approx \delta_G$$

Three groups of structural grids defined as Grid1, Grid2 and Grid3 are generated for the flow field with systematic refinement ratio  $r_G = \Delta x_{G1}/\Delta x_{G2} = \Delta x_{G2}/\Delta x_{G3}$  to estimate numerical errors and uncertainties due to grid size. The typically used refinement ratio  $r_G = \sqrt{2}$  is used in verification, and the grid spacing in the normal direction of the cylinder are 2.0 mm (coarse grid, Grid1) and 1.0 mm (fine grid, Grid3). Using of this refinement ratio also makes a great increase of grid amount, and the total quantity of coarse/medium/fine grids are about 35K/70K/140K correspondingly.

Three cases are investigated, and the forced rolling period  $T$  of each case is 2 seconds while the maximal roll angle  $\alpha$  are  $10^\circ$ ,  $20^\circ$  and  $30^\circ$  respectively. The solutions of the damping moments of the forced rolling motion in 10 periods with Grid1, Grid2, and Grid3 are  $S_1$ ,  $S_2$  and  $S_3$  and are shown in Fig.2, where the time coordinate of the damping moments history are rolling periods.

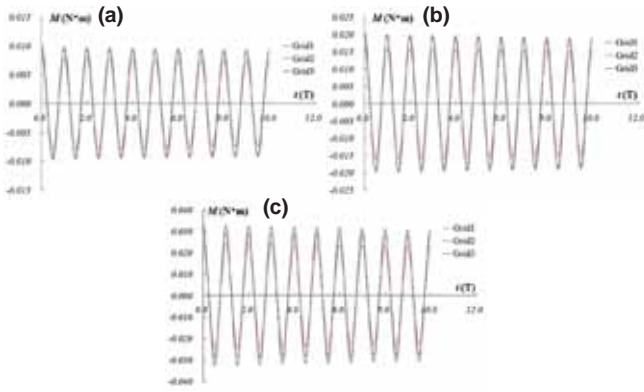


Fig. 2. Solution of each condition for (a) CASE1 ( $T=2.0s$ ,  $\alpha=10^\circ$ ) (b) CASE2 ( $T=2.0s$ ,  $\alpha=20^\circ$ ) and (c) CASE3 ( $T=2.0s$ ,  $\alpha=30^\circ$ )

Examination of solution changes between coarse/medium,  $\epsilon_{21} = S_2 - S_1$  and medium/fine,  $\epsilon_{32} = S_3 - S_2$  grids shows monotonic convergence  $\epsilon_{32} < \epsilon_{21}$  as shown in Fig.3. Where T indicates rolling period.

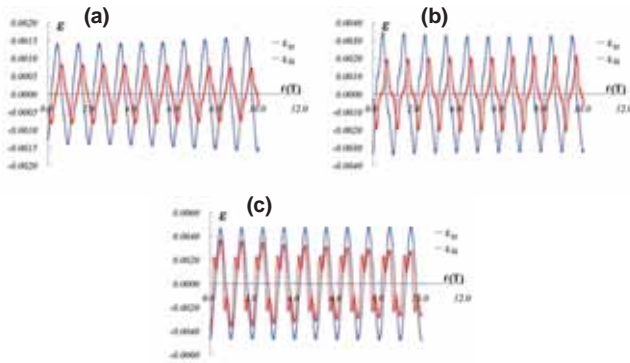


Fig. 3. Verification of predicted moment for 2-D cylinder of forced rolling for (a) CASE1( $T=2.0s$ ,  $\alpha=10^\circ$ ) (b) CASE2( $T=2.0s$ ,  $\alpha=20^\circ$ ) and (c) CASE3( $T=2.0s$ ,  $\alpha=30^\circ$ )

So that the convergence ratio  $R_G$  can be determined by

$$\langle R_G \rangle = \frac{\|\epsilon_{32}\|_2}{\|\epsilon_{21}\|_2} \quad (9)$$

and Richardson extrapolation (RE) can be used to estimate the order-of-accuracy  $p_G$ , and grid error  $\delta_{G1}$  of Grid1 by

$$\langle p_G \rangle = \frac{\ln(\|\epsilon_{21}\|_2 / \|\epsilon_{32}\|_2)}{\ln(r_G)} \quad (10)$$

$$\langle \delta_{G1} \rangle = \frac{\|\epsilon_{32}\|_2}{r_G^{\langle p_G \rangle - 1}} \quad (11)$$

where the correction factor  $C_G$  is given by

$$\langle C_G \rangle = \frac{r_G^{\langle p_G \rangle} - 1}{r_G^{\langle p_G \rangle_{est}} - 1} \quad (12)$$

where  $p_{G_{est}}$  is an estimate for the limiting order of accuracy as spacing size goes to zero and the asymptotic range is reached so that  $C_G \rightarrow 1$ . When solutions are far from the asymptotic

range,  $C_G$  is sufficiently less than or greater than 1 and only the magnitude of the error is estimated through the uncertainty  $U_G$ :

$$U_G = \left[ |C_G| + |1 - C_G| \right] \delta_{G1} \quad (13)$$

When  $C_G$  is less than 1, it can be estimated by

$$U_G = \left[ 2|1 - C_G| + 1 \right] \delta_{G1} \quad (14)$$

When solutions are close to the asymptotic range,  $C_G$  is close to 1 so that  $U_{GC}$  is estimated by

$$U_{GC} = \left| (1 - C_G) \delta_{G1} \right| \quad (15)$$

And the result is given in Table1.

Tab. 1. Verification of predicted damping moment for cylinder without bilge keels

No.	$P_G$	$C_G$	$\delta_{G1}$	$U_G$ %
CASE1	2.02	1.02	0.02	2.25
CASE2	1.87	0.91	0.05	0.06
CASE3	1.15	0.49	0.20	0.39

From the convergence tests, it was found that solution  $S_3$  with the fine grid, Grid3, suffice for the convergence of the moment histories converged. The pressure gradient at the region around bilge keels varies significantly due to the presence of vortices, refining the grid size in the flow field will provide more accurate results. Therefore, Grid3 is used for the present simulation and the total number of elements is 140000.

## NUMERICAL RESULT AND ANALYSIS

In the primary research, the widths of the bilge keels are  $b = 0, 10$  and  $30$  mm ( $b = 0\%D$ ,  $b = 1\%D$  and  $b = 3\%D$ ), and  $b = 0$  mm means that no bilge keel is appended on the cylinder. The rolling periods are  $T = 2.0, 3.0$  and  $4.0$  s respectively, and the maximal rolling angle  $\alpha$  are  $10^\circ, 20^\circ$  and  $30^\circ$ . Calculations of the total damping moments of all the conditions in 10 rolling periods are performed and the results are shown in Fig 4, which has rolling periods as time coordinate.

Where T is the rolling period. An interesting thing is shown in Fig 4 that when the width of the bilge keel equals to 10 mm, the damping moments are less than the one of the cylinder without bilge keels. A problem arisen from the results is, the total damping moments of the cylinder with bilge keels which are of special size may be less than the those in the condition that without bilge keels. Analysis of the data suggests that the minimal damping moment can be obtained while the width of the bilge keel is about 4 mm. The damping moments of the cylinder without bilge keels and those of the cylinder with 4 mm width bilge keels are compared in Fig.5, and the damping moment history has rolling period as time coordinate. The rolling periods are  $T = 2.0, 3.0$  and  $4.0$  s, and the maximal rolling angle  $\alpha$  are  $10^\circ, 20^\circ$  and  $30^\circ$  respectively.

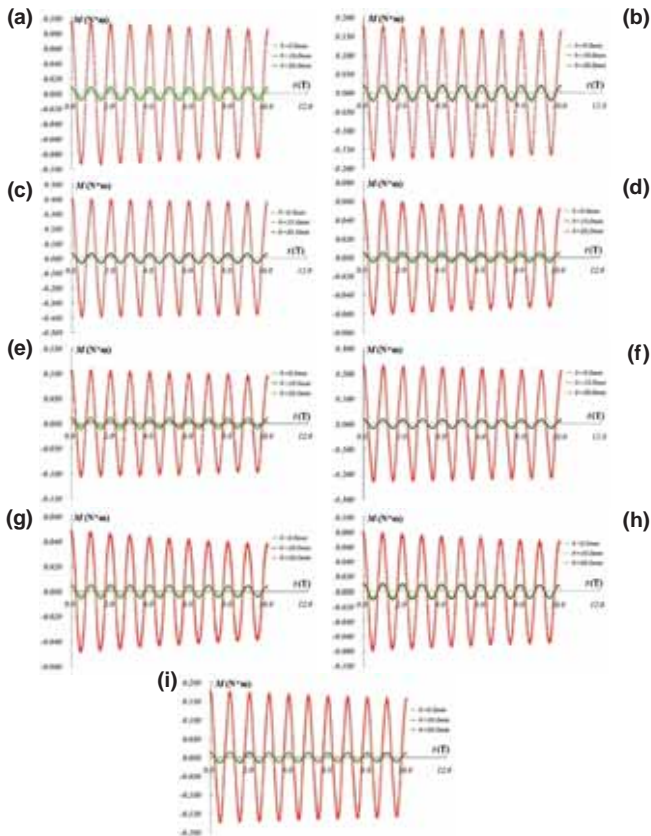


Fig. 4. Comparisons of the primary numerical results for (a)  $T=2.0s$ ,  $\alpha=10^\circ$ , (b)  $T=2.0s$ ,  $\alpha=20^\circ$ , (c)  $T=2.0s$ ,  $\alpha=30^\circ$ , (d)  $T=3.0s$ ,  $\alpha=10^\circ$ , (e)  $T=3.0s$ ,  $\alpha=20^\circ$ , (f)  $T=3.0s$ ,  $\alpha=30^\circ$ , (g)  $T=4.0s$ ,  $\alpha=10^\circ$ , (h)  $T=4.0s$ ,  $\alpha=20^\circ$  and (i)  $T=4.0s$ ,  $\alpha=30^\circ$

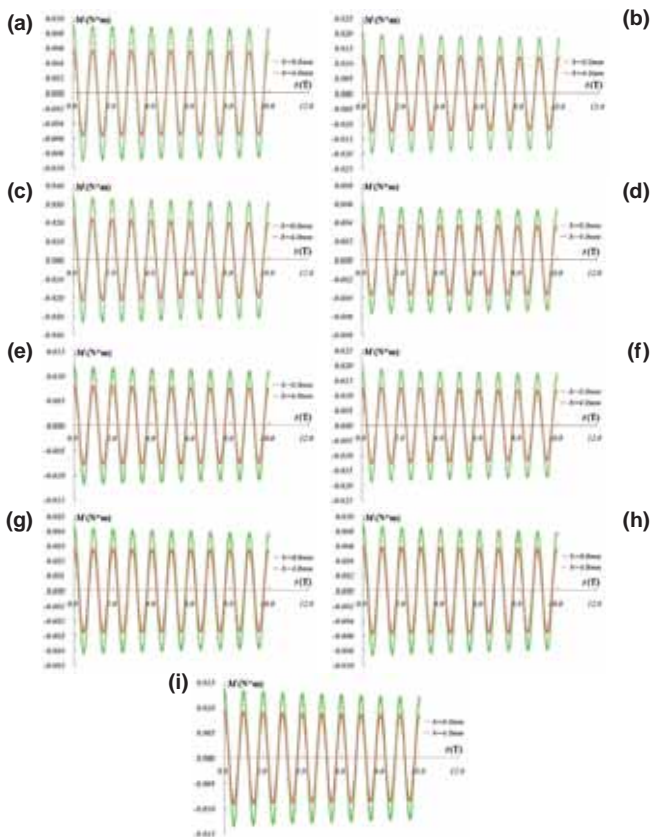


Fig. 5. Damping moment of the cylinder with bilge keels of given width for (a)  $T=2.0s$ ,  $\alpha=10^\circ$ , (b)  $T=2.0s$ ,  $\alpha=20^\circ$ , (c)  $T=2.0s$ ,  $\alpha=30^\circ$ , (d)  $T=3.0s$ ,  $\alpha=10^\circ$ , (e)  $T=3.0s$ ,  $\alpha=20^\circ$ , (f)  $T=3.0s$ ,  $\alpha=30^\circ$ , (g)  $T=4.0s$ ,  $\alpha=10^\circ$ , (h)  $T=4.0s$ ,  $\alpha=20^\circ$  and (i)  $T=4.0s$ ,  $\alpha=30^\circ$

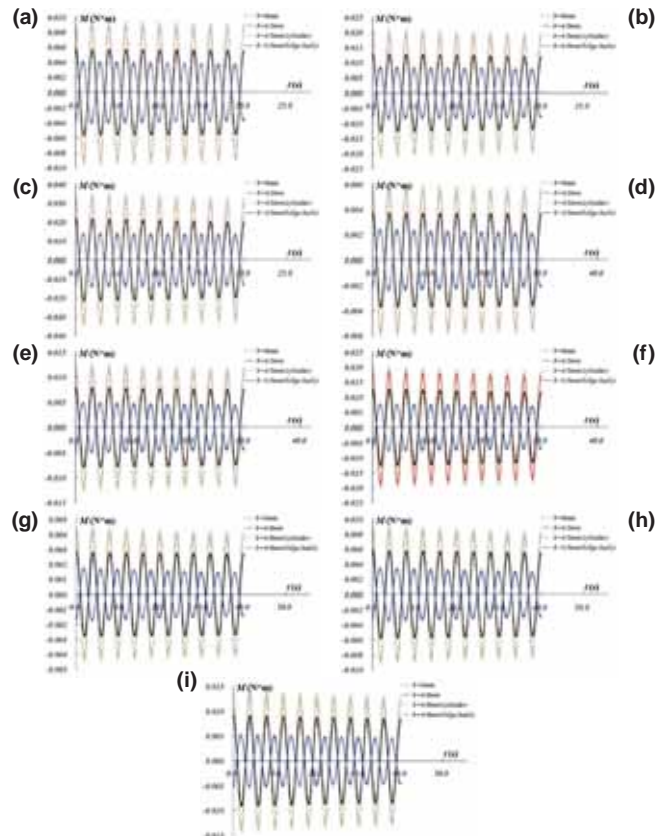


Fig. 6. Comparison of the damping moment composition for (a)  $T=2.0s$ ,  $\alpha=10^\circ$ , (b)  $T=2.0s$ ,  $\alpha=20^\circ$ , (c)  $T=2.0s$ ,  $\alpha=30^\circ$ , (d)  $T=3.0s$ ,  $\alpha=10^\circ$ , (e)  $T=3.0s$ ,  $\alpha=20^\circ$ , (f)  $T=3.0s$ ,  $\alpha=30^\circ$ , (g)  $T=4.0s$ ,  $\alpha=10^\circ$ , (h)  $T=4.0s$ ,  $\alpha=20^\circ$  and (i)  $T=4.0s$ ,  $\alpha=30^\circ$

Where the curve of  $b = 0$  mm indicates the damping moment history of cylinder without bilge keels, the curve of  $b = 4.0$  mm indicates the total damping moment history of cylinder with 4.0 mm width bilge keels, the curve of  $b = 4.0$  mm (cylinder) indicates the history of the damping moment induced only by the cylinder, and the curve of  $b = 4.0$  mm (bilge keels) indicates the history of the damping moment induced by bilge keels in the same condition. It is shown clearly in Fig.6 that the damping moment induced by the cylinder is not effected obviously whether the bilge keels are attached or not, but there is a phase difference between the damping moments induced by cylinder and the one induced by bilge keels. What is more, the magnitudes of these two damping moments are almost the same, so the total damping moments are reduced in the conditions that the 4 mm width bilge keels are attached. The result is interesting and useful for the design of the bilge keels.

It is shown in Fig.4 that if the width of the bilge keels is increased, the total damping moment increases also. In order to analyse the result carefully, two different cases which get the maximal and the minimum angular velocities are simulated, the rolling period is  $T = 2.0$  s and the maximal rolling angle  $\alpha$  is  $30^\circ$  for one case, and the rolling period is  $T = 4.0$  s and the maximal rolling angle  $\alpha$  is  $10^\circ$  for the other case. Comparison of the damping moments are performed in Fig.7, in which  $t$  is computation time.

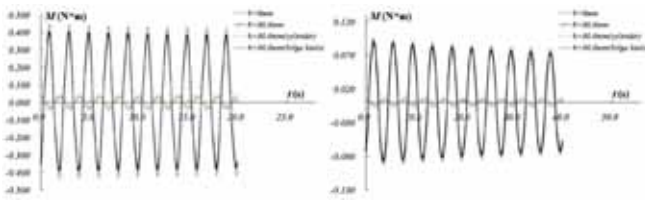


Fig.7. Comparison of the damping moment composition for (a)  $T=2.0s$ ,  $\alpha=30^\circ$ , (b)  $T=4.0s$ ,  $\alpha=10^\circ$

where the curve of  $b = 0$  mm indicates the damping moment history of cylinder without bilge keels, the curve of  $b = 30.0$  mm indicates the total damping moment history of cylinder with 30.0 mm width bilge keels, the curve of  $b = 30.0$  mm (cylinder) indicates the history of the damping moment induced only by the cylinder, and the curve of  $b = 30.0$  mm (bilge keels) indicates the history of the damping moment induced by bilge keels in the same condition. It can be seen from Fig.7 that the magnitudes of the damping moments induced by the cylinder are almost the same even the width of the bilge keels are 30.0 mm, but the damping moment induced by the bilge keels is increased obviously. There is still a phase difference between the damping moment induced by cylinder and the one induced by bilge keels, but the damping moment induced by the bilge keels is quite larger than the one induced by cylinder and becomes the dominant part of the total damping moment.

Some calculations about the total damping moment are performed, in which the bilge keel width is 50.0 mm, in order to investigate the influence of the bilge keel width on the damping moment. Comparisons of the total damping moments in 10 periods induced by cylinder without bilge keels, with 30.0 mm width bilge keels and 50.0 mm width bilge keels are performed in Fig.8, in which the damping moment history has computation time as time coordinate. The rolling periods are  $T = 2.0$  and  $4.0$  s respectively, and the maximal rolling angle  $\alpha$  are  $10^\circ$  and  $30^\circ$ .

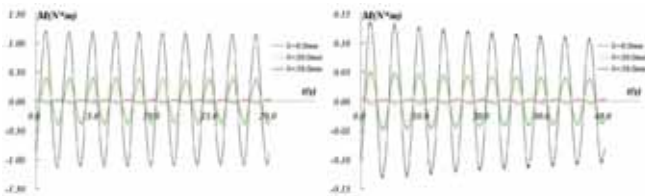


Fig.8. Comparison of the damping moments for (a)  $T=2.0s$ ,  $\alpha=30^\circ$ , (b)  $T=4.0s$ ,  $\alpha=10^\circ$

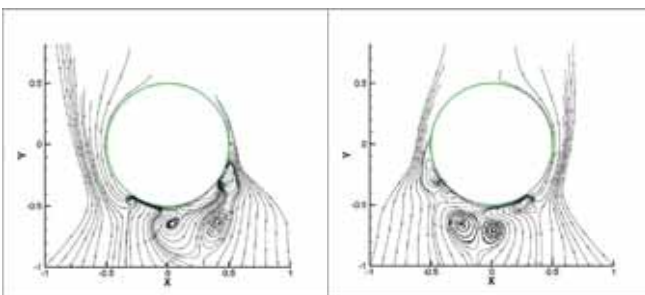


Fig. 9. Formation and shedding of vortices for (a)  $t = 1/4 T$ , (b)  $t = 3/4 T$

It is clearly shown in Fig.8 that when the cylinder is attached with 50.0 mm width bilge keels, the total damping moments induced by the cylinder and the bilge keels are larger than those induced by cylinder and 30.0 mm width bilge keels obviously, and they have the same trends which are different from those of the damping moments induced by the cylinder without bilge keels. It means that the damping moment induced by the bilge keels is increased rapidly while the width is increased, and it is the dominant part in the total damping moment.

The total damping moment induced by the cylinder with bilge keels in the present work is increased along with the increase of the bilge keel width when the width of the bilge keels is larger than the special size, and the primary damping mechanism arising from a bilge keel is the formation and shedding of vortices. The formation and shedding of vortices in a case is shown in Fig.9 in order to investigate the damping moment induced by bilge keels, in which the rolling period  $T$  is 4.0s, and the maximal rolling angle  $\alpha$  is  $30^\circ$ .

In Fig.9, it is shown that the flow field is affected by the bilge keels, and the vortices are formed around the bilge keels. Because of the rolling of the cylinder, the vortices are shedding from the bilge keels latter. After that, the vortices exist in the flow field for a long time and affect each other, for which the location and diameter of the vortices are affected. The formation and shedding of vortices are important reasons for the damping moment induced by the bilge keels, and Fig.9 shows an illustration for them. In the present work, the basic equation for the flow field is Reynolds Average Navier-Stokes equation, so the averaged velocity is used in the calculation and some of the small vortices are ignored.

## CONCLUSION

In order to investigate the effect of bilge keels on the damping moment, a special two dimensional model is designed and studied. In this way, some factors such as the influence of the surface wave, the interaction between the cylinder and the induced wave, as well as the effect of the length of the bilge keels are ignored. A viscous code based on the SST  $k - \omega$  viscous model is developed and used for the simulation of the forced rolling motion; the results are verified and validated by suggested method. An interesting issue shown in the results is that there is a phase difference between the damping moment induced by the cylinder and bilge keels, so the total damping is mitigated when the bilge keel width gets a special size. If the width of the bilge keel is increased and larger than the special size, the damping moment induced by the cylinder is not changed obviously, which means the flow field around the cylinder is affected by the bilge keel size weakly. But the damping moment induced by the bilge keels is increased quickly, and become the dominant part in the total damping moment. The formation and shedding of vortices is shown in detail. The numerical model used in the paper seems significant for the investigation of the bilge keels' effect. The viscous method is well known, but the usage of it for the analysis of the damping moment components and the relationship seems to be new and turns out to be useful for the design of the bilge keel.

## ACKNOWLEDGEMENTS

The support has been provided by the Fluid Mechanics Group led by DUAN Wen-yang of Harbin Engineering University. These Financial support has been provided by the National Natural Science Foundation of China (Grant No. 51209048; 51309069; 51379045); Research on Analysis and Forecasting Technology of Trimaran Hydrodynamic Performance; Research on the Distribution of Ship Energy Consumption and Energy Efficiency; National Defense Basic Research Foundation of China (Grant No. B2420132001); Fundamental Research Funds for the Central Universities (Grant No. HEUCF140101; P013513013)

## REFERENCES

1. Chakrabarti, S. Empirical calculation of roll damping of ships and barges, *Ocean Engineering*, Vol. 28, pp. 915-932, 2001.
2. Cueva, M, Hansen, AS, Silva, JLB, Faria, F, Morato, A. HYDRODYNAMICS OF AN INSTALLATION BARGE WITH BILGE KEELS AND STINGER, 29th ASME International Conference on Ocean, Offshore and Arctic Engineering, Shanghai, PEOPLES R CHINA, JUN 06-11, 2010.
3. D. Mylonas, P. Sayer. The hydrodynamic flow around a yacht keel based on LES and DES, *Ocean Engineering*, Vol. 46, pp. 18-32, 2012.
4. Dai, CM, Miller, RW, Percival, AS. HYDRODYNAMIC EFFECTS OF BILGE KEELS ON THE HULL FLOW DURING STEADY TURNS, *OMAE*, Vol. 5, pp. 571-580, 2009.
5. E.P. Bangun, C.M. Wang, T. Utsunomiya. Hydrodynamic forces on a rolling barge with bilge keels, *Applied Ocean Research*, Vol. 32, pp. 219-232, 2010.
6. Froude, W. On the Rolling of Ships, Ph.D. thesis, Royal Institute of Naval Architects, 1861.
7. H.H. Chun, S.H. Chun, S.Y. Kim. Roll damping characteristics of a small fishing vessel with a central wing, *Ocean Engineering*, Vol. 28, pp. 1601-1619, 2001.
8. IKEDA Y., HIMENO Y, TANAKA N. On eddy making component of roll damping force on naked hull, *Journal of the Society of Naval Architects of Japan*, Vol. 142, pp. 54-64, 1977.
9. ITTC QM Procedure (2002). 7.5- 03- 01- 01.
10. ITTC QM Procedure (2002). 7.5- 03- 02- 01.
11. Kinnas, S. A., Yu, Y. H., Kacham, B., Lee, H. A Model of the Flow Around Bilge Keels of FPSO Hull Sections Subject to Roll Motions, *Proceedings of the 12th Offshore Symposium, Soc. Naval Arch. Mar. Engr.. Houston TX.*, 2003.
12. Kinnas, S. A. FPSO Roll Motions, Technical Report, Minerals Mgt. Service, USA, 2005.
13. Kwang Hyo Jung, Kuang-An Chang, Erick T. Huang. Two-dimensional flow characteristics of wave interactions with a free-rolling rectangular structure, *Ocean Engineering*, Vol. 32, pp. 1-20, 2005.
14. LI Yi-le, LIU Ying-zhong, MIAO Guo-ping. Potential flow solution using higher order boundary element method with Rankine source, *Journal of Hydrodynamics(Ser. A)*, Vol. 14, no 1, pp. 80-89, 1999.
15. LUO Min-li, MAO Xiao-fei, WANG Xiao-xia. CFD based hydrodynamic coefficients calculation to forced motion of two-dimensional section, *CHINESE JOURNAL OF HYDRODYNAMICS*, Vol. 26, no. 4, pp. 509-515, 2011.
16. M. Eissa, A.F. El-Bassiouny. Analytical and numerical solutions of a non-linear ship rolling motion, *Applied Mathematics and Computation*, Vol. 134, pp. 243-270, 2003.
17. Maimun, A. Priyanto, K.S. Wong, M. Pauzi, M. Rafiqul. Effects of side keels on patrol vessel safety in astern waves, *Ocean Engineering* 2009; 36: 277-284.
18. Pablo M. Carrica, Hamid Sadat-Hosseini, Frederick Stern. CFD analysis of broaching for a model surface combatant with explicit simulation of moving rudders and rotating propellers, *Computers & Fluids*, Vol. 53, pp. 117-132, 2012.
19. PU Jin-yun, ZHANG Wei-kang, JIN Tao. Melnikov's method for non-linear rolling motions of a flooded ship, *Journal of Hydrodynamics(Ser. B)*, Vol. 17, no. 5, pp. 580-584, 2005.
20. Qiuxin Gao, Dracos Vassalos. Numerical study of damage ship hydrodynamics, *Ocean Engineering*, Vol. 55, pp. 199-205, 2012.
21. Robert V. Wilson, Pablo M. Carrica, Fred Stern. Unsteady RANS method for ship motions with application to roll for a surface combatant, *Computers & Fluids*, Vol. 35, pp. 501-524, 2006.
22. Souza Jr., J.R., Fernandes, A.C., Masetti, I.Q., da Silva, S., Kroff, S.A.B.. Nonlinear rolling of an FPSO with larger-than-usual bilge keels, *Proceedings of the International Conference on Offshore Mechanics and Arctic Engineering – OMAE*, Lisbon, Portugal; July 5, 1998 - July 9, 1998.
23. Stern F, Wilson R, Coleman H, Paterson E. Comprehensive approach to verification and validation of CFD simulations—Part 1: Methodology and procedures, *ASME J Fluids Eng.*, Vol. 123, pp. 793-802, 2001.

24. Tanaka, N., Hishida, T. A Study on the Bilge Keels. Part 1. Two Dimensional Model Experiments, *J. Soc. Nav. Archit. Jpn.*, Vol. 101, pp. 99-105, 1957.
25. Tanaka, N. A Study on the Bilge Keels. Part 2. Full Sized Model Experiment, *J. Soc. Nav. Archit. Jpn.*, Vol. 103, pp. 69-73, 1958.
26. Tanaka, N. A Study on the Bilge Keels. Part 3. The Effect of the Ship Form and the Bilge Keel Size on the Action of the Bilge Keel, *J. Soc. Nav. Archit. Jpn.*, Vol. 105, pp. 27-32, 1959.
27. Tanaka, N. A Study on the Bilge Keels. Part 4. On the Eddy making Resistance to the Rolling of a Ship Hull, *J. Soc. Nav. Archit. Jpn.*, Vol. 109, pp. 205-212, 1960.
28. Thiagarajan, Krish P., Braddock, Ellen C. Influence of Bilge Keel Width on the Roll Damping of FPSO, 24th International Conference on Offshore Mechanics and Arctic Engineering, Halkidiki, GREECE; JUN 12-17, 2005.
29. Vaidhyathan, M. Separated Flows Near a Free Surface. Ph.D. thesis, University of California, Berkeley, CA., 1993.
30. Wilson R, Stern F, Coleman H, Paterson E. Comprehensive approach to verification and validation of CFD simulations—Part 2: Application for RANS simulation of a cargo/container ship, *ASME J Fluids Eng.*, Vol. 123, pp. 803-810, 2001.
31. Wilson R, Shao J, Stern F. Discussion: Criticisms of the correction factor verification method, *ASME J Fluids Eng.*, Vol. 125, pp. 732-733, 2003.
32. YANG Bo, WANG Zuo-chao, WU Ming. Numerical Simulation of Naval Ship's Roll Damping Based on CFD, *Procedia Engineering*, Vol. 37, pp. 14-18, 2012.
33. YANG Chun-lei, ZHU Ren-chuan, MIAO Guo-ping, FAN Ju. Numerical simulation of rolling for 3-D ship with forward speed and nonlinear damping analysis, *Journal of Hydrodynamics(Ser. B)*, Vol. 25, no. 1, pp. 148-155, 2013.
34. Yeung, R.W., Liao, S.-W., Roddier, D. Hydrodynamic coefficients of rolling rectangular cylinders, *Eighth International Journal of Offshore and Polar Engineers*, Vol. 8, pp. 242-250, 1998.
35. Yeung, R., Roddier, D., Alessandrini, B., Gentaz, L., and Liao, S.-W. On Roll Hydrodynamics of Cylinders Fitted With Bilge Keels, *Proceedings 23rd Symposium Naval Hydrodynamics*, Washington, DC., 2000.

## CONTACT WITH AUTHOR

Rui Deng  
e-mail: dengrui@hrbeu.edu.cn

Wenyang Duan

Shan Ma

Yong Ma

Shipbuilding Engineering  
College of Harbin Engineering University  
No.145 Nantong street  
150001 Harbin  
China

Tel.: +86-0451-8251-9901

fax: +86-0451-8251-9910

# MULTI-GRID MODEL FOR CROWD'S EVACUATION IN SHIPS BASED ON CELLULAR AUTOMATA

Miao Chen,

Duanfeng Han,

College of Ship Building, Harbin Engineering University,  
Harbin, China

## ABSTRACT

*In order to enhance the authenticity and accuracy simulation of passengers' evacuation in ships, a new multi-grid model is proposed on the basis of cellular automata theory. By finer lattice the multi-grid model could enhance the continuity of passengers' track and the precision of boundary's qualification compared with traditional cellular automata model. Attraction, repulsion and friction are also quantized in the multi-grid model to present the impact of interaction force among pedestrians. Furthermore, crowd's evacuation simulated by traditional cellular automata and multi-grid model in single exit room and typical cabin environment have been taken as examples to analyze crowd's motion laws. It is found that the laws of passengers' evacuation simulated by the two models are similar, and the simulation authenticity and accuracy is enhanced by the multi-grid model.*

**Keywords:** crowds' evacuation in ships, multi-grid model, cellular automata model, finer lattice, interaction force

## INTRODUCTION

Recently well-published disasters of ships together with trends of largely increased capacity of passenger carrying ships have brought more and more attention to the issue of passengers' evacuation, being the last line of defence. It has become the investigation hotspot all around the worldwide. Mainly, there are three kinds of crowd's motion simulation construction methods. They are macroscopic models microscopic models and mesoscopic models [7].

Firstly the macroscopic model was proposed by J.J. Fruin [2]. The crowd's motion of macroscopic model is constructed by hydrodynamic theory. In macroscopic model pedestrians are taken as a whole and individual's motion detail is not considered. In the macroscopic model crowd's circulation law is simple and the simulation calculation speed is fast. It is suit for large-scale pedestrians' evacuation with less individual's behavior differences. But when individual's behavior differences have a greater impact on the evacuation simulation, the defect that the macroscopic model can't simulate the behavior characteristics will be amplified and the simulation result will not match with the actual evacuation situation.

The research object of microscopic model is the single individual so the microscopic model could simulate the individual's behavior character and interactive forces between them. It is suit for simulate the evacuation in complex building environments. Social Force Model [4-6] is a microscopic model that it could simulate the individual's behavior character more realistically than any other microscopic models. It could simulate the crowds' evacuation phenomenon like fast-is-slow,

self-organization, assembly, crowd congestion etc. But driving the Social Force Model needs enormous computation amount, it is not conducive to the practical engineering application.

Mesoscopic model uses a compromise approach to set up model considering the macro modeling methods and the microscopic modeling methods. It mainly refers to cellular automata models and lattice gas model. Cellular automata model [1, 3, 11] is the general name of a kind of kinetic model with discrete process time and space. Each cell can only take a finite number of discrete states. Cellular motion models are constructed by a series of model rules. The next time step state is calculated for each cell according to the local cellular situations by the same rules and all the cells update synchronously. Cellular automata models are suit for engineering application for high calculation speed. But it often can't simulate the crowds' motion well as the movement rules are oversimplified under complex environments.

Aiming at combine the advantage of social force model and discretion model some scholars have set up new models. The floor field model and friction model can behave the self-driven force [10] and repulsive force [9] preferably. On the base of it CAFE model [12] got similar result with the social force model by quantitative analysis of repulsive force and friction between pedestrians and simulating some basic pedestrian dynamics phenomenon. Whereas those models not only could realize the dislocation distribution of pedestrians practically but also could they consider the impact of boundary qualification and exits condition sufficiently as their partitioned smallest

grid is as big as the area taken up by one person. In order to research the characters of crowd's evacuation more carefully scholars made the grid finer that making one person taking up multi-grids method. Kirchner et al. [8] have simulated the crowd's evacuation process in corridor and single-exit room by method that one person taking up  $2 \times 2$  grids. But he didn't consider the repulsion's and friction's effect. WengWenguo.etc [14] analyzed the relation between evacuation time and the number of grid moved in one time step by setting up small grid model. WeiguoSong and XuanXu et al. [13] have set up a multi-grid model that importing the reciprocity force among pedestrians and reciprocity force between pedestrians and buildings in social force model and the result of the model is close to that of social force model. But in these multi-grid model repulsion and friction was produced by pedestrians' overlapping, that didn't conform to the actual situation. In this paper a new multi-grid model is proposed with quantitative exit attraction, trajectory attraction, repulsion and friction to determine pedestrians' moving direction on the basis of cellular automata. By the model crowd's evacuation process can be simulated more accurately and realistically.

### MULTI GRID MODEL

As the Fig. 1(a) shows, in single-grid model the size of single grid is the same as the area one person possessed. Each person possesses one grid and the size of each grid is  $0.4\text{m} \times 0.4\text{m}$ . But as the fig. 1(b) shows the space is further discrete by multi-grid model, the size of each grid is  $0.1\text{m} \times 0.1\text{m}$ . That is to say, each person possesses  $4 \times 4$  grids and the trajectory's precision can reach  $0.1\text{m}$ . At any moment, the state of each grid is empty or possessed by one person at most. As long as the neighborhood grids are empty the central pedestrian can move up and down, left and right as Fig. 2 shows.



Fig. 1. Movement of pedestrian

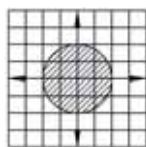
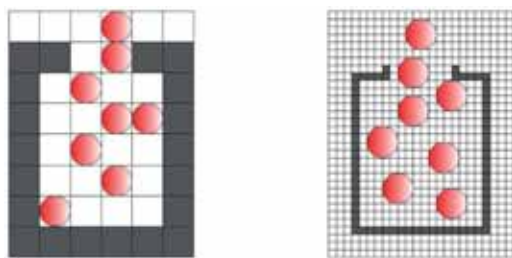


Fig. 2. direction of pedestrian's movement



(a) single-grid model (b) multi-grid model  
Fig. 3. Effect of exit's exclusion

### ADVANTAGES OF MULTI-GRID MODEL

Compared with single-grid model, multi-grid model is improved on the continuity of pedestrian's movement, representation of reciprocity force among pedestrians and reciprocity force between pedestrians and buildings, accuracy of boundary qualification and so on. They are illustrated specifically as below.

For single-grid model each pedestrian stops or moves the length equal to a person possessed in each time step. That is coincident with the practical situation when the density of passengers is low. But the distance that a pedestrian moves could be less than the length of a person possessed when the density of passengers is high. In that situation the single-grid model can't show the fine movement of pedestrians. But for the multi-grid model, the shortest distance that a pedestrian could move is  $0.1\text{m}$ . It could express the finer movement better and make the position of pedestrians vary more continuously.

For single-grid model the space between pedestrians is multiple of the length of grid. But for multi-grid model the space between pedestrians is less than the length of a person as the grid has been discrete. So the multi-grid model could realize the dislocation distribution of pedestrians.

For the multi-grid model the dislocation distribution of pedestrians has emphasized the repulsive effect between pedestrians greatly especially at the exit. As Fig. 3(a) shows it's easy for two pedestrians to pass the exit at the same time in the single-grid model. On the contrary the probability is much lower for two pedestrians to pass the exit at the same time for the effect of the dislocation distribution of pedestrians in multi-grid model. As Fig. 3(b) shows if one pedestrian possesses the middle position of the exit others can't pass through in the multi-grid model. In fact the situation is matched with the practicality. But for the single-grid model the length of exit is multiple of the length of pedestrian, the effect of exit's exclusion will not happen.

In both of the two models the size of the cabin's boundary is multiple of the size of grid. The size of grid in single-grid model is  $0.4\text{m} \times 0.4\text{m}$  but  $0.1\text{m} \times 0.1\text{m}$  in multi-grid model. So the accuracy of boundary qualification is detailed to  $0.1\text{m}$ .

### CIRCULATION PRINCIPLES OF MULTI-GRID MODEL

The movement of pedestrian is determined by probability in the multi-grid model. In each time step the center of pedestrian could stop or move to one of the adjacent 4 grids according to the state of pedestrian. As the Fig. 4 shows a preferential matrix  $P$  is adopted here to describe the probability value of the directions one pedestrian could move to. The value of the probability is determined by four reciprocity elements: exit attraction, trajectory attraction, repulsion and friction between pedestrians and between pedestrians and buildings. The probability of a pedestrian moving to grid  $(i, j)$  can be calculated as below after considering the four elements in general.

	$P_{0,y}$	
$P_{x,0}$	$P_{0,0}$	$P_{x,0}$
	$P_{0,\gamma}$	

Fig. 4. Matrix P

$$p_{ij} = N \cdot \exp(k_E E_{ij} + k_T T_{ij} + k_r (F_r + F_f)) \cdot (1 - n_{ij}) \quad (1)$$

$$N = \sum p_{ij}^{-1} \quad (2)$$

In formula 1 and 2, N the standardization coefficient can make  $\sum p_{ij} = 1$ .  $n_{ij}$  represents the state of grid (i,j) at time t.  $n_{ij} = 0$  shows that nobody is in grid (i, j) and  $n_{ij} = 1$  shows that the grid (i,j) is possessed by somebody or any other obstacles at the moment. As the formula 3 and 4 shows represents the character of floor and its biggest value is at the exit.  $E_{ij}$  is the value of the exit attraction at the present position. E's value gradually decreases from the position of the door to a position away from the door.  $k_E$  is the attraction coefficients of  $E_{ij}$ .

$$E_{ij} = |x_i - x_{exit}| + |y_i - y_{exit}| \quad (3)$$

$$E_{ij} = \max(E_{ij}) - E_{ij} \quad (4)$$

$T_{ij}$  is the value of trajectory attraction and  $T_{ij}$  represents the attraction from the trace of pedestrians. The value of  $T_{ij}$  could be got by formula 5. In formula 5  $\varphi(T)$  is the c attenuation function and it represents the residual proportion of information seconds ago in the current time.

$$D_{ij}(T) = \sum_{k=0}^T \varphi(T-k) D_{ij}(k) \quad (5)$$

$$\varphi(0) = 1, \quad \varphi(1) = \frac{1}{3}, \quad \varphi(T)|_{T>0} > 0, \quad \lim_{\delta T \rightarrow \infty} \varphi(T) = 0$$

Furthermore the final moving direction is also determined by repulsion's and friction's impact.  $F_r$  and  $F_f$  represent the repulsion and friction between pedestrians separately.  $k_r$  represents the attraction coefficient of repulsion and friction.

$$F_r = k_r \frac{\frac{\beta}{1 - e^x}}{1 + e^x} \quad (6)$$

The repulsion generates when there is the trend of danger distance between pedestrians, pedestrian and walls. The pedestrian will dodge and avoid [8, 12, 13, 14]. According to formula (6) each pedestrian's repulsive force can be got. In formula (6), the Sigmoid function is introduced to describe the repulsive force considering the pedestrian's avoiding behavior is a neural reflection behavior,  $\beta$  is the hardness factor it relies to the pedestrians' physical endurance limitation. As Fig. 5 shows  $F_r$  reduces when the distance between pedestrians enlarges or the value of  $\beta$  decreases.

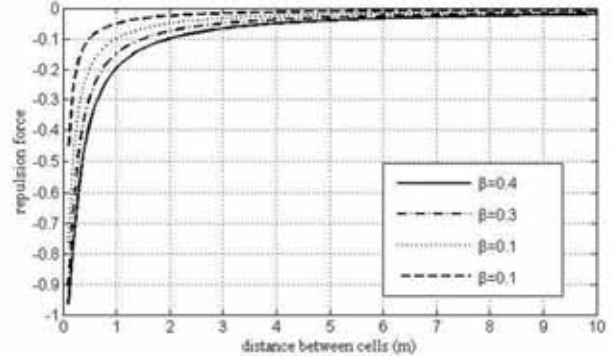


Fig.5. Impact on repulsion force for the distance between cells

According to formula 7 and 8 each pedestrian's friction can be got. The hurt triggered by the head-on collision is always bigger than the side impact triggered by friction so  $\theta$  is used to link the two factors,  $\theta \in [0,1]$ . V represents the relative velocity. For two pedestrians' opposite movement  $V = 2 \times v$ . When one pedestrian moves and the other one stands still  $V = v$ . For a moving pedestrian and a wall  $V = v$ . v is the actual speed of a pedestrian. l is the Line area between pedestrians and L is the length of one cell as Fig. 6 shows.  $\gamma$  is the repulsion ratio,  $\gamma \in [0,1]$ .

$$F_f = \theta F_r \quad (7)$$

$$\theta = \gamma \cdot \left| \frac{l}{L} \right| \cdot \left| \frac{V}{v} \right| \quad (8)$$

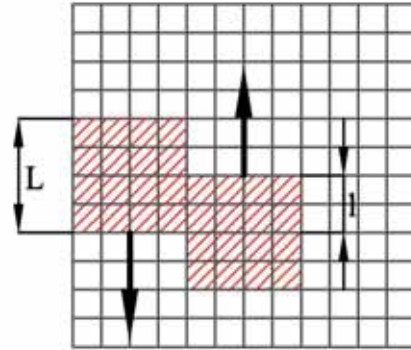


Fig.6. Friction diagram

## CIRCULATION PRINCIPLES OF THE MULTI-GIRD MODEL FOR MULTI-LEVEL EXITS ENVIRONMENT

Network flow theory is adopted for simulating the arrangement of cabins in ships in traditional model. The cabins, corridors, rooms before the stairs, stairs, muster station and other construction entities are simplified to network units. As the network units are connected with doors or openings a distributed connectionist network has formed. In traditional model, each network unit has an independent self-driven field from the center of its exit. The movement is controlled by the network's self-driven field. But when the grid is discrete and the number of cabin structures is big the amount of storage

data is great. It is too complex to simulate by traditional method since too many circulation times have decrease the efficiency in the extreme. Therefore, the self-driven fields are simplified into two: cabin field and exit field for the multi-level exits environment in this paper. The cabin field is made up of superposition of all cabins' field and the exit field is made up of superposition of all exits' field. In the process of his movement the pedestrian judges his location in the whole cabin structures firstly. If he is in a cabin he'll move to the exit of the cabin under the control of cabin floor field. Or if he is on an exit or opening he'll move to the next level cabin under the control of exit field. At last he'll reach to the final exit after such reiteration.

According to the analysis upwards, passengers' movement will be updated orderly in new principles in every time step, as the Fig. 7 shows.

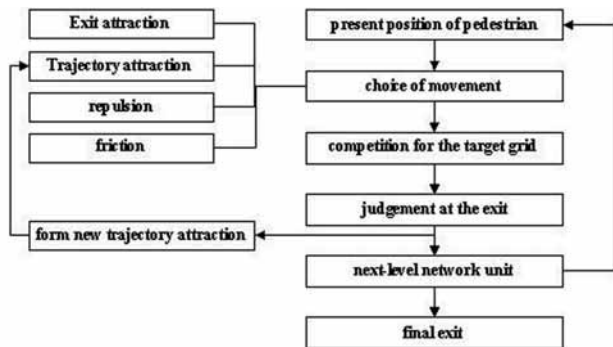


Fig. 7. Simulation principles

1) All the pedestrians choose the movement directions according to the state of adjacent grids and the principles of cabin floor field of multi-grid model.

2) According to the hypothesis one grid can only be possessed by one pedestrian in each time step. If more than one pedestrian compete for one target grid only one of them could moved to the grid and all the others have to go back the original places. In addition the chance for going to the target grid is fair to all the pedestrians.

3) When somebody reaches the exit or opening he will choose movement directions under the control of exit floor field.

4) New dynamic floor field will be formed when new trajectory is formed by pedestrians in new positions.

5) If some pedestrian moves to the next level network he will move by the principles from (1)~(4) again.

6) If somebody reaches the final exit the point on behalf of the person will be removed standing for getting away from the evacuation area.

## SIMULATION AND ANALYSIS

### EVACUATION ANALYSIS FOR SINGLE EXIT ROOM

Tab. 1. Parameters in model

coefficients	value	explanation
$k_s$	1.0	attraction coefficient of static floor field
$k_d$	1.0	attraction coefficient of dynamic floor field
$k_r$	1.0	attraction coefficient of repulsion and friction
$\varphi$	0.3	attenuation coefficient
$\beta$	0.4	hardness coefficient
$\gamma$	0.3	friction coefficient

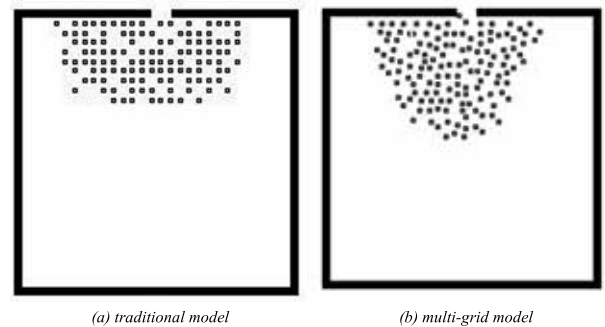


Fig. 8. Comparison of two models'queue in the single exit room

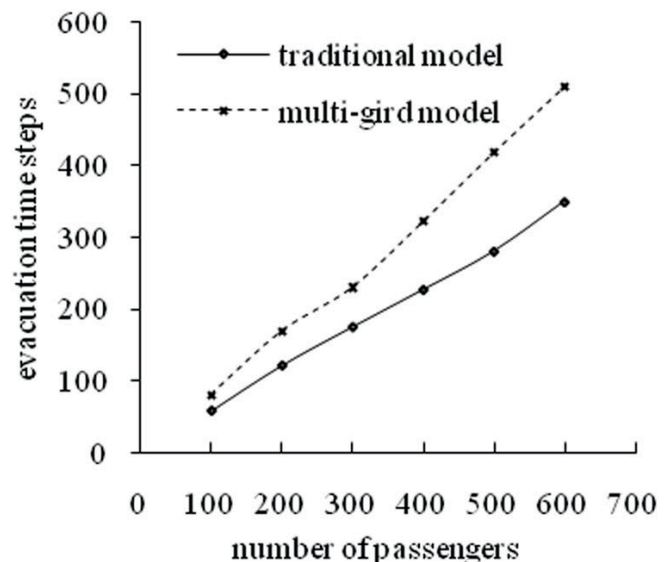


Fig. 9. Comparison of evacuation time between traditional cellular automata model and multi-grid model

The value of coefficients is lay out above as the Tab. 1 shows. Compared with traditional cellular automata model the distance moved in one time step by multi-grid model doesn't match with the defined length of pedestrian, dislocation appears among pedestrians and the exit can't be made good use of as the Fig. 8 shows. So it needs more time to finish evacuation by multi-grid model. Fig. 9 shows the situation of

evacuation of traditional cellular model and multi-grid model when pedestrian's velocity is 1 m/s. It is found that the bigger the density of passengers is the longer the evacuation time needs. It is caused of passengers' disorderly arrangement and low utilization ratio of exit.

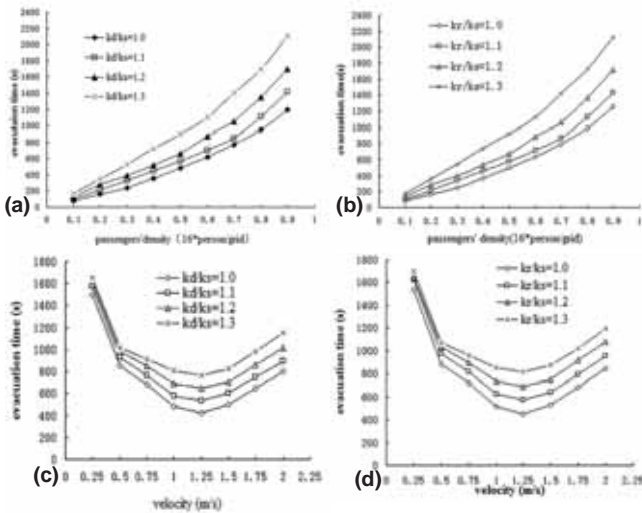


Fig. 10. The impact on evacuation time of interaction force

The value of  $k_r/k_s$  and  $k_D/k_s$  have an important impact on evacuation time to multi-grid model. As Fig. 10 shows, as the density of passengers increases the evacuation time increases more quickly when the value of  $k_r/k_s$  and  $k_D/k_s$  increase. But as the maximum velocity,  $k_r/k_s$  and  $k_D/k_s$  increases the evacuation time demonstrate the trend of rising before inhibition. At the same time  $k_r/k_s$  have greater impact on evacuation time for the effect of friction.

### EVACUATION ANALYSIS FOR TYPICAL CABIN ARRANGEMENT ENVIRONMENT

Considering the fire prevention the cabin environment of large vessels is usually separated into several main vertical zones. Each main vertical zone is closed and so independent aisles are formed. At the same time a typical cabin arrangement environment is formed on each deck of some main vertical zone according to the symmetry of cabins. Fig. 11 shows a typical cabin arrangement environment. It is made up of 42 cabins, 2 corridors, 1 room before stairs and two stairs. The area of it is 44 m×20 m, the size of each cabin is 4 m×4 m, the width of corridor is 1.6 m, the width of each cabin's door is 1.2m and the width of stairs is 2 m. It is supposed that the movement of ship doesn't have an effect on the velocity of pedestrians, cabins are not on fire and there is no other passenger impact the movements in the typical cabin arrangement environment after the passengers move to the stairs.

All the passengers are distributed randomly in the 42 cabins before evacuation. They move to the stairs after receiving the evacuation information by the velocity of 1 m/s. Fig. 12 shows the evacuation process of traditional cellular automata model and multi-grid model when the density of pedestrians is 20% grids occupied. It is found that the arrangement of passengers in multi-grid model is much tighter than that in traditional

model. The phenomenon of the passengers' arrangement in multi-grid model is more in line with practical situation. The main reason is that pedestrians in multi-grid model have more optional movement directions and dislocation distribution of pedestrians and better continuity movement of pedestrians can realized by discretion of grid.

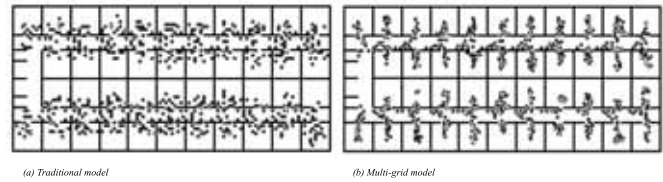


Fig.11. Evacuation of passengers

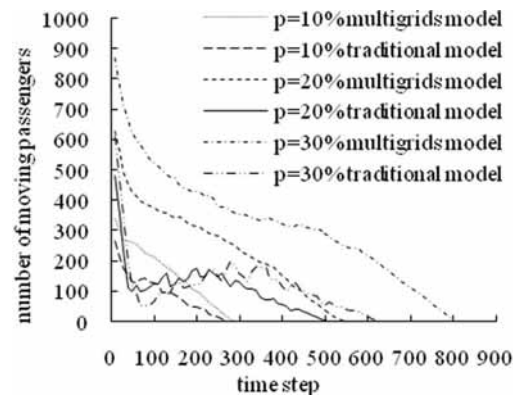


Fig. 12. Moving passengers' number for different distributing amount of passengers

Fig. 12 shows the trend of moving passengers' number varying with the evacuation time with different original density of passengers. It is found that the number of moving pedestrians decreased with the increase of evacuation time. In the process of evacuation the number of moving passenger decreases as a lot of passengers moved to the long and narrow corridors. But the crowd situation is lightened when more and more passengers finish the evacuation task. For the traditional model the reduction of the number of moving pedestrians has a repeated process. But for the multi-grid model the speed of reduction of the passengers' number is quicker for more optional movement directions, and smaller movement distance 0.1 m. After all, the trend of the number of moving passengers' variation doesn't change.

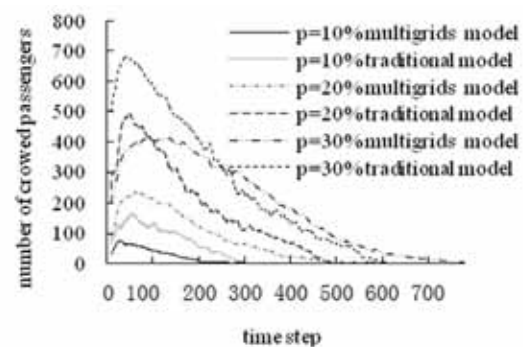


Fig. 13. Congested passengers' number for different distributing amount of passengers

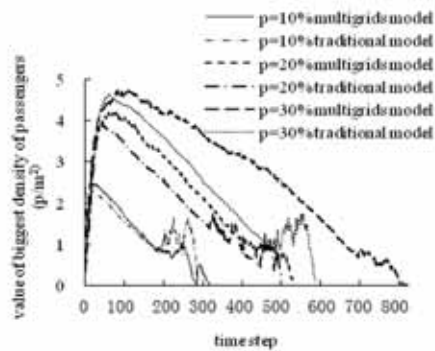


Fig. 14. Maximum density of passengers for different distributing amount of passengers

Fig.13 shows the trend of crowded pedestrians number varying with the evacuation time with different density of passengers. For the two models the number of crowded passengers increases firstly and decreased then till 0 as the increase of evacuation time. But for multi-grid model the number of crowded pedestrians is lower when the original density of passengers is the same for higher movement continuity.

Fig.14 shows the trend of the maximum density varying with evacuation time with different original density of passengers. In the beginning of evacuation process the maximum density appears in the cabins. As more and more passengers moved to the corridors the maximum passengers density transformed to the corridors. And then the passengers' density decreased in the corridors for more and more passengers finish the evacuation task. Till to a moment that the passengers' density in the corridors are the same to that in the rooms before stairs. The maximum will appear in corridors and the rooms before stairs alternately until all the passengers leave the final exits. For the two models their trend of the maximum density variation is close. But the value of the maximum density of multi-grid model is higher for lower utilization ratio of exits caused of dislocation distribution of passengers.

## CONCLUSION

Multi-grid model can simulate the evacuation situation better than traditional cellular automata model after comparison. It could reproduce the dislocation distribution of passengers, enhance the accuracy of boundary qualification and the continuity of movement trajectory and simulate evacuation process more accurately by quantizing the interaction force between passengers. According to the evacuation simulation experiment tests it is proved that the two models have similar movement laws but the multi-grid model can finish the simulation more truly and accurately.

## ACKNOWLEDGMENT

This work is supported by the Ph.D. Programs Foundation of Ministry of Education of China (Grant No.20102304110018), and supported by the Foundation Research Funds for the Central Universities (Grant No.HEUCF140107).

## REFERENCES

- Burstedde C, Klauek K , Schadschneider A and Zittartz J, Simulation of Pedestrian dynamics using a two-dimensional cellular automaton, *Physica A*, Vol. 295, pp. 507-525, 2001.
- Fruin J J, *Pedestrian Planning and Design*, Metropolitan Association of Urban Designers and Environmental Planners, New York, USA, 1971.
- Hao Yue, Hongzhi Guan, Juan Zhang and Chunfu Shao, Study on bi-direction pedestrian flow using cellular automata simulation, *Physica A*, Vol. 389, pp. 527-539, 2010.
- Helbing, D., Farkas, I., and Vicsek, T, Simulating dynamical features of escape panic, *Nature*, Vol.407, no. 6803, pp. 487-490, 2000.
- Helbing D, Keltseh J, Molnar P, Modelling the evolution of human trail systems, *Nature*, Vol.388, no. 6637, pp. 47-50. 1997.
- Helbing D, Molnar P, Social force model for Pedestrian dynamics, *Physical Review E*, Vol. 51, no. 5, 4282-4286, 1995.
- Jinyi. G, Shuang L, Shaokuan C. Review of Pedestrian Movement Simulation Studies, *Journal of System Simulation*, Vol.20, no. 9, pp. 2237-2241, 2008.
- Kirchner A, Klupfel H, Nishinari K, Schadschneider A and Schreckenberg M, Discretization effects and the influence of walking speed in cellular automata models for pedestrian dynamics,
- Kirchner A, Nishinari K and Schadschneider A, Friction effects and clogging in a cellular automaton model for pedestrian dynamics, *Physical Review E*, Vol.67, no. 056122, 2003.
- Kirchner A, Schadschneider A. Simulation of evacuation processes using a bionics-inspired cellular automaton model for pedestrian dynamics, *Physica A*, Vol. 312, pp.260-76, 2002.
- Masakuni Muramatsu, Takashi Nagatani, Jamming transition of pedestrian traffic at a crossing with open boundaries, *Physica A*, Vol.286, pp.377-390, 2000.
- Song WG, Yu YF, Wang BH and Fan WC, Evacuation behaviors at exit in CA model with force essentials: a comparison with social force model, *Physica A*, Vol. 371, pp. 658-66, 2006.
- Journal of Statistical Mechanics-theory and Experiment - J STAT MECH-THEORY EXP*, vol. 10, no. 10, 2004.

14. Weiguo Song, Xuan Xu, Bing-Hong Wang and Shunjiang Ni, Simulation of evacuation processes using a multi-grid model for pedestrian dynamics, *Physica A*, Vol. 363, pp.492–500, 2006.
15. W.G. Weng, L.L. Pan, S.F. Shen and H.Y. Yuan, Small-grid analysis of discrete model for evacuation from a hall, *Physica A*, Vol.374, pp.821–826, 2007

## CONTACT WITH AUTHOR

Miao Chen  
e-mail: chenmiao@hrbeu.edu.cn  
Mobile: 0086-18646010200  
Fax: 0086-0451-82518443

Duanfeng Han  
e-mail: handuanfeng@hrbeu.edu.cn

College of Ship Building  
Harbin Engineering University  
Harbin, Heilongjiang Province  
China

# A SIMULATION MODEL OF SEAWATER VERTICAL TEMPERATURE BY USING BACK-PROPAGATION NEURAL NETWORK

Ning Zhao<sup>1,2)</sup>, M. S.

Zhen Han<sup>1,3)</sup>, Ph. D

<sup>1)</sup> College of Marine Sciences, Shanghai Ocean University, Shanghai 201306  
China

<sup>2)</sup> Interdisciplinary Graduate School of Engineering Sciences, Kyushu University, Kasuga 8168580  
Japan

<sup>3)</sup> Collaborative Innovation Center for Distant-water Fisheries, Shanghai Ocean University, Shanghai  
201306, China

## ABSTRACT

*This study proposed a neural-network-based model to estimate the ocean vertical water temperature from the surface temperature in the northwest Pacific Ocean. The performance of the model and the sources of errors were assessed using the Gridded Argo dataset including 576 stations with 26 vertical levels from surface (0 m)–2,000 m over the period of 2007–2009. The parameter selection, model building, stability of the neural network were also investigated. According to the results, the averaged root mean square error (RMSE) of estimated temperature was 0.7378 °C and the correlation coefficient R was 0.9967. More than 67% of the estimates from the four selected months (January, April, July and October) lay within  $\pm 0.5$  °C. When counting with errors lower than  $\pm 1$  °C, the lowest percentage was 83%.*

**Keywords:** neural network; Argo data; vertical structure; surface temperature

## INTRODUCTION

As development of remote sensing progressed, large amounts of sea surface information could be obtained daily. However, few data were available for the subsurface and deeper ocean. For many reasons, obtaining in-situ data has always posed a difficult problem. Obtaining such data costs exorbitant amounts of time and money. Even over recent years, the problem of lack of in-situ observations of ocean subsurface data is still not solved [1].

Swain et al. (2006) introduced an artificial neural network to estimate the mixed layer depth from surface parameters [2]. Ballabrera-Poy et al. (2009) compared linear and non-linear models of the vertical salinity structure based on temperature observations and proposed that the neural network method performs better than the linear models when the models introduced the surface observations [3]. Comparing with the traditional methods, as Ballabrera-Poy et al. and Swain et al. mentioned [2, 3], the neural network method seems to have a great potential ability in estimating ocean structure.

In accordance to previous studies, this study introduced a back-propagation neural network model to simulate the sea vertical temperature structure. After training with the

historical temperature data, this model could use ocean surface measurements (SST) only as input parameters and estimate the unknown current subsurface temperature structure (the available range of depth depends on the initial field for model building). Following this subsection, data and methods are presented in the section 2; results and discussion are described in section 3; the section 4 is devoted to summary and conclusion, respectively.

## DATA

The main dataset of this paper was obtained from the China Argo Real-time Data Centre (<http://www.argo.org.cn>) covering the region of 20–35°N and 145–180°E in the period 2007-2009. This dataset is a gridded monthly average temperature product with a spatial resolution of 1°×1°. The dataset contains data for 576 stations with 26 vertical levels from surface (0 m)–2,000 m. Each level in every station and every month was picked as one set of data. As a result, 538,632 data sets were generated (the stations at 32°N, 173°E and 35°N, 172°N only had 19 levels from 0–1000 m).

For the model building, two other datasets were used. The original Argo profiles data were obtained from the database of the Global Ocean Data Assimilation Experiment (<http://www.usgodae.org>). The reference series of the weekly maps of absolute dynamic topography (ADT) products were obtained from the website of AVISO and this product contains gridded sea surface heights above geoid [4]. The weekly data were obtained and averaged to match the time resolution of the main dataset in this study.

For the comparison and discussion of results, the reanalysis data obtained from the database of the MyOcean2 project were used [5]. Because of the differences of resolution between the results and the reanalysis data, the weekly data had been averaged by month and processed to match the spatial resolution of estimated data in this paper using the Ordinary Kriging method [6]. Following the former processing, the reanalysis data were also divided in the same way as the Gridded Argo data and a total of 13,238 sets were obtained within each month.

## METHODS

In order to simulate the vertical temperature structure, an initial field of temperature was required. In this research, the data from 2007 were selected as the initial field for building the model, while the rest (data in 2008 and 2009) were used for simulation. During the model building phase, 70% of data in 2007 were used as training data and 30% for testing. According to the complexity of the vertical temperature structure, the model was based on a simplified mapping relationship and built by a back-propagation neural network (BP-NN). In this network, one single hidden layer between the input layer and the output layer was used [7]. As the main aim of this study was to reconstruct the unknown vertical temperature structure from surface parameters which could be directly or easily obtained from remote sensing, some parameters, such as the subsurface heat advection, radiation and surface heat fluxes, should be excluded from the list. Subsequently, eight parameters were selected as candidates including: geographical location (longitude and latitude), sea surface temperature (SST), Depth (D), sea surface height anomalies (SSHA), absolute dynamic topography (ADT) and noisy data (N1 and N2). The noisy data N1 and N2 were random numbers to ensure the result of the method is reliable.

The Mean Impact Value (MIV) method was used in this experiment which could determine the impacts of the each input parameter on output [8, 9]. The degree of impact could be described by the absolute value of the MIV. The experimental model had eight input neurons for the eight parameters including the geo-geographical location, ten hidden neurons and one output neuron. It should be noted that all parameters were normalized to avoid unwanted influences and outliers by using the Standardized Moment. For example, for a set of numbers  $X(x_1, x_2, x_3, \dots, x_n)$ , the basic equation of the standardized moment method could be described as follows:

(1)

where:

$a_r$  is the  $r$ th standardized moment ( $r=1$  in this study)

$\mu_r$  is the  $r$ th moment about the mean

$\sigma$  is the standard deviation

$z_i$  is calculated by:

$$z_i = (x_i - \bar{x}) / \sigma$$

$\bar{x}$  is the mean value of  $X$  and  $a_r$  should be zero.

To reduce the uncertainty of this simple neural network, this model was trained ten times and the absolute values of the result were averaged to show the impact degrees of each parameter. As shown in Tab. 1, the randomly created N1 and N2 played insignificant roles in the model. In addition, it was not surprising that SST and depth showed great impact on the model output. Interestingly, two other parameters (SSHA and ADT) did not have considerable distinct impacts relative to SST and depth. Their MIVs were quite small.

Tab. 1. The averaged MIVs of six parameters after ten times trained.

Parameters	SST	SSHA	Depth	ADT	N1	N2
Average MIV	0.0169	0.0004	0.0885	0.0011	0.0012	0.0013

Concerning the results of the selection experiment, the mapping relation between water temperature and other parameters in this study could be simply shown as follows:

$$F(\text{SST}, \text{D}, \text{Lon}, \text{Lat}) \rightarrow T \quad (2)$$

In this network, the input layer is composed of: 1) four neurons for the four input parameters (SST, depth, longitude and latitude); 2) the hidden layer (layer 1) neurons are set to have a hyperbolic tangent activation function (the numbers of the neurons in hidden layer will be discussed in the later section); 3) the output layer (layer 2) has a single neuron whose activation function is the identity function and its value is equal to water temperature ( $T$ ). Each function has its own set of coefficients (weights  $w$  and biases  $b$ ). The values of each neuron  $i$  in the hidden layer (layer 1) are calculated by:

$$H_i = f_i^1 \left( \sum_{j=1}^4 w_{ij}^1 x_j + b_i^1 \right) \quad (3)$$

$$i=1, 2, 3, \dots, n; j = 1, 2, 3, 4$$

where:

$H_i$  is the value of neuron  $i$  in the hidden layer

$f_i^1$  is the transfer function (hyperbolic tangent sigmoid function)

$x_j$  is the value of input parameter

$j$  is the number of neurons in the input layer

$i$  is the number of neurons in the hidden layer

The value of the neuron in the output layer is calculated by:

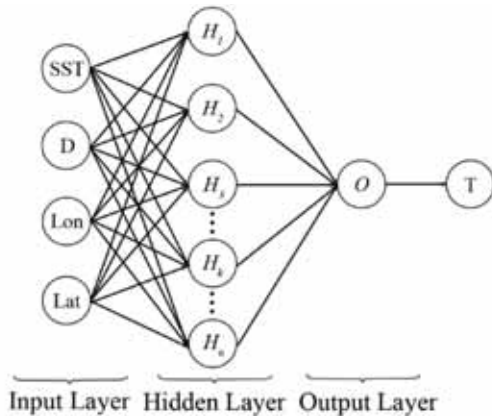
$$O = f\left(\sum_{i=1}^n v_i H_i + b\right) \quad (4)$$

where:

O is the value of the neurons in the output layer (layer 2)  
f is the transfer function (linear function).

All the parameters and transfer functions of this BP-NN are shown in Table 2. In this network, the Levenberg-Marquardt back-propagation algorithm was used for training networks [10].

Fig. 1. Structure of the back-propagation neural network.



The dataset was divided by months and years. The data for 2007 was set for model building and others for estimation (the data for 2008 and 2009). Two test indicators were used to assess the models: the root mean square error (RMSE) and the Pearson's correlation coefficient (R):

$$RMSE = \sqrt{\frac{1}{n} \sum_{i=1}^n (T_{1i} - T_{2i})^2} \quad (5)$$

$$R = \frac{\sum_{i=1}^n (T_{1i} - \bar{T}_{1i})(T_{2i} - \bar{T}_{2i})}{\sqrt{\sum_{i=1}^n (T_{1i} - \bar{T}_{1i})^2 \sum_{i=1}^n (T_{2i} - \bar{T}_{2i})^2}} \quad (6)$$

where:

n is the number of datasets

T<sub>1i</sub> is the estimated temperature

T<sub>2i</sub> is the observed temperature

Before the models were built, the number of neurons in the hidden layer required a solution first by an experimental model. Fig. 2 shows the RMSE and the Pearson's product-moment coefficient (R) of the experimental model within different number of neurons in the hidden layer. It is shown that the model of this experiment had over fitted the training data when using more than fourteen neurons in the hidden layer. In Fig.2b, the same result could be found. For this reason, the neural network of this study was built by using fourteen neurons in the hidden layer.

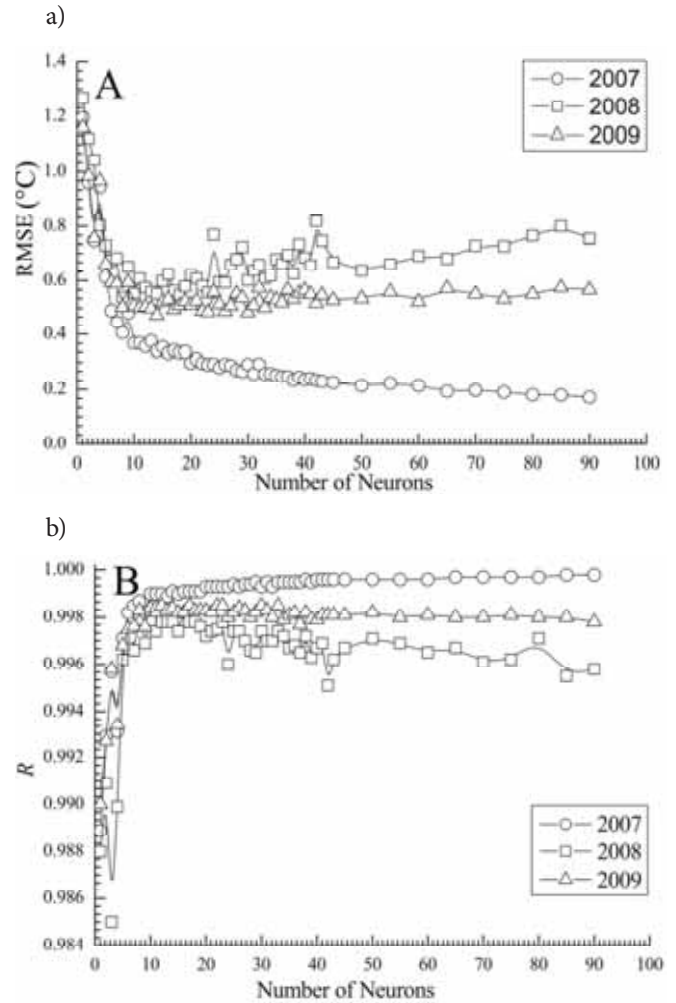


Fig. 2. Comparison of networks with different number of neurons in the hidden layer: (a) RMSE. (b) coefficient (R).

## RESULTS

After the model was built, the data were calculated month by month and year by year. The results are presented in Table 2. Two indicators show that the BP-NN model was fluctuating narrowly on a monthly time scale (RMSE < 1 °C and R > 0.99).

The quantities of errors over the four months were also counted and the results are shown in Tab. 3 (14,962 sets data in each month). During all four months, over 67% of data errors were lower than 0.5 °C. When counting with errors lower than 1°C, the lowest percentage was 83%.

## DISCUSSION AND CONCLUSION

In this study, a simulation model of ocean vertical water temperature was performed by using the back-propagation neural network. After training the model with the historical temperature data, it could use ocean surface measurements (SST) only as input parameters and estimate the unknown current subsurface temperature structure. In this model, there were 538,632 sets of data calculated month by month and year by year. The total RMSE is 0.7378 °C and the correlation

Tab.2. Results of BP-NN.

Month	2007		2008		2009	
	RMSE (°C)	R	RMSE (°C)	R	RMSE (°C)	R
1	0.3693	0.9989	0.5815	0.9976	0.5127	0.9984
2	0.3657	0.9989	0.6167	0.9972	0.5711	0.9975
3	0.3739	0.9989	0.6582	0.9961	0.5612	0.9975
4	0.3752	0.9990	0.8937	0.9952	0.5255	0.9980
5	0.4245	0.9988	0.7847	0.9959	0.7957	0.9963
6	0.5319	0.9983	0.6984	0.9972	0.9404	0.9943
7	0.5580	0.9982	0.8205	0.9962	0.8922	0.9959
8	0.4640	0.9988	0.9324	0.9962	0.8728	0.9960
9	0.4811	0.9987	0.7933	0.9966	0.8380	0.9967
10	0.4695	0.9987	0.6396	0.9977	0.8355	0.9967
11	0.5076	0.9983	0.6045	0.9977	0.9295	0.9950
12	0.5081	0.9982	0.5448	0.9979	0.8633	0.9951
Average	0.4524	0.9986	0.7140	0.9968	0.7615	0.9965

coefficient R is 0.9967. All the results shown this BP-NN model has a good performance.

**SELECTION EXPERIMENT**

During the first part of model building, a selection experiment was made to decide which parameter should be chosen as the input parameter. An interesting aspect of this experiment was that the SSHA and ADT did not show any considerable impact on the output data and the impact was even lower than that of the noisy data N1 and N2. Indeed, as mentioned in many studies concerning the upper ocean, the sea surface height is an important parameter. This parameter could be used to calculate the geo-strophic current or estimate the mixed layer depth [2]. And it could also provide a way to estimate the upper ocean heat content which could greatly influence the temperature profiles [11]. However, in this study, it did not play an important role, contrary to previous studies. One possible explanation is: the neural network was focused on the relationship between the input and the output and reconstructed the whole system via numerical experiments which used the different weights and biases in the equations to

try to rebuild that relation. Obviously, this approach simplified the complex inner processes. And it might also because of that the historical vertical structures had already been input when the model was building.

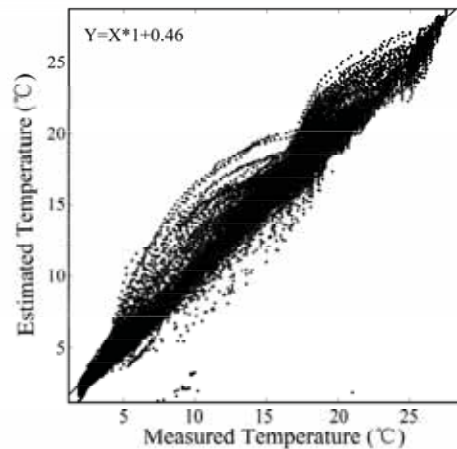


Fig. 3. The model performance when the original Argo profiles data were input.

Tab. 3. Errors over four months during 2008 and 2009.

Error	2008		2009	
	< 0.5 °C	0.5 ~ 1 °C	< 0.5 °C	0.5 ~ 1 °C
Jan	12338(82.46%)	1770(11.83%)	12175(81.37%)	1974(13.19%)
Apr	10074(67.33%)	2449 (16.37%)	12549(83.87%)	1916(12.81%)
Jul	11137(74.44%)	2612(17.45%)	10916(72.95%)	2551(17.05%)
Oct	12422(83.02%)	1901(12.71%)	10628(71.03%)	2365(15.81%)

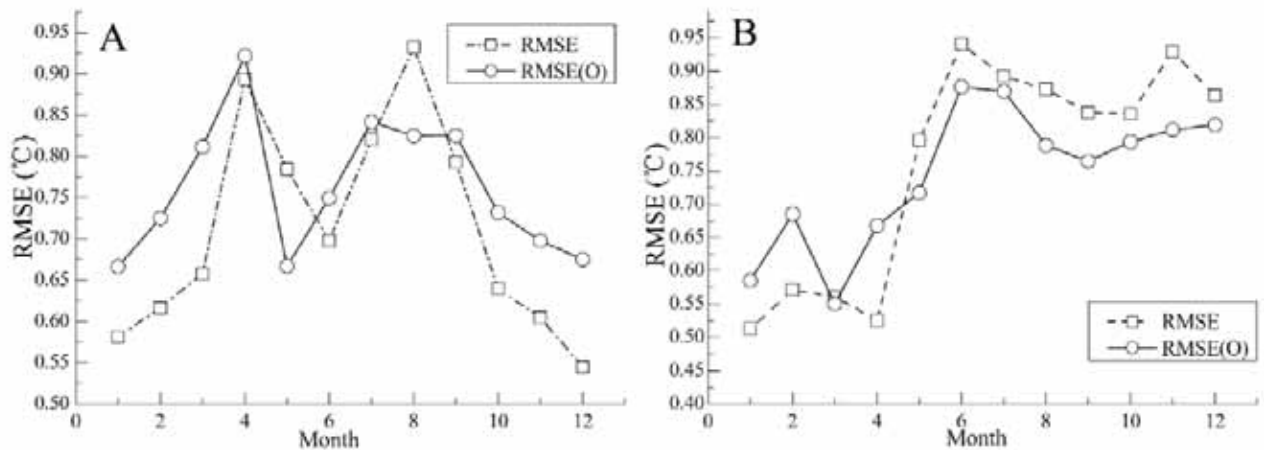


Fig. 4. Model performances and the differences between initial fields and test fields: (a) 2008. (b) 2009

### GRIDDED ARGO PRODUCT AND ORIGINAL PROFILES

It is obvious that the regular dataset had a stabilizing effect on the neuron network. However, the model would have to be assessed for suitability for practical applications. In addition, this is a good opportunity to assess the potentiality of the artificial neural network. Thus, a further experiment was performed to assess the model when using the original Argo profile data. During this experiment, the initial temperature field was still based on the gridded Argo data during 2007. The original Argo profile data during January 2008 was picked for the simulation including 320 profiles within 26,512 sets of data.

The RMSE was 1.2605 °C and the coefficient R was 0.9880. Fig. 3 gives the linear regression of the results in this experiment. The slope was still 1 and the intercept was slightly higher than before (intercept=0.46). These indicated the BP-NN model was still effective.

### INTER-ANNUAL VARIATION AND INITIAL FIELD

In the simulation model, a reliable initial field is obligatory.

During this study, the initial temperature field was based on the gridded dataset (monthly averaged and vertically delimited). Both initial and simulated data were set in the same month but over different years to ensure the external conditions are similar.

But it should be pointed out that the inter-annual variation and its influences on ocean vertical structure were not considered in this model. This could give a great impact on the model performance. To confirm that, the differences between the data in 2007 and data in 2008-2009 are given in Fig. 4 (as the RMSE(O)).

As expected, a high correlation was found between those two lines:  $R=0.7517$  during 2008 and  $R=0.9129$  during 2009. Some studies indicated that it could further ascribe these errors to the deficiency of the initial field [12]. A reliable reason might be seen from the comparison between estimated temperature and reanalysis data. Fig. 5 gives this comparison. This reveals that a major part of the error in this model is due to the differences between the data for model building (initial fields) and model simulation. The solution is to expand the samples in the initial field and adding the temporal parameters into the model.

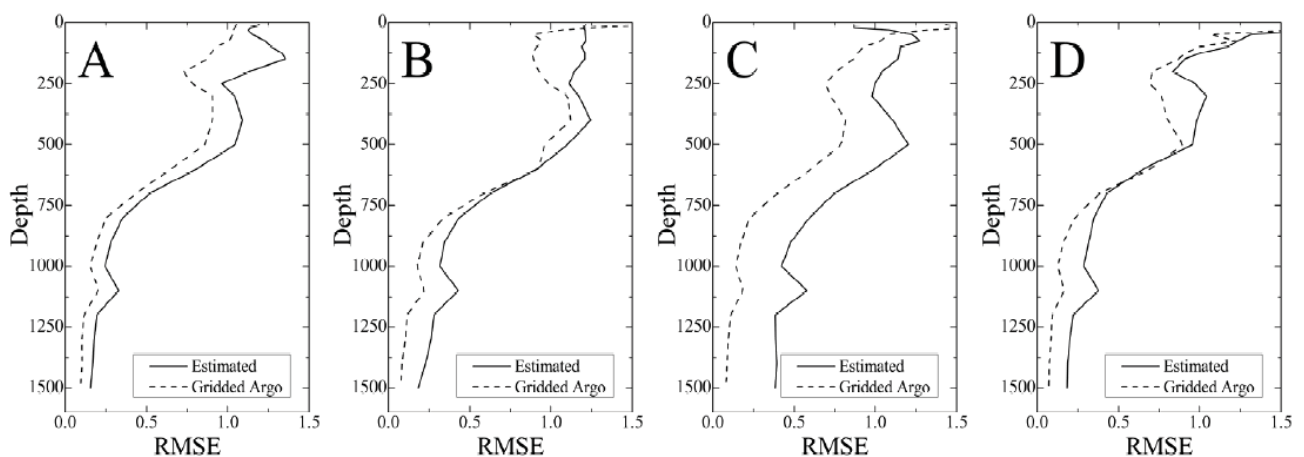


Fig. 5. The relation between RMSE and differences of two kinds of data (Gridded Argo and reanalysis) as a function of depth: (a) January. (b) April. (c) July. (d) October.

## ERRORS WITH DEPTH

The RMSE values over four months as a function of depth is shown in Fig. 6. The lowest error appeared at the surface and the depth over 800 m while some depths between 0–800 m showed higher errors.

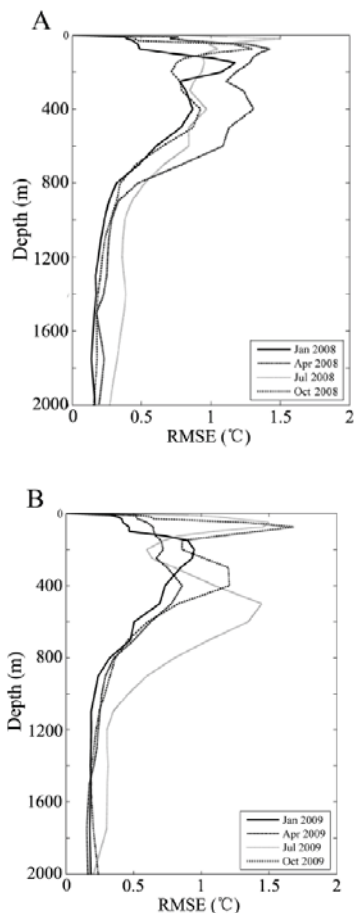


Fig. 6. RMSE of four months as a function of depth: (a) 2008. (b) 2009.

At some depth between 0–800 m, the errors became higher than 1 °C. The first peak values appeared at the surface part and the second appeared at the depth of about 400 m. To reduce these errors, the segment-based model from the study of Chu et al. (2000) might be helpful [13]. For further research, the possible procedure might be described as follows: divide the historical temperature data into several layers based on the vertical parameters (e.g. historical mixed layer depth and thermocline depth) and train the model layer by layer. This could not only reduce the quantity of the samples allowing the model to run faster, but also make the training data more representative.

## ACKNOWLEDGMENTS

We thanked the Argo project, AVISO group and MyOcean2 project for access to their climatological and observation database. This paper was financially supported by the

Foundation of Key Laboratory of Integrated Monitoring and Applied Technology for Marine Harmful Algal Blooms (MATHAB) 201401.

## BIBLIOGRAPHY

1. Nardelli B.B. and Santoleri R.: Methods for the reconstruction of vertical profiles from surface data: Multivariate analyses residual GEM and variable temporal signals in the North Pacific Ocean, *J. Atmos. Ocean. Technol.*, 22 (11), 1762–1781, 2005.
2. Swain D., Ali M.M., Weller R.A.: Estimation of mixed layer depth from surface parameters, *J. Mar. Res.*, 64, 745–758, 2006.
3. Ballabrera-Poy J., Mourre B., Garcia-Ladona E., et al.: Linear and non-linear T-S models for the eastern North Atlantic from Argo data: Role of surface salinity observations, *Deep-Sea Res. I*, 56, 1605–1614, 2009.
4. AVISO: Ssalto/Duacs User handbook: (M)SLA and (M) ADT Near-Real Time and Delayed Time Product. Ref: CLS-DOS-NT-O6-034, 39–41, 2012.
5. Cressie N.: The Origins of Kriging, *Math. Geol.*, 22(3), 239–252, 1990.
6. MyOcean: MyOcean catalogue of products v2.1: the ocean in one click, 2012.
7. Elsken T.: Even on finite test sets smaller nets may perform better, *Neural Netw.*, 10(2), 369–385, 1997.
8. Dombi G.W.; Nandi P.; Saxe J.M., et al.: Prediction of rib fracture injury outcome by an artificial neural network. *J. Trauma*, 39(5), 915–921, 1995.
9. Li Z.D. and Sun W.: A new method of calculate weights of attributes in spectral clustering Algorithms, *IEEE: Int. Conf. Inf. Technol. Comput. Eng. Manag. Sci.*, 8–60, 2011.
10. Hagan M.T., Demuth H.B., Beale M.N.: *Neural Network Design*, PWS Publ. Co. Int. Thomson Publ. Inc., Boston, 1996.
11. Kelly K.A., Thompson L., Vivier F.: Heat content changes in the Pacific Ocean, *Sci.*, 284, 1735, 1999.
12. Hashemi M.R., Ghadampour Z., Neill S.P.: Using and artificial neural network to model seasonal changes in beach profiles, *Ocean Eng.*, 37, 1345–1356, 2010.
13. Chu P.C., Fan C., Liu W.T.: Determination of vertical thermal structure from sea surface temperature, *J. Atmos. Ocean. Technol.*, 17 (7), 971–979, 2000.

## CONTACT WITH THE AUTHORS

Ning Zhao, M. S.  
Zhen Han, Ph.D.

College of Marine  
Sciences, Shanghai  
Ocean University,  
Shanghai 201306  
**CHINA**

e-mail: ningz1120@riam.kyushu-u.ac.jp  
e-mail: zhhan@shou.edu.cn

# DYNAMIC STRENGTH AND ACCUMULATED PLASTIC STRAIN DEVELOPMENT LAWS AND MODELS OF THE REMOLDED RED CLAY UNDER LONG-TERM CYCLIC LOADS: LABORATORY TEST RESULTS

Jian LI, Ph. D.,

Shanxiong CHEN, Ph. D.,

Lingfa JIANG, Ph. D.,

State Key Laboratory of Geomechanics and Geotechnical Engineering

Institute of Rock and Soil Mechanics

Chinese Academy of Sciences

## ABSTRACT

*The dynamic strength and accumulated plastic strain are two important parameters for evaluating the dynamic response of soil. As a special clay, the remolded red clay is often used as the high speed railway subgrade filling, but studies on its dynamic characteristics are few. For a thorough analysis of the suitability of the remolded red clay as the subgrade filling, a series of long-term cyclic load triaxial test under different load histories are carried out. Considering the influence of compactness, confining pressure, consolidation ratio, vibration frequency and dynamic load to the remolded red clay dynamic property, the tests obtain the development curves of the dynamic strength and accumulated plastic strain under different test conditions. Then, through curve fitting method, two different hyperbolic models respectively for the dynamic strength and accumulated plastic strain are built, which can match the test datum well. By applying the dynamic strength model, the critical dynamic strength of the remolded red clay are gained. Meanwhile, for providing basic datum and reference for relevant projects, all key parameters for the dynamic strength and accumulated plastic strain of the remolded red clay are given in the paper.*

**Keywords:** remolded red clay; dynamic property; dynamic strength; accumulated plastic strain

## INTRODUCTION

As a special soil, the red clay is widely distributed in southwest and south central areas of China. Through simple treatment, the remolded red clay is often used as the high speed railway subgrade filler. Therefore, whether the high speed railway subgrade filled with remolded red clay meets the relevant requirements is an urgent research topic.

As the base of the high speed railway, the subgrade is the key for ensuring the high speed railway safety operation. Numerous studies [1,2,3,4] show that on one hand the dynamic load caused by the high speed train run aggravates the vibration of the high speed railway subgrade and directly undermines the dynamic stability of the subgrade, on the other hand under long term dynamic load the subgrade dynamic strength would be cumulatively weakened and the plastic strain would be accumulated, which also influences the subgrade stability gradually. Thus, for the high speed railway engineering, the dynamic characteristics of the subgrade filler are the key to influence the engineering stability. As a result, research on the

development laws and the describing models of the remolded red clay dynamic strength and accumulated plastic strain under long term cyclic loads has an important significance for evaluating the suitability of the remolded red clay as the high speed railway subgrade filler.

Due to the rare studies on the dynamic properties of the remolded red clay which directly influence the stability of the high speed railway subgrade, a series of cyclic dynamic triaxial tests under different load histories and dynamic load have been carried out, which focus on the development laws of the remolded red clay dynamic strength and accumulated plastic strain under different dynamic loads and obtain their description models. The research achievements have a certain academic value and engineering application value.

# DYNAMIC TRIAXIAL TEST OF THE REMODED RED CLAY

## BRIEF INTRODUCTION OF THE DYNAMIC TRIAXIAL APPARATUS

The dynamic triaxial test used the computer-controlled electro-hydraulic servo dynamic triaxial test system SDT-10. The test system can provide a maximal axial dynamic load of 10kN. The triaxial pressure cell can bear a maximal confining pressure of 1 MPa. The precision of the deformation sensor is better than 0.5%. The precision of the tested strain can reach 10<sup>-4</sup>. The sample size is Φ39.1\*80mm. The provided axial and lateral exciting frequency is 0~5Hz. The provided wave can be sine wave, triangular wave, square wave, trapezoidal wave and user-defined wave and the controlling type can be stress-controlled or strain-controlled.

## TEST PROGRAM

The soil sample used in this paper is obtained in the area around the interurban railway from Wuhan to Xianning and is remolded soil, whose physical properties can refer to the front work of the authors [5].

For comprehensive analyzing the developmental and various regulations of the accumulated plastic strain and dynamic strength of the remolded red clay under different long term cyclic loads, the applied dynamic load amplitude remains unchanged. The test procedure is that firstly different load histories were applied on the remolded red clay sample and then different cyclic loads were applied. In the test procedure, the dynamic mechanical properties of the testing soil sample impacted by different load histories were monitored. The tests are stress-controlled.

The tests considered four factors such as compactness, confining pressure, consolidation ratio and vibration frequency. The specific test programs are shown in tab. 1.

Tab. 1 Short-time dynamic triaxial test program

Test ID	Influencing Factors			
	Compactness	Confining Pressure	Consolidation Ratio	Vibration Frequency
DT1-1 DT1-2 DT1-3	0.80 0.85 0.95	50	4.0	1Hz
DT2-1 DT2-2 DT2-3	0.8	25 50 100	3.0/4.0	1Hz
DT3-1 DT3-2 DT3-3	0.8	50	1.0 2.0 3.0	1Hz
DT4-1 DT4-2 DT4-3	0.8	50	3.0	1Hz 2Hz 5Hz

## TEST RESULTS AND ANALYSIS

### DEVELOPMENT AND MODEL FOR THE ACCUMULATED PLASTIC STRAIN

### TEST CURVES OF ACCUMULATED PLASTIC STRAIN

Through dealing with the test datum, several accumulated plastic strain curves under different load histories are obtained as shown in Fig.1~4.

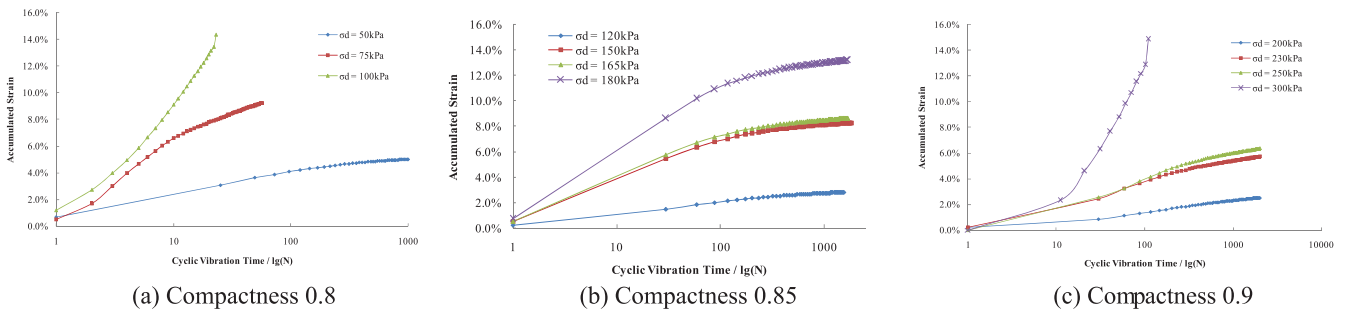


Fig.1 Accumulated strain curves under different compactness ( $k_c=4.0$ ,  $\sigma_3=50kPa$ ,  $f=1Hz$ )

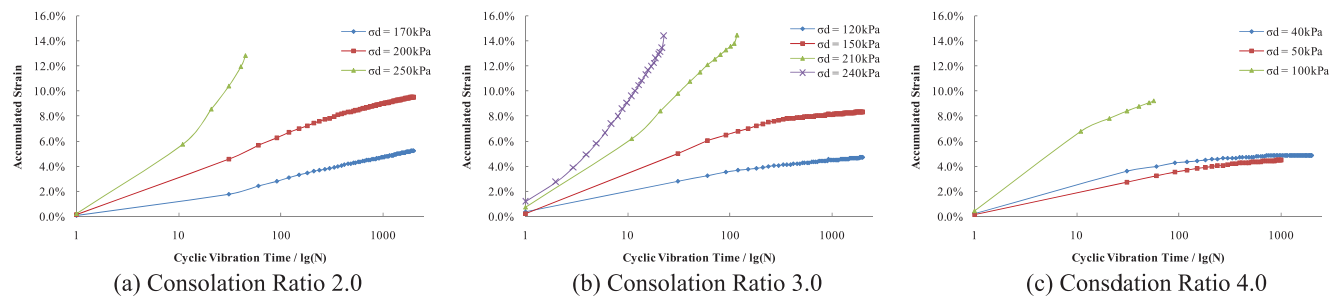


Fig.2 Accumulated strain curves under different consolidation ratio ( $\lambda_c=0.80$ ,  $\sigma_3=50kPa$ ,  $f=1Hz$ )

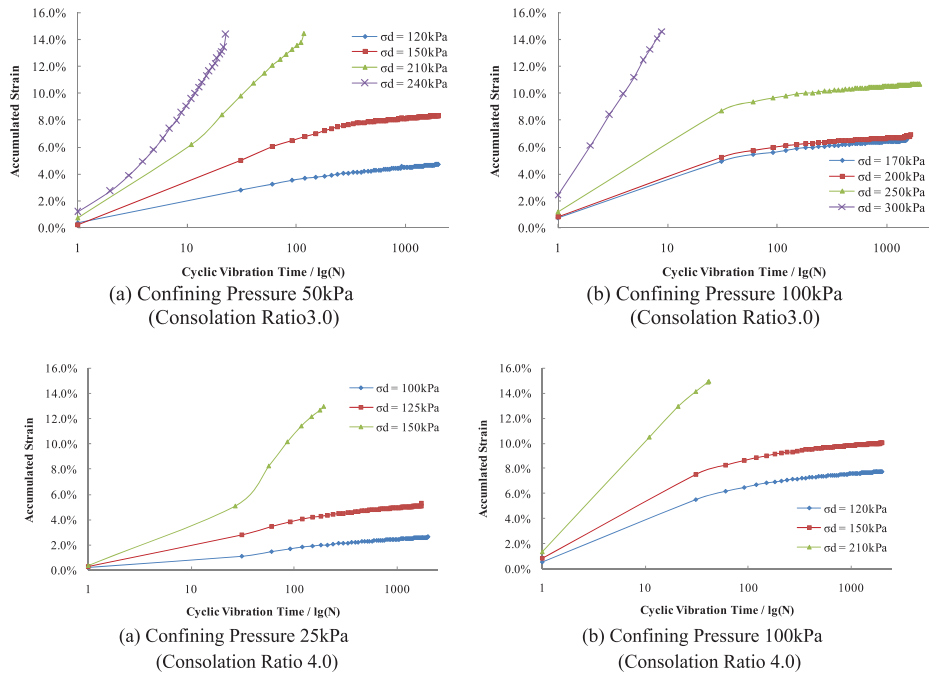


Fig.3 Accumulated strain curves under different confining pressure ( $\lambda_c=0.80, f=1\text{Hz}$ )

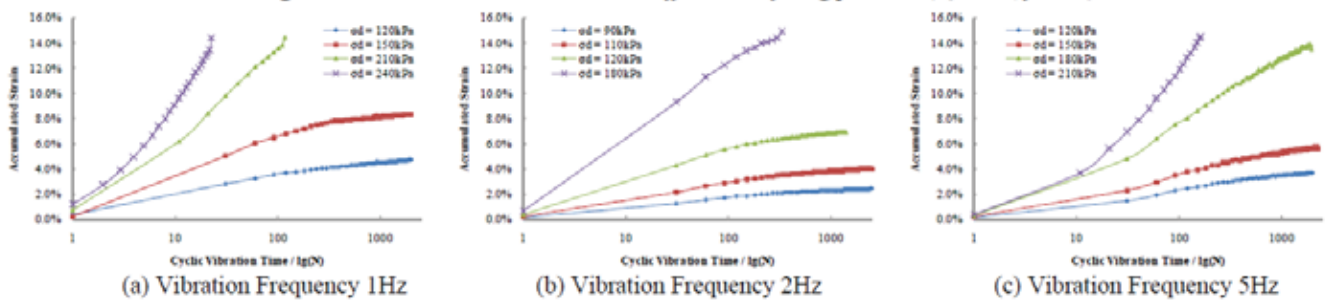


Fig.4 Accumulated strain curves under different vibration frequency ( $\lambda_c=0.80, \sigma_3=50\text{kPa}, kc=3.0$ )

From fig. 1~4, it is known that under relatively small dynamic load, the accumulated plastic strain of the remolded red clay develops rapidly in the initial loading stage and as time goes on, it stabilizes gradually due to the compaction of the soil; under relatively large dynamic load, the accumulated plastic strain develops rapidly yet the same in the initial loading stage, but its developing rate is still large in the later loading stage and even under larger dynamic load, the developing rates in all the loading stages are the same and the soil damage in a short time.

### MODEL ANALYSIS OF THE ACCUMULATED PLASTIC STRAIN

From the developing curves of the accumulated plastic strain of the remolded red clay, it is known that they can be roughly divided into three types: (1) stable type curve; (2) damage type curve; (3) developmental type curve, which are shown in fig. 5.

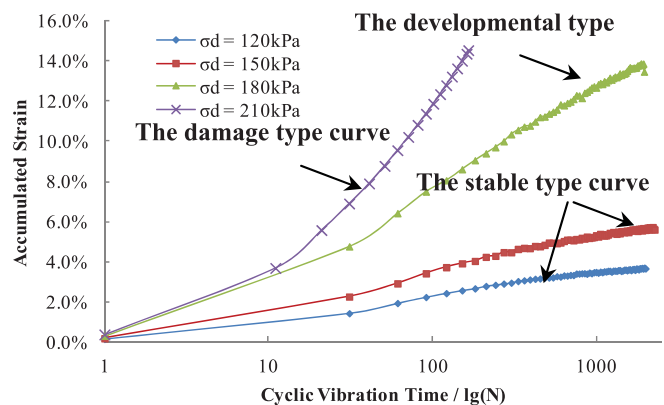


Fig.5 Typical curves of the remolded red clay

As for the describing model of the accumulated plastic strain, there are several proposed models such as the Monismith model [6] and semi-logarithmic model put forward by Stewart and CAI [7,8] etc. But from analysis, it is known that the proposed models mentioned above cannot fit the accumulated plastic strain curve well because they usually aim at a certain type

curve, for example, the models are divergent in the late stage, which cannot reflect the stable type curve. In addition, the fitting effect of these models on the developmental type and damage type curves is also unsatisfactory. As a consequence, a new model is proposed in this research to reflect the development of the remolded red clay accumulated plastic strain.

$$\varepsilon_p = (aN^b) / (1 + cN^b)$$

Where,  $\varepsilon_p$  is accumulated plastic strain; N is vibration time; a, b, c are model parameters.

From eqn. above, it is known that when the vibration time N tends to infinity, the accumulated plastic  $\varepsilon_p$  is equal to a/c, which mean  $\varepsilon_p$  tends to a certain value; the shape of the  $\varepsilon_p$  curve can be reflected by adjusting the parameter b; and the parameter c can reflect the vibration time when  $\varepsilon_p$  tends to a certain value.

## DEVELOPMENT AND MODEL FOR THE DYNAMIC STRENGTH

### TEST CURVES OF THE DYNAMIC STRENGTH

The soil dynamic strength is different due to the loading rate and cyclic impacting effect of the dynamic stress. It is usually understood to be the stress when the strain reaches a certain damage criterion under some impacting vibration times of the dynamic load [9]. Here, the definition of the dynamic strength means that it is changeable under different conditions. In addition, the dynamic strength is closely related to the cyclic vibration time and the damage criteria. Therefore, how to determine the damage strain is important for discussing the soil dynamic stress.

According to vast researches [10,11,12], the criteria of the dynamic strength are usually divided into three categories:

the first criterion is strain; the second criterion is inflection point of the accumulated strain curve; the third criterion is liquefaction. From analysis, it is known that the third criterion is definitely not suitable for clay and the second criterion mainly aims at the saturated soft clay and do not goes for stiff clay. As a consequence, the first criterion is used as the criterion to determine the dynamic strength of stiff clay. For the traffic engineering such as high speed railway, in pursuit of safety and comfort, the subgrade deformation is asked for being less than a certain value in the engineering design and there are requirements for the settlement of the first year, which demand that the dynamic strength criterion must be safe and conservative. Therefore, the criterion for determining dynamic strength in this research is when the accumulated plastic strain reaches 5%.

Fig. 6(a)~6(d) gives the dynamic strength varieties of the remolded red clay under different conditions. It is known that under different test conditions the soil dynamic strength  $\sigma_d$  decreases in a nonlinear rule with the vibration time. Under effect of relatively large dynamic stress, the soil damage rapidly and along with the decrease of the dynamic load, the damage vibration time gradually increases.

In addition, from the figures it is also known that the soil dynamic strength is improved when the compactness, confining pressure of the soil and the vibration frequency of the dynamic stress is enhanced. But the relation between the consolidation ratio and the dynamic strength is adverse to the other influencing factors. On the other hand, different factors have different effect on the soil dynamic strength. For example, the improvement effect of the soil compactness on the soil dynamic strength is especially apparent, but the influencing effects of other factors are relatively weaker. All these regulations describe the influence of the load histories to the dynamic strength of the remolded red clay.

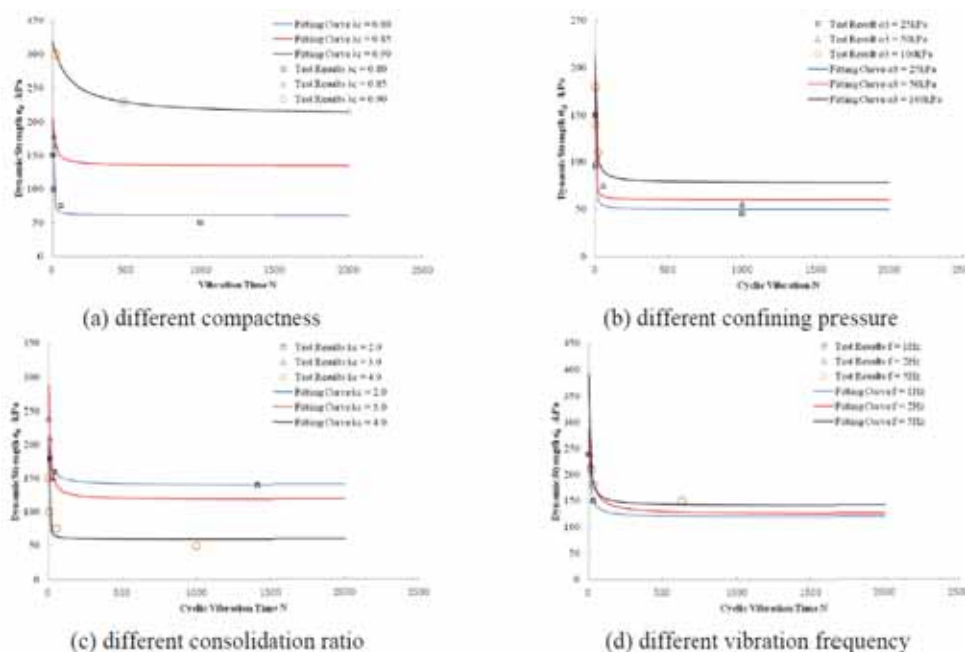


Fig.6 The remolded red clay dynamic strength and the model fitting effects

## THE DYNAMIC STRENGTH VARIETY MODEL AND CRITICAL DYNAMIC STRENGTH

The dynamic strength is an important dynamic parameter of soil under dynamic load to reflect whether the soil damage, therefore, research on variety of the soil dynamic strength has a great significance. In addition, from the analysis above, when the dynamic stress decrease, the vibration time when the soil damage increase and as a consequence, when the dynamic stress is less than a certain value, which is called critical strength  $\sigma_{cr}$  defined by Health[13] and demonstrated by many researcher [9,10,11,12,14,15], the soil cannot damage forever.  $\sigma_{cr}$  can be gained by the dynamic strength model as following:

$$\sigma_d = c \left( 1 - \frac{N}{a + bN} \right)$$

The fitting effects and parameters are shown in Fig.6(a)~6(d). It is known that the fitting effect is well and the square of correlation coefficients reach more than 0.95.

From fig. 6(a)~6(d), it is known that the dynamic strength tends to stable when decreasing to a certain level, which means under this level of the dynamic load, the needed failure vibration time tends to infinity, but the accumulated plastic strain is forever smaller than 5%. This phenomenon demonstrates the existence of the critical dynamic strength  $\sigma_{cr}$  from the point of test yet.

The critical dynamic strength of the remolded red clay under different load histories can be gained and can be calculated by the following equation:

$$\sigma_{cr} = 1003.48\lambda_c - 41.43k_c + 0.33\sigma_3 + 8.996f - 597.6$$

## CONCLUSION

Through a large number of cyclic dynamic triaxial tests under different load histories and dynamic load, the development laws of the remolded red clay dynamic strength and accumulated plastic strain were studied in detail and on this base their description models were obtained. The main conclusions are as follows:

1. Load histories have a great effect on the dynamic properties of the remolded red clay, but different load histories have different influencing laws. By improving the compactness, confining pressure and vibration frequency, the soil ability to resist external load is improved which lead that the accumulated plastic strain development is slowed down and the soil critical dynamic strength is improved, but due to the influence of the nature and state of the soil itself, the effects of compactness and confining pressure are more obvious. On the contrary, the accumulated plastic strain is accelerated to develop and the critical dynamic strength is lowered by improving the consolidation ratio because it causes relatively large partial stress and promotes the development of the local damage in soil.
2. The dynamic strength and accumulated plastic strain

of the remolded red clay can be well described by the models proposed in this paper. The models can reflect the three different test curves at the same time and has a high correlation coefficient with the test datum. At the same time, the empire equation for the critical dynamic strength of the remolded red clay is also given. All these models can provide basic datum and reference for the related engineering.

3. For the high speed railway engineering, in pursuit of safety and comfort, the criterion for determining dynamic strength is suggested to be when the accumulated plastic strain reaches 5%.

## ACKNOWLEDGMENTS

Financial supports from the National Natural Science Foundation of China (Grant Nos. 51027002) and from the Natural Science Foundation of Hubei Province (Grant Nos. 2011CDA124) and the National Science and Technology Support Plan of China (Grant Nos. 2011BAB10B02) are gratefully acknowledged.

## BIBLIOGRAPHY

4. Niki D. Beskou, Dimitrios D. Theodorakopoulos: *Dynamic effects of moving loads on road pavements: A review*, Soil Dynamics and Earthquake Engineering, 2011(31): 547-567.
5. CHEN Shang-yong, SUN Hong-lin: *Experimental Analysis of Long-term Stability of Soaking Subgrade for High Speed Railway*, Journal of Railway Engineering Society, 2012(12): 40-44.
6. ZHOU Yuan-heng, WANG Yong-he, QING Qi-xiang, et al.: *Experimental study of long-term stability of improved granitic residual soil subgrade for high-speed railway*, Rock and Soil Mechanics, 2011, 32(S1): 596-602.
7. LI Jian: *On Dynamic Response of the Red Clay Foundation under High-speed Train Loading*, Wuhan: Institute of Rock and Soil Mechanics, Chinese Academy of Sciences, 2013.
8. LI Jian, CHEN Shanxiong, JIANG Lingfa, et al.: *Experimental study on influence of stress history on dynamic properties of remolded red clay*, Chinese Journal of Geotechnical Engineering. 2014, 36(9): 1657-1665.
9. Monismith C L, Ogawa N, Freeme C R: *Permanent Deformation Characteristics of Subgrade Soils due to Repeated Loading*, Transportation Research Record, 1975(537): 1-17.
10. Stewart H E: *Permanent Strain From Cyclic Variable-Amplitude Loadings*, Journal Geotechnical Engineering, ASCE, 1986,112(6): 646-660.
11. Cai Ying, Cao Xinwen: *Study of the Critical Dynamic*

*Stress and Permanent Strain of the Subgrade-Soil under the Repeated Load*, Journal of Southwest Jiaotong University, 1996, 31(1): 1-5.

12. XIE Dingyi: *Soil Dynamics*, Xi'an: Xi'an Jiaotong University, 1986.
13. Seed H B, Chan C K: *Effect of duration of stress application on soil deformation under repeated loading*, Proceedings 5th international congress on soil mechanics and foundations. 1961, 1: 341-345.
14. Lee K L: *Cyclic Strength of a Sensitive Clay of Estern Canada*, Canadian Geotechnical Journal, 1979,16(1):163-176.
15. ANDERSEN K H, LAURITZSEN R.: *Bearing capacity for foundations with cyclic loads*, Journal of Geotechnical Engineering, ASCE, 1988 (114):540-555.
16. Heath D L, Waters J M, Shenton M J, *et al.*: *Design of conventional rail track foundations*, ICE Proceedings. Thomas Telford, 1972, 51(2): 251-267.
17. ZHOU Jian: *Research on Properties of the Saturated Soft Clay under Cyclic Loads*, Hangzhou: Zhejiang University, 1998.
18. Tang Yiqun, Huang Yu, Ye Weimin, *et al.*: *Critical Dynamic Stress Ratio and Dynamic Strain Analysis of Soils around the Tunnel under Subway Train Loading*, Chinese Journal of Rock Mechanics and Engineering, 2003, 22(9): 1566-1570.

## CONTACT WITH THE AUTHORS

Jian LI, Ph.D.  
Shanxiong CHEN, Ph.D.  
Lingfa JIANG, Ph.D.

State Key Laboratory of Geomechanics and Geotechnical  
Engineering  
Institute of Rock and Soil Mechanics  
Chinese Academy of Sciences  
**CHINA**

e-mail: lij@whrsm.ac.cn  
e-mail: sxchen@whrsm.ac.cn  
e-mail: lfjiang@whrsm.ac.cn

## DESIGN METHOD OF WINCH DRIVEN BY CONTACTLESS MAGNETIC COUPLING UNDER DEEPWATER

B. Zhang<sup>a</sup>

Z. Wang<sup>a</sup>

T. Wang<sup>b</sup>

H.J. Yu<sup>a</sup>

<sup>a</sup>College of Mechanical and Electrical Engineering, Harbin Engineering University, China

<sup>b</sup>School of Mechanical Engineering, Hebei University of Technology, China

<sup>c</sup>College of Mechanical and Electrical Engineering, Jilin University of chemical technology, China

### ABSTRACT

*Through the combination subject of scientific research, the design method of the winch driven by contactless magnetic coupling is researched for the core purpose of the turning shaft sealing in a deepwater environment. This method has six design phases, including domestic and foreign information query and retrieval, graphic analyses of relevant structures, innovative design of 2D assembly sketches, a theoretical computation of structure parameters, the 3D modeling and motion simulation and engineering drawing. This method is of generality, which can provide examples for the post-graduate students and engineering personnel in self-renovation design of scientific research.*

**Keywords:** magnetic coupling, winch, graph analysis, CAD

### INTRODUCTION

The deepwater pipeline's tieback technology belongs to the deepwater oil and gas exploitation technology. We can make good use of the existing facility when the new development oilfield pass through the production pipeline and merge into the established establishedestablishedestablishedestablishedestablishednetwork of pipe lines, so it will make the little boundary oilfield's exploitation around the main oilfield become effective and economic. In order to complete tieback work between the two connecting pipeline under the sea, we need to measure the distance and the pose between the middle of the two pipe flange. People can prefabricate a length of transition pipe which fit the two hard pipe's connection on board [1]. We call this kind of measuring technology as a deep-sea pipeline pose measurement technology. It is not much study in our country. But there are mainly the divers assisted rope measuring system; ROV auxiliary rope measuring system and

acoustic measurement system in foreign companies, so in order to achieve this technology becoming percentage of home-made parts and research on independent innovation, the project has been listed as national "863" key projects in 2006[2,3]. The winch is the key equipment in the drawstring measurement system. But bottleneck problem is the deep rotation axis seal problem. This paper will use magnetic coupling nonmetallic materials to study in dynamic sealing drive scheme.

### METHOD FOR DETERMINING THE WINCH DESIGN SCHEME

It is the most important stage to ensure the design of the scheme in the research of scientific research project. It directly affects the success of the project study. Therefore, it will cost a

longer period of time for the planner to analysis and research.

First of all, put the research project and the solve problem into technological classification. We can only have a definite object in view to formulate solutions under the background of full understanding of the relevant technical institute of technology.

Secondly, this paper summarizes the technique according to the check information at home and abroad. The winch of this measurement system belongs to the hoisting rope drum category, it plays a role as to tighten up or loosen the measuring cable, and the lifting rope drum is used in different depth (1500~15000 m) under the sea. It needs to solve the motor output shaft seal of underwater moving bottleneck problem. So it needs to retrieval the underwater sealing technology.

Finally, we should creative the thinking according to the query data. We can take the progressive layer by layer, interlocking questioning manner analysis. The design scheme of the winch use the motor drive and non metallic magnetic transmission can be fully enclosed motor static sealing, bearing the pressure more than 150MPa, at the same time; the rotation of the motor is transferred to the external drive the reel to rotate by magnetic force [4].

## STRUCTURE DESIGN METHOD OF THE WINCH

For the winch's design, the magnetic transmission for the design is of the core. From the information available to the German Fluid Systems Co., Ltd. (GFS) produced for the coupled magnetic stirrer corrosion, inflammable, explosive environments. The three-dimensional structure model is shown in fig.1. The assembly and the disassembly analysis conducted by the three-dimensional structure model in fig.1. Interpreting the images from right to left side, the flange from the left site and the isolation of the motor (part4) cover the right flange connection of part 1 into a whole through the bolt closed part 7. The output shaft of the motor through the key and the inner magnetic rotor (part2) connection is sealed in the isolation cover (part 1) isolated from the outside world. the outer magnetic rotor (part6) and impeller (part5) connected by a sliding bearing isolation cover (part1) fixed on the left axis, thus, the output shaft of the motor drives the inner rotor (part2) turn to the part3, transferring to the outside through the magnetic coupling magnetic rotor (part6), The external magnetic rotor (part6) drives the stirring wheel (part5) rotating mixing corrosive materials.

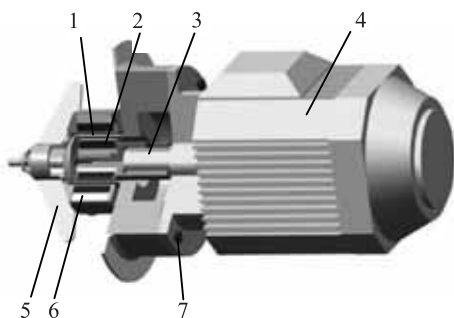


Fig.1 Magnetic coupling blender of a German company

There are two methods the assembly in mechanical drawing, painting respectively from outside to inside and from inside to outside. According to the three-dimensional model of foreign graphic assembly analysis, we can determine the assembly design winch that is taken from inside to outside. So the magnetically-couple's local assembly is the main line. Using graphics software such as CAD, CAXA, and 2D assembly drawing design is shown in fig.2 on the computer.

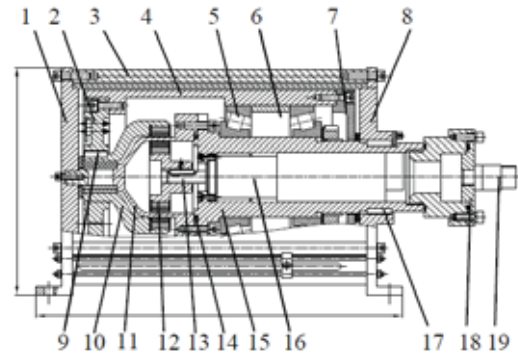


Fig.2 Winch 2D assembly structure

## STRUCTURE PARAMETERS OF THE WINCH

The rope winch as the measurement vector rope measuring system is used in addition to erect its gravity and is also supported from the impact load, water buoyancy. Thus, we select the stainless steel wire rope, specifications: 6X7+IWS round strand, nominal diameter d: 3mm, the minimum breaking force, weight: 6.37kN theory, 3.7kg/100m.

In the measurement of the deepwater, the wire rope needs to pass through the stretching tight, so making a similar cable tension structure. As shown in fig.3, the rope's two points is A, B, height difference is C, span L.

For the analysis of the suspension mechanism theory, it usually must meet the following two conditions: (1) the cable is the ideal flexible, neither compression, not bending. (2) The cable material is in accordance with Hooke's law. The analysis of the wire rope tension of suspension structure can be used in the calculation of single cable theory. For the analysis of the internal force of steel wire rope, we intercept in a very small part as dx, the force analysis of it is as shown in fig.4 the differential unit. Because the steel rope is equivalent to the ideal flexible suspension, so the rope's tension tangent the curve with a differential unit direction of T, taking the horizontal component of H, and the tension's T angle is  $\theta$ , the vertical component is

$$V = Htg\theta = H \frac{dz}{dx}$$

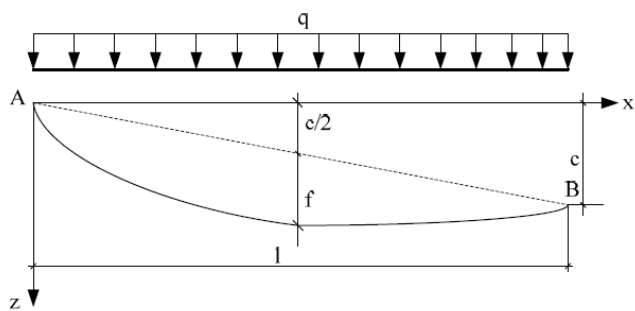


Fig. 3 The gravity loads distributed along the span steel wire

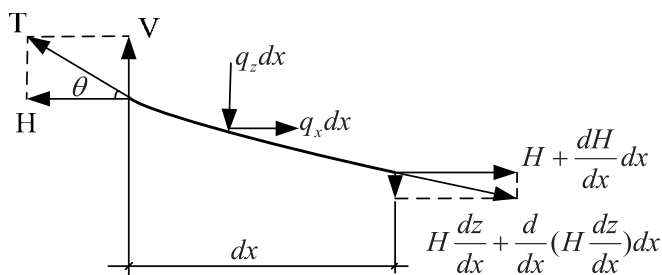


Fig. 4 Force analysis of wire rope differential unit

According to the condition of the static equilibrium differential unit can be listed as follows and be listed as follows the wire rope balance equation.

$$\begin{aligned} \sum X=0, \frac{dH}{dx} dx + q_x dx &= 0 \\ \frac{dH}{dx} + q_x &= 0 \end{aligned} \quad (1)$$

$$\begin{aligned} \sum Z=0, \frac{d}{dx} \left( H \frac{dz}{dx} \right) dx + q_z dx &= 0 \\ \frac{d}{dx} \left( H \frac{dz}{dx} \right) + q_z &= 0 \end{aligned} \quad (2)$$

Due to external force is only considered the gravity load distribution, so  $q_x=0$ , equation (2) can be written as

$$H \frac{d^2 z}{dx^2} + q = 0 \quad (3)$$

After the integral two times, we can get:

$$z = -\frac{q}{2H} x^2 + C_1 x + C_2 \quad (4)$$

By the equation form we know that this is a parabola, we can determine the integration constants  $C_1, C_2$  by further defining boundary conditions. According to fig.3,  $X=0, z=0, x=l, z=c, C_2=0$ . EQ (4) after finishing the parabolic equation is obtained.

$$z = -\frac{q}{2H} x(l-x) + \frac{c}{l} x \quad (5)$$

By the formula (5), when the gravity load of wire rope distributes along the span, the shape of wire rope is a parabola. When the wire rope span and the length of two support points are equal, the shape of the parabolic is determined by the horizontal tension  $H$  and the vertical distributed load  $q$ .

For the same wire rope between A and B, the parabolic equation can be determined as long as the horizontal tension  $H$  of the wire rope is known. Similarly, if the parabolic equation of the wire rope is known, the horizontal tension can be obtained. As shown in fig.3, the sag of the wire rope in the span midpoint is  $f$ . That is:

$$x = \frac{l}{2}, \quad z = \frac{c}{2} + f \quad (6)$$

Put the result into the formula (5), the horizontal tension can be obtained:

$$H = \frac{ql^2}{8f} \quad (7)$$

According to the formula (7), the horizontal tension is proportional  $H$  to the vertical distributed load  $q$  and is inversely proportional to the sag  $f$  which reflects the stretch degree of the wire rope. These are consistent with the actual situation.

When the curve equation of wire rope  $z(x)$  is determined, the tension  $T$  of each point can be obtained by the following formula (8) according to the previous analysis:

$$T = H \sqrt{1 + \left( \frac{dz}{dx} \right)^2} \quad (8)$$

By the formula (5), we can obtain:

$$\frac{dz}{dx} = -\frac{4f}{l} \left( 1 + \frac{c}{4f} - \frac{2x}{l} \right) \quad (9)$$

Therefore, the tension  $T$  of wire rope is

$$T = H \sqrt{1 + \frac{16f^2}{l^2} \left( 1 + \frac{c}{4f} - \frac{2x}{l} \right)^2} \quad (10)$$

According to the formula (10), it is easy to know when the  $x$  is equal to  $l/2$ ; the tension force of wire rope has a maximum value  $T_{max}$ .

$$T_{max} = H \sqrt{1 + \frac{16f^2}{l^2} \left( 1 + \frac{c}{4f} \right)^2} \quad (11)$$

When the sag  $f$  compared with the span  $l$  is a very small value, it is far less than the span  $l$ , so the tension  $T$  is equal to the horizontal tension  $H$ .

Tab. 1 The tension value of wire rope corresponding to different sag

D	F <sub>bmin</sub>	T				
		N				
mm	kN	f=500	f=1000	f=1500	f=2000	f=2500
1.0	1.03	10.40	7.37	6.03	5.23	4.68
1.5	1.99	20.39	14.45	11.81	10.24	9.17
2.0	3.38	34.75	24.62	20.13	17.45	15.63
2.5	5.45	56.18	39.80	32.54	28.22	25.27
3.0	7.28	65.95	46.72	38.20	33.13	29.67

As shown in the Tab.1, it gives the tension value of wire rope corresponding to different sag f. In the Tab.1, D is the outside diameters of wire rope, F<sub>bmin</sub> is the minimum breaking force of wire rope, T is the tension of wire rope.

From these data given in the Tab.1, it can be seen that the tension of wire rope corresponding to different sag is far less than the minimum breaking force of wire rope, which proves the result meets the strength requirement.

By using the tension value T, we can obtain the motor power P of the winding wire rope. The motor power can be determined by the following formula:

$$P=T \times v \quad (12)$$

By the formula (5), we can obtain the required motor power corresponding to different sag for 30 meters wire rope with different diameter, as shown in Tab.2.

Similar to the tension of wire rope, the motor power P of the winding wire rope relates to the outside diameters D of wire rope and the sag f of wire rope. The greater is the diameter, the bigger the sag, and the higher the power.

For example, if d=3mm, f=1500mm, the corresponding motor power P=46.72 w.

Tab.2 the required motor power corresponding to different sag

D	T				
	N				
mm	f=500	f=1000	f=1500	f=2000	f=2500
1.0	10.40	7.37	6.03	5.23	4.68
1.5	20.39	14.45	11.81	10.24	9.17
2.0	34.75	24.62	20.13	17.45	15.63
2.5	56.18	39.80	32.54	28.22	25.27
3.0	65.95	46.72	38.20	33.13	29.67

## WINCH THREE-DIMENSIONAL MODEL AND ITS MOVEMENT SIMULATION

When the structure parameters of the system are determined, the main view of two-dimensional assembly sketches needs to be modified and refined before the design of three-dimensional model. But some designers and graduate students eager to obtain the three-dimensional model and miss this step, which cause the three-dimensional model inaccuracy. The case brings difficulty for analysis of quality characteristics, interference checking and motion simulation, which makes the accuracy of two-dimensional engineering graphics low when the three-dimensional model are converted to two-dimensional engineering graphics. In this case, we have to re-make the engineering graphics and face the situation of heavy workload and inefficiency.

The design process of winch three-dimensional model is as follows: when the structure parameters are determined, we need to determine the details of the main view of assembly sketches in fig.2, and then we can construct the winch three-dimensional model from the two-dimensional assembly sketches by the outside-in approach through three-dimensional design software, such as pro-E, Solid works, Inverter, UG and so on, as shown in fig.5 [5, 6].

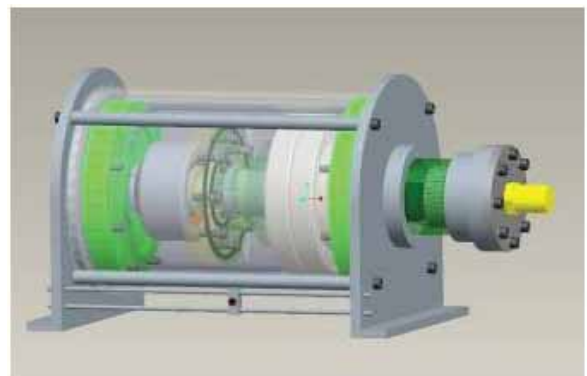


Fig. 5 The winch three-dimensional mode

After the winch three-dimensional model is constructed, we can analyze its quality characteristics, interference checking and motion simulation.

After the winch three-dimensional model is constructed, the winch motion simulation needs to be conducted to check the feasibility of the design. The movements of the winch include the rotations of the motor, the magnetic coupler and the roller. The rotation of roller completes the operation of winding rope.

In the three-dimensional design software, the winch can be carried on the movement simulation by the simulation steps, such as creating the mechanism, defining the elements, the preparation for analysis, model analysis, checking the result and so on. Meanwhile the movement process can form video data and is stored in \*.mpg or \*.avi format. The movement condition can be observed by the media player software and the design can be proved to be feasible by observing the motion simulation. It can also be converted from the three-dimensional model to the design of engineering drawing in

the graphic software [7].

## CONCLUSION

According to the above design method of the winch, we can complete the design of the parts and make the winch prototype. The correctness and feasibility of the design can be verified by the following tests, such as spreading and rolling up the rope, tensile test, under water sealing performance testing and so on. Meanwhile the winch prototype is also prepared to conduct the sea trials in combination with other parts of the machine. As is shown in fig. 6, part 1 is the winch and part 2 is the motor for testing. The project has passed the expert's acceptance.

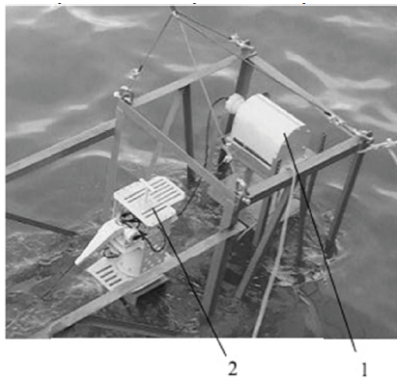


Fig. 6 The sea trials of the winch

## ACKNOWLEDGEMENTS

This paper is funded by NSFC (CONTRACT NAME: Research of Analysis and Experiments of Gripping and Bearing Mechanism for Large-scale Holding and Lifting Tools on Ocean Foundation Piles), (CONTRACT NUMBER: 51479043), the views expressed are authors' alone.'

## BIBLIOGRAPHY

1. Zhou, C.C.: *The technology of marine engineering on underwater connection*, Journal of Beijing Institute of Petro-chemical Technology, Beijing, 2006.
2. Den N.: *System for subsea diverless metrology and hard-pipe connection of pipelines*, United States, New York, 2004.
3. Vincent M.G.: *Method of obtaining acoustic metrology data*. United States, New York, 2006.
4. Cui, C.D.: *Mechanical drawing*, Higher Education Press, Beijing, 2004.
5. Win, J.M.: *Pro/E Windfire3.0 Basis of 3D design and the example of engineering*, Tsinghua University Press, Beijing, 2008.
6. Wan, Q.C.: *Pro/E Windfire3.0 Basis of construction, heat, movement analysis and the typical example*, Publishing House of Electronics Industry, Beijing, 2008.

7. Zhao, Q.L.: *SolidWorks 2006-The application examples of product design*, Tsinghua University Press, Beijing, 2008.

## CONTACT WITH THE AUTHORS

B. Zhang<sup>a</sup>  
Z. Wanga<sup>\*c</sup>  
T. Wang<sup>b</sup>  
H.J. Yu<sup>a</sup>

<sup>a</sup>College of Mechanical and Electrical Engineering,  
Harbin Engineering University

CHINA

<sup>b</sup>School of Mechanical Engineering, Hebei University of  
Technology

CHINA

<sup>c</sup>College of Mechanical and Electrical Engineering, Jilin  
University of chemical technology

CHINA

\*Corresponding author: Nantong Street No.145  
in Nangang District of Harbin

email: jlwzh@163.com

## STRUCTURAL INTERPRETATION OF THE QINGDONG AREA IN BOHAI BAY BASIN FROM SHIPBORNE GRAVITY DATA

Chunguan Zhang<sup>a</sup>

Jingguo Chen<sup>b</sup>

Mingyi Song<sup>c</sup>

Jinkuan Wang<sup>b</sup>

Bingqiang Yuan<sup>a</sup>

<sup>a</sup>School of Earth Science and Engineering, Xi'an Shiyou University, Xi'an 710065, Shaanxi, China

<sup>b</sup>Huabei Department, BGP Inc. of CNPC, Renqiu 062552, Hebei, China

<sup>c</sup>Geological Exploration Institute of Nonferrous Metal Geological Exploration Bureau of Guangdong Province, Guangzhou 510080, Guangdong, China

School of Earth Science and Engineering, Xi'an Shiyou(Petroleum) University, No. 18 East Section, Xi'an Dianzi 2 Road, Xi'an, China

### ABSTRACT

*The Qingdong area, located in Bohai bay basin, was suspected good exploration prospects. In order to study tectonic features and find out favourable petroleum prospects in the area, the gravity data at a scale of 1:50,000 were interpreted. This paper, through data processing and synthetic interpretation of the high-precision gravity data in the area, discusses characteristics of the gravity field and their geological implications, determines the fault system, analyses features of the main strata, divides structure units and predicts favourable petroleum zones. The results showed that the faults controlled the development of the Mesozoic and Cenozoic strata and the distribution of local structures in this area. The study revealed that the Qingtuozi uplift and the Kendong uplift in the north were formed in Mesozoic, and the Qingdong depression in the middle was the rift basin in Mesozoic and Cenozoic. Thicker strata in Mesozoic and Cenozoic developed in the Dongying depression and the Qingdong depression, so there is abundant hydrocarbon in these two depressions, and then the Guangligang rise-in-sag and the Qingdong rise-in-sag developed in the center in these two depressions are also favorable places for prospecting*

**Keywords:** gravity anomaly, seismic profile, rise-in-sag, structure Unit, the Qingdong depression

### INTRODUCTION

In recent years, small and medium basins in the eastern China have been paid more attention for hydrocarbon exploration by geologists. Several pools in the Changling rift of Songliao basin and the Nanpu depression and the Bozhong depression of Bohai bay basin have been explored with potential exploration prospects. Since 1990th, a lot of works have been done in the Qingdong depression by Shengli Oilfield, SinoPec, especially focused on Cenozoic evolution [4,13,15], reservoir conditions and potentiality of hydrocarbon resources [3,12], and then good exploration prospects was suspected in the Qingdong depression. However, affected by

Tancheng-Lujiang fault [2,6], the structures are complicated in this area, and the depression is located in a shallow sea and other factors, more work in details need to be done for properties of basement, structures and sedimentary evolution in the Qingdong depression.

The authors studied the features of gravity anomaly in Qingdong area, quantitatively fitted and comprehensively interpreted two gravitational profiles, discussed the characteristics of basement and sedimentary rules of the Mesozoic and Cenozoic strata. The structural framework was determined, tectonic units were divided and the favorable places for prospecting were discussed in this paper.

## GEOLOGICAL BACKGROUND

The Qingdong area is situated in Bohai bay basin. Like a square in its shape, the study area has a 39 km long southern boundary and a 60 km long eastern boundary. The total area in survey is about 2,430km<sup>2</sup> (Fig. 1). The study area is located in Laizhou bay with sea area in the east and larger slope for the sea floor. There is smaller area in which water depth is less than 2 m and most area ranges in 4-8 m. Within the east edge of this area and the Yellow River estuary, the water depth is more than 10m. Near the Yellow River estuary, there is a unique transition zone characterized with shallow water and thick mud.

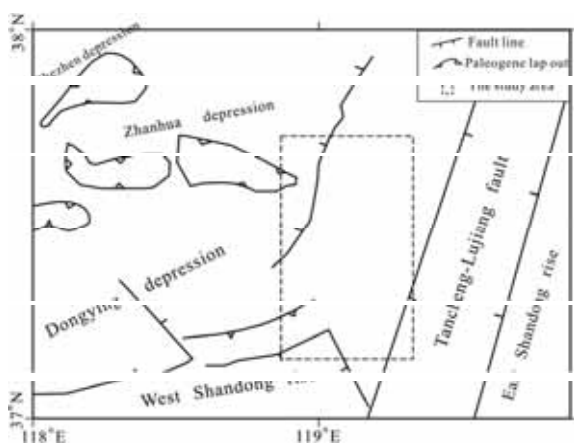


Fig. 1. The regional location of the study area (modified after Li et al. (2008))

Based on well data from Well Qing 1, Well Lai 101, Well Yanggu 1, Well Kendong 3, Well Qingdong 2 and Well Qingdong 4, the stratigraphic pattern includes Taishan group, Cambrian, Ordovician and Carboniferous - Permian, Jurassic - Cretaceous, Paleogene (Kongdian group, Shahejie group and Dongying group), Neogene (Guantao group and Minghuazhen group) and Quaternary (Plain group).

This study area is located in the connection zone of the Jiyang sag and Tancheng-Lujiang fault [2]. It is complex for the distribution of basement and seals that are Taishan group or Cambrian without Paleogene and in which Neogene layers overlain the basement of Mesozoic - Neopaleozoic. The thicker Shanhejie - Kongdian groups develop in the Qingdong depression while Dongying groups and Shahejie groups are in the Zhanhua depression.

The Qingdong depression was deposited fast and stable in Paleogene [2,6]. Shahejie group was found when Well Qingdong 4 was drilled 828m, in which Member 3 and 4 of Shahejie group are the dominant source rocks. Well Qingdong 5 has 3 oil formations in Member 3 of Shahejie group and 4.37t oil could output per day.

## DATA PROCESSING METHOD AND TECHNIQUE

Three methods of sliding trend analysis, regularized filtering and extraction of vertical second derivative were

applied to separate the gravitational anomalies. Through strict comparison for the results obtained from the above methods, those results better fitting the regional geology (especially the sedimentary cover) and seismic data were selected to be the reliable reference maps. The normal methods for detecting boundary of potential field source mainly are directional derivative, vertical derivatives, extreme points or null points of horizontal gradient [8,11]. In this study, for extracting the information of fault structure, the horizontal total gradient of gravitational anomaly has been used in computation. In addition, we applied 2.5-D interactive forward fitting software in processing gravitational data. The software is to simulate the deep geological structure using 2.5-D model and through comparison between the theoretic gravity anomalies generated by the model and the measured anomalies. To modify the geology-mathematics model step by step to fit the actual anomaly for inverting the geometry shape and define the physical properties of geologic bodies at depth.

Densities were measured from the rock samples, and they identically reflect that a sufficient density difference exist between the Pre-Mesozoic basement and the overlying strata. Moreover, the densities show that obvious density difference is still present in between the Tertiary and Mesozoic layers, which means that certain density interfaces exist in the several main sequences overlying the Pre-Mesozoic basement. Thus, there is the geophysical basis for calculating the interface depths using the gravity data.

For the consideration of the regional geology and stratigraphic formations in this area, the arithmetic mean values of the densities from the sample measurement were used in the quantitative fitting calculation of gravity. And the density mean values for different strata are: the Quaternary-Tertiary strata,  $2.19 \times 10^3 \text{ kg/m}^3$ ; the Mesozoic strata,  $2.50 \times 10^3 \text{ kg/m}^3$ ; the Pre-Mesozoic strata,  $2.70 \times 10^3 \text{ kg/m}^3$ .

## FEATURES OF GRAVITY ANOMALIES AND STRUCTURAL INTERPRETATION

### FEATURES AND GEOLOGIC IMPLICATION OF GRAVITY ANOMALIES

The map of Bouguer gravity anomaly of the Qingdong area, with the scale of 1:50,000, shows that the dominant trend of gravity anomaly is NNE trending which shows the main structural direction is NNE trending, and the gravitational field is characterized with clear zoning (Fig. 2). From northwest to southeast, the Bouguer gravity anomaly indicates double "highs" and "lows" (low-high-low-high) in this work area, the gravity low of Yellow River Farm in northwest corner, the gravity high of Qingtuo-Well Qingdongxie 6 in northwest, the gravity low of Guangli-Well Qingdong 2-Well KL20-1-2 in the middle and the gravity high of Yangjiaogou-Well KL20-3-1 Southeast in south. These gravity highs indicate the basement uplift in northwest corner and the center, while these gravity lows indicate the basement sag in northwest and south in this work area.

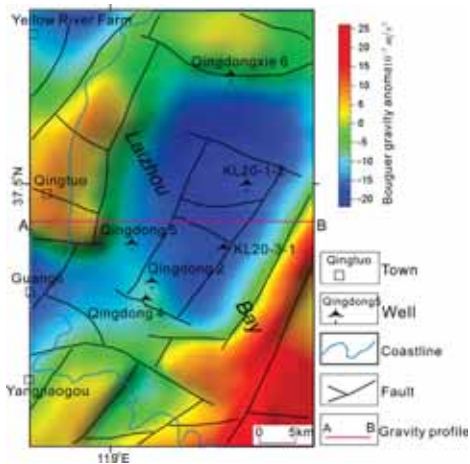


Fig. 2. Bouguer gravity anomaly with the fault distribution

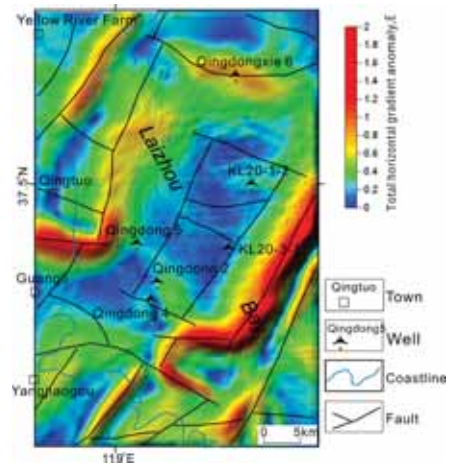


Fig. 4. Fault distribution map with total horizontal gradient anomaly

The gravity low of Well Qingdong 2–KL20-1-2 with NNE trending is the Qingdong depression which has the complete form of Bouguer gravity anomaly. The gradient changes gradually in the middle and largely in the edge. Many gradient zones of gravity anomaly developed in this area, which indicates the complex structure. There are a lot of faults in Qingdong area, and these uplifts contact these depressions by faults.

The regularized filter is applied for calculating the local gravity anomaly, where the wavelength of filter is 15km. The map of local gravity anomaly of the Qingdong area shows that the dominant trend of local gravity anomalies is also NNE trending which is consistent with the trending of Bouguer gravity anomaly that indicates the distribution of local structures is NNE trending in Qingdong area (Fig. 3). There are some gravity highs with different magnitude and ranges in the local gravity anomaly map shows the features of local rise in the middle of these depressions, while these areas show gravity lows in the Bouguer gravity anomaly map, such as the gravity low of Yellow River Farm, Guangli – Well Qingdong 2 and Well Qingdong 2 – KL20-1-2. On the contrary, there are some gravity lows with different magnitude and ranges in the local gravity anomaly map shows the features of local low in these uplifts, while these areas show gravity highs in the Bouguer gravity anomaly map, such as the gravity high of Qingtuo – Well Qingdongxie 6 and Yangjiaogou – Well KL20-3-1 Southeast.

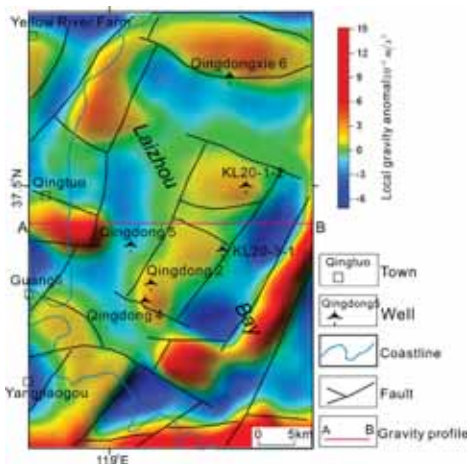


Fig. 3. Local gravity anomaly with the fault distribution

## FAULT STRUCTURE SYSTEM

To determine the fault structure system, we first identified and marked the different linear structure from the maps including the Bouguer gravity anomaly map, the local gravity anomaly, and the horizontal total gradient map (Fig. 4), and then compared them with structures from the regional geology and the inferred faults from certain seismic profiles. On the basis of the above work, the fault structure system in this area has been established.

From Fig. 1 to Fig. 4, it can be seen that the faults are well developed and the structures are complicated in this area. The faults can be divided into NE (NNE)-trending and NWW-trending groups and the former group is dominant and has a strike consistent with the regional fault structure.

As the basement faults control the boundaries of the structure units in the study area, most NE (NNE)-trending faults on a large-scale stretch a long distance and have a large fault throw and deep cut, while the NWW-trending faults, developed in the sedimentary cover, are on a small-scale and cross cut the NE (NNE)-trending faults in most cases. Due to the faulting, the fault blocks are well developed. In general, the framework of the study area is characterized with East-West zoning and South-North blocking. The NE-trending depressions and uplifts were alternatively distributed. This pattern may have been the strike slip motion of the Tancheng-Lujiang Fault. On the one hand, thus, the strike slip motion could have produced the NE (NNE)-trending faults. On the other hand, it probably caused the development of the NWW-trending faults along the weak structure bands. The NE- and NWW-trend faulting acted together and forged the structure framework of East-West zoning and South-North blocking.

## INTERPRETATION OF GRAVITATIONAL PROFILE

In order to study the structural characteristics and determine the distribution of main sedimentary stratum and the contact between tectonic units in Qingdong area, gravity anomaly profiles were used for quantitative interpretation combined

with seismic data and well data. These chosen profiles should be perpendicular to the main tectonics of this work area [1,14]. In this paper, A-B profile were chosen to carry out quantitative interpretation.

The A-B profile passes through the middle of the study area with an EW trending. From west to east, this profile starts at the Qingtuozi uplift, and the western part of the A-B profile coincides with the 1094 offset seismic profile. Across the middle of the Qingdong depression, this profile arrives at the Weibei uplift. The 1094 profile shows that the quality of the seismic data is poor in the deep and better in the superficial part, which indicates obvious fluctuation in the Cenozoic. From west to east, the Bouguer gravity anomaly displays high-low-high features (Fig. 5). In the western part of the A-B profile, the Qingtuozi uplift, the maximum value of Bouguer gravity anomaly displays  $8 \times 10^{-5} \text{ m/s}^2$ . In the middle of the Qingdong depression, the value of Bouguer gravity anomaly decreases to  $-18 \times 10^{-5} \text{ m/s}^2$ , with a decrease of  $26 \times 10^{-5} \text{ m/s}^2$ . In the eastern part of this profile, the Weibei uplift, the value of Bouguer gravity anomaly increases to  $9 \times 10^{-5} \text{ m/s}^2$ . The east-west changes of Bouguer gravity anomaly indicate the features of basement relief in this area.

Combined with seismic data and well data, the A-B profile was quantitatively fitted and comprehensively interpreted, and the results are shown in Fig. 5. The results of quantitative interpretation show that the basement rises up in the western part of the A-B profile, and the basement depth is more than 1,400m in the Qingtuozi uplift while less than 5,500 m in the Qingdong depression. In the Weibei uplift, the basement depth rises rapidly to less than 500 m, with the lifting amplitude of 4,500 m. In the middle of the Qingdong depression, the lifted block developed in Mesozoic.

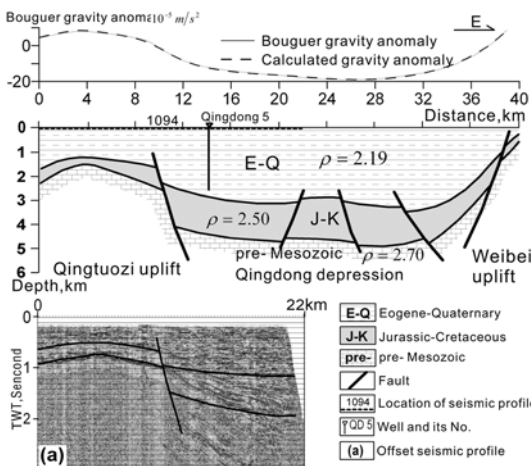


Fig. 5. Map of integrated interpretation on the A-B profile

## TECTONIC FEATURES

Coupling the gravity-seismic-well integrated interpretation and the previous study of regional structural background [5,7,10] with the above study of the gravitational field and the fault system, the Qingdong area can be divided into the following eight tectonic units (Fig. 6): the Zhanhua depression, the Kendong uplift, the Qingtuozi uplift, the Qingdong depression, the Dongying depression, the Guangrao uplift,

the Weibei uplift, and the Laohe depression.

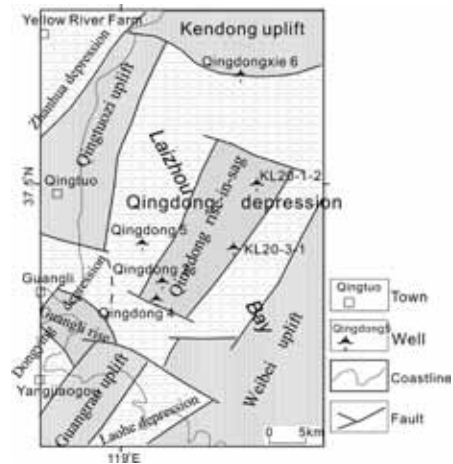


Fig. 6. Map of tectonic units

The Qingdong depression is the main body of the study area and a Mesozoic-Cenozoic depression. Its north, west, southwest and southeast portions contact the Kendong uplift, the Qingtuozi uplift, the Guangrao uplift and the Weibei uplift by faults, respectively. In the Qingdong depression, the Bouguer gravity anomaly displays a NNE trending gravity low with a large area. The gravitational value changes gradually in the middle of the gravity low and gravity gradient zones change largely in its southeast, west and north. These features of the gravitational field indicate that the Qingdong depression is controlled by faults in its southeast edge, west edge and north edge, and a large difference of basement depth between the Qingdong depression and its surrounding uplifts. The depression is basically a Mesozoic and Cenozoic basin with thick Mesozoic and Cenozoic deposit. Because of faulting, the depression can be further divided into some sub-depressions and the Qingdong rise-in-sag. The Qingdong rise-in-sag is located in Well Qingdong 2 – KL20-1-2 area, with a NE trending. Obviously, the Qingdong rise-in-sag is a lifted block, and the conditions of migration and accumulation are better.

The study area relates only to a part of the Fulin sub-depression, which is a negative tectonic unit in the southeast of the Zhanhua depression. The Bouguer gravity anomaly displays an open-to-north gravity low, and there is a gravity gradient zone between the Zhanhua depression and the Qingtuozi uplift and the Kendong uplift, which indicates that the Zhanhua depression contacts these two uplifts by faults in its southeast. The Dongying depression is located in the southwest corner of the Qingdong area and a Mesozoic-Cenozoic rifted basin. The study area relates only to a part of the Qingnan sub-depression and the Guangrao uplift, which are subset tectonic units in the east of the Dongying depression. In the Dongying depression, the Bouguer gravity anomaly displays an open-to-west gravity low. The gravitational value changes largely in the north edge and gradually in the south, indicating that the Dongying depression is faulting in the north and overlapping in the south. The Laohe depression is located in the southwest corner of the study area, retained by the Guangrao uplift and the Weibei uplift. In the Laohe depression, the Bouguer gravity

anomaly displays a complete gravity low and the gravitational value changes largely in the northwest and northeast edge and gradually in the southeast, indicating that the Laohe depression is faulting in the north and overlapping in the south and the basement rises gradually from north to south.

The Kendong uplift is a Mesozoic uplift, located in the northeast of the study area. In the Kendong uplift, the Bouguer gravity anomaly displays an open-to-north gravity high, and gravity gradient zones change largely in its south and west, indicating a large difference of basement depth between the Kendong uplift and these two depressions. Obviously, the Kendong uplift is a lifted block. The Qingtuozi uplift is also a Mesozoic uplift, located in the northwest of the study area. In the Qingtuozi uplift, the Bouguer gravity anomaly displays an open-to-southwest gravity high, and gravity gradient zones change largely in its south, east and northwest, indicating that the Qingtuozi uplift contacts the surrounding units by faults. The Guangrao uplift is located in the southwest corner of the study area and the Bouguer gravity anomaly displays an open-to-southwest gravity high. The gravitational value changes largely in the southeast edge and gradually in the north and northwest, indicating that the Guangrao uplift contacts the surrounding units by faults. The Weibei uplift is located in the southeast of the study area and the Bouguer gravity anomaly displays an open-to-east and open-to-south gravity high with a large area and a NNE trending. The gravitational value changes largely in the northwest edge, indicating that the Weibei uplift contacts the Qingdong depression and the Laohe depression by faults and these faults is the west branch of the Tancheng-Lujiang fault. Because of faulting, the Weibei uplift is also a lifted block.

## CONCLUSIONS

1. The macro-distribution of the faults in Qingdong area is consistent with the areal structure of the study area. These faults constitute the boundaries of these tectonic units and control the development of Mesozoic and Cenozoic stratum, the formation of the lifted blocks and graben blocks and the distribution of local structures.
2. The Qingdong area can be divided into the following eight tectonic units: the Zhanhua depression, the Kendong uplift, the Qingtuozi uplift, the Qingdong depression, the Dongying depression, the Guangrao uplift, the Weibei uplift and the Laohe depression. The Qingtuozi uplift were formed Mesozoic, and the thickness of the Mesozoic and Cenozoic strata is less than 2,000m. The basement depth of the Weibei uplift is less than 1,000m. The Qingdong depression is a Mesozoic and Cenozoic rift and develops thicker Mesozoic and Cenozoic strata and its thickness more than 5,000m.
3. The Guangli rise-in-sag and the Qingdong rise-in-sag are the favorable places for prospecting. Development of thicker Mesozoic and Cenozoic strata, abundant hydrocarbon and rise-in-sags in the Dongying depression and the Qingdong depression, the Guangligang rise-in-sag and the Qingdong rise-in-sag

are also the favorable places for prospecting.

## ACKNOWLEDGEMENTS

This work is supported by the Scientific Research Program Funded by Shaanxi Provincial Education Department (Program No. 14JK1579), China. Thanks should be given to Professor Li Jiuliang for instructions in the study, especially discussions on geological interpretation.

## REFERENCES

4. Bauer C., and Fichler C., *Quaternary lithology and shallow gas from high resolution gravity and seismic data in the central North sea*, Petroleum Geoscience, Vol. 8, pp. 229-236, 2002.
5. Cao Z., *Calculation of extension and subsidence of the Cenozoic pull-apart and rift basins along the Yingkou-Weifang fault zone*, Chinese Journal of Geology, Vol. 43, pp. 65-81, 2008.
6. Carolyn Lampe, Guoqi Song, Liangzi Cong, and Xing Mu, *Fault control on hydrocarbon migration and accumulation in the Tertiary Dongying depression, Bohai Basin, China*, AAPG Bulletin, Vol. 96, pp. 983-1000, 2012.
7. Guo X., He S., Liu K., Song G., Wang X., and Shi Z., *Oil generation as the dominant overpressure mechanism in the Cenozoic Dongying depression, Bohai Bay Basin, China*, AAPG Bulletin, Vol. 94, pp. 1859-1881, 2010.
8. Hao F., Zhou X., Zhu Y., Bao X., and Yang Y., *Charging of the Neogene Penglai 19-3 field*, American Association of Petroleum Geologists, Vol. 93, pp. 155-179, 2009.
9. Li C., Xin R., and Li J., *Controls of Tancheng-Lujiang fault on Paleogene depositional system in Qingdong sag, Xinjiang* Petroleum Geology, Vol. 29, pp. 209-213, 2008.
10. Li J., Tian B., Wang W., Zhao L., and Yao Z., *Lateral variation in the sedimentary structure of west Bohai bay basin inferred from P-Multiple receiver functions*, Seismological Society of America, Vol. 97, pp. 1355-1363, 2007.
11. Li L., *Improved edge detection tools in the interpretation of potential field data*, Exploration Geophysics, Vol. 44, pp. 128-132, 2013.
12. Li L., Zhong D., Yang C., Shi X., and Gong H., *The decollement structures in Jiyang depression, Bohai bay basin, China*, Chinese Journal of Geophysics, Vol. 51, pp. 521-530, 2008.
13. Li X., Liu B., Zhao Y., Liu C., and Wu J., *Late Pleistocene-Holocene submarine active structures in the Bohai Sea*, Acta Oceanologica Sinica, Vol. 32, pp. 52-59, 2010.

14. Ma G., *Edge detection of potential field data using improved local phase filter*, Exploration Geophysics, Vol. 44, pp. 36-41, 2013.
15. Shi P., Fang X., Chen T., Fu Z., and Zhang Z., *Petroleum geologic characteristic and prospecting target in Qingdong sag*, Journal of Southwest Petroleum University (Science & Technology Edition), Vol. 31, pp. 43-48, 2009.
16. Wang S., Zhang X., Fang S., Zhang C., Wang F., Zhao J., Zhang J., Liu B., Pan S., and Huang C., *Crustal structure and its features in the northwest margin of Bohai bay and adjacent areas*, Chinese Journal of Geophysics, Vol. 51, pp. 1451-1458, 2008.
17. Wei Y., and Yang Z.J., *The application of combined gravity and seismic data formation separation for revealing deep structure*, Applied Geophysics, Vol. 3, pp. 255-259, 2006.
18. Yang G., *Structural framework and evolution of Qingdong sag, Bohai bay basin*, Petroleum Geology and Recovery Efficiency, Vol. 18, pp. 7-10, 2011.

## CONTACT WITH THE AUTHORS

Chunguan Zhang<sup>a</sup>  
 Jingguo Chen<sup>b</sup>  
 Mingyi Song<sup>c</sup>  
 Jinkuan Wang<sup>b</sup>  
 Bingqiang Yuan<sup>a</sup>

<sup>a</sup>School of Earth Science and Engineering, Xi'an Shiyou University, Xi'an 710065, Shaanxi

**CHINA**

<sup>b</sup>Huabei Department, BGP Inc. of CNPC, Renqiu 062552, Hebei

**CHINA**

<sup>c</sup>Geological Exploration Institute of Nonferrous Metal Geological Exploration Bureau of Guangdong Province, Guangzhou 510080, Guangdong

**CHINA**

School of Earth Science and Engineering, Xi'an Shiyou(Petroleum) University, No. 18 East Section, Xi'an Dianzi 2 Road, Xi'an

**CHINA**

Postcode: 710065

tel: +86 158 0925 2583, fax: +86 29 8823 4429

e-mail: chunguan-zhang@163.com

# ESTABLISHMENT OF MOTION MODEL FOR WAVE CAPTURE BUOY AND RESEARCH ON HYDRODYNAMIC PERFORMANCE OF FLOATING-TYPE WAVE ENERGY CONVERTER

Hongtao Gao

Biao Li

The College of Marine Engineering, Dalian Maritime University

Dalian, 116026, China

## ABSTRACT

*Floating-type wave energy converter has the advantages of high wave energy conversion efficiency, strong shock resistance ability in rough sea and stable output power. So it is regarded as a promising energy utilization facility. The research on hydrodynamic performance of wave capture buoys is the precondition and key to the wave energy device design and optimization. A simplified motion model of the buoys in the waves is established. Based on linear wave theory, the equations of motion of buoys are derived according to Newton's second law. The factors of wave and buoys structural parameters on wave energy absorption efficiency are discussed in the China's Bohai Sea with short wave period and small wave height. The results show that the main factor which affects the dynamic responses of wave capture buoys is the proximity of the natural frequency of buoys to the wave period. And the incoming wave power takes a backseat role to it at constant wave height. The buoys structural parameters such as length, radius and immersed depth, influence the wave energy absorption efficiency, which play significant factors in device design. The effectiveness of this model is validated by the sea tests with small-sized wave energy devices. The establishment methods of motion model and analysis results are expected to be helpful for designing and manufacturing of floating-type wave energy converter.*

**Keywords:** wave energy, linear wave, floating-type, hydrodynamic, absorption efficiency

## INTRODUCTION

With the development of the economy and society, all the countries face increasing energy demand that lead to rapidly growing greenhouse gas emissions and increased pollution, a large portion of which come from conventional energy production and usage. People now turn their attention to renewable energy resources. Sea wave energy is being increasingly regarded as a major and promising resource [7,1,2] in many countries for its advantages of substantial deposits and high energy quality. Wave energy development and utilization are generally achieved by wave energy converters (WECs). High-efficiency WECs can greatly improve the utilizing ratio of wave energy [11]. Various types of WECs, such as oscillating water column (OWC), oscillating buoy, contraction

channel, floating and duck type, have been developed by some colleges and research organizations in the world [5]. Among them, floating-type wave energy converter generally has the advantages of high wave energy conversion efficiency, strong shock resistance ability in rough sea and stable output power [9,16]. So it is regarded as a promising future energy utilization way. "Pelamis" are the most famous WECs in operation that developed by the Scottish company Pelamis Wave Power (PWP) in UK. The Pelamis P2 has five sections linked by four joints. The sections have a diameter of 4m and a length of 36m. The overall machine length is 180m. It is currently rated at 750 kW depending on the conditions at the chosen wave farm site [14].

In this paper, a multi-section floating-type wave energy converter is chosen as study object (Fig.1). The device is

composed of multi-section cylindrical buoys which are hinged together. Their function is to gather wave energy by converting wave kinetic and potential energy of the irregular reciprocating motion to kinetic energy of wave capture buoys in term of resonance in the waves. Power take-off (PTO) system adopts hydraulic energy conversion system that is installed between two adjacent hinged buoys. Its function is to extract kinetic energy of wave capture buoys and provide input energy of the electric generator. The device is arranged along wave direction and partially submerged in seawater. The basic working process is as follow: (1) the angle between adjacent hinged buoys ongoing changes with buoys mechanical motion in wave; (2) hydraulic cylinder pistons are driven to do reciprocating motion; (3) the high pressure oil that produced from hydraulic cylinders drives the hydraulic motor and then turns the generator that connected to it to produce electricity.



Fig. 1. Schematic diagram of the floating-type wave energy converter (1-1~1-4: wave capture buoys; 1-5~1-7: hydraulic energy conversion systems; 1-8: mooring system)

The design of wave capture buoys has important effects on wave energy conversion efficiency and adaptive capacity in rough sea conditions, which ultimately affect the key indicators of the WECs such as generating efficiency, quality of power supply and viability. This paper established a simplified buoys motion model based on linear wave theory, and then discussed the factors of wave parameters and buoys structural parameters on wave energy absorption efficiency.

## MATHEMATICAL MOTION MODEL OF BUOYS

To simplify the problem, the buoys of the floating-type wave energy converter are comprised of two cylindrical pontoons of equal length and equal diameter that are hinged together by a hydraulic energy conversion device and partially submerged in the seawater with weight evenly distributed. The device is arranged in the seawater of appropriate depth. The analysis is based on simplified cases where wave is treated as linear, regular waves with an incidence angle of 0.

### KINEMATIC DECOMPOSITION OF THE BUOYS MOTION

For the dynamic analyses of the device, we can set a single buoy as the object of study. In the rectangular coordinate system (x, y, z) as shown in Fig.2, the buoys motion can be

disassembled into two independent motions: heaving motion along the z-axis and pitching motion around the centre point *O* of the adjacent buoys. The pitching angle of buoys is small because the retractable length of hydraulic cylinder piston is minute compared with the buoys radius and length in the sea conditions of short wave period and small wave height. The movements of buoys can be thought of as heaving motion approximately.

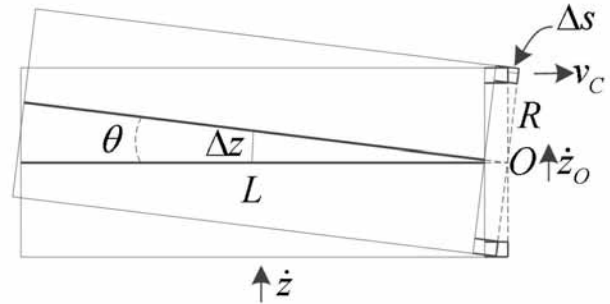


Fig. 2. Schematic diagram of buoy motion decomposition

We assume that the displacement of buoys heaving motion is  $z$  and the speed is  $\dot{z}$ , the speed of centre point along the z-axis is  $\dot{z}_O$ . The displacement and speed of the two hydraulic cylinder pistons are approximately equal respectively. The pitching angle  $\theta$  around the centre point is little.

$$\Delta z = (\dot{z} - \dot{z}_O)\Delta t \approx (L/2) \cdot \sin \theta, \Delta s = v_C \Delta t \approx R \sin \theta \quad (1)$$

Where  $\Delta z$  is the motion displacement of buoys gravity center in the time of  $\Delta t$ ,  $\Delta s$  is the motion displacement of hydraulic cylinder pistons in the time of  $\Delta t$ .

$$(\dot{z} - \dot{z}_O) \cdot t / (L/2) \approx v_C \cdot t / R \quad (2)$$

Where  $v_C$  is the speed of hydraulic cylinder pistons,  $r$  is introduced as the proportionality coefficient of speed:  $r = \dot{z}_O / \dot{z}$ .

$$v_C \approx 2(1-r)R\dot{z}/L \quad (3)$$

### EQUATIONS OF BUOYS MOTION

As shown in Fig.3, according to the force analysis of single buoy, the buoy mainly accepts gravity  $mg$ , buoyancy  $F_f$ , wave force  $F_V$ , hydrostatic restoring force  $F_S$  and hydraulic damping force  $f$ . Among them, gravity and buoyancy are equal and opposite. According to the analysis mentioned above, the motion of the buoys is simplified as heaving motion. Based on the principle of energy equivalence, an equivalent damping force  $F_C$  along z-axis is assumed that it can achieve the same working effect to buoys as that of the hydraulic damping force  $f$ . The buoys make simple harmonic vibration affected by these forces in vertical direction. The equivalent damping force  $F_C$  and wave force  $F_V$  are opposite in direction. The force

analysis is made according to Newton's second law as following.

$$(m + m_w) \cdot \ddot{z} = F_V + F_C + F_S \quad (4)$$

Where  $m$  is the buoy mass,  $m_w$  is the added mass of buoy,  $m_w = \pi\rho R^2 L/2$  [10] (horizontal cylinder),  $\ddot{z}$  is the heaving motion accelerated speed.

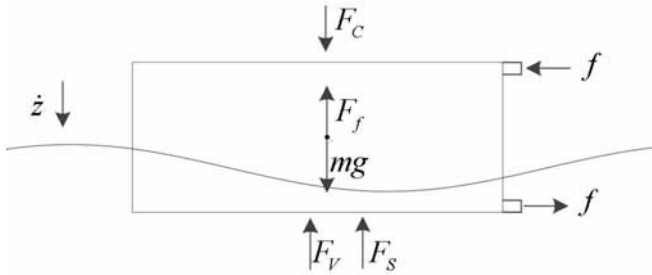


Fig. 3. Schematic diagram of buoy force analysis

The hydraulic cylinders adopt linear damping, based on the equivalent principle mentioned above, the following equation is derived.

$$\int F_C \cdot (\dot{z} - \dot{z}_o) dt = \int -2f \cdot v_c dt, \quad \text{so: } F_C \cdot (\dot{z} - \dot{z}_o) = -2f \cdot v_c \quad (5)$$

by using the equation (3) and (5):

$$F_C = -2f \cdot v_c / (\dot{z} - \dot{z}_o) = -2C \cdot v_c^2 / (1-r) \cdot \dot{z} = -8C(1-r)R^2 \cdot \dot{z} / L^2 \quad (6)$$

Where  $C$  is damping coefficient,  $f = Cv_c$ .

Wave force of buoys in the linear wave can be represented as follow:

$$F_V = F_0 \cos \omega t \quad (7)$$

Where  $F_0$  is amplitude of wave force that can be solved by the methods of theoretical analysis or numerical simulation,  $\omega$  is wave circular frequency.

The hydrostatic restoring force  $F_S$  of buoys in the waves can be calculated by the following formula [12]:

$$F_S = -\rho g A_{WP} z \quad (8)$$

Where  $\rho$  is the seawater density,  $A_{WP}$  is the wetted surface of buoy,  $A_{WP} = 2L\sqrt{2dR - d^2}$  (horizontal cylinder).  $d$  is the immersed depth of buoy.

Take formula (6), (7) and (8) into formula (4), the equations of motion of buoys are derived.

$$(m + m_w) \cdot \ddot{z} + 8C(1-r)R^2 \cdot \dot{z} / L^2 + \rho g A_{WP} z = F_0 \cos \omega t \quad (9)$$

## WAVE ENERGY CONVERSION EFFICIENCY OF THE WECS

Wave energy conversion efficiency of WECs can be expressed as wave energy absorption efficiency [13]. This paper uses  $\eta_1$  and  $\eta_2$  to represent the wave energy absorption efficiency of buoys and hydraulic system respectively.

$$\eta_1 = \bar{P}_F / P_{SEA}, \quad \eta_2 = \bar{P}_C / P_{SEA} \quad (10)$$

Where  $\bar{P}_F$  is the average wave energy absorption power of buoys,  $\bar{P}_C$  is the average wave energy absorption power of hydraulic system,  $P_{SEA}$  is the input power of wave [6].

$$P_{SEA} = \rho g^2 H^2 T \cdot B / 32\pi \quad (11)$$

Where  $B$  is the immersed width of buoys,  $H$  is wave height,  $T$  is wave period.

$$\bar{P}_F = \frac{1}{T} \int_0^T P_F dt = \frac{1}{T} \int_0^T F_V \cdot \dot{z} dt \quad (12)$$

Where  $P_F$  is the wave energy absorption power of buoys.

$$\bar{P}_C = \frac{1}{T} \int_0^T f v_c dt = \frac{1}{T} \int_0^T C v_c \cdot v_c dt = \frac{C}{T} \int_0^T \left[ \frac{2(1-r)R\dot{z}}{L} \right]^2 dt \quad (13)$$

## RESULT AND ANALYSIS

Wave energy absorption efficiency of the device is computed and analyzed using the above motion model of wave capture buoys. The wave parameters are from the China's Bohai Sea with short wave period and small wave height [15].

### ANALYSIS ON INFLUENCE OF WAVE PARAMETERS ON WAVE ENERGY ABSORPTION EFFICIENCY

1. Variation of wave energy absorption efficiency with wave period

The effects of the wave period on the wave energy absorption efficiency of buoys and hydraulic system are analyzed in the case that the length of buoy is 8.0m, radius is 1.0m and the damping coefficient of hydraulic system is  $5.0 \times 10^4 \text{ N}\cdot\text{s/m}$ , it's result shown in Fig.4.

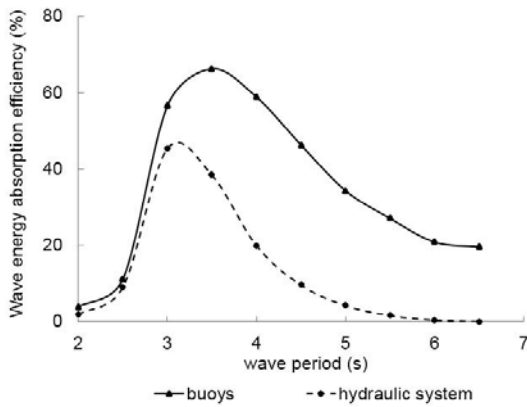


Fig. 4. Variation of wave energy absorption efficiency with wave period

Wave energy absorption efficiency of buoys and hydraulic system attain their maximum that are 65% and 45% respectively when the wave period is in the range of 3.0 s to 3.5 s. Outside this range, both of them quickly drop. The natural frequency of the buoys is also in the range. When the wave period is 2.5 s, their efficiencies can reduce to less than 10%. When the wave period exceeds 6.0 s, the wave energy absorption efficiency of hydraulic system is already close to 0 although the buoys' still remains at the levels of 20%. The calculation result verified that the main factor which affects the dynamic responses of wave capture buoys is the proximity of the natural frequency of buoys to the wave period [3, 4]. This is the primary factor for design of the WECs.

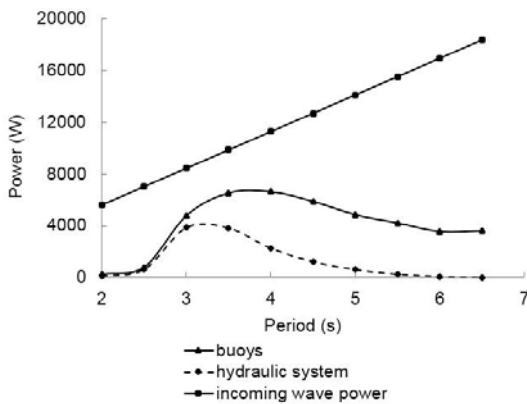


Fig. 5. Variation of absorbing power of device and incoming wave power with wave period

Fig.5 shows the variation of absorbing power of device and incoming wave power with wave period. We can see that the incoming wave power increases with wave period. Wave energy absorbing power of buoys and hydraulic system attain the maximum when the wave period is 3.7 s and 3.2 s respectively, and then start to decrease. Therefore, incoming wave power is a minor factor which affects the dynamic responses of wave capture buoys at constant wave height.

(2) Variation of wave energy absorption efficiency with wave height

Fig.6 shows the variation of absorbing power of device with wave height.

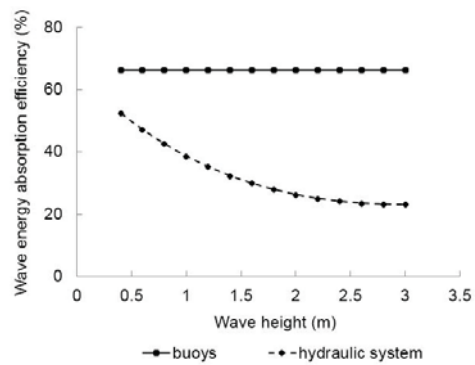


Fig. 6. Variation of wave energy absorption efficiency with wave height

For a floating-type WEC with permanent structures, no matter how the wave height changes, the wave energy absorption efficiency of buoys usually keeps unchanged, but the wave energy absorption efficiency of hydraulic system will decrease gradually. Therefore, smaller wave height can help to promote the wave energy absorption efficiency of hydraulic system. But enough force of hydraulic cylinder piston cannot be produced possibly that the system operating time reduces. This would finally cause insufficient of output power. Instead, if the wave height is too high, the force of hydraulic cylinder piston would exceed the allowable maximum working pressure that will cause the system to break. Therefore, an important consideration for hydraulic system design is the wave height in the site sea.

#### ANALYSIS ON INFLUENCE OF BUOYS STRUCTURAL PARAMETERS ON WAVE ENERGY ABSORPTION EFFICIENCY

The buoys structural parameters mainly include the length, radius and immersed depth. Next up are selecting the sea conditions that the wave height is 1.2 m and period is 3.5 s.

1. Variation of wave energy absorption efficiency with length of buoy

Fig.7 shows the variation of wave energy absorption efficiency with length of buoy. Both wave energy absorption efficiency of buoys and hydraulic system attain their maximum when the length is in the range of 7.0m to 8.0m. The main influence factors include the wave force, buoys mass, added mass and immersed area.

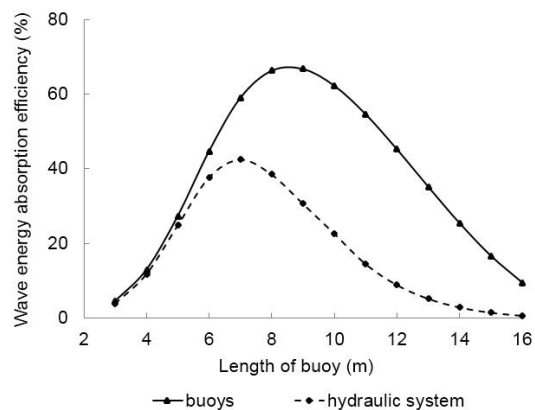


Fig. 7. Variation of wave energy absorption efficiency with length of buoy

2. Variation of wave energy absorption efficiency with radius of buoy

As shown in Fig. 8, both wave energy absorption efficiency of buoys and hydraulic system attain their maximum when its radius is about 1.8 m. Wave energy absorption efficiency of buoys tops out at 98% and resonance can be thought to occur.

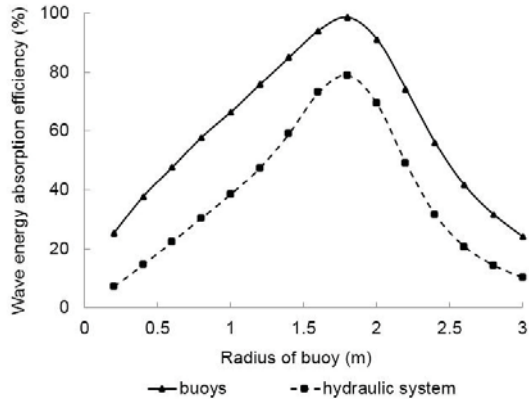


Fig. 8. Variation of wave energy absorption efficiency with radius of buoy

3. Variation of wave energy absorption efficiency with immersed depth of buoy

Fig.9 shows the variation of wave energy absorption efficiency with immersed depth of buoys when the length is about 8.0 m and the radius is 1.0 m. Both wave energy absorption efficiency of buoys and hydraulic system attain their maximum at the immersed depth of about 1.5 m, then starts to decline sharply. Their efficiencies fall below 10% with the immersed depth exceeding 1.8 m. The immersed depth depends on the buoys mass that changes the action area of wave force. Within certain realms of immersed depth of buoy, both wave force and mass inertia tend to continuously increase until the maximum number is attained. The main reason is that the growth rate of wave force exceeds the growth rate of mass inertia at the initial stages. After that, the immersed area of buoy decrease rapidly leading to reduce of wave force. And then the efficiency would be falling more quickly under the joint action of decrease of wave force and increase of mass inertia.

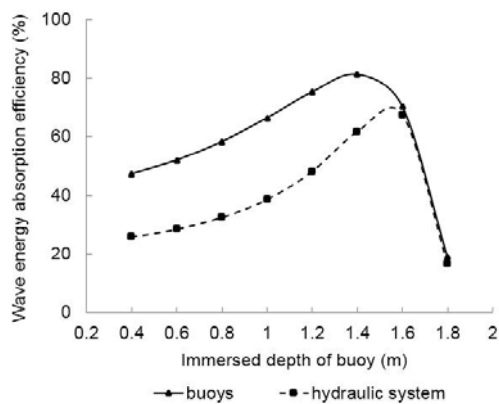


Fig. 9. Variation of wave energy absorption efficiency with immersed depth of buoy

## MODEL VALIDATION

Research team of Professor Gao Hongtao, Dalian Maritime University in China, has carried out several sea tests with small-sized floating wave energy devices in Dalian sea area in 2012 and 2013. The wave capture buoys of testing apparatus are made up of several cylindrical buoys that can hinge together freely. The radius of power buoys is 0.5 m and the wave height is in the range of 0.4 m to 0.6 m. The device length is determined by changing the number of buoys combinations and the buoys immersed depth are adjusted by changing the self weight of device. Fig.10 is the generation power distribution diagram which the length is 4.0 m. The test results showed that the average output power is about 40W in the sea tests of 2013, and the maximum output power can achieve 100W when the instant wave height is about 1.0 m. In the sea tests of 2012, the average output power is about 20W that the test wave height measured is 0.5m when the length of buoy is 2.5 m. The energy conversion efficiency of the hydraulic system is about 15% in the on-land-experiment [8]. As shown in Fig.11 which are average generation output powers according to the model, the calculation values of the model basically agrees well with sea tests results. So we can get the conclusion that the model that we established in this paper is effective and available.

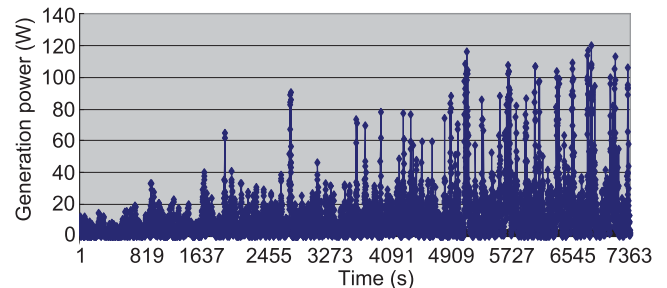


Fig. 10. Generation power distribution in 2013

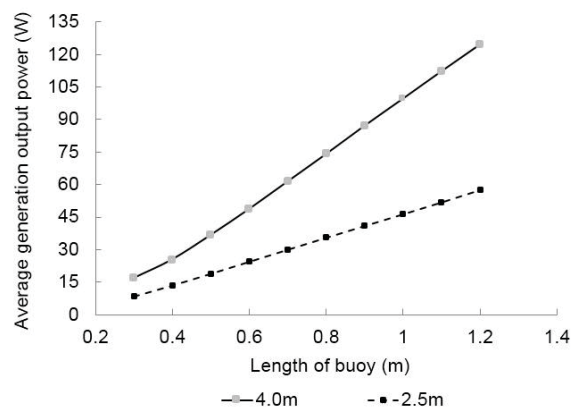


Fig. 11. Variation of average generation output power with wave height when the length of buoy is 4.0m and 2.5m

## CONCLUSIONS

This paper takes the floating-type wave energy converter as research object. Based on linear wave theory, the equations of motion of buoys are derived according to Newton's second law and the factors of wave parameters and buoys structural parameters on wave energy absorption efficiency are discussed.

The main conclusions are as follows:

1. For a floating-type wave energy converter whose structure size and hydraulic damping are determined, the main factor which affects the dynamic responses of wave capture buoys is the proximity of the natural frequency of buoys to the wave period. And the incoming wave power takes a backseat role to it at constant wave height.
2. Buoys structural parameters such as length, radius and immersed depth can impact the wave energy absorption capacity under the condition of the constant wave parameters. There is always a maximum in absorption efficiency.

The effectiveness of this model was validated by comparing this model calculation results with the sea test data from small-sized wave energy devices. The results showed that the two results are approximately identical.

## ACKNOWLEDGEMENTS

The authors extend their thanks to the financial support by the Maritime Safety Administration of the People's Republic of China Foundation (No.2012\_26). Special thanks are given to Liaoning Maritime Safety Administration of the People's Republic of China for the help to make the project go through.

## REFERENCES

3. Behrens S., Hayward J., Hemer M., etc, *Assessing the wave energy converter potential for Australian coastal regions*, *Renewable Energy*, Vol. 43, pp. 210-217, 2012.
4. Boyle G., *Renewable Energy*, Oxford: Oxford University Press, pp. 298-337, 2004.
5. Budal K., Falnes J., *A resonant point absorber of ocean-wave power*, *Nature*, Vol. 256, pp. 478-479, 1975.
6. Budal K., Falnes J., *Power generation from ocean waves using a resonant oscillating system*, *Marine Science Communication*, Vol. 1, pp. 269-288, 1975.
7. Clément, Alain, McCullen, Pat, Falcão, António, etc., *Wave energy in Europe: current status and perspectives*, *Renewable and Sustainable Energy Reviews*, Vol. 6, pp. 405-431, 2002.
8. Entec UK Ltd., *Marine Energy Glossary*, London: Carbon Trust, 2005.
9. Falcão, António F. de O., *Wave energy utilization: A review*

*of the technologies*, *Renewable and Sustainable Energy Reviews*, Vol. 14, no. 3, pp. 899-918, 2010.

10. Gao H. T., Guan S. F., Zhou D. L., *Experimental test on a kind of floating-type wave energy converter*, *ACTA ENERGIAE SOLARIS SINICA*, Vol. 34, no. 1, pp. 177-180, 2013.
11. Gong Y., *Development trend of wave power generation technology in the world*, *POWER DSM*, Vol. 10, no. 6, pp. 71-72, 2008.
12. Michael E., McCormick, *A modified linear Analysis of a Wave-Energy Conversion Buoy*, *Ocean Engineering*, Vol. 3, no. 3, pp. 133-144, 1976.
13. Ruellan M., Ben Ahmed H., Multon B., etc., *Design Methodology for a SEAREV Wave Energy Converter*, *IEEE TRANSACTIONS ON ENERGY CONVERSION*, Vol. 25, no. 3, pp. 760-767, 2010.
14. Sun Z. F., *Research of oscillating buoy wave energy device*, Shanghai: Shanghai University, pp. 31, 2007.
15. Wang X. N., Li X. L., Wang J., etc., *Study on the Assessment of Performance of the Wave Energy Conversion Systems*, *OCEAN TECHNOLOGY*, Vol. 31, no. 4, pp. 75-78, 2012.
16. Yemm R., Pizer D., Retzler C., etc., *Pelamis: experience from concept to connection*, *PHILOSOPHICAL TRANSACTIONS R. Soc. A*, pp. 365-380, 2012.
17. Yin W. Y., Zhang Y. N., *Statistical analysis of wind and features at Bohai straits*, *Journal of Dalian Maritime University*, Vol. 32, no. 4, pp. 84-88, 2006.
18. Zhang L. Z., Yang X. S., Wang S. M., etc., *Research Status and Developing Prospect of Ocean Wave Power Generation Device*, *Hubei Agricultural Sciences*, Vol. 50, no. 1, pp. 161-164, 2011.

## CONTACT WITH THE AUTHOR

Hongtao Gao  
Biao Li

The College of Marine Engineering  
Dalian Maritime University  
Dalian, 116026  
Tel./fax: +86-411-8472-3126  
e-mail: gaohongtao@dlmu.edu.cn

CHINA

## CHARACTERISTIC STUDIES OF MICRON ZINC PARTICLE HYDROLYSIS IN A FIXED BED REACTOR

Ming Lv, Ph. D.

Haiqiang Liu, Ph. D.

Xin Nie, Ph. D.

School of Mechanical Engineering, Hangzhou Dianzi University, Hangzhou

Muhammad Aqeel Ashraf, Ph.D.

Department of Geology, Faculty of Science, University of Malaya 50603 Kuala Lumpur, Malaysia

Faculty of Science & Natural Resources, Universiti Malaysia Sabah, 88400 Kota Kinabalu, Sabah,  
Malaysia

### ABSTRACT

*Zinc fuel is considered as a kind of promising energy sources for marine propeller. As one of the key steps for zinc marine energy power system, zinc hydrolysis process had been studied experimentally in a fixed bed reactor. In this study, we focus on the characteristics of micron zinc particle hydrolysis. The experimental results suggested that the steam inner diffusion is the controlling step of accumulative zinc particles hydrolysis reaction at a relative lower temperature and a relative higher water partial pressure. In other conditions, the chemical reaction kinetics was the controlling step. And two kinds of chemical reaction kinetics appeared in experiments: the surface reaction and the gas-gas reaction. The latter one occurs usually for larger zinc particles and high reaction temperature. Temperature seems to be one of the most important parameters for the dividing of different reaction mechanisms. Several parameters of the hydrolysis process including heating rate, water partial pressure, the particle size and temperature were also studied in this paper. Results show that the initial reaction temperature of zinc hydrolysis in fixed bed is about 410 oC. And the initial reaction temperature increases as the heating rate increases and as the water partial pressure decreases. The total hydrogen yield increases as the heating rate decreases, as the water partial pressure increases, as the zinc particle size decreases, and as the reaction temperature increases. A hydrogen yield of more than 81.5% was obtained in the fixed bed experiments.*

**Keywords:** Hydrogen; Zinc Hydrolysis; Thermal Chemistry; Fixed bed

### INTRODUCTION

Metal fuel is considered as a kind of promising energy sources for marine propeller, especially for military application [1]. Compared to conventional gaseous and liquid fuel, metal fuel usually has very high volumetric energy densities. And the marine energy power system based on the metal fuel can use ocean water as part of propellant oxidizing agent directly, which can save a great part of space and weight for fuel carrier underwater.

Zinc is considered as a kind of promising candidate of metal fuel for marine energy power system. It has been widely studied for power generation via the two-step thermochemical cycle based on Zn/ZnO redox pair for its brilliant hydrolysis ability [2,3,4]. The Schematic diagram of the marine energy power system based on zinc fuel is shown in Fig.1. Firstly ocean water

is introduced into the first combustion room, where the zinc powder fuel hydrolysis with the water and the hydrogen gas is produced at a relative low temperature. This reaction is a heat releasing reaction, and the reactant can be heated to reaction temperature automatically [5]. Secondary, the produced hydrogen is introduced into the second combustion room, where the hydrogen combusts with oxidant and release great amount of heat at a very high temperature. The residual ocean water in combustion room is heated to be vapor and then be sprayed out with the final combustion products.

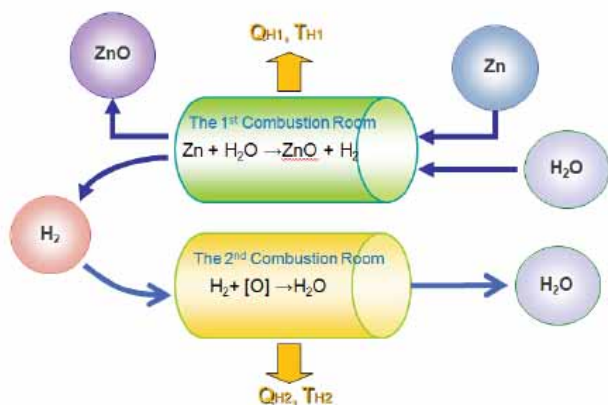


Fig. 1. Schematic diagram of the marine energy power system based on zinc fuel.

As one of the key steps for marine energy power system based on zinc fuel, several studies were carried out on the zinc hydrolysis reaction. In a series of thermogravimetric analyses of commercial zinc powder and solar zinc powder in a temperature range of 350-500 °C, Weidenkaff et al. [3] found that the hydrolysis reaction proceeded faster for molten zinc and for zinc containing impurities, but a layer of ZnO prevented the reaction from reaching completion. The hydrolysis of submicron Zn particles in a temperature range of 330-360 °C was also studied by thermogravimetric analyses, and a fast surface reaction, corresponding to a mass increase of 2%, followed by a slow diffusion-limited reaction was observed [5]. The oxidation of liquid zinc with water vapor was studied by bubbling water vapor through bulk of liquid zinc at 450-500 °C [6], and the results showed that the specific reaction rate increases as the water partial pressure increases, the main determining step of the hydrolysis reaction is the diffusion of reactants through the product zinc oxide layer. The oxidation of zinc vapor of about 750°C and 800 °C with water vapor was also studied using a tubular aerosol flow reactor which features three temperature-controlled zones [7], up to 83% of zinc conversion could be obtained while the temperature of reaction zone is just below the Zn(g) saturation temperature. And several reaction parameters of the H<sub>2</sub> production by steam-quenching of Zn vapor were also studied in a hot-wall aerosol flow reactor, the results shows that high zinc conversions could get at a low quenching rate at the expense of low particle yield [8].

Detailed studies on the hydrolysis kinetics of zinc powder was also conducted by Vishnevetsky et al. [9], they found that the hydrolysis of zinc proceeded in two stage, and increasing the beginning temperature of the reaction is advantageous to the hydrolysis process, the reactivity of Solar Zinc is much higher than commercial zinc, which is agreed with paper [3]. Thermogravimetric analysis of the hydrolysis of zinc particles was also take out in a temperature range of 200-1000°C [10], two kinds of reaction mechanism of the zinc hydrolysis were revealed by Lv et al, in which the rate of hydrolysis reaction was limited by the evaporation of zinc and the diffusion of

zinc through ZnO layer respectively.

The hydrolysis of zinc particle with nano scale was studied by Ma et al [11] and Bhaskar et al [12]. The complete conversion of Zn nano crystals with 70nm average size was achieved at 175°C with a 19% water vapour mole fraction [11]. A hydrogen yield of 80% was achieved at 600 °C for the hydrolysis of a unique Zn nano particle (~25nm) which was dispersed on carbon micro-nano fibers [12].

In this paper, detailed thermodynamic studies were carried out for the hydrolysis process of micron zinc particles in a fixed bed reactor. We tried to Fig. out the characteristics of the zinc hydrolysis process, especially in high water partial pressure. The influences of several important process parameters such as heating rate, reaction temperature, water partial pressure and particle size were also studied here. We focused not only on the final hydrogen yield, but also on the influences on the characteristics of reaction process.

## EXPERIMENTAL

The fixed bed experimental system is depicted schematically in Fig.2. The steam supplied by a steam generator (Shanghai Fengxian, model KQ-BII) was preheated to temperature T<sub>1</sub> and then mixed with the inert carrier gas. The mixed gases were introduced into the reaction zone of a quartz tube reactor (with a inner diameter of 25mm). The quartz tube reactor was placed in the furnace of a high temperature tube furnace (Shanghai Sanya, model SK2-2.5-13TS). A ceramic boat with sample zinc particles inside was placed in the reaction zone of the quartz tube reactor. The exhaust gases from the tube reactor were cooled by a water cooler and dried by a silica gel dryer, and then went through an in situ hydrogen concentration analyzer and a rapid flowmeter FC2 (Swiss Sensrion), and finally be vented into atmosphere.

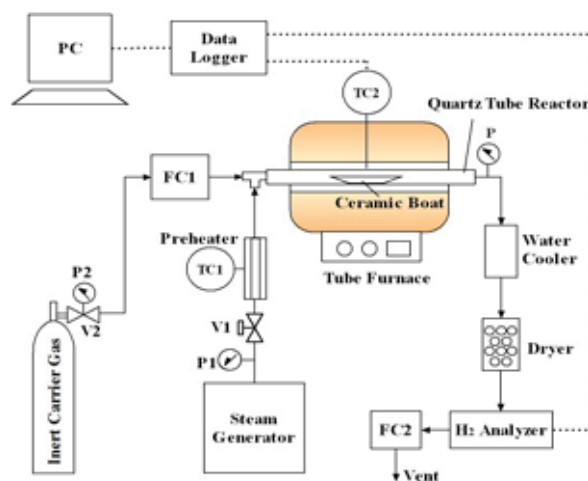


Fig. 2 Schematic diagram of the fixed bed experimental system.

The inert carrier gas used argon gas with a purity of 99.99%. It's flow rate was controlled by a mass flow rate controller FC1 (Qixing Huachuang, model D07). The flow rate of steam was controlled by a needle valve V1. The reaction zone of the quartz tube reactor was heated by the tube furnace, which has 3 Levels

of heating power to choose. The heating curve of each power Level is shown in Fig.3. As Fig. 3 shows, the heating curve of temperature versus time of the tube furnace follows logarithm curve approximately. And when the heating temperature rises from 200 °C to 900°C, the average heating rates at Level 1 to Level 3 heating power were calculated as 1.17, 2.50 and 4.61 °C/min respectively.

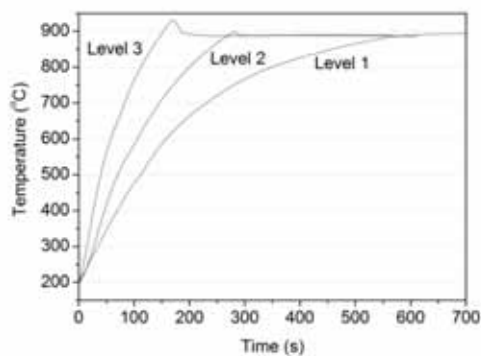


Fig. 3 The heating temperature of tube furnace versus time at 3 Levels of heating power (the initial temperatures were set at 200 °C).

The temperature of reaction zone  $T_2$  was measured by a K type thermocouple TC2, as shown in Fig.2. The in situ hydrogen concentration analyzer (Hitech, model K522) was used to measure the volume concentration of hydrogen in argon-hydrogen mixture. It has a measuring scale of 0-30% and an accuracy of 1% F.S. The pressure of the reaction zone  $p$  was tested in situ by a pressure sensor (Shanghai Tianmu, model NS-F) at the outlet of tube reactor. The data of reaction temperature  $T_2$  and hydrogen concentration were collected continuously and simultaneously by a data logger (Agilent, Model 34970A).

There are two kinds of sample zinc. One is the high purity zinc powder (by Sinopharm Chemical Reagent Co., Ltd) with purity of 99.99%, and its mean particle size is 13  $\mu\text{m}$ . The other kind is the common commercial Zn powder (by Changsha Wellink Zinc Material Co., Ltd) with purity of 99%, and four groups of common Zn powder with different mean particle size (11  $\mu\text{m}$ , 45  $\mu\text{m}$ , 108  $\mu\text{m}$  and 178  $\mu\text{m}$ ) were used in the experiments to discuss the influence of particle size. In experiments, the zinc powder samples were hold by a ceramic boat with a size of 77 mm $\times$ 12 mm $\times$ 9 mm. The sample weight  $m_{\text{Zn},i}$  in each experimental case was weigh about 0.50 $\pm$ 0.05g. The sample zinc powders were dispersed equally at the bottom of ceramic boat.

In each experimental case, the initial gauge pressure of inert carrier gas was set at 0.05 Mpa; And the flow rate of inert carrier gas was set at 200 ml/min; The initial gauge pressure of steam from steam generator was set at 0.1 Mpa; The temperature  $T_1$  of steam preheater was set at 180-200 °C.

There were two kinds of experimental cases: isothermal cases and non-isothermal cases. The isothermal cases were mainly used to study the influences of reaction temperature. Experimental methods are described as follows:

#### (a) isothermal cases

Firstly the sample was placed at the reaction zone of

the quartz tube reactor. And then argon gas with fixed pressure and flow rate was introduced into tube reactor for 10min to purge out the residual air in tube reactor. Then the heating temperature of tube furnace was heated to the required isothermal temperature. Once the required heating temperature was reached, the valve V1 was open to introduce the steam with fixed temperature, pressure and flow rate into tube reactor. After the completion of reaction (when the in situ scanned hydrogen concentration was observed as zero again), the flow rate of steam was measured.

#### (b) non-isothermal cases

Firstly the sample was placed at the reaction zone of the quartz tube reactor. And then argon gas with fixed pressure and flow rate was introduced into tube reactor for 10min to purge out the residual air in tube reactor. Then the heating temperature of tube furnace was heated from room temperature to 200 °C, and the heating power of tube furnace was set at the required Level. And then the valve V1 was open to introduce the steam with fixed temperature, pressure and flow rate into tube reactor. And the heating temperature was raised from 200 °C to 900 °C under fixed power Level and then be kept at 900 °C. After the completion of reaction, the flow rate of steam was measured.

From the pressure  $p$  measured at the outlet of tube reactor in experiments (Fig.2), it is showed that the reaction pressure in our experimental setup was always kept at atmospheric pressure. The system pressure changed every little during the whole experiments. So it is reasonable to consider the reaction in fixed bed system as an atmospheric reaction.

A dryer was used to measure the mass flow rate of steam  $F_{\text{H}_2\text{O}}$  (mg/min) after each cases. It was weighed before and after each measurement in a fixed drying time, the flow rate of steam was calculated as the weight change of dryer divided by the drying time. As the flow rate of carrier gas (Ar) was constantly set to 200 ml/min, the water partial pressure (bar) in each case can be calculated as follows:

$$P_{\text{H}_2\text{O}} = p_{\text{system}} \times F_{\text{H}_2\text{O}} \times 22.4 / (F_{\text{H}_2\text{O}} \times 22.4 + 18 \times 200)$$

The elements of solid products were analyzed by energy dispersive x-ray spectroscopy (EDX, FEI Model SIRION-100). The morphologies of the solid products were examined by scanning electron microscopy (SEM, FEI Model SIRION-100).

## RESULTS AND DISCUSSION

### TYPICAL SOLID PRODUCTS ANALYSIS

In fixed bed experiments, the solid products of zinc hydrolysis appeared as white or grey solid blocks, as Fig.4 shows. The colour of solid products depends on the conversion of zinc in each case. The SEM pictures of typical solid product were shown in Fig.5. It is shown that the solid product of zinc particle hydrolysis in fixed bed reactor has a porous structure. The EDX analysis results showed that the main element of solid products is zinc oxide. As Fig.5(b) &(d) shows, the porous solid products are constructed by a serials of zinc oxide

spherical shells. The average thickness of spherical shells was measured about 1-2 $\mu\text{m}$ . The average diameter of spherical shells was measured about 10 $\mu\text{m}$ , which is similar to the average particle size of reactant zinc particles. This kind of product structure for hydrolysis of zinc particles was also discovered in thermogravimetric analysis [12]. It is suggested that the hydrolysis of micron pure zinc particles in our experiments is a surface reaction. For surface reaction between gas-solid reactants, the reaction rate is usually controlled by the chemical reaction kinetics or the gas reactants diffusion. There are two kinds of chemical reaction mechanism of zinc particle hydrolysis, which says that the rate of hydrolysis reaction is limited by the evaporation of zinc or the diffusion of zinc through ZnO layer respectively [12]. The former one usually happens for larger particles with a diameters above 100 $\mu\text{m}$  [12]. In our experiments, obviously the latter mechanism is the right chemical reaction mechanism for the hydrolysis of pure zinc particle samples.

In TG experiments just as in literature [12], the sample weight is quite small and the layer thickness of reactant zinc particles accumulation in sample holder is very thin, so the influence of reactant gas diffusion could be ignored. But in fixed bed experiments here, the sample weight was respectively larger, and the average layer thickness of reactant zinc particles accumulation in ceramic boat was measured about 1 mm, which was thick enough to consider the influence of steam diffusion in reaction. In addition, the porous structure of solid products, as Fig.5 (d) shows, confirms the necessity of steam diffusion consideration.

### TYPICAL HYDROLYSIS PROCESS ANALYSIS IN FIXED BED REACTOR

The typical hydrogen concentration curves in non-isothermal cases were shown in Fig.6. From the Fig. we can see obviously that there are two reaction stages in non-isothermal cases. Each reaction stage corresponds to a peak of hydrogen concentration curve in different temperature ranges. Obviously the control mechanisms of the two stages are different. As analyzed before (see 3.1), the controlling step of zinc particle hydrolysis in fixed bed may be the chemical reaction kinetics or the diffusion of reactant steam. In following discussion we tried to Fig. out the right control mechanism of each reaction stage.

We defined five characteristic points to analyze the hydrolysis process, as shown in Fig. 6(a) &(b). Each point represents a special meaning, just as follows:

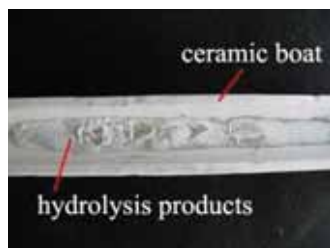


Fig. 4 Photo of typical solid products of zinc hydrolysis in ceramic boat.

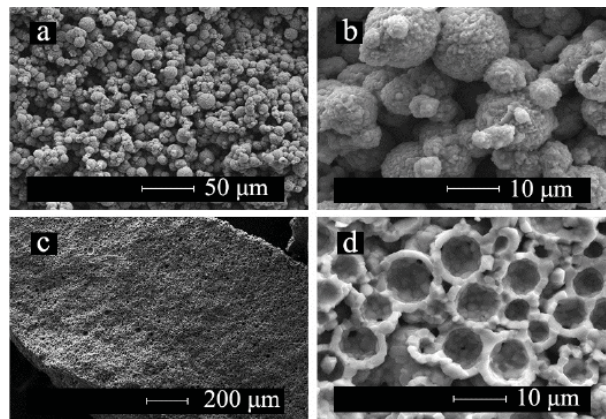


Fig. 5 SEM micrographs of solid products for experiments at a typical parametric setting ( $p=0.1\text{ MPa}$ ,  $p_{\text{H}_2\text{O}} = 0.76\text{ bar}$ , Level 1 heating power, pure zinc powders,  $m_{\text{Zn}}=0.45\text{g}$ ):(a)&(b)the micrographs of the top surface of products;(c)&(d)the micrographs of the cross section of the products.

Point A: The initial reaction point, when hydrogen concentration was observed at the first time in each case. The time of Point A represents the initial reaction time  $t_i$ . And the temperature of Point A represents the initial reaction temperature  $T_i$ .

Point B: The peak hydrogen concentration point in the first stage. The hydrogen concentration of Point B  $n_{\text{max},1}$  is used to represent the maximum reaction rate in the first reaction stage.

Point C: The valley bottom point between two neighbouring peaks. The temperature of Point C  $T_D$  is used to represent the dividing temperature of the two reaction stages.

Point D: The peak hydrogen concentration point in the second stage. The hydrogen concentration of Point D  $n_{\text{max},2}$  is used to represent the maximum reaction rate in the second reaction stage.

Point E: The finish point of reaction, while the hydrogen concentration dropped to zero again. The time of Point E represents the final reaction time  $t_f$ . And the temperature of Point E represents the final reaction temperature  $T_f$ . Comparing the curves in Fig. 6(a) and (b), we can see that the heating temperature went into isothermal stage in the typical case before the end of reaction. So there's no discussion meaning for  $T_f$ .

In each case, the total hydrogen yield  $V_{\text{H}_2}$  can be calculated as follows:

$$V_{\text{H}_2} [L] = \int_{t_i}^{t_f} V(t) dt$$

Where  $V(t)$  is the function of produced hydrogen flow rate versus time. It is given by:

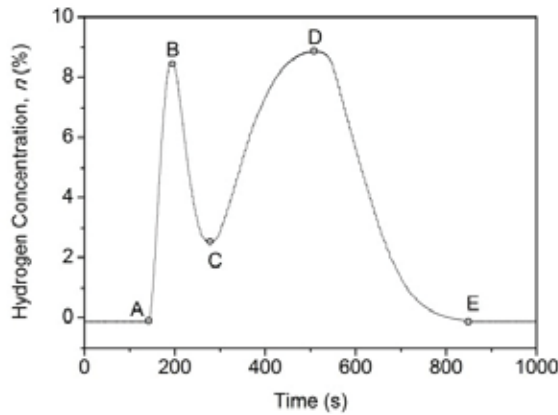
$$V(t) [L/s] = \frac{(V_{\text{Ar}} / 60) \times n}{100 - n}$$

Where  $V_{\text{Ar}}$  is the flow rate of argon carrier gas, L/min;  $n$  is the data of hydrogen concentration measured in situ by the hydrogen analyzer, %.

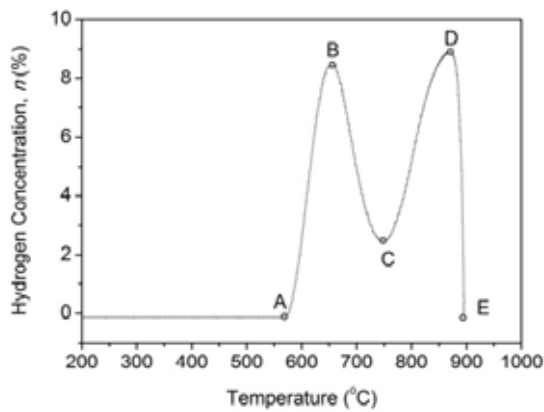
So the total hydrogen yield percentage in each case can be calculated as:

$$H_2 \text{ Yield } [\%] = (V_{H_2} / 22.4) / (m_{Zn,i} / 65)$$

Where  $m_{Zn,i}$  is the initial sample weight of zinc particles, g.



(a) Time curve



(b) Temperature curve

Fig. 6 Typical hydrogen concentration curve in non-isothermal cases ( $p=0.1$  MPa,  $p_{H_2O} = 0.76$  bar, Level 1 heating power, pure zinc powders,  $m_{Zn,i}=0.45$ g).

### THE INFLUENCE OF HEATING RATE

Keeping the water partial pressure as constant approximately, the influences of heating rate were studied. As described before, the average heating rates at Level 1, Level 2 and Level 3 heating power were 1.17, 2.50 and 4.61 °C/min respectively, when the heating temperature rises from 200 °C to 900°C. So the influences of Levels of heating power represent the influences of heating rates in other hand.

Experimental results were shown in Fig.7 and Tab. 1. The two-peak structure of hydrogen concentration curve is more prominent under Level 1 heating power. The initial reaction temperature rises as heating rate rises, as Tab. 1 shows. The  $T_i$  in Level 1 heating power case was about 572°C, while the  $T_i$  in Level 3 heating power case was about 770 °C. The TG studies show that the initial reaction of micron zinc particle hydrolysis is about 600°C [12]. So it is suggested that the non-isothermal experiments carried out under low heating rate with Level 1 heating power can reflect more real reaction characteristics. So the heating powers of tube furnace in the following cases

were all set at Level 1.

The results also show that the hydrogen yield decreases slightly from about 77% to 72% as the heating power increases from Level 1 to Level 3.

Tab.1 Influences of heating power ( $p=0.1$  MPa,  $p_{H_2O} = 0.75-0.76$  bar, pure zinc powders,  $m_{Zn,i}=0.45-0.46$ g).

Heating Power	H <sub>2</sub> Yield / %	n <sub>max,1</sub> / %	n <sub>max,2</sub> / %	T <sub>i</sub> / °C	T <sub>D</sub> / °C
Level 1	76.95	8.53	8.91	572	750
Level 2	75.59	--	17.00	702	--
Level 3	72.27	7.78	16.72	770	--

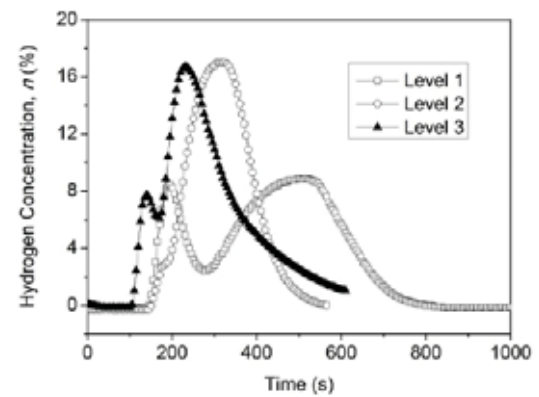


Fig. 7 Hydrogen concentration vs. time at 3 Levels of heating power ( $p=0.1$  MPa,  $p_{H_2O} = 0.75-0.76$  bar, pure zinc powders,  $m_{Zn,i}=0.45-0.46$ g).

### THE INFLUENCE OF WATER PARTIAL PRESSURE

Experiments were carried out to study the influences of water partial pressure in a scale of 0.59 bar to 0.90 bar, as Fig. 8 shows. A water partial pressure as high as 0.90 bar under atmospheric system pressure could be got in our fixed bed experiments. The characteristic parameters of hydrolysis process under different water partial pressures are listed in Tab. 2.

From the experimental results we can see that as the water partial pressure decreases, the hydrogen yield decreases, the initial reaction temperature increases, and the dividing temperature increases either, as Tab. 2 shows. The height of hydrogen concentration peak in the first stage decreases quickly while the water partial pressure decreases. The height of hydrogen concentration peak in the second stage increases as the water partial pressure decreases, just appears opposite tendency to the first stage, as Fig.8 shows. And when the water partial pressure was as low as 0.59 bar, only one peak appears. Considering the temperature range of that peak and the change rule of the peak height versus the water partial pressure, it is reasonable to deduce that the remaining one peak represents the second stage of reaction. In other words, the hydrogen

concentration peak in the first stage disappeared under low water partial pressure.

As mentioned before, there are two kinds of controlling steps of zinc particle hydrolysis in the two reaction stages, the chemical reaction kinetics or the diffusion of reactant steam. According to the general surface reaction theory, the diffusion rate of steam depends very much on the water partial pressure. And as the water partial pressure decreases, the diffusion rate of steam will decrease too. Meanwhile for the chemical reaction kinetics of zinc particles hydrolysis in these cases, the diffusion rate of zinc through ZnO layer depends more on temperature, and little on water partial pressure. Considering that in the first reaction stage with lower temperature range, the hydrogen peak height decreases as the water partial pressure decreases, which has the similar change rule with the diffusion rate of steam versus water partial pressure. Obviously the steam diffusion seems to be the right controlling step of the first reaction stage in lower temperature range. Be more precisely speaking, the steam's diffusing inside the accumulative zinc particles (which can be seen as porous block) is the controlling step in the first reaction stage. It could be called as "inner diffusion" in surface reaction. Meanwhile the chemical reaction kinetics, that the diffusion of zinc through ZnO layer, is suggested to be the controlling step of the second reaction stage in higher temperature range.

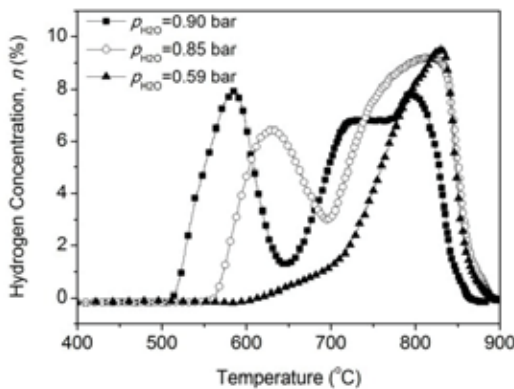


Fig. 8 Hydrogen concentration vs. temperature under different water partial pressures ( $p=0.1$  MPa,  $p_{H_2O} = 0.59-0.90$  bar, Level 1 heating power, pure zinc powders,  $m_{Zn,i}=0.52-0.53$ g).

Tab. 2 Influences of water partial pressure ( $p=0.1$  MPa,  $p_{H_2O} = 0.59-0.90$  bar, Level 1 heating power, pure zinc powders,  $m_{Zn,i}=0.52-0.53$ g).

$p_{H_2O}$ /bar	$H_2$ Yield / %	$n_{max,1}$ / %	$n_{max,2}$ / %	$T_i$ / °C	$T_D$ / °C
0.90	75.98	7.93	7.85	512	653
0.85	70.09	6.43	9.22	558	698
0.59	55.06	0.00	9.53	596	--

## THE INFLUENCE OF ZINC PARTICLE SIZES

Experiments were carried out to study the influences of zinc particle sizes, as shown in Fig. 9 and Fig. 10. The characteristic parameters of hydrolysis process for different size of zinc

particles are listed in Tab. 3.

The experimental results show that the peak hydrogen concentration in the first and the second stages both decrease as the mean particles size increases. And the hydrogen yield dropped from 77.45% to 11.27% when the mean particle size increased from 11 $\mu$ m to 178 $\mu$ m, as Fig.10 shows.

Furthermore, there were three hydrogen concentration peaks appeared in the hydrolysis process of sample Zn-4, which has a mean diameter of 178 $\mu$ m, as Fig.9 shows. The initial temperature of the third reaction stage is about 752 °C. From the past research results of literature [12], the controlling step of the third reaction stage is speculated to be the evaporation of zinc nucleus. That means the chemical reaction mechanism in the third stage for sample Zn-4's hydrolysis is mainly gas-gas reaction, but not surface reaction. And the typical microstructure of solid products in gas-gas zinc hydrolysis reaction was discovered in the SEM pictures of sample Zn-4's hydrolysis products, as Fig.11 shows. There were many small zinc oxide crystal needles covered outside of ZnO spherical shell, as Fig.11(b) shows.

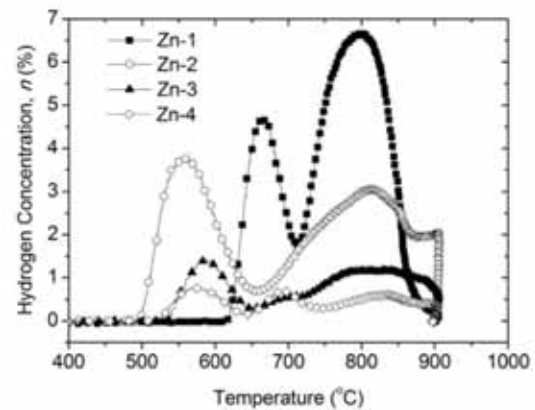


Fig. 9 Hydrogen concentration vs. temperature for different zinc particle sizes ( $p=0.1$  MPa,  $p_{H_2O} = 0.75-0.77$  bar, Level 1 heating power, common commercial zinc powders, the mean particle size for Zn-1, Zn-2, Zn-3 and Zn-4 is 11 $\mu$ m, 45 $\mu$ m, 108 $\mu$ m and 178 $\mu$ m respectively,  $m_{Zn,i}=0.51-0.52$ g).

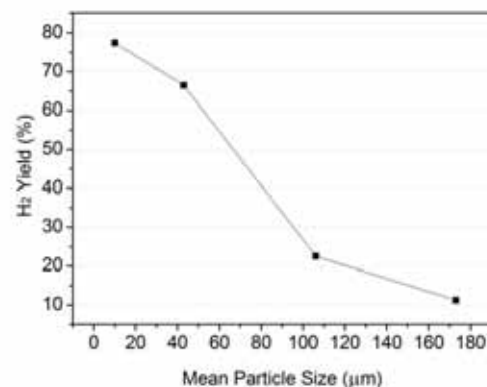


Fig. 10 The influences of particle size on  $H_2$  yield ( $p=0.1$  MPa,  $p_{H_2O} = 0.75-0.77$  bar, Level 1 heating power, common commercial zinc powders,  $m_{Zn,i}=0.51-0.52$ g).

Tab. 3 Influences of zinc particle size ( $p=0.1$  MPa,  $p_{H_2O} = 0.75-0.77$  bar, Level 1 heating power, common commercial zinc powders,  $m_{Zn,i}=0.51-0.52$ g).

Mean particle size / $\mu\text{m}$	H <sub>2</sub> Yield/ %	$n_{\text{max},1}$ / %	$n_{\text{max},2}$ / %	$n_{\text{max},3}$ / %	$T_i$ / °C	$T_{D1}$ / °C
11	77.45	4.69	6.68	--	647	742
45	66.47	3.77	3.06	--	496	661
108	22.54	1.63	1.39	--	534	655
178	11.27	0.77	0.69	0.60	522	645

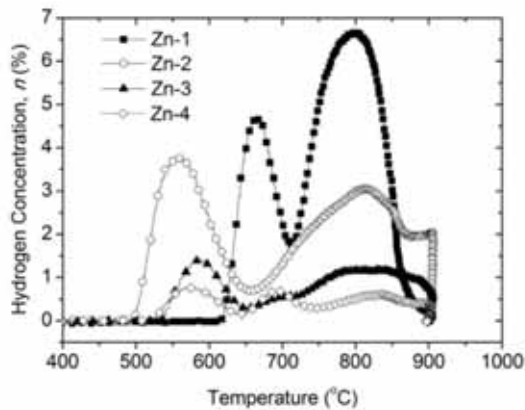


Fig. 11 SEM micrographs of solid products for the hydrolysis of zinc particles with a mean particle size of 178  $\mu\text{m}$  ( $p=0.1$  MPa,  $p_{H_2O} = 0.76$  bar, Level 1 heating power, common commercial zinc powders,  $m_{Zn,i}=0.51$ g).

### THE INFLUENCE OF REACTION TEMPERATURE IN ISOTHERMAL CONDITIONS

A series of isothermal experimental cases were carried out to study the influence of reaction temperature, as Fig.12 shows. In this part of discussion, we focused on the initial reaction temperature of zinc particles. So the temperature scale of isothermal cases was mainly from 400 °C to 600 °C. In addition, the zinc hydrolysis isothermal case with a temperature of 900 °C was carried out as well to study the reaction process near the boiling point of zinc.

The experimental results are shown in Fig.12-Fig.14. It should be pointed out firstly that because of the restriction of heating rate, when the fixed reaction temperature was higher than the melting point of zinc, the zinc sample would be exposed in flowing inert carrier gas for a period of time. Because of the melting and evaporating of zinc particles, there will be a little loss of the zinc sample before the reaction start. Obviously, higher the temperature fixed, larger the zinc sample loss. This is another reason why the most of our isothermal cases carried out in low temperature range.

From Fig.12 we can see that there was no hydrogen produced at a temperature of 400 °C, while the hydrogen peak appeared in the case of 450 °C. That means the initial reaction temperature of zinc particle reaction in fixed bed reactor is between 400-450 °C. A series of isothermal experiments with very small temperature step were carried out. And the results show that the initial reaction temperature of micron zinc particle hydrolysis in fixed bed is about 410 °C.

Be different from the multi-peak structure in non-isothermal cases as mentioned previously, the hydrogen

concentration curve in isothermal cases usually had only one peak, as Fig.12 shows. That suggested that the temperature is one of the most important characters for the reaction mechanism.

When the temperature is lower than 600 °C, the peak hydrogen concentration and hydrogen yield both increase almost linearly as the isothermal temperature increases, as shown in Fig.13 and Fig.14. Obviously at a temperature near the boiling point of zinc such as 900 °C, the hydrolysis of zinc proceeded more well, as the peak hydrogen concentration was as large as 22.9%, and the hydrogen yield was as large as 81.5%. Considering the sample loss before the reaction starting in this case, the real hydrogen yield for 900 °C case should be larger than 81.5%. That may because the gasification of zinc at very high temperature becomes more violently, so the hydrolysis process based on gas-gas reaction proceeds more quickly.

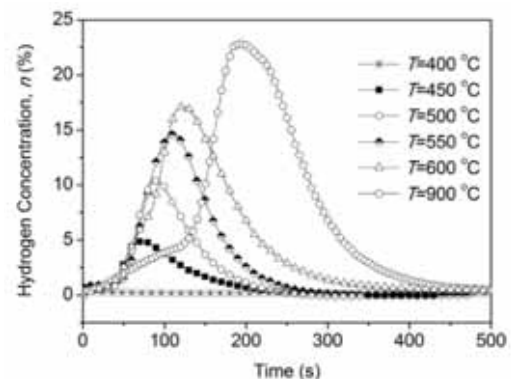


Fig. 12 Hydrogen concentration vs. time under different temperatures in isothermal cases ( $p=0.1$  MPa,  $p_{H_2O} = 0.75-0.77$  bar, Level 1 heating power, pure zinc powders,  $m_{Zn,i}=0.49-0.51$ g).

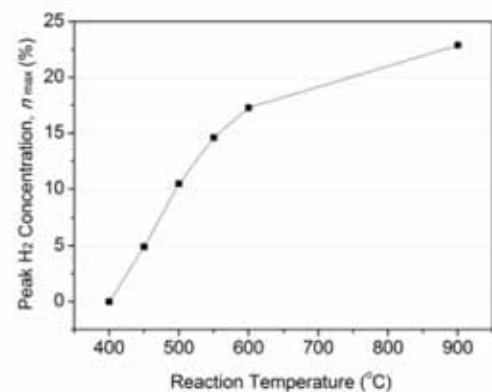


Fig. 13 The influences of temperature on peak hydrogen concentration ( $p=0.1$  MPa,  $p_{H_2O} = 0.75-0.77$  bar, Level 1 heating power, pure zinc powders,  $m_{Zn,i}=0.49-0.51$ g).

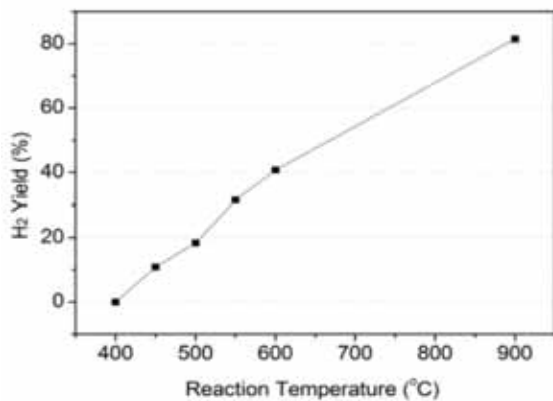


Fig. 14 The influences of temperature on H<sub>2</sub> yield ( $p=0.1$  MPa,  $p_{\text{H}_2\text{O}} = 0.75$ - $0.77$  bar, Level 1 heating power, pure zinc powders,  $m_{\text{Zn}_i} = 0.49$ - $0.51$ g).

## CONCLUSION

A series of experiments in a fixed bed reactor were carried out to study the characteristics of micron zinc particle hydrolysis process. The experimental results suggested that the steam inner diffusion is the controlling step of accumulative zinc particles hydrolysis reaction at a relative lower temperature and a relative higher water partial pressure. In other conditions, the chemical reaction kinetics was the controlling step. And two kinds of chemical reaction kinetics appeared in experiments: the surface reaction and the gas-gas reaction. The latter one occurs usually for larger zinc particles and high reaction temperature. Temperature seems to be one of the most important parameters for the dividing of different reaction mechanisms.

Several parameters of the hydrolysis process including heating rate, water partial pressure, the particle size and temperature were also studied in this paper. Results show that the initial reaction temperature of zinc hydrolysis in fixed bed is about 410 °C. And the initial reaction temperature increases as the heating rate increases and as the water partial pressure decreases. The total hydrogen yield increases as the heating rate decreases, as the water partial pressure increases, as the zinc particle size decreases, and as the reaction temperature increases. A hydrogen yield of more than 81.5% was obtained in the fixed bed experiments.

## ACKNOWLEDGEMENTS

Authors wish to acknowledge the sponsor of the National Natural Science Foundation of China (No.51209062, No. 51305113).

## BIBLIOGRAPHY

1. Committee on Technology for Future Naval Forces, Commission on Physical Sciences, Mathematics, and Applications, National Research Council.: *Technology for the United States Navy and Marine Corps, 2000-2035*, Volumn 2, National academy press, Washington, D.C., 1997.

2. Steinfeld, A., Kuhn, P., Reller, A., Palumbo, R., Murray, J., Tamaura, Y.: *Solar-processed metals as clean energy carriers and water-splitters*. International Journal of Hydrogen Energy, 1998.
3. Weidenkaff, A., Reller, A.W., Wokaun, A., Steinfeld, A. : *Thermogravimetric analysis of the ZnO/Zn water splitting cycle*, Thermochemica Acta , 2000.
4. Lv, M., Zhou, J.H., Zhou, Z.J., Yang, W.J., Liu, J.Z., Cen, K.F. : *A novel system of near zero emission clean coal energy utilization based on Zn/ ZnO*. Journal of Power Engineering, 2008.
5. Ernst, F.O., Steinfeld, A., Pratsinis, S.E.: *Hydrolysis rate of submicron Zn particles for solar H<sub>2</sub> synthesis*, International Journal of Hydrogen Energy, 2009.
6. Berman, A., Epstein, M.: *The kinetics of hydrogen production in the oxidation of liquid zinc with water vapor*. International Journal of Hydrogen Energy, 2000.
7. Wegner, K., Ly, H.C., Weiss, R.J., Pratsinis, S.E., Steinfeld, A.: *In situ formation and hydrolysis of Zn nanoparticles for H<sub>2</sub> production by the 2-step ZnO/Zn water-splitting thermochemical cycle*. International Journal of Hydrogen Energy, 2006.
8. Melchior, T., Piatkowski, N., Steinfeld, A.: *H<sub>2</sub> production by steam-quenching of Zn vapor in a hot-wall aerosol flow reactor*, Chemical Engineering Science , 2009.
9. Vishnevetsky, I., Epstein, M.: *Production of hydrogen from solar zinc in steam atmosphere*, International Journal of Hydrogen Energy, 2007.
10. Lv, M., Zhou, J.H., Yang, W.J., Cen, K.F.: *Thermogravimetric analysis of the hydrolysis of zinc particles*, International Journal of Hydrogen energy, 2010.
11. Ma, X., Zachariah, M.R.: *Size-resolved kinetics of Zn nanocrystal hydrolysis for hydrogen generation*. International Journal of Hydrogen Energy, 2010.
12. Bhaduria, B., Verma, N.: *A zinc nanoparticles-dispersed multi-scale web of carbonmicro-nanofibers for hydrogen production step of ZnO/Znwater splitting thermochemical cycle*, Chemical Engineering Research and Design, 2014.

## CONTACT WITH THE AUTHORS

Haiqiang Liu, Ph.D.

School of Mechanical Engineering  
Hangzhou Dianzi University  
Hangzhou  
**CHINA**  
*e-mail: liuhaiqiang1980@126.com*

# CONSTRUCTION METHOD OF THE TOPOGRAPHICAL FEATURES MODEL FOR UNDERWATER TERRAIN NAVIGATION

Lihui Wang

Le Yu

Yanhua Zhu

Key Laboratory of micro-inertial instrument and advanced navigation technology,  
Ministry of education, School of instrument science and engineering,  
Southeast University Nanjing 210096,  
China

## ABSTRACT

*Terrain database is the reference basic for autonomous underwater vehicle (AUV) to implement underwater terrain navigation (UTN) functions, and is the important part of building topographical features model for UTN. To investigate the feasibility and correlation of a variety of terrain parameters as terrain navigation information metrics, this paper described and analyzed the underwater terrain features and topography parameters calculation method. Proposing a comprehensive evaluation method for terrain navigation information, and constructing an underwater navigation information analysis model, which is associated with topographic features. Simulation results show that the underwater terrain features, are associated with UTN information directly or indirectly, also affect the terrain matching capture probability and the positioning accuracy directly.*

**Keywords:** Terrain Aided Navigation, terrain features, Terrain Navigation Information Content (TNIC), correlation

## INTRODUCTION

Terrain Aided Navigation (TAN) combined the terrain database with terrain contour matching, which improved the positioning accuracy of inertial navigation of autonomous underwater vehicle (AUV) [1,2]. Terrain Elevation Matching (TEM) is the key technology of TAN. Once system hardware performance and matching area have been identified, the performance of TEM determines the navigation accuracy of TAN. The accuracy and reliability of underwater terrain navigation (UTN) depend on the richness of the terrain information [3-5]. The more abundant of the underwater terrain features, the better the robustness of matching algorithm is, and the more reliable matching results are. Analysis algorithms for different terrain navigation performance, including choosing

terrain matching area, have been a focus research of TAN, and are an obstacle for TAN widely used.

One core of terrain matching aided navigation system is the characteristics of the terrain [6,7]. As local statistical characteristics of the terrain, terrain information is a property of terrain itself, which is independent of the specific terrain matching algorithm [8,9]. Therefore, this paper established an analysis model of UTN, theoretically analyzed the measures of terrain height standard deviation, Fisher terrain information and terrain elevation entropy, these terrain features which are closely related to the amount of information and terrain navigation, and their impacts on matching performance, and discussed the weighting comprehensive assessment of topographic information.

## A TERRAIN NAVIGATOR ANALYSIS MODEL

East to the location, the position of the north, east velocity, north velocity are considered as a state quantity of the “position velocity model” of UTN [10]. East acceleration and north acceleration are regarded as the control amount. East velocity, north velocity and water depth  $f$  are regarded as dynamic model measurements.

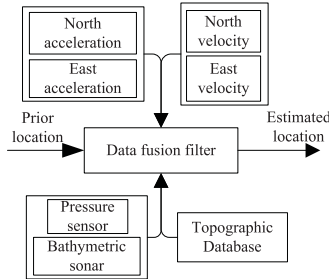


Fig. 1. Schematic diagram of the underwater terrain navigation simulation system

State vector:

$$\mathbf{x}(t) = [x(t) \quad y(t) \quad v_x(t) \quad v_y(t)]^T \quad (1)$$

Control vector:

$$\mathbf{u}(t) = [a_x(t) \quad a_y(t)]^T \quad (2)$$

Measurement vector:

$$\mathbf{z}(t) = [v_x(t) \quad v_y(t) \quad h_r(t) + h(t)]^T \quad (3)$$

System Model:

$$\dot{\mathbf{x}}(t) = \mathbf{A}\mathbf{x}(t) + \mathbf{B}\mathbf{u}(t) + \mathbf{L}\mathbf{w}(t)$$

$$= \begin{bmatrix} 0 & 0 & 1 & 0 \\ 0 & 0 & 0 & 1 \\ 0 & 0 & 0 & 0 \\ 0 & 0 & 0 & 0 \end{bmatrix} \begin{bmatrix} x(t) \\ y(t) \\ v_x(t) \\ v_y(t) \end{bmatrix} + \begin{bmatrix} 0 & 0 \\ 0 & 0 \\ 1 & 0 \\ 0 & 1 \end{bmatrix} \begin{bmatrix} a_x(t) \\ a_y(t) \end{bmatrix} + \begin{bmatrix} 0 & 0 \\ 0 & 0 \\ 1 & 0 \\ 0 & 1 \end{bmatrix} \begin{bmatrix} w_{a_x}(t) \\ w_{a_y}(t) \end{bmatrix} \quad (4)$$

$$\mathbf{z}(t_k) = h(\mathbf{x}(t_k)) + \mathbf{e}(t_k) = \begin{bmatrix} v_x(t_k) \\ v_y(t_k) \\ h_d(x(t_k), y(t_k)) \end{bmatrix} + \begin{bmatrix} e_{v_x}(t_k) \\ e_{v_y}(t_k) \\ e_h(t_k) \end{bmatrix} \quad (5)$$

where  $w(t)$  and  $e(t)$  are respectively the process noise and measurement noise, which covariance matrices are  $Q$  and  $R$

respectively, both are zero-mean white noise. Discrete state points are estimated by way of the UKF system model. In case that error in the initial position is not so high, UKF is capable of real-time navigation system error correction with high matching accuracy, it has a better prospect of engineering application. Without linearization, we can use the discrete state differential equations directly.

$$\mathbf{x}_k = F(\mathbf{x}_{k-1}, \mathbf{u}_{k-1}, \mathbf{w}_{k-1}) = \Phi_{k/k-1} \mathbf{x}_{k-1} + \mathbf{B}^* \mathbf{u}_{k-1} + \mathbf{L}^* \mathbf{w}_{k-1} \quad (6)$$

$$\mathbf{z}_k = h(\mathbf{x}_k) + \mathbf{e}(k) = \begin{bmatrix} v_x(k) \\ v_y(k) \\ h_d(x_k, y_k) \end{bmatrix} + \begin{bmatrix} e_{v_x}(k) \\ e_{v_y}(k) \\ e_h(k) \end{bmatrix} \quad (7)$$

## UNDERWATER TERRAIN NAVIGATION INFORMATION OF EXPRESSION

Some statistical characteristics of the underwater topography (such as terrain height entropy), directly or indirectly, are related with the amount of information about the terrain navigation [4,11]. These features are characteristic of the spatial shape of the ground described with an intuitive meaning [9]. The terrain height standard deviation, Fisher terrain information and terrain elevation entropy, those parameters reflect the size of the terrain informative to some extent.

## THE UNDERWATER TOPOGRAPHY DEPTH STANDARD DEVIATION

The terrain standard deviation reflects the high degree of deviation from the scope of the terrain average terrain elevation, DTED map the terrain matching region into discrete square area  $A$ . Set to be investigated terrain elevation sequence  $h(i, j)$ :

$$\left\{ \begin{array}{l} \sigma = \sqrt{\frac{1}{m(n-1)} \sum_{i=1}^m \sum_{j=1}^n [h(i, j) - \bar{h}]^2} \\ \bar{h} = \frac{1}{mn} \sum_{i=1}^m \sum_{j=1}^n h(i, j) \end{array} \right. \quad (8)$$

where  $\sigma$  is the terrain standard deviation, deviation of terrain elevation values centered around gathering described by the standard deviation terrain. Regardless of the order in terrain elevation variance, terrain structure is unrelated to viewing direction.  $h(i, j)$  indicates the depth reference for reference map.  $\bar{h}$  is the average depth of the local computation window. In most cases, the average elevation

of the terrain elevation value reflects the topography of the central gathering.

### FISHER TERRAIN INFORMATION

The famous Cramer - Rao (Cramer -Rao) Fisher information inequality can measure topographic information which contains the amount of terrain information [12].

$$FIC = \sqrt{\frac{1}{N} \sum_{i=1}^N \|\nabla h(x_i)\|^2} \quad (9)$$

In the formula,  $x_i$  is flat position that coordinates point in matching region which is uniform distributed. The range of Fisher terrain information content is from 0 to infinity, in fact terrain Fisher quantity can't be infinity, and its upper bound is a big positive number. Fisher information matrix which is common in estimate problem will be introduced.

$$J = E(-\nabla_x \nabla_x^T \log p(X, y)) = \frac{1}{\lambda} E(\nabla_x h(X) \nabla_x^T h(X) - (y - h(X)) \nabla_x \nabla_x^T h(X)) \quad (10)$$

where  $h(i, j)$  is a group of sample values which is uniform distributed in the region. Fisher information matrix  $J$  defines the sampling mean.

$$\hat{J} = \sum_{i=1}^N \nabla_x h(X)|_{x=x_i} \nabla_x^T h(X)|_{x=x_i} \quad (11)$$

It can be used as a quantity in DTED map, and it has nothing to do with the noise variance  $\lambda$  and the area of  $A$  (small square area). Obviously

$$\lim_{n \rightarrow \infty} \frac{1}{\lambda A} \hat{J} = J \quad (12)$$

where  $\hat{J}$  can be used to measure the amount of information in different terrain region of DTED map. Terrain Fisher quantity FIC is proportional to the sample mean  $\hat{J}$  of Fisher information matrix  $J$ , reacted the size of Fisher information matrix  $J$  to some extent. So it can link to C-R inequality.

### THE TERRAIN ENTROPY

According to the definition of entropy, entropy indicates the average degree of uncertainty system. Terrain entropy represents uncertainty of terrain height, set a square region  $S$  in arbitrary DEM map, corresponding to a terrain entropy  $H_f(i, j)$ , which included  $n$  elements position sets and  $m$  terrain height value sets in the DEM map, it can be defined as

$$\begin{cases} P_i(i, j) = \frac{h(i, j)}{\sum_{i=1}^m \sum_{j=1}^n h(i, j)} \\ H_f(i, j) = - \sum_{i=1}^m \sum_{j=1}^n P_i(i, j) \log P_i(i, j) \end{cases} \quad (13)$$

Local terrain entropy reflects the quantity of the information contained in the terrain, so the local terrain entropy can describe the nature of the terrain [14]. If a local area elevation values change more dramatic, and undulating changes greater, the more unique topography is, the smaller calculated entropy of local terrain is, otherwise, the entropy is greater. Smaller entropy area is suitable for matching area. The range of terrain height entropy vary from 0 to  $\lg N$ ,  $N$  represents the calculation of the number of representatives, to the image element within the window of sample values. Terrain height equal to 0 indicates that the entropy calculation window is a flat terrain, that means values of all the pixels is the same height. The calculation is equal to  $\lg N$  represents the window is a rugged terrain terrain, every point is different height values.

### THE AMOUNT OF TERRAIN CODING DISTORTION

From the perspective of information theory, plane position information is the source, and the terrain height value is the signal transmitted in the channel after information source coding [13,15]. Physical terrain matching area plays the role of the encoder, which provides the terrain height values by plane location information. Generally, physical terrain matching area is the encoder with a distortion. Usually, because in a certain region with the terrain matching area, it is impossible that terrain height is not the same at all locations, yet there is always one position with a same terrain height value, the terrain matching region is generally not an one to one encoder. The random error coding between encoding input and decoding output is called distortion, the function of distortion amount  $d(x_i, x_j)$  represents the distortion of location  $x_i$  turning into  $x_j$  after decoding the encode.

$$d(x_i, x_j) = \|x_i - x_j\| = \sqrt{(x(x_i) - x(x_j))^2 + (y(x_i) - y(x_j))^2} \quad (14)$$

The average value  $\bar{d}$  of the function of distortion amount  $d(x_i, x_j)$  is able to be the distortion amount to express terrain matching region encoding.

$$\bar{d} = \sum_{i=1}^N p(x_i) \sum_{j=1}^N p(x_j) d(x_i, x_j) \quad (15)$$

The distortion amount  $\bar{d}$  is one of the important indicators to balance the performance of an encoder, ranging from 0 to

$N/2$ , and  $N$  being the side of the square calculating window (the number of pixels).if the value of terrain encoding distortion amount equals to 0, then it represents the area is one with abundant information in the calculating window. By the terrain height value, we can estimate plane location, however, supposing that the amount is  $N/2$ , then it represents the area is a one with little information in the calculating window, which is not suitable for being a terrain matching region.

## COMPREHENSIVE EVALUATION METHOD

The topographic features may be interrelated. In order to find out quantitative relationship between positioning accuracy of matching area and terrain features, assuming there are polynomial relations combining the positioning error mean square with these parameters by regression analysis [10], as following formula:

$$\begin{aligned}
 RMS = & \alpha_0 + \alpha_1\sigma_T + \alpha_2FIC + \alpha_3ENT + \\
 & + \alpha_4DIS + \alpha_5\sigma_T FIC + \alpha_6\sigma_T ENT + \alpha_7\sigma_T DIS \quad (16) \\
 & - \alpha_8FIC * ENT + \alpha_9FIC * DIS + \alpha_{10}ENT * DIS - \\
 & + \alpha_{11}\sigma_T^2 + \alpha_{12}FIC^2 + \alpha_{13}ENT^2 + \alpha_{14}DIS^2
 \end{aligned}$$

RMS represents positioning error mean square of terrain matching algorithm,  $\sigma_T$  represents the depth of standard deviation. FIC represents terrain fisher character information, ENT represents terrain height entropy. DIS represents the amount of coding distortion terrain,  $\alpha_0 \sim \alpha_{14}$  represent the coefficients. These terrain features don't represent all of the terrain features, the polynomial is not necessarily universal adaptability, but it can reflect the sensitivity of terrain to some extent.

## SIMULATION OF UNDERWATER TERRAIN NAVIGATION INFORMATION

Through the experimental analysis of the relationship between terrain parameters and navigation errors, terrain parameters used to choose the terrain can be determined. This article is wrote by being measured from the depth of standard deviation, Fisher terrain information, terrain entropy, coding distortion amount of terrain measure and its impact on terrain matching. Figure 2 shows standard deviation of water depth and topography. All measurements were carried out utilizing Monte Carlo simulation. Terrain height standard deviation and the degree of information-rich of terrain feature are corresponding, terrain standard deviation values are large in local area where owning more violent topography and rich feature information, while terrain standard deviation values are small in local area where owning slow topography and deficient feature information. So the local topography standard deviation can be used as a quantitative index to measure the amount of information of the terrain feature. Figure 3 shows Fisher features information. Qualitative say, terrain matching area with bigger FIC contains bigger information of terrain navigator. Compared with small FIC of flat area, FIC of area

on undulating terrain is large. Figure 4 shows height entropy of terrain. The terrain is more unique and the information of this area is richer. Flat area has small height entropy while rugged area has large height entropy. Terrain coding distortion of flat area is large and rugged area is small. The smaller the terrain coding distortion is, the more terrain navigation information area contain, the more suitable match for the terrain height. Therefore, when selecting terrain matching area, you should try to choose a small amount of terrain coding distortion.

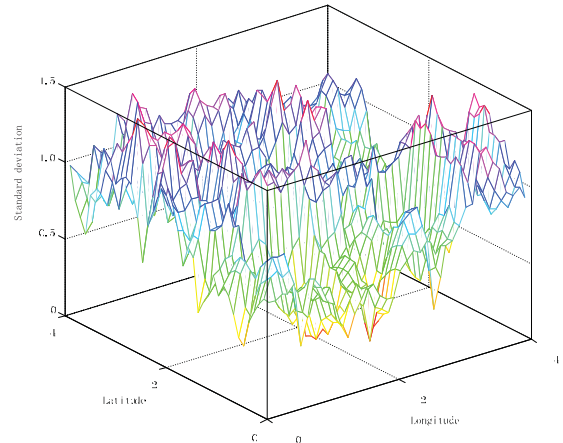


Fig. 2. The standard deviation of water depth and topography

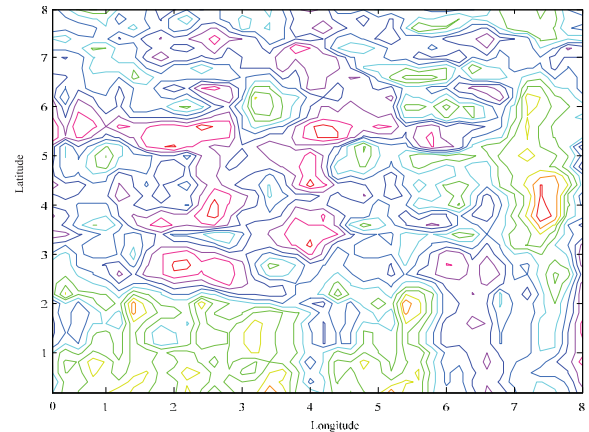


Fig. 3. Fisher terrain features information

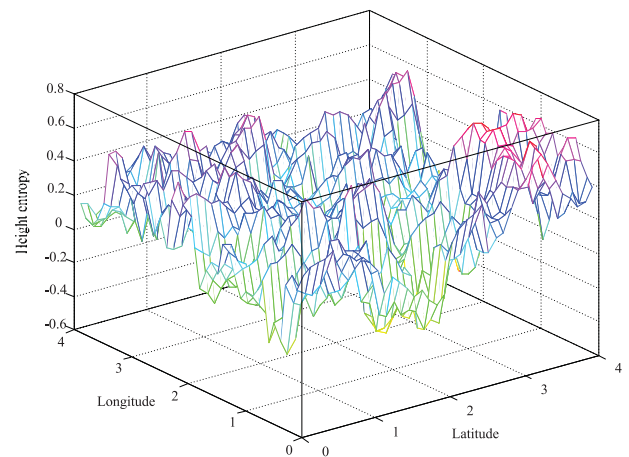


Fig. 4. Height entropy of terrain

## CONCLUSIONS

Terrain contour matching aided navigation is a hot research direction in recent years. However, besides matching algorithm, matching performance also related to the amount of information of matching area. By using the UKF nonlinear filtering, we established models of the underwater terrain analysis, obtained that terrain height standard deviation, Fisher terrain information and terrain elevation entropy, then, built quantitative relationships with matching performance, and simulated the models. We presented methods of terrain features correlation analysis, which can be used as a reference standard to select matching area in underwater terrain navigation.

## ACKNOWLEDGMENTS

The project is supported by the following funds: National Natural Science Foundation of China (61203192, 51477028), Fundamental Research Funds for the Central Universities (2242013R30016), Natural Science Foundation of Jiangsu Province (BK2012326, BK20130628), Research Fund of China Ship Industry (13J3.8.4), Foundation of Key Laboratory of Micro-Inertial Instrument and Advanced Navigation Technology, Ministry of Education (201103).

## REFERENCES

1. Anonsen, K.B. and Hagen, O.K., *An analysis of real-time terrain aided navigation results from a HUGIN AUV*, OCEANS, Vol. 10, pp. 1-9, 2010.
2. Anonsen, K.B. and Hagen, O.K., *Terrain aided underwater navigation using pockmarks*, OCEANS, pp. 1-6, 2009.
3. Ayanna, M.H., *Fuzzy-logic based selection of surface feature observations for small body proximity operations*, WAC '06. World Automation Congress, pp. 1-6, 2006.
4. Bagnell, J. A., Bradley, D., and Silver, D., *et al.*, *Learning for autonomous navigation*, Robotics & Automation Magazine, Vol. 17, no. 2, pp. 74-84, 2010.
5. Carreno, S., Wilson, P., Ridao, P., *et al.*, *A survey on terrain based navigation for AUVs*, OCEANS, Vol. 10, pp. 1-7, 2010.
6. Deborah K. Meduna, Stephen M. Rock, Robert S. McEwen. *Closed-loop terrain relative navigation for AUVs with non-inertial grade navigation sensors*, 2010 IEEE/OES Autonomous Underwater Vehicles (AUV), pp. 1-8. 2010.
7. Feng, Q.T., *A new method of terrain matching and its environmental adaptability reseach*, University of Defense Technology, 2004.
8. Kjetil Bergh Anonsen, Ove Kent Hagen. *Recent developments in the HUGIN AUV terrain navigation system*, OCEANS, Vol. 9, pp. 1-7, 2011.
9. Nordlund, P.J. and Gustafsson, F., *Marginalized particle filter for accurate and reliable terrain-aided navigation*, Aerospace and Electronic Systems, Vol. 45, no. 4, pp. 1385-1399, 2009.
10. Marvin, W., Roe, M.E., and Trenchard, M.C.L., *Integrating vector overlay information into naval digital map systems*. IEEE/AIAA 30th Digital Avionics Systems Conference, pp. 6B5-1 - 6B5-9, 2011.
11. McPhail, S., Stevenson, P., Pebody, M., *et al.*, *Challenges of using an AUV to find and map hydrothermal vent sites in deep and rugged terrains*, 2010 IEEE International Conference on Autonomous Underwater Vehicles (AUV), pp. 1-8, 2010.
12. Panahandeh, Ghazaleh, Jansson, Magnus. *Vision-aided inertial navigation using planar terrain features*. International Conference on Robot, Vision and Signal Processing, pp. 287-291, 2011.
13. Pullen, J.D. and Allen, J.S., *Modeling studies of the coastal circulation off Northern California: shelf response to a major Eel river flood event*, Continental Shelf Research, Vol. 20, pp. 2213-2238, 2000.
14. Reynaud, S. and Louis, C., *A universal navigability map building approach for improving Terrain-Aided-Navigation accuracy*. 2010 IEEE/ION Conference on Position Location and Navigation Symposium (PLANS), pp. 888-896, 2010.
15. Stalder, S., Bleuler, H., and Ura, T., *Terrain-based navigation for underwater vehicles using side scan sonar images*. OCEANS, pp. 1-3, 2008.

## CONTACT WITH THE AUTHORS

Lihui Wang  
Le Yu  
Yanhua Zhu

Key Laboratory of micro-inertial instrument and advanced navigation technology  
Ministry of education, School of instrument science and engineering  
Southeast University Nanjing 210096  
tel.: +86 02583793911, fax: +86 02583793911  
e-mail: wlhseu@163.com  
**CHINA**

# NUMERICAL INVESTIGATION OF THE UNDRAINED COMPRESSION AND PULL-OUT CAPACITY OF SUCTION FOUNDATIONS IN CLAY

Jiaqing Du<sup>a</sup>  
Shouji Du<sup>a</sup>  
Shuilong Shen<sup>a</sup>  
Zhenyu Yin<sup>a,b</sup>

<sup>a</sup>Department of Civil Engineering and State Key Laboratory of Ocean Engineering, Shanghai Jiao Tong University, Shanghai 200240, China

<sup>b</sup>LUNAM University, Ecole Centrale de Nantes, GeM UMR CNRS, 6183, Nantes, France

## ABSTRACT

*This paper presents the results of three-dimensional finite difference analysis of suction foundations in uniform and non-uniform clays under undrained conditions. The Tresca criterion was used to simulate the stress-strain response. The bearing capacity of the foundations was investigated, with the degree of nonhomogeneity ( $kD/\text{sum}$ ) of soil varying from 0 to 5, and the embedment depth being up to four times the foundation diameter. The end bearing capacity factor in compression and the reverse bearing capacity factor in tension were both calculated and were compared with each other under different foundation displacements. Numerical results showed that the ultimate bearing capacity factor can have the same value in cases of both compression and tension. The recommended ultimate bearing capacity factor is determined on the basis of the embedment ratio and displacement magnitude, and the displacement is not more than 30% of the foundation diameter. Finally, two equations are proposed to evaluate both the bearing capacity factor and the effective depth factor.*

**Keywords:** bearing capacity factor, displacement, compression, tension, depth factor

## INTRODUCTION

The suction foundation is a large diameter cylinder, which is open ended at the bottom and closed at the top. Suction foundations are so called because they are installed by pumping water out of the cylinder in order to generate a lower pressure or “suction” in its interior than that outside the cylinder after having settled under its self-weight. The difference between the hydrostatic water pressure outside the cylinder and the reduced water pressure inside creates a differential pressure that acts as an additional penetration force. Once installed, the foundation acts like a short rigid pile and is capable of resisting both lateral and axial loads [1]. With the advantages of easy installation, short installation time, high degree of reliability and low cost, suction foundations have been used

extensively in offshore facilities, such as foundations of jacket structures, current and wind turbines, subsea systems seabed protection structures and as anchors for floating production storage and offloading (FPSO) units, tension leg platforms (TLP), and SPAR platforms [2].

Suction foundations have a larger diameter and longer side wall compared to traditional pile foundations and shallow foundations. After installation, the interior is sealed off and the pullout loading creates a passive suction, which mobilizes the end bearing resistance of the soil at the skirt tip. Considering passive suction, it is assumed that the suction foundation has the same bearing capacity in uplift and compression. Currently the ultimate uplift capacity of a suction foundation is calculated by side friction and the reverse bearing capacity:

$$q_{ult} = N_c s_{u,tip} + 4 \frac{L}{D} \alpha s_{u,av} + q_{plug} - q_0 \quad (1)$$

where  $q_{ult}$  is the ultimate bearing stress on the foundation.  $\alpha$  is the adhesion factor, usually taken as 0.5 to 1.0.  $L$  is the embedment depth and  $D$  is the foundation diameter.  $N_c$  is the bearing capacity factor of the circle footing and varies with the embedment ratio. The value of the surface of the foundation resting on cohesive and frictionless soil is 6.05 [3].  $s_{u,tip}$  is the undrained shear strength of the soil at the foundation tip level,  $s_{u,av}$  is the average undrained shear strength over the penetration depth.  $q_{plug}$  is the self-weight of soil plug and  $q_0$  is the surcharge at the foundation base level.

There are many studies referring to the bearing capacity factor in compression and its relationship to the shear strength [4,5]. Hu et al. investigated the bearing response of skirted foundations on uniform and nonhomogeneous soil using a displacement finite element analysis approach, in which the embedment ratio of the skirted foundation varied from 0 to 0.5 [4]. Houlsby and Martin considered a conical footing embedded in clay using the stress field method [5]. A finite element limit analysis method was employed by Salgado et al. to investigate the upper- and lower-bound solutions of circular foundations embedded in clay [6]. Edwards et al. investigated the bearing capacity factor of embedded foundations using a displacement finite element analysis approach with the embedment ratio of the foundation varying from 0 to 4 [7]. Generally, a suction foundation needs a large displacement in compression to achieve ultimate capacity [4]. Hu et al. reported that the penetration displacement of a deeply embedded foundation may be at least 4D to reach a limit load. However, a large displacement is not necessary to achieve ultimate pull-out capacity in an uplift loading case. Furthermore, the difference in displacement magnitude between compression and tension cases may have a great effect on bearing capacity factors. Finn and Byne proposed a reverse bearing mechanism under uplift in undrained conditions, and recommended that the reverse capacity factor for the uplift loading case is taken as the same value as the compression case [8]. There are a number of centrifuge tests for investigating the difference of skirted foundations ( $L/D \leq 1$ ) under the condition of compression and uplift. Watson et al. and Mana et al. reported the same magnitudes of undrained uplift capacity and compression capacity, while Acosta-Martinez et al. observed 30% reduction in uplift capacity compared to compression capacity [9-11]. The magnitude of passive suction is the key factor to mobilize the reverse capacity. However, the magnitudes of loading rate and preload are the uncertain factors to affect the mobilized uplift capacity. Chatterjee et al. investigated the undrained compression and uplift capacity using large-deformation numerical methods and concluded that the two cases have the same bearing capacity [12]. However, both the centrifuge tests and numerical modeling were aimed at the smaller embedment ratio, the bearing factor increased with the embedment ratio and the larger displacement is needed to mobilize the capacity for longer foundation. Therefore, a range

of embedment ratios were investigated to establish the bearing factors and displacement magnitudes in the cases of undrained compression and uplift.

The objective of this paper is to investigate the difference in the bearing capacity factors of suction foundations in cases of both compression and tension. These factors include the embedment depth, the degree of nonhomogeneity, and the foundation displacement. The results will be useful for the design of suction foundations and have potential applications in offshore marine engineering.

## NUMERICAL MODELLING

This study focuses on the comparison of the bearing factors in the cases of undrained compression and uplift. In the numerical modeling, the suction foundations were simplified as solid foundations and the reasons are listed as followed: (1) both the failure faces of suction foundations in undrained compression and uplift cases are under the base of foundation, this is similar with solid foundation; (2) the bearing capacity factor is calculated based on the undrained shear capacity of soil below the foundation; (3) both the soil and foundation were set weightless to make the effects of soil plug and surcharge vanished. Small-strain analysis of embedded suction caisson foundations was conducted using the FLAC3D software. In order to be consistent with existing design methods and to compare with the results from other studies, the soil was modelled as a linear elastic-perfectly plastic model based on the Tresca failure criterion.

### HOMOGENEOUS CLAY

A constant undrained shear strength,  $s_u$ , equal to 5 kPa and a Young's modulus,  $E_u$ , of  $400 \times s_u$ , were assigned to the soil. A Poisson's ratio of 0.495 was applied to simulate the constant volume response of clay under undrained conditions. The suction caisson foundation had a Young's modulus of  $E = E_u \times 106$ , and was considered to be rigid. The interfaces in the foundation base and side were assumed to be rough and smooth respectively. The rough case was to restrain the horizontal movement of nodes. In the uplift case, any detachment between the foundation base and soil was prevented.

Loading was applied using the displacement-controlled method as it is more suitable than the stress-controlled method to obtain the failure load. All analysis was conducted by applying uniform vertical displacements and zero horizontal displacements to the nodes of the foundation until the failure state was reached. The ultimate load on the footing was then calculated as the sum of the vertical reaction forces on the nodes. This load is equal to the net bearing force, whose value is equivalent to  $N_c s_u A$ . The effect of side friction and surcharge were not included in the load, since the side interface was assumed to be smooth and the soil was weightless. The calculated area  $A$  should contain half the zone width adjacent to the footing edge (since forces are exerted on the footing by this zone, it is assumed that the forces are divided equally between the left and right grid points).

Fig. 1 shows a typical mesh used in the present study.

Owing to the symmetry in geometry and loading conditions, only half of the domain was discretised.  $L$  is the embedded length and  $D$  is the diameter of the foundation. The  $L/D$  ratio had the values of 0 (surface foundation), 0.5, 1, 2, 3, and 4. Displacements at the lower boundary were fully fixed in the  $x$ ,  $y$ , and  $z$  directions. Normal displacements at the lateral boundaries were constrained. The size of the soil elements increased gradually from the foundation to the domain boundary. The length from the foundation to the domain boundary was set at  $5.5D$  (including  $1D$  finer areas under foundation) to minimize the boundary effects. Initially, in order to establish the accuracy of the finite difference analysis, the grid was adjusted to obtain a suitable bearing capacity factor by comparing with the known solutions. A factor  $N_c$  of 6.10 was obtained for the suction foundation, which is 0.8% in error compared with the solution obtained by Eason and Shield (1960) with a factor of 6.05.

### NONHOMOGENEOUS CLAY

In a normally consolidated or a lightly overconsolidated marine clay, suction caissons need to penetrate deeper due to the soft clay in the shallow seabed being unable to provide sufficient strength. This is because for marine sediment, the shear strength increases with depth. The undrained shear strength,  $s_u$  may be idealised as approximately linearly with depth, which can be expressed as

$$s_u = s_{um} + kz \quad (2)$$

where  $s_{um}$  is the soil strength at the seabed (mud line);  $k$  is the strength gradient; and  $z$  is the soil depth (see Fig. 2). The dimensionless ratio  $kD/s_{um}$  is taken to quantify the degree of strength nonhomogeneity beneath the foundation. The value of  $k$  is typically found in the range of 0.6-3.0 kPa/m for clay materials [13]. Typically, the foundations have diameters (or widths),  $D$ , ranging from 3 to 10 m (but may be much larger for skirted foundations of gravity platforms), and the embedment ratio is not more than 6. Five values of the dimensionless ratio,  $kD/s_{um} = 1, 2, 3, 4, 5$ ; and the embedment ratio varying from 0 to 4 were examined in the studies described below.

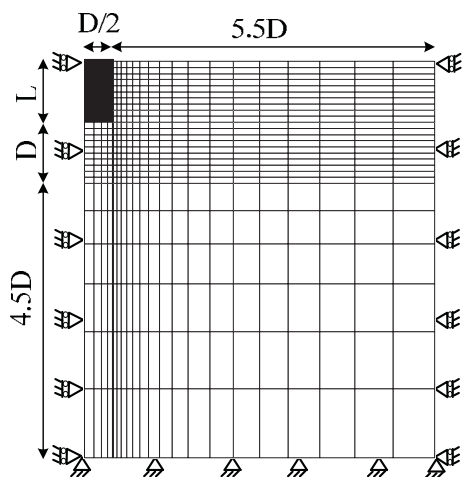


Fig. 1 Finite difference mesh in homogeneous clay

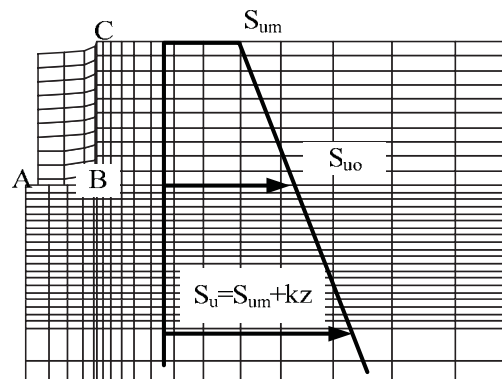


Fig. 2 Finite difference mesh in nonhomogeneous clay

## ANALYSIS RESULTS

### HOMOGENEOUS CLAY

Fig. 3 summarises the results from the suction foundation analysis in compression, and compares the solutions with those of Hu et al. (1999), Houlsby and Martin (2003), Salgado et al. (2004), Edwards et al. (2005) and Hansen (1970) [4-7,14]. The diagram shows the variation of  $N_c$  with embedment ratio  $L/D$ . The rough condition at the base of the footing and the uniform undrained shear strength condition in the soil are employed in the model. The finite difference analysis results for the smooth-sided footings are very close to the finite element analysis results of Edwards et al. (2005), and both fall within the range of the upper- and lower-bound solutions of Salgado et al. (2004). This confirms the accuracy of the finite difference analysis. The curves obtained from the finite element analysis of Hu et al. (1999) are above those of Hansen (1970) and below other studies (excluding the stress field method, Houlsby and Martin (2003)) for  $L/D > 1$ . The reason for this may be that the  $N_c$  value (Hu et al. 1999) was obtained when the foundation displacement was equal to  $0.3D$ , and the displacement magnitude cannot reach the limit load for  $L/D > 1$ . However, it is possible to achieve limit load at  $0.3D$  displacement for  $L/D \leq 1$ . Therefore, the results from Hu et al. (1999) are similar to other finite element and finite difference analyses for  $L/D \leq 1$ .

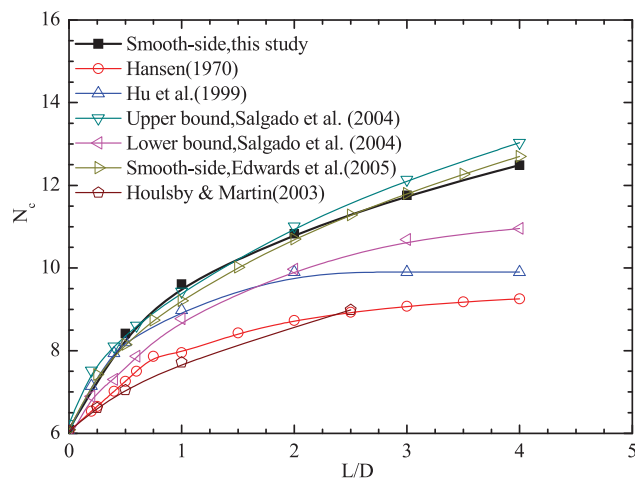


Fig. 3 Comparison of vertical bearing capacities

Fig. 4 presents the normalised vertical load-displacement curves in compression and tension. In the compression case, the ultimate bearing capacity was mobilised at different displacement magnitudes with various embedment ratios. The limit displacements 0.05D, 0.3D, 0.5D, 2D, 3D, and 3D correspond to embedment ratios of 0, 0.5, 1, 2, 3, and 4. 2D displacement is required to achieve the limit load for  $L/D > 1$ . In the tension case, the limit displacement magnitude is identical to that for the compression case for  $L/D \leq 1$ ; the curves overlap and the bearing capacity factors  $N_c$  converge at 10.3, while the displacement reaches 0.8D for  $L/D > 1$ .

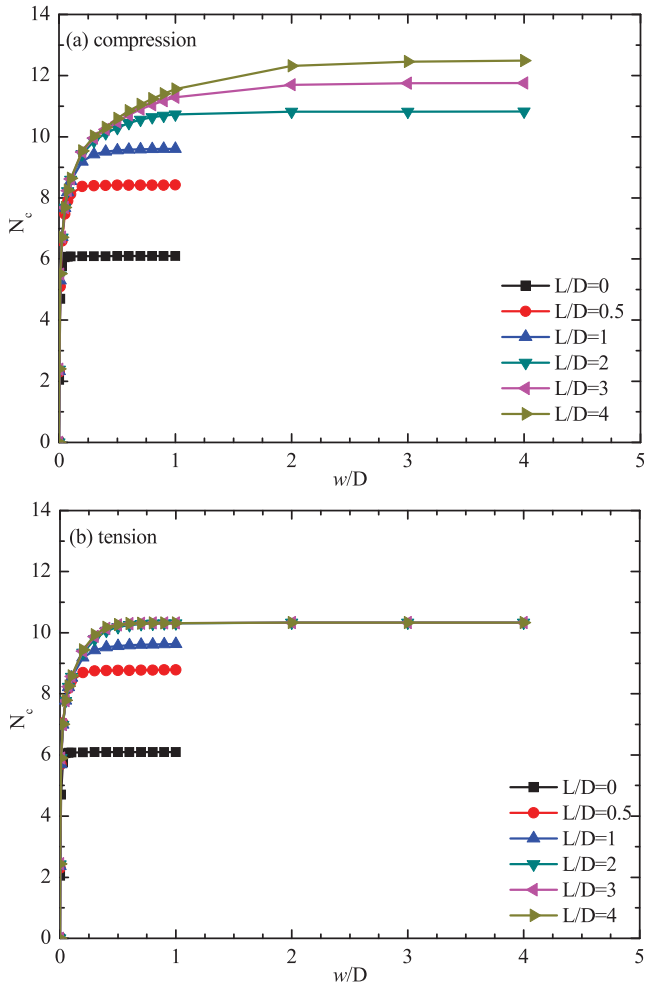


Fig. 4 Normalised load-displacement curve according to  $L/D$  ratios

In engineering practice, a large displacement would affect the normal use of a foundation or super structure so that a smaller displacement would usually be taken as the ultimate displacement of the foundation. Fig. 5 presented the statistic datas from a range of centrifuge tests [10,11,15,16] and 1g tests [17-20]. The ultimate displacements are not more than 0.1D and 0.2D when the embedment ratios less than 1 and 2. Furthermore, the ultimate displacements are merely around 0.3D even for the embedment ratios exceed 4. Therefore, the displacements of 0.1D, 0.2D, and 0.3D were selected to compare with the limit displacement in numerical modeling. Figure 6 shows the vertical capacity of the foundation according to the  $L/D$  ratios. The diagram presents a comparison of bearing capacity factors at 0.1D, 0.2D, 0.3D, and limit displacement

(corresponding to the limit load) in compression and tension. As shown in Fig. 6, the bearing factor curves in compression and tension show very little difference at 0.1D, 0.2D, and 0.3D displacement, however, they show a great difference at limit displacement. Therefore, the same bearing capacity factor can be taken in compression and tension design when the displacement is relatively small. Comparing the results shown in Fig. 3 and Fig. 6, it can be seen that the curve derived from Hansen's results is most close to the results of 0.1D and 0.2D displacement, which suggests that Hansen's formula is still useful in engineering practice.

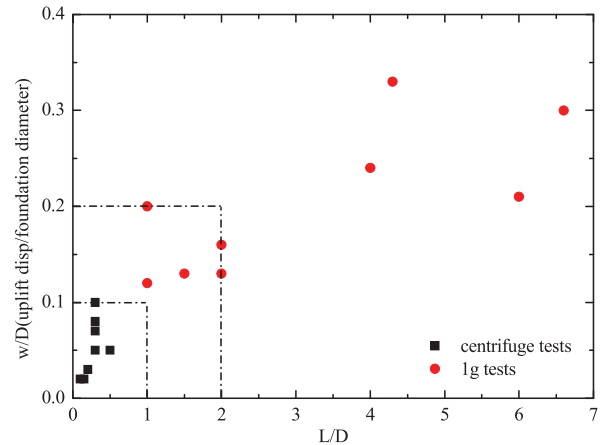


Fig. 5 Normalised uplift displacement with  $L/D$  ratios

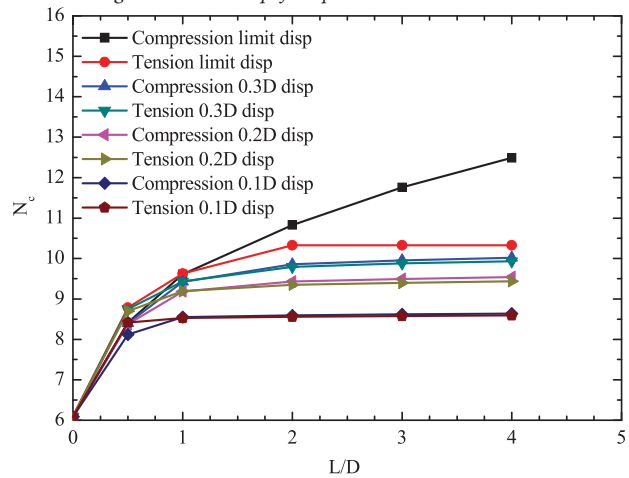


Fig. 6 Vertical bearing capacity according to  $L/D$  ratios

### NONHOMOGENEOUS CLAY

Fig. 7 presents the bearing capacity factors from finite difference analysis according to  $L/D$  ratios in heterogeneous soils. There are a few comparisons which can be made with published work, where the dimensionless ratio  $kD/s_{um}$  varies from 1 to 5. Hu et al. (1999) has investigated the bearing capacity factors with the embedment ratio varying from 0 to 0.5 using the upper boundary method and finite element analysis. As shown in Fig. 6, the finite difference solution is close to the finite element result and the plots are both below the upper-boundary curve. In contrast, the curve from the

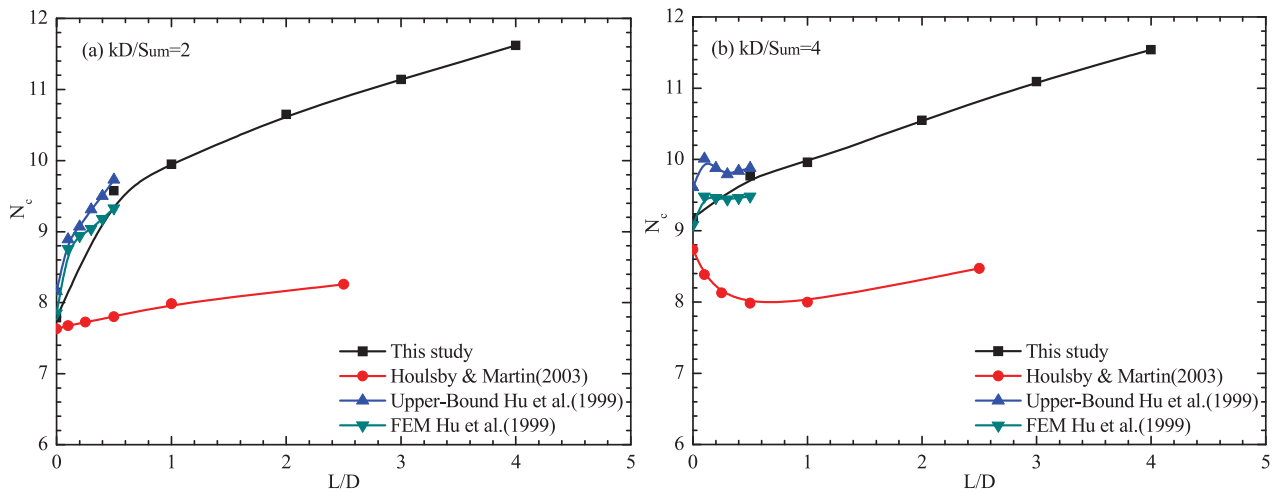


Fig. 7 Comparison of vertical bearing capacity in nonhomogeneous soil

stress field method proposed by Houlsby and Martin (2003) shows significant differences from the plots derived from the finite difference analysis. The stress field solutions predict much smaller bearing capacity factors than the current finite difference analysis. From the comparison of published solutions for homogeneous soil (see Fig. 3), it can be seen that the stress field solutions are even smaller than the lower-bound solutions. Thus, the results from Houlsby and Martin (2003) can be taken as lower-bound solutions in nonhomogeneous soil.

Fig. 8 and 9 show the curves of bearing capacity factors with embedment ratio at different footing displacements in compression and in tension respectively. In the compression case, the curves are indistinguishable up to  $L/D=0.5$ , after which the 0.1D displacement curve begins to deviate from others. The 0.2D displacement curve does not separate from the other curves until  $L/D=1.0$ . Therefore, the resistance corresponding to 0.1D displacement and to 0.2D displacement can be taken as the limit load for  $L/D < 1$  and  $1 \leq L/D < 2$  respectively. The curves in the tension condition have a similar tendency to the compression case for  $L/D \leq 1$ . When the embedment ratio reaches 2, the 0.3D displacement curve also diverges from the limit displacement curve in the compression case. In contrast, the 0.3D displacement curve differs little from the

limit displacement curve in the tension case. In practice, the resistance corresponding to 0.3D displacement can be taken as the limit load for  $L/D \geq 2$  in both the compression and tension cases.

Fig. 10 and 11 show the curves of bearing capacity factors with the degree of nonhomogeneity at different footing displacements, in compression and tension, respectively. In the case of compression, the bearing capacity factor increases linearly with the degree of heterogeneity for the surface foundation. The growth of bearing capacity factor is slow with the increasing heterogeneous degree for embedded foundations, especially in the range where the nonhomogeneous degree varies from 1 to 5. The increment is largely in the transition zone from uniform to nonhomogeneous soil (where  $kD/s_{um}$  varies from 0 to 1), after which the curves become flat. In the limit displacement condition, bearing capacity factors in the uniform soil are even higher than the factors in nonhomogeneous soil for  $L/D \geq 2$ . In the case of tension, the trend of the bearing capacity factor curve was similar to that in compression to a great extent. Comparison of the curves show that when the footing displacement reaches the limit values, the values of  $N_c$  change little with the increase of degree of nonhomogeneity and are almost equal to 10.3 for  $L/D \geq 2$ .

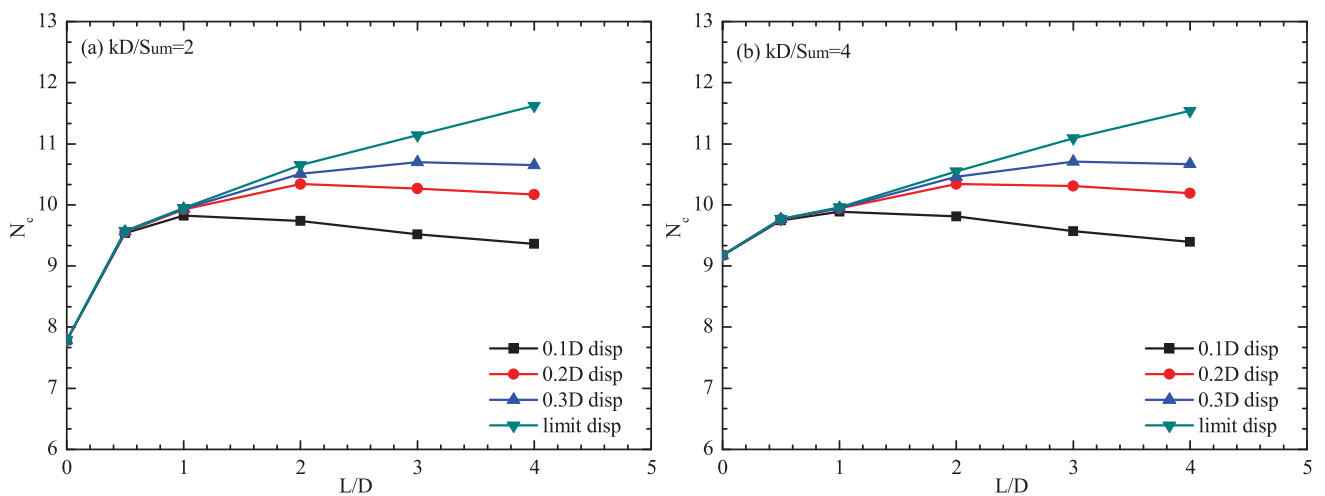


Fig. 8 Bearing capacity of suction foundation with smooth side in compression

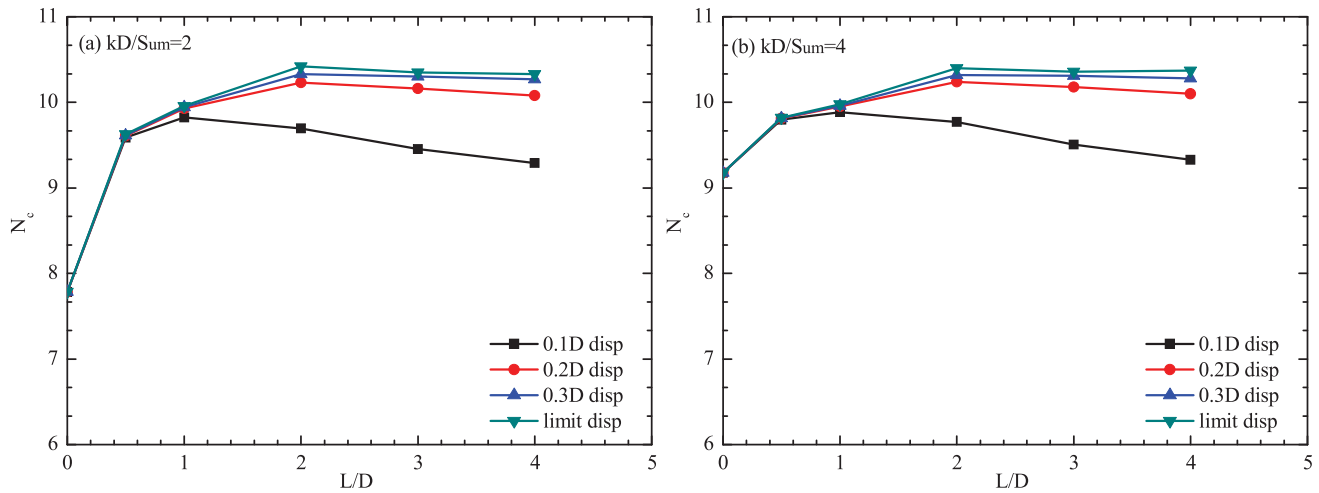


Fig. 9 Bearing capacity of suction foundation with smooth side in tension

## DISCUSSION

Fig. 12 presents the recommended bearing capacity corresponding to the appropriate displacement with embedment ratio. The displacement 0.1D, 0.2D, and 0.3D is taken for  $L/D < 1$ ,  $1 \leq L/D < 2$ , and  $L/D \geq 2$ , respectively. Since the bearing capacity values and tendency are similar in the compression and tension case, the same value can be taken in design. The undrained shear strength of soil has a significantly effect on the bearing factor also. There are some experimental methods to measure the undrained strength. Triaxial compression, triaxial extension and direct shear test were used to measure the undrained shear strength regularly,

and some in-situ methods such as Vane, CPT and T-bar were employed also. However, there are some differences among the tests results. Regularly, triaxial compression has a higher value, triaxial extension has a lower value and simple shear test has a mean value. The results from vane test are higher than other tests [21]. Randolph and Hose (2002) reported that the averaged shear strength obtained from triaxial compression, triaxial extension and simple shear tests have 30% and 50% reduction compared to triaxial extension strength and triaxial compression strength respectively [22]. In order to minimize the influences of anisotropy, the averaged shear strength was suggested to represent the undrained shear strength in calculation of bearing factors. Several researchers

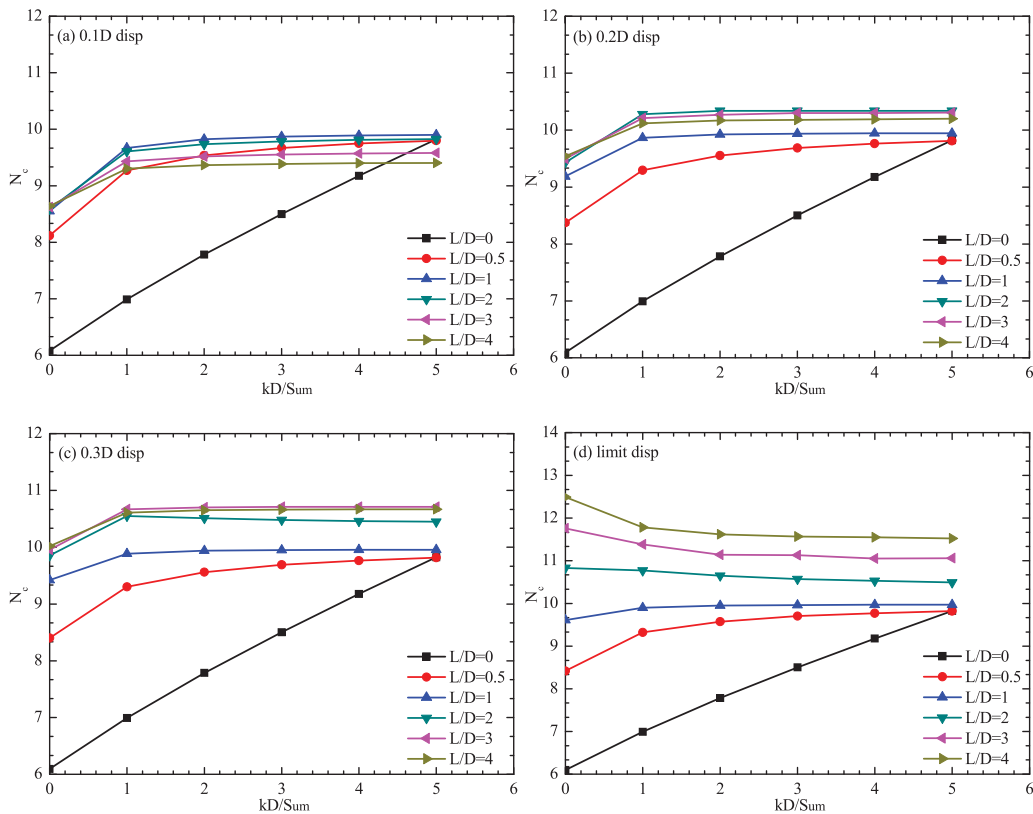


Fig. 10 Bearing capacity of suction foundation with a degree of inhomogeneity in compression

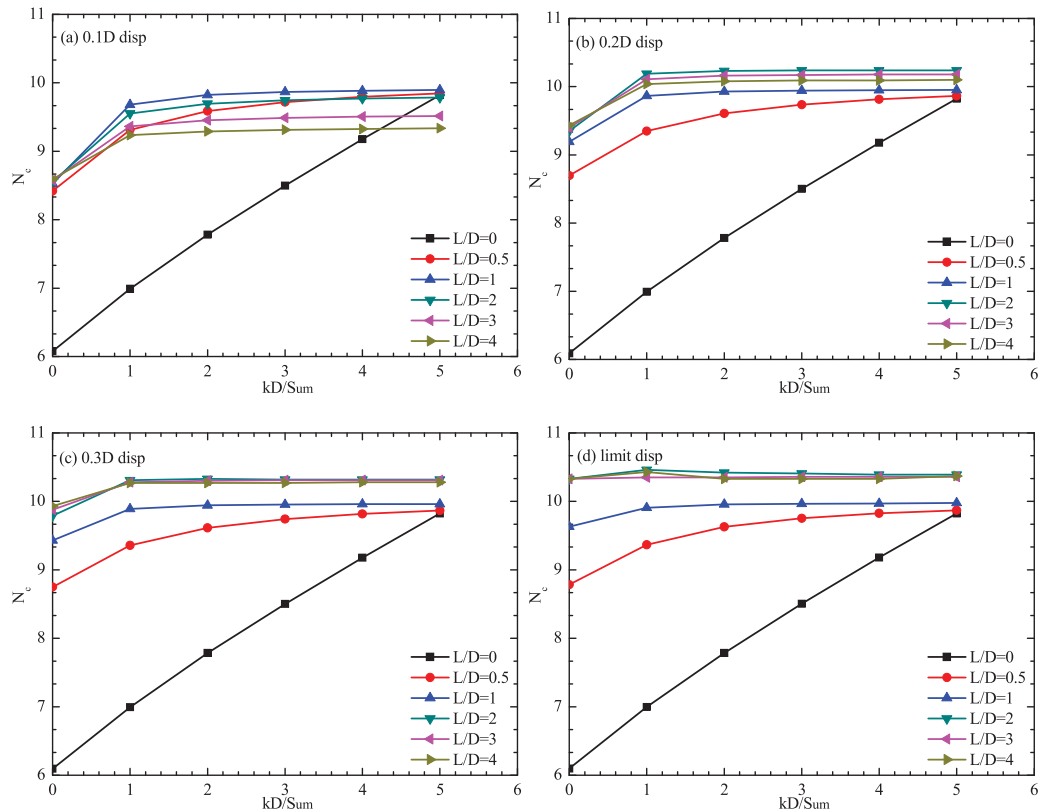


Fig. 11 Bearing capacity of suction foundation with a degree of inhomogeneity in tension

have suggested that  $s_u$  can be taken as the value at depth  $D/3$ ,  $D/4$  or  $D/10$  [23-25] below the skirt tip. Fig. 13 presents the bearing capacity factor results of  $s_u$  at depth  $D/10$  below the base of foundation. Regardless of the compression or tension case, the curves for nonhomogeneous soil almost overlap. Comparing with the curves from Fig. 12, the bearing capacity curves for non-uniform clay are much closer to those for uniform clays. Therefore, the bearing capacity value in uniform clay can be used as a substitute for the value in non-uniform clay for the approximation, and it is conservative in design. Fig. 4 shows the back-calculated  $N_c$  according to the  $L/D$  ratios, and Eq. (3) fits with the data points very well. In addition, the depth factor  $d_c$  is often used to describe the relationship

between the bearing capacity factor and the embedment ratio. Eq. (4) was suggested to evaluate depth factor  $d_c$ , and the value of  $d_c$  is not more than 1.7.

$$N_c = 6.08 [1 + 0.45 \arctan(2L/D)] \quad (3)$$

$$d_c = 1 + 0.45 \arctan(2L/D) \quad (4)$$

Fig. 15 indicates the comparison results of fitted curves of depth factor in this study with other studies [14,25-27].

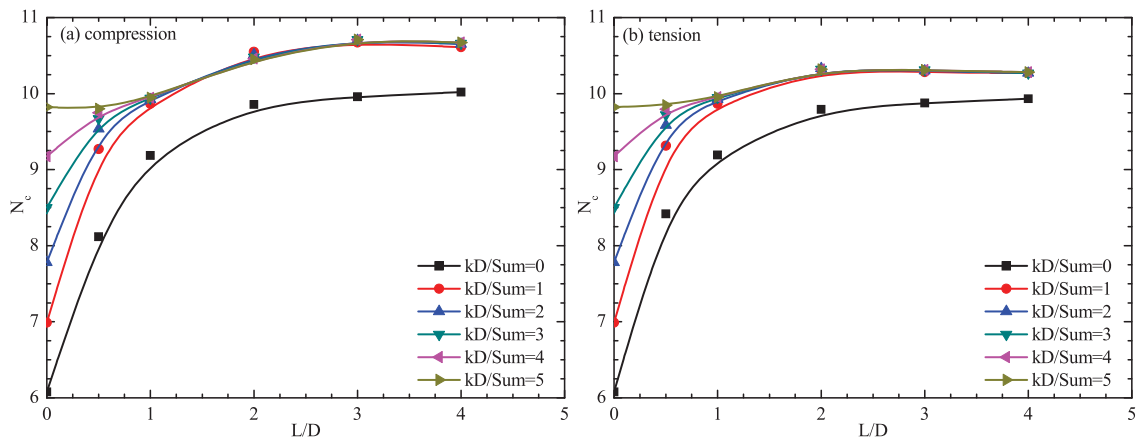


Fig. 12 Recommended bearing capacities with embedment ratios ( $s_u$  at the base of foundation)

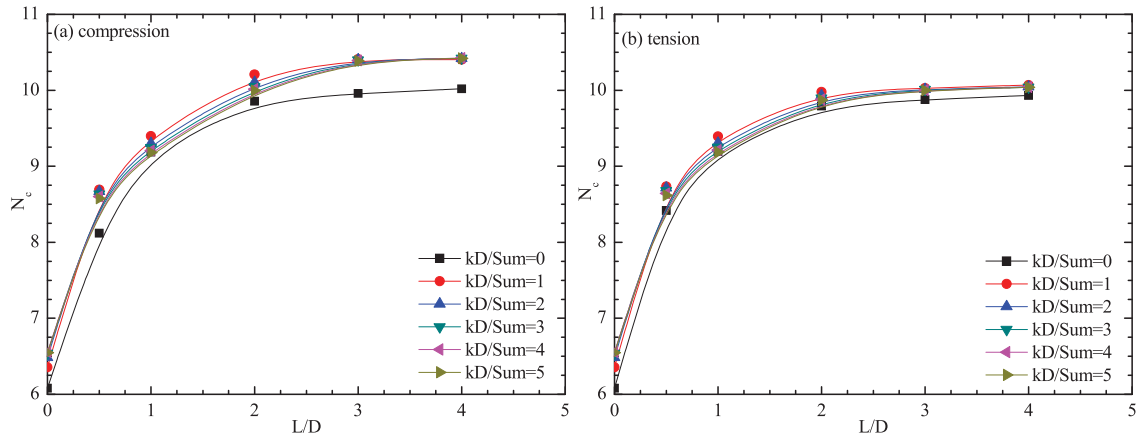


Fig. 13 Recommended bearing capacities with embedment ratios ( $s_u$  at the depth  $D/10$  below the foundation)

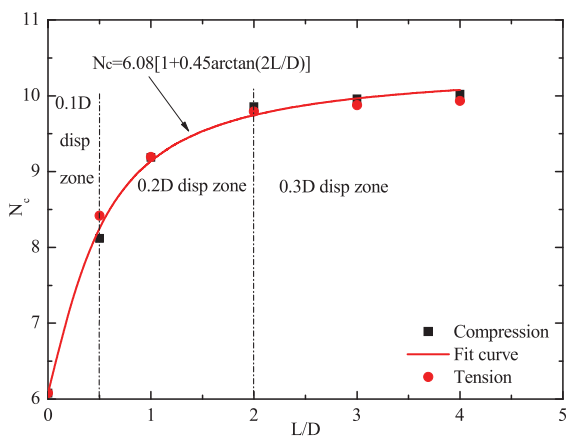


Fig. 14 Fitted curve using the results in uniform clay

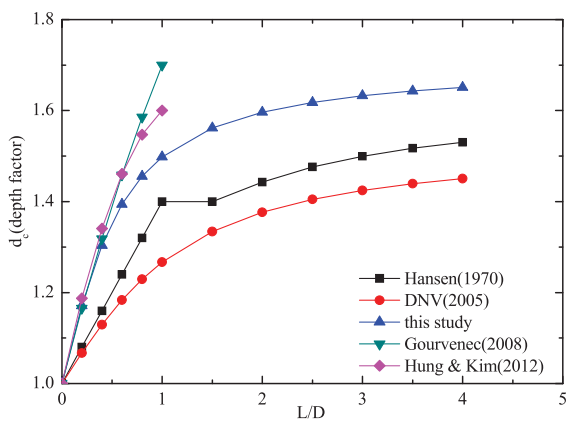


Fig. 15 Comparison of vertical depth factors

The results from finite element analyses proposed a quadratic relationship between ultimate vertical capacity and embedment ratio, for  $L/D \leq 1$  [11,25]. Hansen (1970) suggested a linear relationship for  $L/D \leq 1$  and an arctangent relationship for  $L/D > 1$  [14]. Over the range of embedment ratios  $0 \leq L/D \leq 4$ , the depth factors of this study and DNV can be described by

the arctangent expression. The factors in this study are similar with Gourvenec and Hung's research in the section of  $L/D < 1$ , but have higher values compared to Hansen's and DNV's in the section of  $L/D > 1$ . The reason of the difference is that the larger displacement is allowed in the higher embedment ratios.

## CONCLUSION

This paper presents the comparison results of a finite difference investigation on the undrained bearing capacity of suction foundations under situations of both compression and tension in uniform and non-uniform clay. The following conclusions were drawn:

1. There is a small difference in ultimate bearing capacity between compression and tension loading for the case that the embedment depth is less than two diameters. When the embedment ratio increases from 2 to 4, the ultimate capacity in compression increases by sixteen percent, but the capacity in tension almost remains at the same level.
2. The bearing capacity factors change significantly when the clay varies from homogeneity to heterogeneity. There is a small change when the nonhomogeneous degree varies from 1 to 5. The bearing capacity factors increase with the growth of nonhomogeneous degree.
3. In practical engineering, the values of bearing capacity factors corresponding to the displacement of less than 30% diameters (0.3D) can be taken as the ultimate bearing capacity factors, for both compression and tension cases. The bearing capacity factors in non-uniform clay are approximate to the factors in uniform clay when the  $s_u$  was selected at depth  $D/10$  below the skirt tip.
4. Considering the embedment ratio, a new equation for calculating depth factor is proposed.

## ACKNOWLEDGEMENTS

The research work described herein was funded by the National Nature Science Foundation of China (NSFC) (Grant

No. 41372283), and the Innovative Research Project of Shanghai Municipal Education Commission (Grant No. 13ZZ021). These financial supports are gratefully acknowledged.

## REFERENCES

1. Andersen, K.H., Murff, J.D., Randolph, M.F., Clukey, E.C., Erbrich, C.T., Jostad, H.P., et al.. Suction anchors for deepwater applications. In: Proceedings of the 1st International Symposium on Frontiers in Offshore Geotechnics, ISFOG, Perth. pp. 3-30, 2005.
2. Hossain, M. S. Lehane, B. M. Hu, Y. Gao, Y.. Soil flow mechanisms around and between stiffeners of caissons during installation in clay. *Can. Geotech. J.* 49(4), 442–459, 2012.
3. Eason, G. & Shield. R. T.. The plastic indentation of a semi-infinite solid by a perfectly rough circular punch. *J. Appl. Math. Phys.* 11, No. 1, 33-43, 1960.
4. Hu, Y., Randolph, M. F., and Watson, P. G.. Bearing response of skirted foundation on nonhomogeneous soil. *J. Geotech. Geoenviron. Engng., ASCE* 125, No. 11, 924–935.
5. Houlsby, G. T. and Martin, C. M.. Undrained bearing capacity factors for conical footings on clay. *Géotechnique* 53, No. 5, 513–520, 2003.
6. Salgado, R., Lyamin, A. V., Sloan, S. W. & Yu, H. S.. Two and three-dimensional bearing capacity of foundations in clay. *Geotechnique* 54, No. 5, 297–306, 2004.
7. Edwards, D.H., Zdravkovic, L., Potts, D. M.. Depth factors for undrained bearing capacity. *Géotechnique* 55, No. 10, 755–758, 2005.
8. Finn, W.D.L. and Byne, P.M.. The evaluation of the breakout force for a submerged ocean platform. *Offshore Technology Conference, OTC 1604, Houston*, pp351-365, 1972.
9. Watson, P. G., Randolph, M. F., and Bransby, M. F.. “Combined lateral and vertical loading of caisson foundations.” *Proc., Annual Offshore Technology Conf., Offshore Technology Conference, Houston, OTC 12195*, 2005.
10. Mana, D. S. K., Gourvenec, S. M., and Randolph, M. F.. “Experimental investigation of reverse end bearing of offshore shallow foundations.” *Can. Geotech. J.*, 50(10), 1022–1033, 2013.
11. Acosta-Martinez, H.E., Gourvenec, S.M., and Randolph, M.F.. An experimental investigation of a shallow skirted foundation under compression and tension. *Soils and Foundations*, 48(2): 247–254, 2008.
12. Chatterjee, S., Randolph, M. F., and White, D. J.. “Large-deformation numerical modeling of short-term compression and uplift capacity of offshore shallow foundations.” *J. Geotech. Geoenviron. Eng.* 140(3) 04013021-1-9, 2014.
13. Tani, K., Craig, W.H.. Bearing capacity of circular foundations on soft clay of strength increasing with depth. *Soils and Foundations*, 35(4), pp 21-35, 1995.
14. Brinch Hansen, J.. A revised and extended formula for bearing capacity, *Bulletin NO.28. Danish Geotechnical Institute*, 1970.
15. Acosta-Martinez, H.E., Gourvenec, S.M., and Randolph, M.F.. Effect of gapping on the transient and sustained uplift capacity of a shallow skirted foundation in clay. *Soils and Foundations*, 50(5): 725–735, 2010.
16. Gourvenec, S., Acosta-Martinez, H.E., Randolph, M.F.. Experimental study of uplift resistance of shallow skirted foundations in clay under transient and sustained concentric loading. *Géotechnique* 59, No. 6, 525–537, 2009.
17. Rao, S.N., Ravi, R., Prasad, B.S.. “Pullout behavior of suction anchors in soft marine clays.” *Marine georesources & geotechnology*, 15(2), 95-114, 1997.
18. El-Gharbawy. S. L. The pullout capacity of suction caisson foundations. *PhD thesis, The University of Texas at Austin*, 1998.
19. Villalobos, F. A., Byrne, B. W., Houlsby, G. T. Model testing of suction caissons in clay subjected to vertical loading. *Applied Ocean Research*, 32(4): 414-424, 2010.
20. Guo, Zhen, Wang, Li-Zhong, Yuan, Feng. Set-up and Pullout Mechanism of Suction Caisson in a Soft Clay Seabed. *Marine Georesources & Geotechnology*, 32(2): 135-154, 2014.
21. Watson, P.G., Suemasa, N. and Randolph, M.F.. “Evaluating undrained shear strength using the vane shear apparatus.” *Proc. 10th Int. Conf. On Offshore and Polar Engng, ISOPE 99, Seattle*, 2, 485-493, 2000.
22. Randolph, M. F., House, A.R.. “Analysis of suction caisson capacity in clay” *Proc., Annual Offshore Technology Conf., Offshore Technology Conference, Houston, OTC 14236*, 2002.
23. Skempton, A. W.. The bearing capacity of clays. *Proc. Building Research Cong. London*, 1, 180–189, 1951.
24. Byrne, B.W., Cassidy, M.J.. Investigating the response of offshore foundations in soft clay soils. In: *Proceedings of the 21st International Conference on Offshore Mechanics and Arctic Engineering OMAE’02, Oslo*, paper OMAE2002- 28057, 2002.

25. Hung, L. C. Kim, S. R. Evaluation of vertical and horizontal bearing capacities of bucket foundations in clay. *Ocean Engineering*, 52, pp.75–82, 2012.
26. Gourvenec, S. Effect of embedment on the undrained capacity of shallow foundations under general loading *Géotechnique*, 58(3):177-185, 2008.
27. Det Norske Veritas. Geotechnical Design and Installation of Suction Anchors in Clay. DNV Recommended Practice RP-E303, 2005.

#### **CONTACT WITH THE AUTHORS**

Jiaqing Du<sup>a</sup>  
Shouji Du<sup>a</sup>  
Shuilong Shen<sup>a</sup>  
Zhenyu Yina<sup>b</sup>

<sup>a</sup>Department of Civil Engineering and State Key  
Laboratory of Ocean Engineering  
Shanghai Jiao Tong University  
Shanghai 200240  
**CHINA**  
email: dusj@sjtu.edu.cn

<sup>b</sup>LUNAM University  
Ecole Centrale de Nantes  
GeM UMR CNRS, 6183  
Nantes  
**FRANCE**

# MODEL TESTS FOR SHALLOW-WATER SHIP MANEUVERABILITY IN THREE GORGES RESERVOIR

Chuang Cai, Xinyong Cai, Yi Li

School of River and Ocean Engineering, Chongqing Jiaotong University  
China

## ABSTRACT

*This paper conducts calibration tests on the shallow-water maneuverability of 1:100 ship models for the typical navigation fleets in Three Gorges Reservoir. Major influential factors for the maneuverability similitude between models and prototypes and for scale effect were identified. A correction method for model scale was also established through model tests. Test results indicate that, by correcting the model scales of various fleets based on scale effect, the maneuverability indexes  $K'$  (dimensionless of  $K$ ) and  $T'$  (dimensionless of  $T$ ) of ship models are suitable for shallow-water tests, and properly reflect the maneuvering characteristics of prototypes. The findings provide an experimental basis for the navigation safety in Three Gorges Reservoir.*

**Keywords:** shallow-water test of ship model, simulated computation, maneuverability calibration, scale effect, Z shape test,  $K$  and  $T$  indexes, navigation safety

## INTRODUCTION

The Yangtze River Three Gorges Hydro Project navigation ship fleet model with a 1:100 scale is made for studying a series of navigation problem of Three Gorges Project, the scale of ship model is in line with normal hydraulic model. Before the test, ship model maneuverability calibration must consult the actual ship, maneuverability similarity of ship model and actual ship is found, and maneuverability need to be corrected properly, made ship model test have actual ship navigation feature, to ensure ship fleet navigation safety [8]. Ship fleet is 2640 HP, respectively pushing 3, 6 and 9 kilotons covered barge, make up three different times ship fleets: recent, late and forward.

Test of ship model and hydraulic model is based on gravity similar rule. Because  $Re$  is different, maneuverability of ship model is different from actual ship. It is defined as maneuverability scale effect. In order to ensure maneuverability similarity of ship model and actual ship, ship model scale effect is needed to be corrected.

In order to study maneuverability similarity of ship model and actual ship, the shallow water test focuses on the depth similar to navigation channel of Three Gorges Project.

## ACTUAL SHIP INFORMATION IN GENERAL

China the Yangtze shipping science institute has done actual ship hydrostatic maneuverability test in Poyang lake of Jiangxi

province, relevant ship fleet  $K'$ ,  $T'$  value in (Tab.1). According to the existing ship, combine the recent shipbuilding plan, the ship fleet is selected as Three Gorges Project standard navigation ship fleet [2]. The recent is 2640 HP+3×1000 t pusher barge ship fleet, trial speed is 4.289 m/s; The late is 2640HP+6×1000t pusher barge ship fleet, trial speed is 3.567 m/s; The forward is 2640HP+9×1000t pusher barge ship fleet, trial speed is 3.15 m/s. The above three formations must be 100, 150, and 200 Z shape experiment. Actual ship report suggested that calibration prototype data of three ship fleet models' Z shape experiment was based on 150 rudder angle  $K'$ ,  $T'$  value. According to test requirement, this ship model maneuverability calibration test focuses on two ship model formations: 3×1000 t and 9×1000 t (Fig.1). The ship fleet standard hydrostatic navigation speed is the average value of every ship formation.

## SHIP MODEL TEST IN GENERAL

Test model: According to geometric similarity, ship is made of glass fiber reinforced plastics, step-less steering remote control, transform speed, test camera with beat flash and laser scanning are installed.

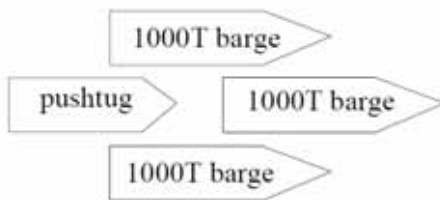
Test basin: Built in a closed trial hall, the test is not affected by outside wind and highlight. The size is 42 m×13.5 m×1.4

m, the depth of water can adjust in a range of 0 m and 1.4 m, flatness error of the bottom is less than  $\pm 1$  mm, it can be used as ship model shallow water test.

Tab. 1. Actual  $K'$ ,  $T'$  Index and Trial Speed

Index	Rudder Angle( $^{\circ}$ )	3 Barges	6 Barges	9 Barges
$K'$	10	2.050	1.775	1.715
	15	1.680	1.640	1.540
	20	1.590	1.460	1.340
$T'$	10	0.998	0.780	0.773
	15	0.695	0.653	0.640
	20	0.681	0.626	0.429
trial speed (m/s)		4.289	3.567	3.155

(a)



(b)

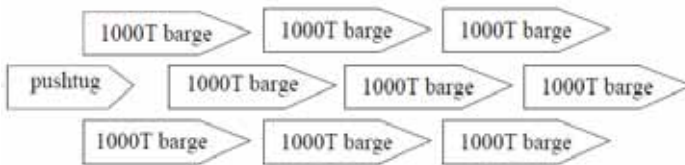


Fig. 1. Ship model maneuverability calibration test fleets (a. Recent navigation 3000t ship model fleet with a scale 1:100; b. Recent navigation 9000t ship model fleet with a scale 1:100)

Test system: Test uses CMZ-3B ship model automatic test system. The test system can non-contact rapidly scan ship model movement by using laser scanning instrument, computer will realize real-time telemeter, control and compute for operation posture and maneuverability element of ship model, test will happen automatically. It is able to do the test of ship model sailing, Z shape and turning, and watch the dynamic process after test [1].

### TEST METHOD

The channel of Three Gorges Project is narrow and changeful; ship fleet is mainly sail with frequent small rudder angle, so it meets the actual circs better for analyzing maneuverability of navigation ship model by Z shape test. Before the test, ship model is adjusted for straight course, trail speed was set. When reaches to the specific conditions of test, begin to steer first rudder, CMZ-3B system will finish the whole process of calibration test. Computer can provide real-time process curve, and watch sailing dynamic process from digital display window. After the test, CMZ-3B system can work rapidly data processing, real-timely output every maneuverability parameter, and draw process related diagrams.

### COMPUTATIONAL METHOD

The analysis and computation of ship model maneuverability test date is on the basis of ship linear first-order maneuverability movement differential equation [5-8].The Equation as follows:

$$T d\dot{\theta}/dt + \dot{\theta} = K\delta \quad (1)$$

Where:  $\theta$  = rotary angular velocity;  $t$  = time;  $\delta$  = rudder angle;  $K$  = revolving index;  $T$  = steering quality index.

First according to telemetry data, we can obtain relationship of Time ( $t$ ), Heading angle ( $\theta$ ) and Rudder angle ( $\delta$ ), draw procedure chart  $\theta$ - $t$ ,  $\delta$ - $t$ . In the chart  $\theta$ - $t$ ,  $\delta$ - $t$ , characteristic parameter of different period of times into Equation (1), compose simultaneous differential equations, ship maneuverability index  $K$ ,  $T$  and normalized index  $K'$ ,  $T'$ , facilitates comparison of ship model and actual ship.

Analysis and calculation process of  $K$ ,  $T$  as follows:

$\delta=0$ , ship cannot directly sail under water flow influence of outside conditions, constant modifications  $\delta_y$  need to be taken into account  $\delta_r$ , first-order Equation (1) can be given

Tab. 2. Ship Model Z Shape Test Result (15°Rudder Angle)

Ship Fleet		Rudder Area (%)	$K'$		$T'$	
			Numerical Value	Error (%)	Numerical Value	Error (%)
Actual	9 Barges	100	1.540		0.640	
	3 Barges	100	1.680		0.695	
Model	9 Barges	100	1.408	-8.57	0.564	-11.88
		80	1.371	-10.97	0.646	+0.94
	3 Barges	100	1.498	-10.83	0.638	-8.20
		80	1.451	-13.63	0.716	+3.02

as follows:

$$T d\dot{\theta}/dt + \dot{\theta} = K(\delta + \delta_\gamma) \quad (2)$$

t(0,t) integrate Equation (2)

$$T\dot{\theta} + \theta = K\delta_\gamma t + K \int_0^t \delta(t) dt \quad (3)$$

When:  $\theta$  reaches to maximum, put  $t = (t_e, t_e', t_e'')$  separately into Equation (3) now angular velocity  $\dot{\theta} = (\dot{\theta}_e, \dot{\theta}_e', \dot{\theta}_e'')$  tend to be 0. We can obtain:

$$\theta_e = K \int_0^{t_e} \delta(t) dt + K\delta_\gamma t_e \quad (4)$$

$$\dot{\theta}_e' = K \int_0^{t_e'} \delta(t) dt + K\delta_\gamma t_e' \quad (5)$$

$$\dot{\theta}_e'' = K \int_0^{t_e''} \delta(t) dt + K\delta_\gamma t_e'' \quad (6)$$

$K, \delta_\gamma$  can be found by Equation (5) and Equation (6), put  $\delta_\gamma$  into Equation (4), obtains  $K$ , defined as  $K_4$ . Integrate  $t_2 \rightarrow t_e$  interval into Equation (3) become to:

$$T(\dot{\theta}_2 - \dot{\theta}_0) = \theta_e - \theta_2 - K \int_{t_2}^{t_e} \delta dt - K\delta_\gamma(t_e - t_0) \quad (7)$$

Plug  $K_4, \delta_\gamma$  in Equation (7), obtain  $T_4, T_6, T_8$  can be deduced by analogy.

In order to facilitate comparison of ship model and actual ship normalized  $K, T$ :

$$K' = K \cdot \frac{L}{V_s}, T' = T \cdot \frac{V_s}{L} \quad (8)$$

Ship maneuverability index  $K, T$ , eliminate the effect of scale and velocity, can directly compare the maneuverability similarity of actual ship with model under various conditions. Revolution index  $K$  is large, shows revolution is good, steady turning radius is small; Steering quality index  $T$  is small, shows stability is good, steerage is good.

The analysis of model and actual ship maneuverability index  $K, T$  is found by using the above method, (Tab. 2) shows the result.

## SHIP MODEL TEST SCALE EFFECT AND CORRECTION

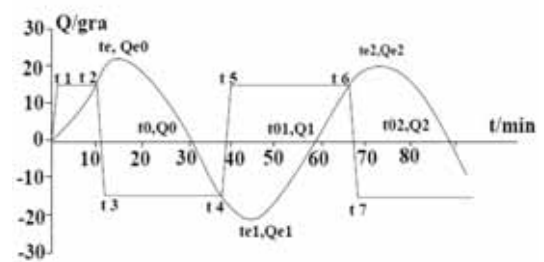
Ship resistance is divided into residual resistance and friction resistance [10], residual resistance relative to Froude number ( $Fr$ ), friction resistance only relative to Reynolds number ( $Re$ ). Ship model and hydraulic model are usually on the basis of gravity similar principle ( $Fr$  equal number), residual resistance part similar of prototype and model. Under gravity similar condition, ship model have to satisfy  $Re$  similar also, because  $Re$  of model is always less than actual ship, results to different maneuverability, this behavior is defined as maneuverability scale effect. In order to ensure maneuverability similar, ship model is need to be corrected scale effect. At present, the

common method of scale effect correction is reducing push wheel edges rudder area, correct rudder effect.

First is 9 barges and 3 barges ship model Z shape calibration test (100% rudder area). In the research work of china inland channel and across buildings standard ship model test, it is put forward that  $T'$  error margin between ship model and actual is no more than 5%,  $K'$  is no more than actual ship 80% [3,4]. The test result shows that 9 barges and 3 barges ship model (100% AR)  $T'$  are respectively reduce 11.98% and 8.20% relative to actual ship, all exceed 5%, ship model scale effect is obvious, which is need to be corrected.

According to result analysis of original rudder ship model maneuverability calibration test, appropriate negative correction to ship model original rudder. Determined by comprehensive analysis, we can reduce 20% of full rudder area, which is on the basis of actual ship maneuverability calibration procedures, for 9 barges and 3 barges ship model Z shape calibration test. Comparing with 100% AR (Fig.4), test result of reduce 20% rudder area (80% AR) (Fig.2, Fig.3) showed that,  $T'$  has a significant increase,  $K'$  is just a small decrease. When pushing wheel edges rudder area is reduced, gyration moment of rudder is decreasing,  $K'$  is decreasing. Meanwhile, caudal role of rudder has been weakened; gyration moment of resistance  $N$  is decreasing,  $K'$  has been weakened, so  $K'$  is just a small decrease. When rudder area is reduced, gyration damping moment  $N$  of ship model is decreasing, gyration moment of inertia  $I$  is not changed, so  $T'$  has a significant increase when rudder area is decreased. In this calibration test, with rudder area changing, trends of  $K'$  and  $T'$  is reasonable. Ship model of 9 barges and 3 barges are corrected,  $K'$  is respectively to be 10.97% and 13.63% smaller than actual ship,  $T'$  is respectively to be 0.94% and 3.02% larger than actual ship. Compare with actual ship, error of  $T'$  is no more than 5%,  $K'$  is no less than 80%. It shows that ship model maneuverability can satisfy navigation conditions of test after corrected.

(a)



(b)

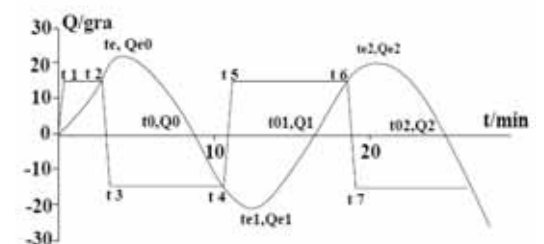


Fig. 2. Various ship model fleets with a scale 1:100 15°Z shape test (80% AR,  $H = 5m$ ) (a. 9 barges fleet; b. 3 barges fleet)

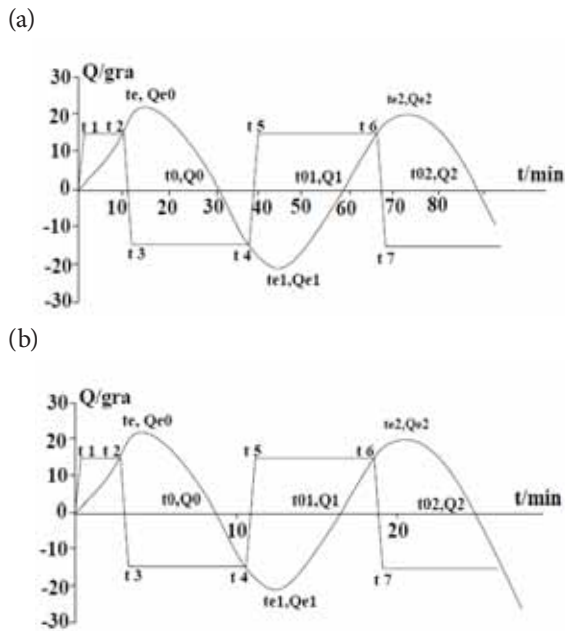


Fig. 3. Various ship model fleet with a scale 1:100 15°Z shape test (80% AR, H = 5m)(a. 9 barges fleet; b. 3 barges fleet)

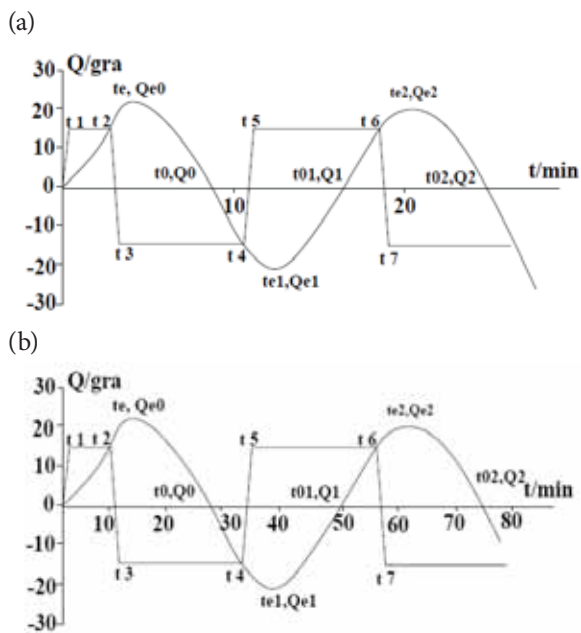


Fig. 4. Various ship model fleets with a scale 1:100 15°Z shape test (100% AR) (a. 9 barges fleet; b. 3 barges fleet)

The analysis of ship test data is on the basis of large ship model simulated computation result, which is put forward in the research of Three Gorges Project standard navigation maneuverability motion mathematic model and correlation technology. Test computation result (Tab.3) showed that, shallow water ship model test (H=5 m), compare with H=∞, hydrostatic navigation speed is lower, K', T' increase, the trends is in line with simulated computation results. According to various numerical values, the change direction of ship model speed is similar to simulated computation speed of 9 barges ship fleet. Ship model test (H=5 m) compares with test (H=∞, 80% AR), K', T' and simulated computation are at a similar change rate, T' is slightly bigger. After corrected, 9 barges model (80% AR) at H=5 cm (equal to actual ship H=5m), compares with K', T' of Z shape test simulated computation (H=5 m, 15°rudder angle), it is basically satisfied that error of T' which is no more than 5% and K' is no less than 80%. T' is slightly bigger and it is safe for actual ship.

### CONCLUSIONS

The maneuverability calibration result was based on ship model of 3 barges and 9 barges Z shape test with a scale 1:100, showed that every fleet maneuverability index K', T' is corrected, in agreement with changing regularity of scale and rudder area as a function of actual ship, the trends is reasonable. The dispersion of ship model calibration test result is smaller, stable and reliable. The changing trends and numerical value of ship model shallow water K', T' is in accordance with actual ship simulated computation, meet the requirements of approximate to actual ship and actual ship security. It showed that ship model maneuverability can satisfy navigation conditions of test after rudder area corrected, and have the maneuverability feature of actual ship. Result is safe.

The findings of this paper may significantly facilitate the shallow-water maneuverability calibration of navigation ship fleets.

Notice: H=∞, error is compared with actual ship result; H=5 m, error is compared with simulated computation result (equal to ship model 5 cm).

Tab. 3. Ship model shallow water Z shape test (H=5m, 15°)result compared

Depth	Fleet		Rudder Area (%)	K'		T'		Speed (m/s)
				Numerical Value	Error (%)	Numerical Value	Error (%)	
H=∞	Actual Ship	9 Barges	100	1.540		0.640		3.155
		3 Barges	100	1.680		0.695		4.289
	Ship Model	9 Barges	80	1.371	-10.97	0.646	+0.94	0.3155
		3 Barges	80	1.451	-13.63	0.716	+3.02	0.4289
H=5cm	Ship Model	9 Barges	100	1.487		0.657		3.155
		3 Barges	80	1.598	-10.22	0.995	+5.73	0.2617
H=5m	Simulated Computation	9 Barges	80	1.891		1.067		0.3450
H=5m	Simulated Computation	9 Barges	100	1.780		0.938		2.606

## ACKNOWLEDGEMENTS

The first author would like to thank the help of testing ground for faculty members at Chongqing Jiaotong University. This study is subsidized by National Natural Science Foundation of China (59453600).

## REFERENCES

1. Cai, C. "The development of J G II-V3.0 general software in Three Gorge pivot ship model experiment". Journal of Chongqing Jiaotong University. Vol 20, No 2, pp110-115,2001.(in Chinese)
2. Cai, R-Z. "The Experimental studies on small ship model serviceability calibration and serviceability in shallow water in Three Gorges Project". Southwest Research Institute for Water Transport Engineering. Vol 3, No 8, pp 10-15,1996. (in Chinese)
3. Cai, R-Z. "The experimental studies on small ship model serviceability calibration and serviceability in shallow water in Three Gorges Project's applied fundamental Research". Beijing: Press of University of Science and Technology of China. Vol 2, No 5, pp 88-90,1997. (in Chinese)
4. Jiang, Y-Q, Duan, Y-L, and Liu, R-X. "An unstructured-mesh MATLAB generator and numerical simulation of shallow water problems". Journal of Hydrodynamics. Vol 5, No 3, pp 56-59,2009. (in Chinese)
5. Katsuro K. "On the Maneuvering Performance of a Ship with the Parameter of Loading Condition." SNAJ, Vol 12, No 168, pp 112-130,1990.
6. Muk, CO, Salina, CC, Arthur, TB, Edmond, YM, and Soon KT. "Simulating ship maneuvers in deep and coastal waters." Journal of ship research, Vol 51, No 3, pp 204-216,2007.
7. Sheng, Z-B, and Liu, Y-Z. "Principle of naval architecture". Shanghai Jiaotong University Press, Vol 11, No 6, pp 123-126,2004. (in Chinese)
8. Su, X-Q. Ship maneuverability. National Defense Industry Press,1995.(in Chinese)

## CONTACT WITH THE AUTHOR

Chuang Cai  
Xinyong Cai  
Yi Li

School of River and Ocean Engineering  
Chongqing Jiaotong University  
ul. Xuefu Avenue No.66 Chongqing  
tel.: +86 57 62652770, fax: +86 57 62650204  
**CHINA**

# SEISMIC MATERIAL PROPERTIES OF REINFORCED CONCRETE AND STEEL CASING COMPOSITE CONCRETE IN ELEVATED PILE-GROUP FOUNDATION

**Mi Zhou**

Key Laboratory for Old Bridge Detection and Reinforcement Technology of the Ministry of Transportation, Chang'an University, Xi'an, Shaanxi, China

National Engineering and Research Center for Highways in Mountain Area, Chongqing, China

**Wancheng Yuan**

State Key Laboratory for Disaster Reduction in Civil Engineering, Tongji University, Shanghai 200092, China

**Yue Zhang**

School of Construction and Civil Engineering Xi'an University of Science and Technology, Xi'an, China

## ABSTRACT

*The paper focuses on the material mechanics properties of reinforced concrete and steel casing composite concrete under pseudo-static loads and their application in structure. Although elevated pile-group foundation is widely used in bridge, port and ocean engineering, the seismic performance of this type of foundation still need further study. Four scale-specimens of the elevated pile-group foundation were manufactured by these two kinds of concrete and seismic performance characteristic of each specimen were compared. Meanwhile, the special soil box was designed and built to consider soil-pile-superstructure interaction. According to the test result, the peak strength of strengthening specimens is about 1.77 times of the others and the ultimate displacement is 1.66 times of the RC specimens. Additionally, the dissipated hysteric energy capability of strengthening specimens is more than 2.15 times of the others as the equivalent viscous damping ratio is reduced by 50%. The pinching effect of first two specimens is more obvious than latter two specimens and the hysteretic loops of reinforced specimens are more plumpness. The pseudo-static tests also provided the data to quantitatively assessment the positive effect of steel casing composite concrete in aseismatic design of bridge.*

**Keywords:** pseudo-static tests, material properties, reinforced concrete, steel composite concrete

## INTRODUCTION

The elevated pile-group foundation is widely used in large span or long bridges. Although the foundation form has advantages of strong adaptability, little project cost and short construction period, the disaster investigation shows it still is the vulnerable component in bridge under earthquake. The seismic performance of this type of foundation has not been studied carefully up to now (Zhou Mi and Yuan Wancheng, 2010 [10]; Yuan Wan-cheng and Jun Yang, 2007 [8]). Many bridges have been built in recent years with this type of foundation in China, but almost no existing design guidelines and design codes dealt with the design and computation of large-scale elevated pile-group foundations under dynamic loading. This paper studied the material mechanics properties

of reinforced concrete and steel casing composite concrete under pseudo-static loads. Meanwhile, the seismic behaviors of the elevated pile-group foundation specimens which were cast by these two kinds of materials were compared and analyzed.

Experimental activities on 4 scale-models of the elevated pile-group foundation belonging to a real bridge were studied in the paper. The tests consist of cyclically imposed displacement to 4 specimens, performed in the state key laboratory for disaster reduction in civil engineering of Tongji University. Two specimens named as ST-specimen which were strengthened by steel protective pipe at each pile top to compare with original reinforced concrete specimen named as RC-specimen. In the paper, pseudo-static testing and damage mechanisms of two kinds of specimens were summarized.

## PSEUDO-STATIC MODEL TESTS

The tests consist of cyclically imposed displacement to 4 specimens, performed in the electro-hydraulic servo loading system of Tongji University. Two specimens were steel composite concrete structures and others were reinforced concrete structures which were respectively named as ST-specimen and RC-specimen. The pile-group foundation model was composed by 9 piles. Because the actuator is located at the bottom of loading equipment, models were required to be installed in inversion method. So a combined type soil-box was designed in the paper. When dynamic factors were ignored the soil around pile could be considered as a series of linear or nonlinear springs. The soil-box combined flexural rigidity of steel sheet and axial stiffness of pull rod to simulate the soil-pile interaction. In Fig.1, elevation photos of pile-group foundation model were shown and the special soil box details were expressed in Fig.2. Six rows of steel springs were built for each pile to consider soil-pile-superstructure interaction.

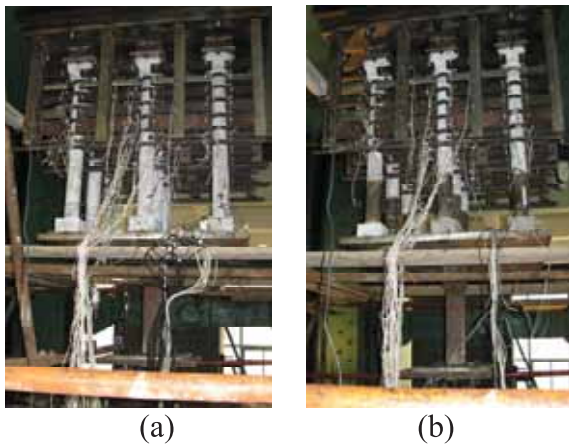
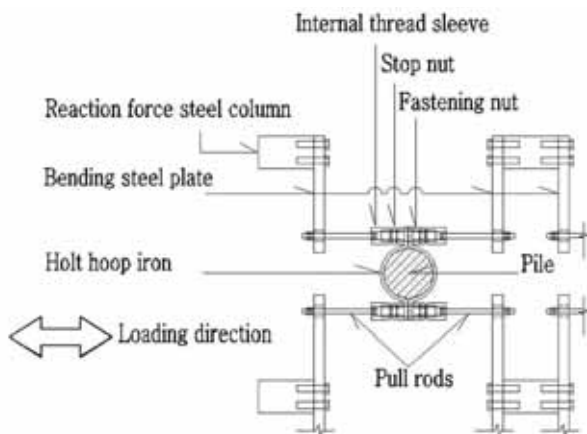


Fig. 1. The elevation photos of pile group foundation models: (a) RC-specimen (b) ST-specimen



(a)



(b)

Fig. 2. The special soil box detail: (a) The layout plan of soil box (b) The 3D schematic plot of the soil box

The amplitude of the cycles is variable from 2 mm to 80 mm. In each load amplitude, three cycles of displacements have been imposed. The frequency of the applied signal is equal to 0.02 Hz in order to realize a quasi-static test [6]. The dead load acting on the scaled pier is equal to 75 kN. Piles were poured by C30 concrete. Correspondingly pile cap and pier were accurately machined by Q235 steel. Design parameters of scaled models were listed in Table 1.

### LOAD-DISPLACEMENT HYSTERETIC PROPERTY OF SPECIMENS

After data analysis, the hysteretic properties are very similar from elevated pile cap system to single component. Hysteretic curves forming process of all specimens are nearly same. The area of hysteretic circle which is consisted of loading- and-unloading curves is very small before concrete crack, resembling a sharp-shuttle (Fig.3).

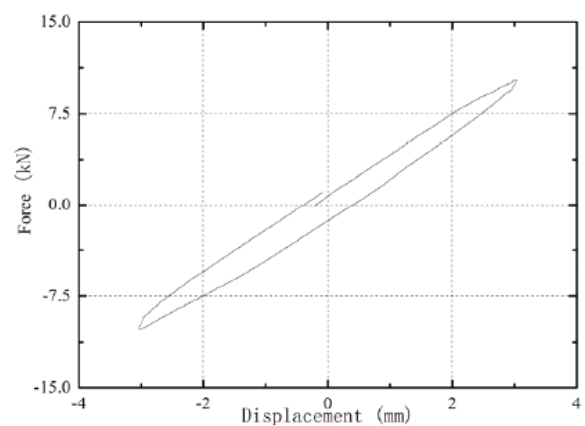


Fig. 3. Hysteretic circle in elastic stage ( $u < 1$ ) Fig. 4. Hysteretic circle in yield stage ( $u > 1$ )

While deformation is getting larger, horizontal cracks in concrete surface begin to appear in succession, and damaged degree of specimen increase gradually. The shape of hysteretic

Tab. 1. Design parameters of models

Specimen number	Scale	Pile diameter	Pile space	Free segment	Main reinforcement ratio	Hoop reinforcement ratio	Steel casing thickness/length	Pier height	Vertical force at the top of pier
		[cm]	[cm]	[cm]	(%)	(%)	[mm]	[cm]	[kN]
RC-1,2	1:20	9.0	44.5	49.0	0.871	0.379	none	72.0	75.0
ST-3,4	1:20	9.0	44.5	49.0	0.871	0.379	1.0/400	72.0	75.0

circle inchmeal achieves transition from a narrow line shape to a relatively full shuttle shape (Fig.4), which shows the typical hysteretic property of bending component, besides, loading and unloading rigidity decrease gradually with the increase of deformation.

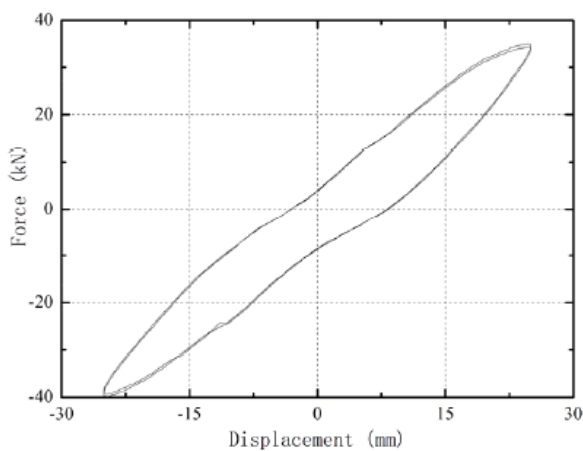


Fig. 4. Hysteretic circle in yield stage ( $u > 1$ )

When the deformation continues increasing, damage becomes more severe, width of horizontal crack is gradual extending, along with which, there are turning up of a small quantity of oblique and vertical cracks. Meanwhile, the hysteretic circle begins to presents certain shrinkage, but there's no such effect on the third and the forth specimen.

In destruction stage, hysteretic circles of RC specimens have the gradual transition from spindles to bows, and there is pinch phenomenon in the middle, which indicates that relatively slide between reinforcing bar and concrete is obvious (Fig.5), as well as  $P - \Delta$  effect has strongly influence on the two specimens [9]. Rigidity variation of the two specimens in the mass is stable, there are typical bending characteristics in damage zone, before failure displacement mainly produces horizontal crack, and oblique ones don't appear. There are vertical cracks on outside concrete due to vertical compression when failure is drawing near. Because the RC specimen is bending failure, in addition to reinforcement ratio is moderate, there are some warning signs before the last limit state. When the displacement on pier top is up to 35mm, concrete on pile head splits apart and rubs off constantly under cyclic loading, and the rigidity of the whole system begins to degenerate more quickly. When reached the limits of displacement, degeneration of rigidity

and strength grows. By the agency of steel pipe, initial rigidity of the third and fourth specimen is greater than the first two specimens. Their hysteretic circles are spindle shape in initial stage. Because the steel tube on pile head has strong confinement effect to core concrete, concrete expansion is restricted and the growth of the cracks in core concrete is also arrested. Moreover, bond-slip between steel and concrete is reduced. The hysteretic circles of the latter two specimens are much full compared with the former two's, and they transform from spindle shape to Z-shape gradually in destruction stage (Fig.6), which indicates that the failure model is shear-slip construction [6]. The reason is that there is an abrupt change of bearing capacity of pile at the end of the steel pipe, which's the just position the second plastic hinge forms. The shear failure of the latter two specimens was caused by the lacking of shear resistance in the position where the cross section is changing.

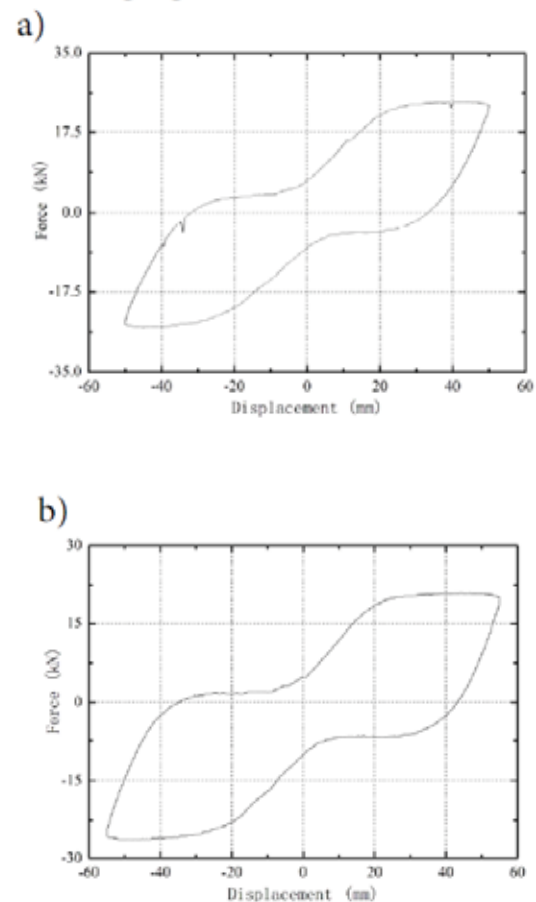


Fig. 5. Hysteretic circle of the RC specimen in destruction: (a) RC-1 specimen (b) RC-2 specimen

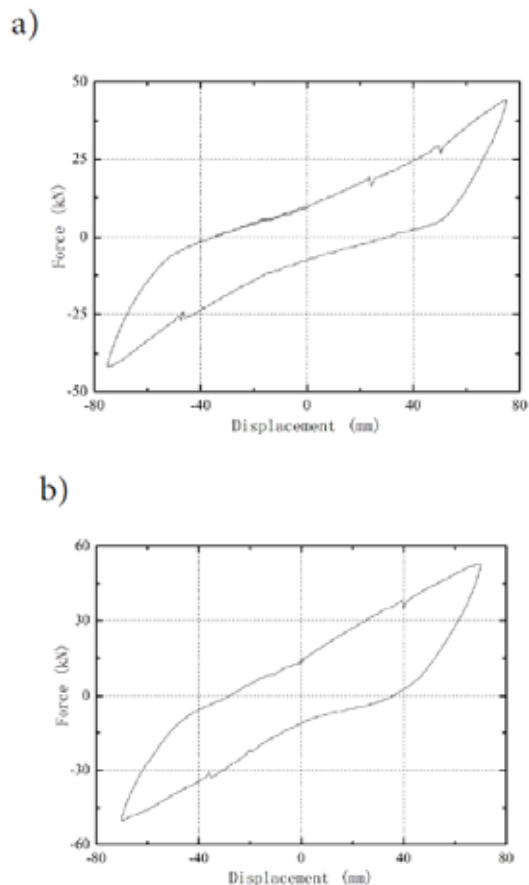


Fig. 6. Hysteretic circle of the ST specimen in destruction: (a) ST-1 specimen (b) ST-2 specimen

In the test, the damages of side piles always occurred prior to middle piles in pile-group foundation. The force-displacement hysteretic curves of side piles are given in Fig.7. The single pile force-displacement hysteretic curves reflect anti-seismic property of components. From comparing the figures, the pinch effect of hysteretic curve is more obvious in reinforced concrete piles. Furthermore, if cyclic displacement imposed at the top of the pier and the base shear force were one to one corresponded with, measured force - displacement cyclic response of specimens are shown in Fig.8. Fig.8 shows that the peak strength of ST specimens is about 1.77 times of the others and the ultimate displacement of ST-specimens is 1.66 times

of the RC-specimens. It indicates that the bearing capacity of the foundation increased obviously by strengthening the plastic hinge zone of piles with steel tubes.

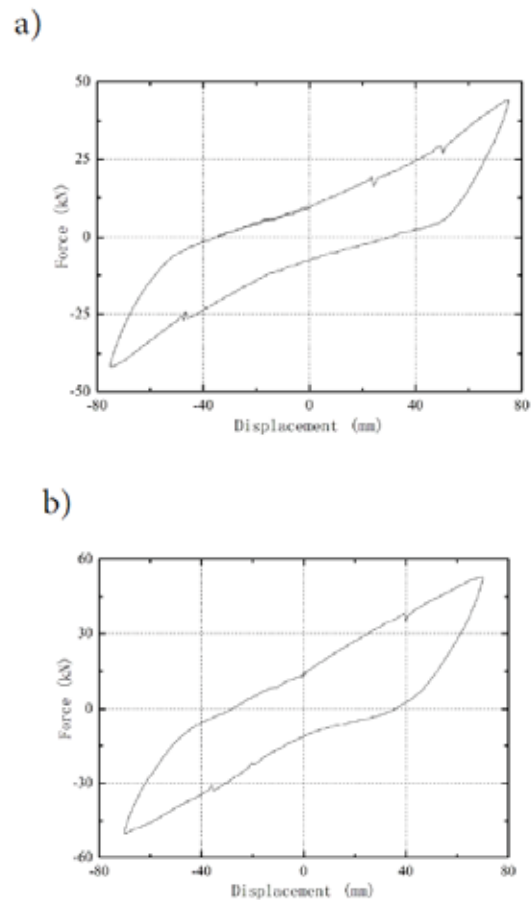


Fig. 7. Force-displacement curve of side pile: (a) RC-1 specimen (b) ST-1 specimen

## SKELETON CURVES OF SPECIMENS

Restoring force characteristics of elevated pile-cap system can be fully expressed by skeleton curves. Measured skeleton curves of specimens were shown in Fig.9, which can be drawn by FEMA356 method. Some laws can be found from

Tab. 2. Characteristics of skeleton curve

Items Specimen number	Positive loading						Reversed loading					
	Yield displacement	Peak displacement	Ultimate displacement	Yield strength	Peak strength	Ultimate strength	Yield displacement	Peak displacement	Ultimate displacement	Yield strength	Peak strength	Ultimate strength
	/mm			/kN			/mm			/kN		
Specimen 1	10.952	23.921	41.093	27.624	35.949	30.556	-10.150	-26.031	-41.239	-27.322	-37.714	-32.057
Specimen 2	12.119	24.328	42.597	28.211	36.321	30.872	-11.114	-28.047	-44.265	-29.238	-40.942	-34.801
Specimen 3	18.086	49.669	67.362	40.603	64.226	54.591	-18.373	-49.548	-68.734	-35.720	-61.247	-52.060
Specimen 4	20.004	49.628	70.208	45.601	68.512	58.235	-19.933	-49.385	-68.892	-43.856	-64.870	-55.140

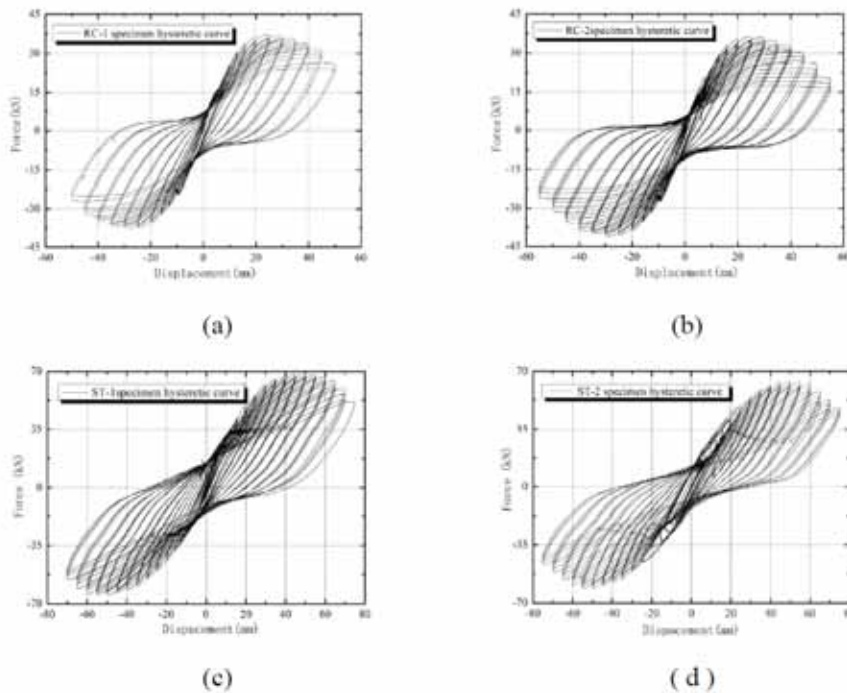


Fig. 8. Measured force - displacement cyclic response of specimens: (a) RC-1 specimen (b) RC-2 specimen (c) ST-1 specimen (d) ST-2 specimen

summarizing the specimens' skeleton curves. All measured skeleton curves can be simplified to three linear models. There is a long strength steady section in skeleton curves of the RC specimens, which shows that the plastic deformation ability of the first two specimens is obvious. Post-yield stiffness of the latter two specimens is 5% to 20% higher than the former two's. Greater post-yield stiffness helps to decrease residual displacement and maintain stability of the structure which is advantage for aseismic design of bridge [4]. For the reason of strengthen function by steel pipe, horizontal resistance and ultimate deformation capacity of elevated pile caps of the latter two specimens improved greatly: peak tensile strength has been raised by 77%~88%, while ultimate displacement has been raised by 55%~63%. For all specimens, skeleton curves of the first three cyclic loading are relatively stable, nearly overlapping in early stage, but there are obvious deviation between every cyclic loading after yield stage.

Referring to reinforced concrete hysteretic model, broken-lined models are commonly used for simpleness and convenience. Skeleton curves of elevated pile caps can be idealized to 3-line sketch curve model [3,7], and the statistics

data are shown in Tab. 2.

### DISPLACEMENT DUCTILITY OF SPECIMENS

Displacement ductility coefficient is an important index which reflects ductility anti-seismic ability of structure. The greatest displacement ductility coefficients of the four specimens are given in Table 3. In the table, the coefficient  $u_{mi}$  can be given as:

$$u_{mi} = \frac{\Delta_u}{\Delta_{yi}} \quad (1)$$

where  $\Delta_u$  is the ultimate displacement in skeleton curves of specimen and  $\Delta_{yi}$  is the first yield displacement in skeleton curves of specimen. The coefficient  $u_{me}$  can be described as following equation:

$$u_{me} = \frac{\Delta_u}{\Delta_{ye}} \quad (2)$$

where  $\Delta_u$  is the ultimate displacement in skeleton curves

Tab. 3. Statistics of displacement ductility ratio

Items	$\Delta_{ye}$ /mm		$u_{mi}$		$u_{me}$	
	Positive loading	Reversed loading	Positive loading	Reversed loading	Positive loading	Reversed loading
Specimen 1	14.590	-14.072	3.752	4.063	2.816	2.931
Specimen 2	15.135	-16.355	3.515	3.983	2.814	2.706
Specimen 3	26.336	-30.053	3.724	3.741	2.558	2.287
Specimen 4	29.834	-28.445	3.510	3.456	2.353	2.416

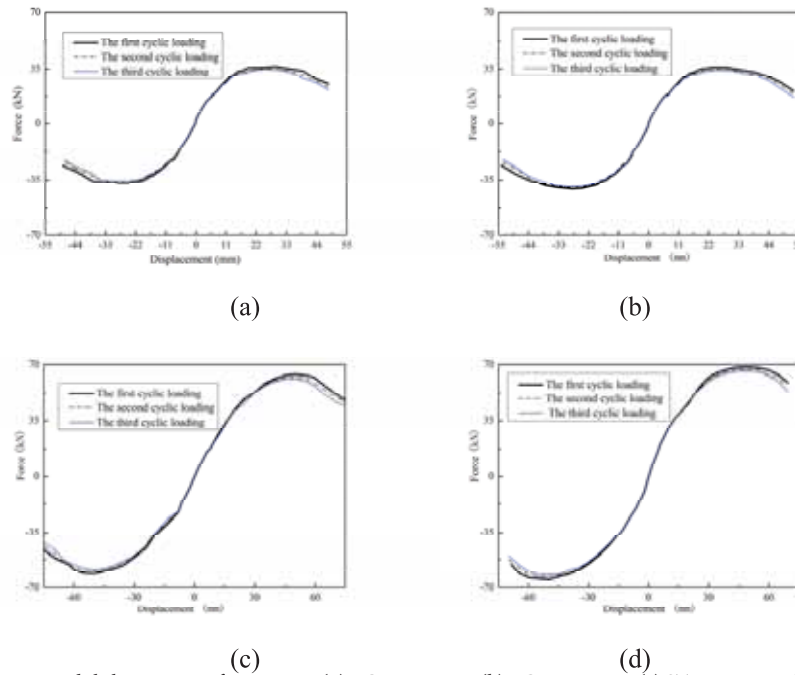


Fig. 9. Measured skeleton curve of specimens: (a) RC-1 specimen (b) RC-2 specimen (c) ST-1 specimen (d) ST-2 specimen

of specimen and  $\Delta_{ye}$  is the equivalent yield displacement in skeleton curves of specimen. The equivalent yield displacement can be calculated by energy balance method (Priestley, 1998[5]; Caltrans SDC, 2001[1]).

The displacement ductility coefficients of the former two specimens are greater than the latter two's, that's mainly because elevated pile cap's yield displacement of RC pile is 50% less than ST specimens. Although the ultimate displacement of the latter two specimens improved highly, depending on minor yield displacement, the displacement ductility capacity of RC specimens is nearly as same as ST specimens. Accumulated displacement ductility coefficient  $N_{\Delta}$  can be obtained according to Formula 3:

$$N_{\Delta} = \sum_{i=1}^n \frac{\Delta_{mi}}{\Delta_{yi}} \quad (3)$$

In the equation,  $\Delta_{mi}$  is the mean value of the largest displacement with both positive and negative loading directions when cyclic loading number is  $i$ ;  $\Delta_{yi}$  is the first yield displacement;  $n$  is the number of laps for cyclic loading.

If define 'drift ratio' as displacement on the pier top under horizontal load divided by the height between pier top and scour line and define 'ultimate destruction' as the horizontal resistance decreases to 85% of the maximum resistance, then ultimate destruction state arrives while drift ratio reach to 4.6% for ST specimens; but the drift ratio is only 2.8% when adopting RC pile foundation when ultimate destruction state arrives. Accumulated displacement ductility ratio and ultimate drift ratio of all specimens are listed in Table 4.

Tab. 4. Statistics of accumulated displacement ductility ratio and drift ratio

Items	Accumulated displacement ductility ratio $N_{\Delta}$	Ultimate drift ratio %	
		Positive direction	Negative direction
specimen 1	71.128	2.758	2.768
specimen 2	88.869	2.859	2.971
specimen 3	104.336	4.521	4.613
specimen 4	94.332	4.712	4.624

Many researchers have pointed out that the conclusion will be limiting when a single displacement ductility index is used to evaluate the ductility of the structure [2]. From the collection of seismic disaster investigation and experimental research, anti-seismic capability of structure is not only relevant to the greatest ductility displacement, but also depending on plasticity energy consumption capacity. Energy-dissipating capacity of two kinds of specimens will be discussed below.

### ENERGY-DISSIPATING CAPACITY OF SPECIMENS

Energy-dissipating capacity as well as ductility ability, is regarded as an important index of structural anti-seismic performance. The energy conservative relation which is expressed by Eqn. 4 is always true if collapse of the bridge structure does not appear.

$$E_K(t) + E_D(t) + E_H(t) + E_E(t) = E_t(t) \quad (4)$$

where  $E_K(t)$  and  $E_E(t)$  are respectively representing for the kinetic energy and elastic deformation energy of the structure;  $E_D(t)$  and  $E_H(t)$  are respectively representing for the damping dissipation energy and hysteretic dissipation energy of structure;  $E_t(t)$  is the total energy of the earthquake input.

Cumulative hysteretic dissipation energy  $E_{AD}$  is defined as the total hysteretic dissipation energy of the specimens under reciprocating load from the beginning to destroy, namely the sum of every hysteretic loop's area:

$$E_{AD} = \sum_{i=1}^n \Delta W_i \quad (5)$$

where  $E_{AD}$  is specimen's cumulative hysteretic dissipation energy;  $n$  is loading number of turns;  $\Delta W_i$  is representing for the hysteretic loops area of the  $i$  level load. The value of  $E_{AD}$  for each specimen is shown in Table 5. The variation trend of dissipation energy with loading level is shown in Fig.10. The test results show that the elevated pile cap's structure cumulative energy-dissipating capacity get improvement after using steel pipe in RC pile. Comparing with RC specimen, the energy dissipation ability of ST specimen improved about two times.

Tab. 5. Cumulative hysteretic dissipation energy of each specimen

Specimen number	Specimen 1	Specimen 2	Specimen 3	Specimen 4
$E_{AD} /(\text{kN}\cdot\text{mm})$	25416.437	34763.099	72213.229	74813.938

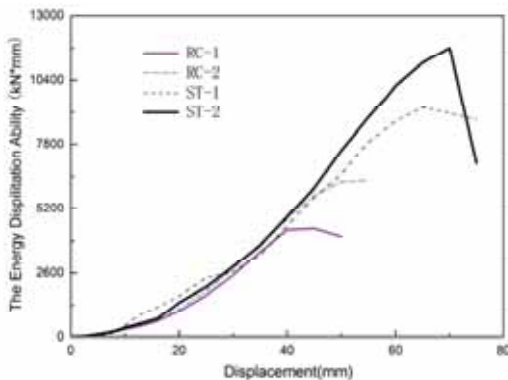


Fig. 10. The dissipated hysteretic energy capability of specimen

Equivalent viscous damping ratio is another significant coefficient in pseudo-static test. It can link structure damping to viscous damping model. Equivalent viscous damping coefficient is defined as follow:

$$\xi_{eq,h} = \frac{1}{2\pi} \frac{E_H(t)}{E_E(t)} \quad (6)$$

where  $\xi_{eq,h}$  is equivalent viscous damping ratio;  $E_H(t)$

and  $E_E(t)$  are respectively representing for the hysteretic dissipation energy and elastic deformation energy of the structure.

Fig. 11 shows the equivalent viscous damping ratio  $\xi_{eq,h}$  increase with the rise of displacement ductility coefficient  $u_i$ . It shows that with the concrete crack or the steel bar yield, the hysteretic energy dissipation of specimens increase. Before the main reinforcement yield, equivalent viscous damping ratio of the first specimen and the second specimen changes between 0.05 and 0.07; for the third specimen and the fourth specimen, it changes from 0.04 to 0.08. After the steel bar yield,  $\xi_{eq,h}$  of the first and second specimen increase observably; when the specimens destroy, the value of  $\xi_{eq,h}$  can reach 0.258 and 0.283 respectively; the equivalent figures of the third and the fourth specimen are 0.136 and 0.164, which also explain that damage degree of pile-group is restrained after steel casing composite concrete is used.

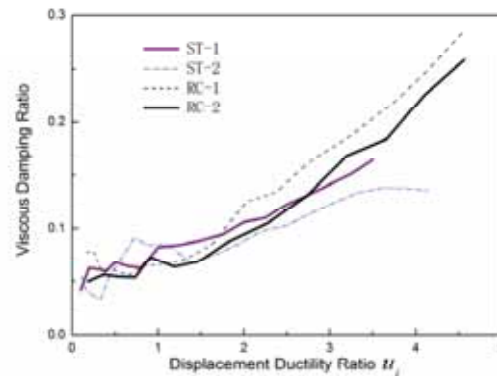


Fig. 11. The equivalent viscous damping ratio of specimen

## CONCLUSIONS

The paper deals with experimental activity on four scale-specimens of elevated pile-group foundation belonging to a real bridge. Two of them are reinforced concrete structure, others are steel composite structure. The experimental results indicated that the seismic capacity of the foundation increased obviously by using steel casing composite concrete in damageable zone of piles. This measure can effectively improve the bending strength of RC pile, delay crushing and failure of concrete, delay the yielding of longitudinal bars in plastic hinge regions and avoid fracture failure of longitudinal bars. According to test, the peak strength of strengthening specimens is about 1.77 times of the others and the ultimate displacement is 1.66 times of the original models. Additionally, the dissipated hysteric energy capability of strengthening specimens is more than 2.15 times of the others as the equivalent viscous damping ratio is reduced by 50%. Finally, other relevant phenomena and failure mechanisms of the elevated pile-group foundation were summarized.

## ACKNOWLEDGEMENTS

This research is supported by Ministry of Transport of China (the project No. is 2015319812010), the Fund of National Engineering and Research Center for Highways in Mountain Area (the project No. is gsgzj-2012-07), China Postdoctoral Science Foundation under Grant No. 2012M511959. The paper is also funded by China Scholarship Council.

## REFERENCES

1. California Department of Transportation (CALTRANS): 'Seismic Design Criteria, Version 1.2', Sacramento, California; published December 2001.
2. Fan Li-chu and Zhuo Wei-dong: 'Ductility anti-earthquake design of bridge', People Traffic Press Beijing, China, 2001.
3. Guo Zi-xiong, Lu Xi-lin: 'Study on frame column restoring force with high axial compression ratio model test', China Civil Engineering Journal, 2004, 37:32-38
4. Macrae, G.A. and Kawashima, K.: 'Post-Earthquake Residual Displacement of Bilinear Oscillators', Earthquake Engineering & Structural Dynamics, 1997, 26, 701-716.
5. Priestley M.J.N.: 'Brief Comments on Elastic Flexibility of Reinforced Concrete Frames and Significance to Seismic Design', Bulletin of the New Zealand National Society for Earthquake Engineering, 1998, 31:246-259
6. R. Giannini, F. Paolacci and E. Sibilio: 'Experimental study on the cyclic response of an existing RC bridge pier', Proceedings of the 14th world conference on earthquake engineering, China, September 2008, Beijing.
7. Takeda T, Sozen M A, Nielson N N.: 'Reinforced concrete response to simulated earthquakes', Journal of Structural Division, 1970, 96 (ST12) :2557-2572
8. Yuan Wan-cheng and Jun Yang: 'Lateral load pattern study of pushover analysis for elevated pile foundation system of bridges', Journal of Tongji University, 2008, 36, 1468-1472.
9. Zhou Mi: 'Experimental and Theoretical Studies on Seismic Performance of Elevated Pile Cap Bridge', PhD thesis, Tongji University, Shanghai, China, 2008, 82-102.
10. Zhou Mi and Yuan Wan-cheng: 'Parameter sensitivity analysis of equivalent anchorage length for elevated pile caps', Journal of Chang'an University, 2010, 30, 47-52.

## CONTACT WITH THE AUTHORS

Mi Zhou

Key Laboratory for Old Bridge Detection and Reinforcement Technology of the Ministry of Transportation  
Chang'an University, Xi'an, Shaanxi  
National Engineering and Research Center for Highways in Mountain Area, Chongqing  
tel.: +86 29 82334868, fax: +86 29 82334434  
email: zhoumi@chd.edu.cn  
**CHINA**

## IMAGE FUSION FOR TRAVEL TIME TOMOGRAPHY INVERSION

**Xinghui Yin**

College of Computer and Information, Hohai University, Nanjing 210098, China

**Linan Liu**

The Fourth Department, Bengbu Naval Petty Officer Academy, Bengbu 233012, China

**Xiaomeng Zhao**

College of Information Engineering, Anhui Science and Technology University, Chuzhou 233100, China

**Muhammad Aqeel Ashraf**

Department of Geology, Faculty of Science, University Of Malaya 50603 Kuala Lumpur, Malaysia

Faculty of Science & Natural Resources, Universiti Malaysia Sabah, 88400 Kota Kinabalu, Sabah, Malaysia

### ABSTRACT

*The travel time tomography technology had achieved wide application, the hinge of tomography was inversion algorithm, the ray path tracing technology had a great impact on the inversion results. In order to improve the SNR of inversion image, comprehensive utilization of inversion results with different ray tracing can be used. We presented an imaging fusion method based on improved Wilkinson iteration method. Firstly, the shortest path method and the linear travel time interpolation were used for forward calculation; then combined the improved Wilkinson iteration method with super relaxation precondition method to reduce the condition number of matrix and accelerate iterative speed, the precise integration method was used to solve the inverse matrix more precisely in tomography inversion process; finally, use wavelet transform for image fusion, obtain the final image. Therefore, the ill- conditioned linear equations were changed into iterative normal system through two times of treatment and using images with different forward algorithms for image fusion, it reduced the influence effect of measurement error on imaging. Simulation results showed that, this method can eliminate the artifacts in images effectively, it had extensive practical significance.*

**Keywords:** tomography; inversion algorithm; wavelet transform; image fusion

### INTRODUCTION

**Cross well** tomography technology is an effective method in geophysical prospecting, it uses the observed data acquired through the omnidirectional scanning of cross well medium, to get optimization inversion calculation results, ultimately get the image which can reflect cross well internal medium structure changes. It can solve many problems in engineering geology, it has been widely used in engineering geological exploration, such as the remaining oil distribution and reservoir precise description of oil and gas field, looking for inter well blind metallic ore or ore reserves prediction and so on. According to the projection data type, cross well tomography can be divided into the travel time tomography, waveform tomography and amplitude tomography etc. Among them, the travel time tomography method has several advantages of simple principle, less interference factors and the

efficient calculation, so it occupies dominant position in cross well tomography application[1-7]. Although the cross well tomography technology has made some progress in theory study, model experiment, detection equipment, observation system, tomography algorithm, parameter inversion and geological interpretation, but at present it is still difficult to meet the practical application needs. This is mainly because in the calculation process of speed tomography, it has to solve these three problems: (1) calculation of ray tracing time in theory; (2) Calculation of the Jacobi matrix; (3) Solving sparse, ill conditioned equations, that is linearized inversion problem. There is a direct relationship between the first two problems and forward algorithms by ray tracing method, however, the geological conditions were varied, it had the lack of widely

applied methods for tomography. Among them, the short path method proposed by Moser[8] and the linear travel time interpolation (LTI) by Asawaka and Kawanaka[9] are better. The short path method advantage is that, in any complex velocity medium condition, it can simulate minimum travel time (including first wave and diffracted wave) ray between each of the shot point / receive point, it does not need to smooth velocity model or use the virtual observation data. While the linear travel time interpolation method (LTI) has the advantages of high precision, fast speed, it is the most widely used ray tracing method in recent years. Therefore, in order to minimize artifacts, highlight the true anomaly area, we can use be different ray tracing methods on the same measuring objects to get the tomographic image, then use wavelet transform fusion method, it can improve the SNR of the tomographic images.

Therefore the first two problems have been solved, the third question cannot be ignored. According to the characteristics of the research object and method, ultimately the core of tomography is attributed to the solving of sparse, ill-conditioned, mixed set or incompatible linear equations. Therefore, it would have direct bearing on the success or failure of tomographic imaging, the accurate numerical solution and stability of inversion algorithm are necessary conditions of tomography realization. So far the effective inversion algorithms mainly include: Cao[10] proposed self-incentive simultaneous algebraic reconstruction algorithm(SASIRT) which was suitable for ray distribution was not uniform or measurement error was larger, however, it had slow calculation speed and low accuracy; Saad and Schultz[11] proposed generalized minimal residual method(GMRES) which could be used for solving non symmetric linear equations, the calculation process would not be interrupted generally until obtaining the exact solution, nevertheless, there may be not converge; Van and Vorst[12] proposed the double stable conjugate gradient method (BICGSTAB), which could be used for solving linear equations whose coefficient matrix was asymmetric, it used short recursive method to reduce residual progressively, so the advantage was it occupied less memory, but the convergence was irregular, the convergence rate may be amplified severely under the condition of finite precision; LSQR with damping factor method (DLSQR) proposed by Yang[13], it improved the inversion precision effectively, avoided numerical instability of LSQR algorithm when the measurement error was large, it was especially suitable for solving the equations whose coefficient matrix was large and sparse, compared with other iteration method, it could obtain faster convergence rate and better acceptable results in solving singular or ill-conditioned problems, currently it is practical inversion method which was most commonly used, however, the occupation of computer memory was large and accuracy should be further improved. In recent years, artificial intelligence method was also applied to the inversion algorithm[14], such as Simulated Annealing(SA) or Genetic Algorithm(GA), but it had strong dependence on the initial model, easily influenced by random disturbance, the distribution reconstruction effect on slightly more complex medium was poor.

According to this, comprehensive utilization of inversion results with different ray tracing can be used[15-17]. Firstly, we use the shortest path method and the linear travel time interpolation method for forward calculation respectively, the ray travel time and Jacobi matrix are obtained; then presenting the improved Wilkinson iteration method to solve the sparse, ill conditioned equations, getting the inversion images with different forward methods; finally, the wavelet transform algorithm is used for image fusion[18]. The performance of the inversion algorithm and the fusion image resolution with new method are improved, it can meet the needs of practical application better.

## METHODOLOGY

### THE IMPROVED WILKINSON ITERATION METHOD

Because the distribution of transmitter and receiver is restricted by the detection of object space position, there are a lot of discrete grids which have no ray passed through, it results in projection data incomplete. So the coefficient matrix obtained from forward calculation is usually sparse, ill-conditioned, large scale or singular. Improved Wilkinson iteration method is good at solving ill-conditioned linear equations system in theory, it will control the iterative convergence error under a very small scale, meanwhile ensure fast convergence rate; iteration may be completed even within two paces at times. However, Wilkinson iteration method requires coefficient matrix is positive definite, which means the coefficient matrix obtained from forward calculation should be treated before using Wilkinson iteration method.

Consider the linear equation

$$Ax = b \quad (1)$$

In which, denotes the coefficient matrix, it is composed of ray length from each discrete grid; is an unknown vector, it represents the slowness vector from each grid cell; B represents a vector which composed of all ray travel time.

In order to get the positive definite coefficient matrix, both sides in the equation (1) are multiplied by , equation(1) is changed into equivalent equation (2).

$$A^T Ax = A^T b \quad (2)$$

In which, represents transposition of , is symmetric and positive definite, so it can meet the requirement of Wilkinson iteration. However, the condition number of is square of 's, when matrix A is ill-conditioned, small measurement error interference will bring greater calculation error, the convergence rate is very slow. Therefore, it is necessary to reduce the condition number of the coefficient matrix A.

Using the super relaxation preprocessing method, make , then the equation (1) changes into:

$$(W^{-T}AW^{-1})Wx = W^{-T}b \quad (3)$$

In which, is preprocessing factor matrix. As the structure of and is getting similar, the condition number of becomes small. So the specific selection method is as follows:

$$D_{ij} = \text{diag} \left( \sqrt{\frac{A_{ij}}{\omega}} \right), (i = j) \quad (4)$$

$$C = D^{-1}(D^2 + L) \quad (5)$$

$$M = \frac{1}{2-\omega} C^T C \quad (6)$$

Among them, is a diagonal matrix, is an upper triangular matrix, is strictly upper triangular matrix of, is relaxation factor, which ranges from  $0 < \omega < 2$ .

Make  $\tilde{A} = W^{-T} A W^{-1}$ ,  $\tilde{x} = Wx$ ,  $\tilde{b} = W^{-T} b$ . Therefore the original equation(1) is changed into equivalent equation(7).

$$\tilde{A}\tilde{x} = \tilde{b} \quad (7)$$

The condition number of coefficient matrix in equation (7) is much smaller than the original matrix A's, then both sides in the equation (7) are multiplied by  $\tilde{A}^T$ , so equation(7) is changed into:

$$\tilde{A}^T \tilde{A} \tilde{x} = \tilde{A}^T \tilde{b} \quad (8)$$

Right now the matrix  $\tilde{A}^T \tilde{A}$  in equation (8) becomes symmetric and positive definite, and the condition number of coefficient matrix is smaller than equation (2).

So the solution of equation (1) is converted to solving equation (8) and getting the slowness vector x from solving  $\tilde{x} = Wx$ . The solving of  $\tilde{x} = Wx$  is very simple, so next we mainly discuss solution of equation (8). In order to solving it more precisely and faster, a small parameter can be introduced to form an improved Wilkinson iteration method.

$$\begin{cases} z_k = (\tilde{A}^T \tilde{A} + \sigma^2 I)^{-1} (\tilde{A}^T \tilde{b} - \tilde{A}^T \tilde{A} \tilde{x}_k) \\ \tilde{x}_{k+1} = \tilde{x}_k + z_k \end{cases} \quad (9)$$

In which,  $\tilde{x}_0 = 0$ ,  $\sigma$  is a small arbitrary constant, I is a unit matrix.

With the treatment of super relaxation precondition and Wilkinson iteration method, the ill conditioned linear equations is changed into normal system, then use equation (9) to get iterative solution.

### USING THE PRECISE INTEGRATION METHOD TO GET INVERSE MATRIX

Although the matrix is improved, but the coefficient matrix A may be singular or singular values are very small, it may cause we cannot get the precise solution by calculating inverse matrix  $\tilde{A}^T \tilde{A} + \sigma^2 I$  directly. Therefore, the precise integration thought is used to get inverse matrix which is more precise.

Make  $F = \tilde{A}^T \tilde{A} + \sigma^2 I$ ,  $H(t) = \int_0^t \exp(-Fs) ds$ , then

$$H(t) = \int_0^t \exp(-Fs) ds = -F^{-1} \exp(-Fs) \Big|_0^t = -F^{-1} \exp(-Ft) + F^{-1}$$

Because F is positive definite, when  $t \rightarrow +\infty$ ,  $\exp(-Ft) \rightarrow 0$  so  $F^{-1} = H(+\infty)$ . Make  $B = -F$ , then

$$\begin{aligned} H(2t) &= \int_0^{2t} \exp(Bs) ds = \int_0^t \exp(Bs) ds + \int_t^{2t} \exp(Bs) ds = \\ &= (I + \exp(Bt)) \int_0^t \exp(Bs) ds \end{aligned}$$

That is

$$H(2t) = (I + \exp(Bt))H(t) \quad (10)$$

Equation (10) provides the recursive algorithm for matrix  $F^{-1}$ , then use the precise integration thought, take a small step  $\Delta t$ , make

$$H_j = H(2^j \Delta t) \quad (j = 0, 1, \dots) \quad (11)$$

Then

$$\begin{cases} H_0 = \Delta t (I + \sum_{i=1}^4 \frac{(B\Delta t)^i}{i!}) \\ H(2^j \Delta t) = \prod_{i=0}^{j-1} (I + \exp(B \cdot 2^i \cdot \Delta t)) H_0 \quad (j = 1, 2, \dots) \end{cases} \quad (12)$$

Calculating  $\exp(B \cdot 2^i \cdot \Delta t)$  with the precise integration method, first do Taylor expansion for  $\exp(B\Delta t)$ , because  $\Delta t$  is very small, it can only retain the first several series in Taylor expansion.

$$\exp(B\Delta t) \approx I + \sum_{i=1}^4 \frac{(B\Delta t)^i}{i!} \quad (13)$$

Make

$$\begin{cases} T^{(0)} = \sum_{i=1}^4 \frac{(B\Delta t)^i}{i!} \\ T^{(i+1)} = 2T^{(i)} + (T^{(i)})^2 \end{cases} \quad (14)$$

The benefit is that, it can separate large variables from small in the calculation, avoid the small variables are ignored when they are added with large, ensure the calculation accuracy.

So

$$\exp(B \cdot 2^i \cdot \Delta t) = I + T^{(i)} \quad (i = 1, 2, \dots) \quad (15)$$

From equation (10) and (15), we can get

$$H_{j+1} = (I + \exp(B \cdot 2^j \cdot \Delta t)) H_j \quad (j = 1, 2, \dots) \quad (16)$$

When j is large enough, we can get more accurate inverse matrix  $F^{-1}$ . Meanwhile, the iterative process is equivalent to multiplying the integral region of H(t), the convergence is carried on with steps of exponential  $2^k$ , hence, the calculation efficiency is very high.

### WAVELET TRANSFORM

Wavelet transform is a time-frequency localization

analysis, it has higher frequency resolution and low time resolution in low frequency part of signal, has low frequency resolution and higher time resolution in higher frequency part of signal. Therefore, the process of image fusion based on wavelet transform is: firstly, the preparative fusion image are decomposed into low frequency and high frequency coefficients, then the high or low frequency coefficients of image are fused to form wavelet Pyramid new structure according to some fusion rules, finally, the fusion image is obtained by wavelet reconstruction. The concrete steps of wavelet coefficients fusion is as follows.

(1) Calculation of high frequency coefficients edge active measure:

Regarding image A, the high frequency coefficients edge active measure:

$$E_j^e(A, p) = [\sum_{i=1}^n W_i * d_j^e(A, p)]^2 \quad (17)$$

Low frequency coefficients edge active measure:

$$E(A, p) = [\sum_{i=1}^n W_i * C_L(A, p)]^2 \quad (18)$$

Where,  $W_i$  is Frei-chen template, \* represents convolution computation,  $C_L(A, p)$  and  $d_j^e(A, p)$  represent low frequency coefficient and high frequency coefficient respectively, A represents decomposition, p represents the pixel position. Similarly we can get the edge active measure coefficient for image B.

(2) Synthesis coefficient

The high or low frequency coefficients of image F fused by images A and B are as follows.

High frequency coefficient:

$$d_j^e(F, p) = d_j^e(A, p)M_j^e(A, p) + d_j^e(B, p)M_j^e(B, p) \quad (19)$$

Among them, if  $E_j^e(A, p) \geq E_j^e(B, p)$ ,  $M_j^e(A, p) = 1$ ; otherwise

$$M_j^e(A, p) = 0, M_j^e(B, p) = 1 - M_j^e(A, p), j = 1, 2, \dots, L$$

Low frequency coefficient:

$$C_L(F, p) = C_L(A, p)M_L(A, p) + C_L(B, p)M_L(B, p) \quad (20)$$

Where, if  $E(A, p) \geq E(B, p)$ ,  $M_L(A, p) = 1$ ; otherwise

$$M_L(A, p) = 0$$

$$M_L(B, p) = 1 - M_L(A, p).$$

## THE STEPS OF IMPROVED ALGORITHM AND ANALYSIS OF CONVERGENCE

### ALGORITHM STEPS BASED ON IMAGE FUSION

Through above analysis, the steps using two kinds of ray tracing method to forward modeling, improved Wilkinson iteration inversion algorithm and wavelet transform fusion are as follows.

First step: The short path method and the linear travel time interpolation method are used to calculate the travel time and the Jacobi matrix;

Second step: Make pretreatment to equation (1) with the super relaxation iteration method, use equations (3) (4) (5) (6) to get (7), then both sides in the equation (7) multiply by  $\tilde{A}^T$  to get equation (8), then the coefficient matrix is positive definite and condition number is smaller;

Third step: Calculate inverse matrix of  $\tilde{A}^T \tilde{A} + \sigma^2$  using the precise integration method, obtain more accurate inverse matrix by iteration using the equation (16);

Fourth step: Select small parameter  $\sigma$  and step  $\Delta t$ , use improved Wilkinson iteration equation (9) to obtain  $\tilde{x}$ , then get slowness vector x by solving  $\tilde{x} = Wx$ , accomplish inversion calculation.

Last step: Fusion with using wavelet transform, the fusion image is obtained with high SNR.

### ANALYSIS OF ALGORITHM CONVERGENCE

Reorganize the iteration formula (9),  $\tilde{x}_{k+1} = G\tilde{x}_k + g$  is obtained, in which,  $G = I - (\tilde{A}^T \tilde{A} + qI)^{-1} \tilde{A}^T \tilde{A}$ ,

$g = (\tilde{A}^T \tilde{A} + qI)^{-1} \tilde{A}^T \tilde{b}$ . Because the equivalent coefficient matrix  $\tilde{A}^T \tilde{A}$  after deformation of original equation is positive definite, make its characteristic values  $\alpha_i$  ( $i = 1, 2, \dots$ ), then characteristic values of G are  $1 - \frac{\alpha_i}{\alpha_i + \sigma^2} > 0$ . So the spectral radius of G is

$$\rho(G) = \max \left( 1 - \frac{\alpha_i}{\alpha_i + \sigma^2} \right) = \max \left( \frac{\sigma^2}{\alpha_i + \sigma^2} \right) < 1 \quad (21)$$

Therefore, from equation (21) it can be seen,  $\rho(G) < 1$  with arbitrary variable  $\sigma$ , the iteration formula (9) is always convergent. So we can obtain the iteration result in an acceptable range all along.

### ANALYSIS OF MODEL SIMULATION

For analyzing the effect of new inversion algorithm in various media conditions better, we design three models: independent anomaly model, layered area model and abnormal S shape model. Use PIW algorithm in this paper for inversion, wavelet transform algorithm for image fusion, compare and analyze the inversion results from

imaging precision, time efficiency and the sensitivity of measurement error.

**THE TEST OF THEORETICAL MODEL**

The velocity distribution model of layered medium is showed in Figure 1. Assume a model which is abnormal velocity S shape in homogeneous background, the velocities in abnormal zone and homogeneous background are 600m/s, 1000m/s respectively. The size of model is m, the source points number is 85, first source point is located at a depth of 0.2m, the interval of source points is 0.1m, 85 source points are distributed evenly in the hole. The position coordinate of right hole surface is (10,0), put the receiver points in the right hole. Similarly, the number is 85, first receiver point is located at a depth of 0.2m, the interval of receiver points is 0.1m, 85 receiver points are distributed evenly in the hole also.

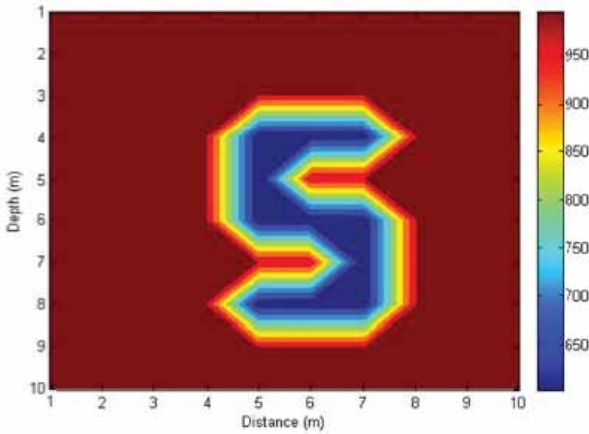


Figure 1. Velocity distribution of Model 1

The shortest path method and the linear travel time interpolation are used for forward ray tracing, add the forward ray travel time 15% random error, then use improved Wilkinson iteration algorithm for inversion, the value of  $\sigma$  is chosen as 0.005, as shown in Figure 2.

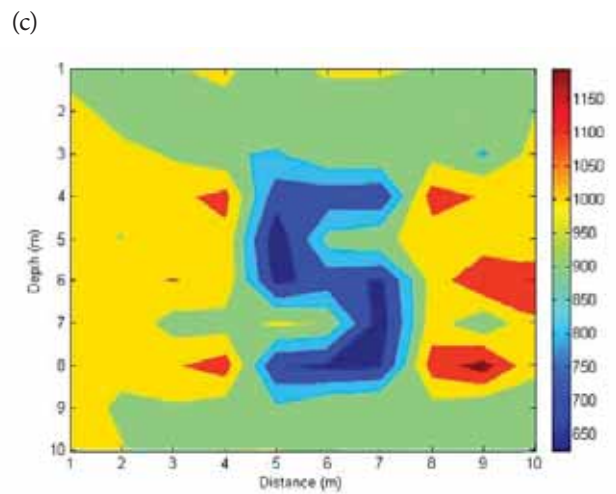
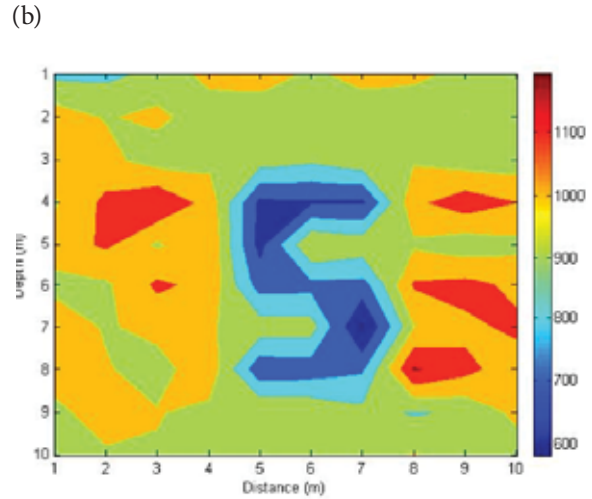
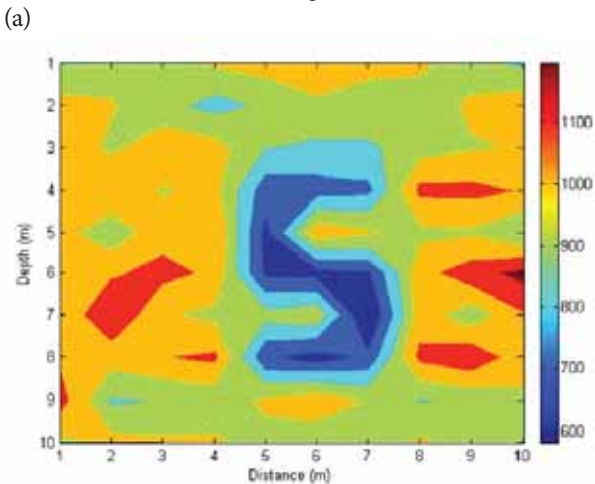


Figure 2. Velocity distribution inversion of Model 1. (a) Shortest path method (b) LTI method (c) Fused image

After adding 15% random error, the low velocity zone in Model can be reflected basically clearly based on two kinds of ray tracking methods, it illustrates two methods are effective for such cross well medium distribution such as karst cave. But there are some high-speed regional artifacts in uniform region, although we can easily distinguish the theoretical model, but it will have adverse effects for the actual geological survey. After fusion low speed region is high-contrast, and it eliminates some high speed artifacts, so it can satisfy the demand of imaging on abnormal regional location and size identification better.

Considering there are more layered velocity model occurred in superficial stratum practical application, a hierarchical model is proposed, high and low velocity anomaly area are shown in Figure 3.

We still use shortest path method and the linear travel time interpolation for forward ray tracing, add the forward ray travel time 15% random error, then use improved Wilkinson iteration algorithm for inversion, the value of  $\sigma$  is chosen as 0.005, as shown in Figure 4.

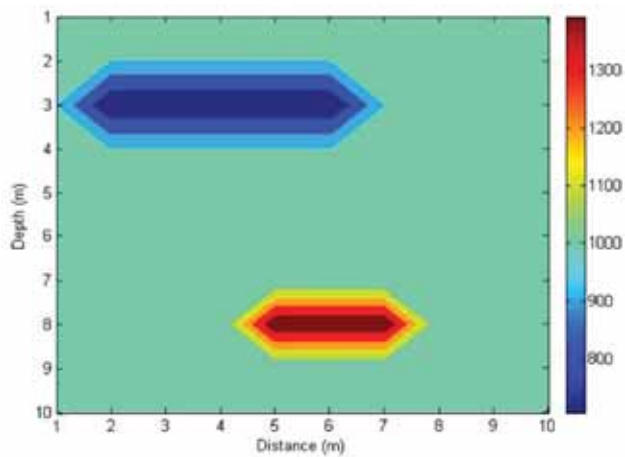


Figure 3. Layered medium velocity distribution of Model 2

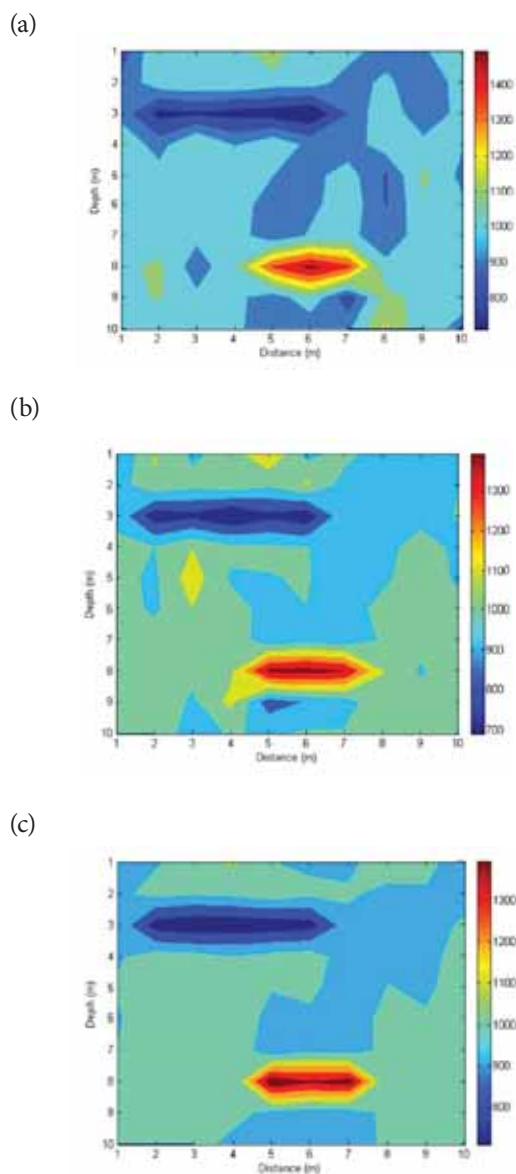


Figure 4. Velocity distribution inversion of Model 2. (a) Shortest path method (b) LTI method (c) Fused image

After adding 15% random error, the layered distribution from top to bottom between wells in two images still can be reflected, it illustrates the effectiveness of two methods. However, artifacts appeared in background of homogeneous regions affect resolution of true anomaly area. After fusion low speed region is high-contrast, edge distribution is clear, it can depict layered distribution of different speed basic faithfully. Because there are many layered distribution in the actual geological detection, imaging for layered media plays a very important role in the practical application, this reflect the practicability of the proposed method.

Using the abnormal regional model and programming ideas in reference [19], modifying the program according to improved Wilkinson iteration algorithm. Regional location, launch or receiving point coordinates are given in Figure 5. Using shortest path method and the linear travel time interpolation for forward ray tracing, inversion image is got after fusion. To reflect inversion image clearly, the original model and inversion image are put together in a chart.

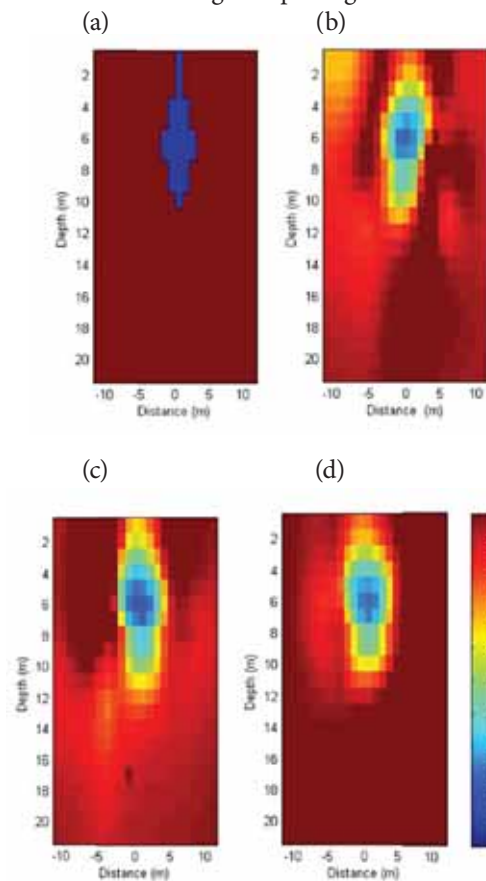


Figure 5. Velocity distribution inversion. (a) velocity distribution of Model 3 (b) Shortest path method (c) LTI method (d) Fused image

It can be seen from Figure 5, after fusing the images of shortest path method and the linear travel time interpolation, although some areas is abnormal, which is determined by the error introduced into the calculation of false information, however the whole image can still ensure the resolution effect very well. It can improve the accuracy and reliability of inversion image with using different methods which provide redundant

information, and the fused image contains more comprehensive, abundant information.

## REFERENCES

### THE INVERSION OF REAL DATA

In order to verify the effect of fusion imaging method, using the following practical cross-well seismic data to tomography[20]. The area of seismic data acquisition locate near a power plant in Paineiras Florida USA , in 2002 Berkeley National Laboratory collected seismic data by using the multi well observation, the purpose of the study is to analyze the pollution liquid distribution in the near surface. Ajo-Franklin used adaptive grid-travel time tomography method to get velocity inversion. We still use shortest path method and the linear travel time interpolation for forward ray tracing, then use improved Wilkinson iteration algorithm for inversion, as shown in Figure 6. As can be seen from the graph, the fusion image can depict of the two low velocity anomaly zone in deep stratum more accurately, this part may be caused by polluting liquid diffusion in deep strata lateral, in comparison to the original image[20], the two low velocity anomaly areas in fused image are depicted more clearly.

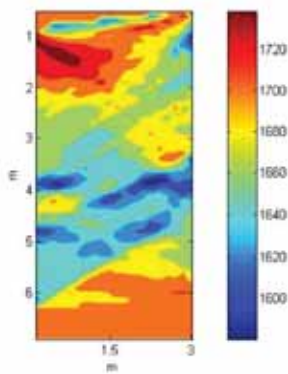


Figure 6. The inversion image of real data

### CONCLUSION

There are many ray tracing methods used in the velocity tomography imaging, different methods show their merits under different geological conditions. Therefore, the using two kinds of commonly used ray tracing methods are used for forward calculation to obtain travel time and the Jacobi matrix; the inversion algorithm is we combined the improved Wilkinson iteration method with super relaxation precondition method to get the iterative slowness values in cross well, the precise integration method was used to solve inverse matrix more precisely in Wilkinson iteration process, finally, wavelet transform is used for image fusion, it effectively eliminates the artifacts in the image, improves the velocity anomaly area recognition in tomography image.

1. H.M. Benz, B.A. Chouet, P.B. Dawson, J.C. Lahr, R.A. Page, and J.A. Hole, "Three dimensional P and S wave velocity structure of Redoubt Volcano". *Journal of Geophysical Research*, vol.101, pp. 8111-8128, 1996.
2. L. Huang, Z.Y. Huang and Y. Wang, "The inversion algorithm of ultrasonic tomography with concrete structure". *Journal of Hunan University (Natural sciences)*, vol. 33, no. 5, pp. 26- 30, 2006.
3. T. Nemeth, E. Normark, and F.H. Qing, "Dynamic smoothing in cross well travel time tomography". *Geophysics*, vol.62, no.1, pp.168-176, 1997.
4. H. Maurer, A.G. Green, and K. Holliger, "Full-Waveform inversion of cross-hole radar data based on 2-D finite-difference time domain solutions of Maxwell's equations". *IEEE transactions on geoscience and remote sensing*, vol.72, no.5, pp.53-64, 2007.
5. S.C. Su, S.D. Wang and L. Wu, "Smoothing SIRT algorithm with cross well tomography". *Journal of China University of Petroleum (Natural sciences)*, vol.25, no.6, pp.29-31, 2001.
6. C. C. Paige and M. A. Saunders, "Sparse linear equations and least squares problems". *ACM Transactions on Mathematical Software*, vol. 8, no.2, pp.195-209, 1982.
7. N. Linde, A. Tryggvason, J.E. Peterson, and S.S. Hubbard, "Joint inversion of cross hole radar and seismic travel times acquired at the South Oyster Bacterial Transport Site". *Geophysics*, vol. 73, no.4, pp.39-50, 2008.
8. Moser T J, "Shortest path calculation of seismic rays". *Geophysics*, vol. 56, no.1, pp. 59~67, 1991.
9. Asakawa, Eiichi and Kawanaka, Taku, "Seismic ray tracing using linear travel time interpolation". *Geophysical Prospecting*, vol.41, no.1, pp.99~ 112, 1993.
10. J.X. Cao and Z.Q. Yan. "Estimation of seismic cross-hole travel time tomography resolution". *Journal of Chengdu University of Science & Engineering*, vol.22, no.4, pp.95-101, 1995.
11. Y. Saad and M.H. Schultz. "GMRES: Generalized minimal residual algorithm for solving non-symmetric line system". *SIAM J.SCI.STAT.COMPUT*, vol.7, no.3, pp.856-869, 1986.
12. G.L.G. Sleijpen and D.R. Fokkema, "Bicgstab (L) for linear equations involving unsymmetric matrices with complex spectrum". *Electronic trasactions on numerical analysis*, vol.1, pp.11 -32, 1993.

13. W.C. Yang and J.Y. Du, "A new algorithm for tomographic imaging and its application in engineering detection". Chinese Journal of Geophysics, vol.37,no.2,pp.239-244, 1994.
14. F. Boschetti, M.D. Dentith and R.D. List, "A fractal-based algorithm for detecting first arrivals on seismic traces". Geophysics, vol.61,no.4,pp.1095-1102,1996.
15. C.X. Chen and H.D. Yin, "Using super relaxation preconditioned conjugate gradient method for solving large sparse equations". Science technology and Engineering, vol.10,no.10,pp. 2389-2394, 2010.
16. X.Y. WU, R. SHAO and Y.R. ZHU, "Iterative improvement of a solution for an ill conditioned system of linear equations based on a linear dynamic system". Computers and Mathematics with Applications,vol.44,pp.1109-1116,2002.
17. W.Z. Zhang and P.Y. Huang, "Precise iterative method for solving ill conditioned algebraic system". Applied Mathematics and Mechanics, vol.34,no.7,pp.736-741,2013.
18. Li H, Manjunath BS and Mitra SK, "Multisensor image fusion using the wavelet transform". Graphical Models and Image Processing,vol.57,no.3,pp.235~245,1995.
19. Adam Pidlisecky, Eldad Haber, and Rosemary Knight, "RESINVM3D: A 3D resistivity inversion package". Geophysics, vol.72,no.2, pp.H1-H10,2007.
20. Ajo-Franklin J B. "Using high resolution borehole geophysics for DNAPL detection and environmental site characterization", California:Department of Geophysics, Stanford University,2005

#### CONTACT WITH THE AUTHORS

Xinghui Yin

College of Computer and Information  
Hohai University Nanjing 210098  
**CHINA**

Linan Liu

The Fourth Department  
Bengbu Naval Petty Officer Academy,  
Bengbu 233012  
**CHINA**

Xiaomeng Zhao

College of Information Engineering  
Anhui Science and Technology University  
Chuzhou 233100  
**CHINA**

Muhammad Aqeel Ashraf

Department of Geology, Faculty of Science  
University Of Malaya 50603 Kuala Lumpur  
**MALAYSIA**

# STABILITY CONTROL OF PROPELLER AUTONOMOUS UNDERWATER VEHICLE BASED ON COMBINED SECTIONS METHOD

QI Duo, FENG Jinfu, LIU An, HU Junhua, XU Hu

Aeronautics and Astronautics Engineering College, Air Force Engineering University, Xi'an 710038, China

LI Yongli

Engineering University of CAPF, Xi'an 710086, China

Muhammad Aqeel Ashraf

Department of Geology, Faculty of Science, University Of Malaya 50603 Kuala Lumpur, Malaysia

Faculty of Science & Natural Resources, Universiti Malaysia Sabah, 88400 Kota Kinabalu, Sabah, Malaysia

## ABSTRACT

*Learning from the motion principle of quadrotor, a symmetric propeller AUV, which has small size and low velocity is designed. Compared with the AUV equipped with rudders, it has better maneuverability and manipulation at low velocity. According to the Newton-Euler method, the 6 DOF kinematic model and dynamic model of the propeller AUV are established. A stability controller that consists of 3 different PID controllers is designed. It makes the depth and attitude angle as trigger conditions, and the relevant controller is chosen in different moving process. The simulation experiments simulate ideal motion state and disturbed motion state, and experiments results show that the stability controller based on combined sections method can make the best of mature technology of PID, and meet the control requirements in different stages. It has a higher respond speed and accuracy, improving the stability of the propeller AUV under the disturbance of complex ocean currents.*

**Keywords:** propeller AUV; dynamic model; stability control; simulation

## INTRODUCTION

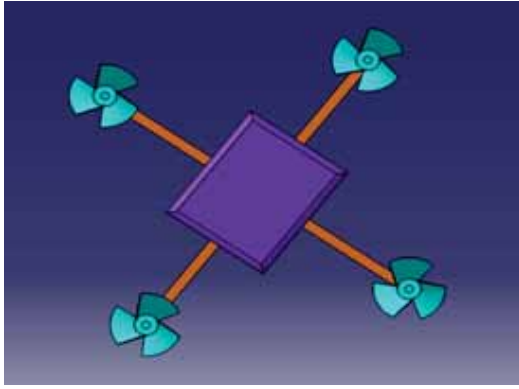
Ocean space is an important competition field of military and economic in the world, and many countries are vigorously developing deep sea exploration technology. As an intercrossed subject of ocean engineering and robot technology, autonomous underwater vehicles (AUVs) have been widely employed in oceanic survey applications, including oceanographic mapping and detection, underwater resources exploration, undersea wreckage salvage, and so on [1-4].

Considering the requirements of machining and reducing the fluid resistance, most of traditional AUVs are revolving body or bionics shape, such as drop type, torpedo type and low-resistance layer fluid type, and they change the velocity and direction by fin, rudder and various propulsions installed at the tail. In this paper, learning from the motion principle of quadrotor, a symmetric propeller AUV is designed. Compared with the shapes of traditional AUV, it has better maneuverability and manipulation at low velocity. By adjusting the rotate speed of four propellers fixed on the rigid cross structure, it can dive, hover, rise, go forward and backward or turn around, which has better maneuverability and flexibility.

Based on the combined sections method, a stability controller is designed as well, improving the stability of the propeller AUV under the disturbance of complex ocean currents.

## THE PROPELLER AUV MODEL

As shown in Fig.1(a) and 1(b), the propeller AUV has four propellers of which the rotating plane is coplanar. The propellers, fixing at four vertexes, are driven by four independent motors. Motors at diagonal position rotate in the same direction, and motors at adjacent position rotate in the opposite direction. The motion principle is approximately described as follows: each propeller provides lift that is vertical to the fuselage. Without considering interference of other external forces, if propellers' rotating speed or the motors have the same output power, AUV is in the condition of rising, diving or hovering. If the output power is different, the force balance and torque balance will be broken, and then cause changes in attitude and motion direction of the AUV.



(a) Three-dimension graph of model



(b) Real model uninstalled control system

Fig. 1. Structure of propeller AUV

As shown in Fig.2, OXYZ represents the earth-fixed coordinate and oxyz represents AUV body-fixed coordinate. 6 DOF kinematic modes and attitude parameters are defined in the coordinate system as shown in Table 1.

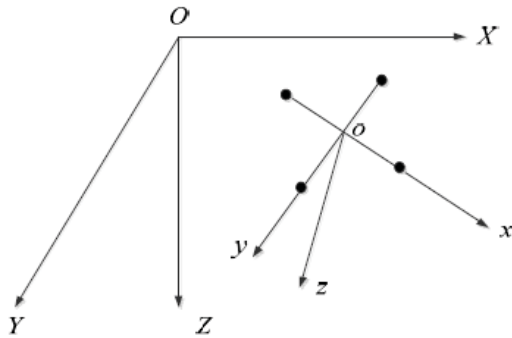


Fig. 2. Earth-fixed coordinate and body-fixed coordinate

According to the parameters in the Table 1, define vectors as follows:  $\eta_1 = (x, y, z)^T$ ,  $\eta_2 = (\phi, \theta, \psi)^T$ ,  $\eta = (\eta_1, \eta_2)^T$ ,  $\tau_1 = (F_x, F_y, F_z)^T$ ,  $\tau_2 = (M_x, M_y, M_z)^T$ ,  $\tau = (\tau_1, \tau_2)^T$ ,  $V = (u, v, w)^T$ ,  $\omega = (p, q, r)^T$ ,  $v = (V, \omega)^T$ , and the center of gravity position is  $r_G = (x_G, y_G, z_G)^T$ .

#### KINEMATIC MODEL

Based on the conclusions of Refs [5], the kinematic model of AUV is given directly as:

$$\begin{cases} \dot{\eta}_1 = J_1(\eta_2)V \\ \dot{\eta}_2 = J_2(\eta_2)\omega \end{cases} \quad (1)$$

Where,  $J_1(\eta_2)$ ,  $J_2(\eta_2)$  represent the transformation matrixes of linear velocity and angular velocity from the body-fixed coordinate to the earth-fixed coordinate, and the concrete expressions are given as follows:

Table 1 Motion modes and attitude parameters of propeller AUV

Degree of freedom	Motion modes	Force/torque (in the body-fixed coordinate)	Linear velocity/angular velocity (in the body-fixed coordinate)	Location/Euler angles (in the earth-fixed coordinate)
1	Back/forward (movement along the x-axis)	$F_x$	$u$	$x$
2	Sway (movement along the y-axis)	$F_y$	$v$	$y$
3	Lift/dive (movement along the z-axis)	$F_z$	$w$	$z$
4	Roll (rotation along the x-axis)	$M_x$	$p$	$\phi$
5	Pitch (rotation along the y-axis)	$M_y$	$q$	$\theta$
6	Yaw (rotation along the z-axis)	$M_z$	$r$	$\psi$

$$J_1(\eta_2) = \begin{bmatrix} \cos \theta \cos \psi & -\sin \psi \cos \phi + \cos \psi \sin \theta \sin \phi & \sin \psi \sin \phi + \cos \psi \cos \phi \sin \theta \\ \sin \psi \cos \theta & \cos \psi \cos \phi + \sin \phi \sin \theta \sin \psi & -\cos \psi \sin \phi + \sin \theta \sin \psi \cos \phi \\ -\sin \theta & \cos \theta \sin \phi & \cos \theta \cos \phi \end{bmatrix} \quad (2)$$

$$J_2(\eta_2) = \begin{bmatrix} 1 & \sin \phi \tan \theta & \cos \phi \tan \theta \\ 0 & \cos \phi & -\sin \phi \\ 0 & \sin \phi \sec \theta & \sec \theta \cos \phi \end{bmatrix} \quad (3)$$

## DYNAMIC MODEL

Based on the theorem of momentum and theorem of angular momentum, the dynamic formulas in body-fixed coordinate are summarized as follows:

$$\begin{aligned} m[\dot{u} - vr + wq - x_G(q^2 + r^2) + y_G(pq - \dot{r}) + z_G(pr + \dot{q})] &= F_x \\ m[\dot{v} - wq + ur + x_G(qp + \dot{r}) - y_G(p^2 + r^2) + z_G(qr - \dot{p})] &= F_y \\ m[\dot{w} - uq + vp + x_G(rp - \dot{q}) + y_G(rq + \dot{p}) + z_G(p^2 + q^2)] &= F_z \\ I_x \dot{p} + (I_z - I_y)qr + m[y_G(\dot{w} + vp - uq) - z_G(\dot{v} + ur - wq)] &= M_x \\ I_y \dot{q} + (I_x - I_z)rp + m[z_G(\dot{u} + wq - vr) - x_G(\dot{w} + vp - uq)] &= M_y \\ I_z \dot{r} + (I_y - I_x)pq + m[x_G(\dot{v} + ur - wp) - y_G(\dot{u} + wq - vr)] &= M_z \end{aligned} \quad (4)$$

While AUV is moving underwater, it is mainly influenced by hydrodynamic forces and control forces, as shown in Eq.(5).

$$\tau = \tau_{AM} + f_v + M_R + f_p \quad (5)$$

Where,  $\tau_{AM}$  is fluid inertia force,  $f_v$  is fluid viscous force,  $M_R$  is restoring force, and the concrete expressions are given in Refs [6]. The hydrodynamic parameters of propeller AUV are obtained by CFD method and hydrodynamic experiments.  $f_p$  is the pull force produced by the propellers, and in body-fixed coordinate.

$$f_p = (0, 0, 0, -\sum_{i=1}^4 F_i, 0, 0, Q) \quad (6)$$

Where,  $F_i$  is the pull force produced by the propeller  $i$ , and  $Q$  is pull torque.

According to the research object and specific issues, some reasonable assumptions are made during the computation process:

- (1) AUV is rigid body.
- (2) The body has two symmetry planes of upper and lower, left and right. The origin of the body-fixed coordinate is buoyant center, which is coincident with the center of gravity, and that means  $r_G = (0, 0, 0)^T$ .
- (3) If AUV moves slightly near the equilibrium position, it is assumed that the relationship between the fluid damping force and motion parameters is linear approximately. Thus,  $\sin \theta = \theta$ ,  $\cos \theta = 1$ .

Based on the analysis above, the transfer functions of depth, pitch angle and roll angle are calculated using MATLAB as follow:

$$G_z(s) = \frac{9.1640s^2 - 134.5019s - 902.4235}{s^4 + 18.0997s^3 + 121.1859s^2 + 390.2967s + 268.4251} \quad (7)$$

$$G_\theta(s) = \frac{-11.378s - 35.0461}{s^4 + 18.0997s^3 + 121.1859s^2 + 390.2967s + 268.4251} \quad (8)$$

$$G_\phi(s) = \frac{-11.378s - 35.0461}{s^4 + 18.0997s^3 + 121.1859s^2 + 390.2967s + 268.4251} \quad (9)$$

## THE STABILITY CONTROLLER

### DESIGN OF A STABILITY CONTROLLER

Due to the presence of external disturbance, whatever the AUV is going forward or backward, even in hover, vertical rise or dive state, it requires a certain pitch angle to maintain the predetermined trajectory. If turning around, it also requires a certain roll angle. According to the AUV model, several attitude angles can't be confirmed in some special situations, the singularity will appear [7]. For example, when  $\theta = \pm 90^\circ$ , the roll angle  $\phi$  is uncertain. Due to the effects of unknown ocean currents in real environment, the attitude angles are easily to change. And the AUV will be instable and even out of control. Various kinds of research have studied the motion control methods, such as self-adaptive control [8-9], neural network control [10-11], and fuzzy logic control [12-13] etc., which make the AUV robust and more resistant to interference. However, most of these new methods are only applied in simulation or experiments, and rarely for engineering and commercial application. It is pointed out in Refs [14] that, when the model is decoupled linearly, each subsystem can be controlled independently using linear control theory. PID controller has advantages of simple algorithm and high reliability. Learning from the idea of combined sections method in Refs.[15], the stability controller of propeller AUV is composed of several PID controllers, and each of them is corresponding to a certain motion state. PID controllers switch each other by triggering critical state value.

As shown in Fig.3, AB represents that propeller AUV dives vertically from water surface to predetermined depth, and DE represents contrary process to AB. During both AB and DE, because the influence of surface wave is obvious, the controller must have a better robustness. In stable motion process BC, attitude angles need to keep within a certain range, and avoid jittering. In case large current interference appears at point C, the augmentation controller should be started to prevent the AUV to be out of control, which is caused by the attitude angles exceeding the critical values. Likewise, the AUV may overturn owing to unforeseen circumstances in diving and rising stages, and it should be taken into consideration when design the controllers.

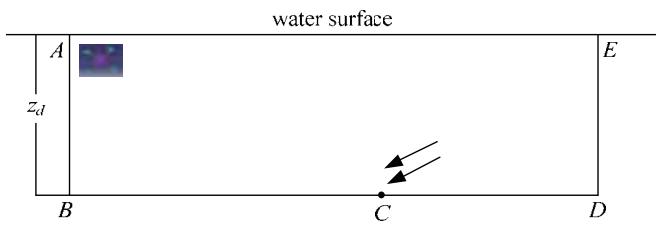


Fig.3 Motion process of AUV in a whole cycle

The stability controller consists of three parts, which are diving/rising controller Ctr1, smooth controller Ctr2 and augmentation controller Ctr3. The diving depth  $Z$ , pitch angle  $\theta$  and roll angle  $\varphi$  are selected as switch triggering variables. Since the roll direction and pitch direction are symmetrical, take  $Z$  and  $\theta$  as examples to introduce the whole process. Starting Ctr1, the propeller AUV begins to dive to a predetermined depth  $Z_d$  ( $Z_d=10\text{m}$ ), with pitch angle  $\theta < 5^\circ$ . After reaching  $Z_d$ , the Ctr2 is started, then adjust the moving velocity according to the actual situation, and make  $5^\circ < \theta < 30^\circ$ , therefore, the AUV will be in a stable state. During the rising process, adjust and keep  $\theta < 5^\circ$ , and Ctr1 is restarted. Whichever stage the AUV is in, if it is disturbed strongly, and make  $\theta > 30^\circ$ , Ctr3 will be started to resume its safe moving attitude. The switch mode of controllers is shown in Fig.4.

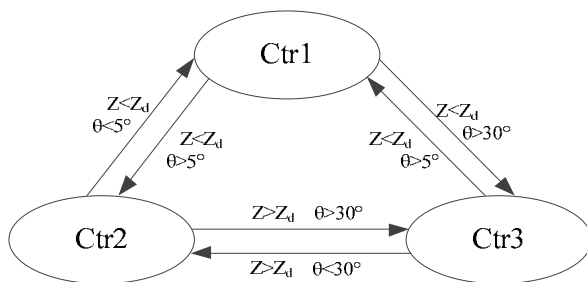


Fig.4 Switch mode of controllers

## THE STABILITY OF CONTROLLER

Based on the Ziegler-Nichols method, the parameters of Ctr1, Ctr2, and Ctr3 after setting are given in Table 2.

Table 2 PID parameters

ID NO.	$K_p$	$K_i$	$K_d$
Ctr1	0.045	0.045	0.30
Ctr2	0.015	0.015	0.20
Ctr3	0.030	0.010	0.35

When Ctr1 works,  $K_p = 0.045$ ,  $K_i = 0.045$ ,  $K_d = 0.30$ .

The transfer function of PID controller is:

$G_{c1} = K_p + \frac{K_i}{s} + K_d s$ , so the system state equation can be get as follow.

$$\begin{cases} \dot{x} = Ax + bu \\ y = Cx \end{cases} \quad (10)$$

Where,

$$A = \begin{bmatrix} -8 & -5.6569 & 0 & 0 \\ 5.6569 & 0 & 0 & 0 \\ -22.6772 & -23.0649 & -10.0997 & -2.8963 \\ 0 & 0 & 2.8963 & 0 \end{bmatrix}, \quad b = \begin{bmatrix} 1 \\ 0 \\ 1 \\ 0 \end{bmatrix}, \quad C = [0 \ 0 \ 0 \ 3.1641] \quad (11)$$

According to the Lyapunov-stability theory and  $AP + PA^T = -Q$ , set

$$Q = \begin{bmatrix} 1 & 0 & 0 & 0 \\ 0 & 1 & 0 & 0 \\ 0 & 0 & 1 & 0 \\ 0 & 0 & 0 & 1 \end{bmatrix} \quad (12)$$

The matrix  $P$  can be obtained:

$$P = \begin{bmatrix} 0.1250 & -0.0884 & 0.0252 & 0.1535 \\ -0.0884 & 0.2500 & -0.2998 & -0.2042 \\ 0.0252 & -0.2998 & 0.7272 & -0.1726 \\ 0.1535 & -0.2042 & -0.1726 & 1.7535 \end{bmatrix} \quad (13)$$

After calculation, the 4 order principle minors of  $P$  are 0.1250, 0.0234, 0.0070 and 0.0078 respectively, and all are greater than zero, which means that  $P$  is positive definite matrix, so the system is stable. Similarly, when Ctr2 or Ctr3 works, the system is stable as well. The system can be proved approximately global stable due to the very short switching time among these three controllers.

## THE SIMULATION RESULTS AND ANALYSIS

### THE SIMULATION CONDITIONS

As shown in Fig.5, the simulation model of pitch channel is established under the circumstance of MATLAB/SIMULINK. It mainly consists of 5 parts: stateflow module, PID module, transfer function module, switch module and display module. Stateflow module, which involves 3 states of diving/rising state, smooth moving state and augmentation moving state, is used

to set AUV's motion states and realize transition. PID module accomplishes attitude control and depth control of the AUV, so as to achieve the predetermined results. Transfer function module describes the AUV's dynamic model. Switch module selects different PID controllers according to the output signal of the state stream. Display module shows the motion state and change trend.  $z$  and  $x$  are depth and pitch angle respectively.

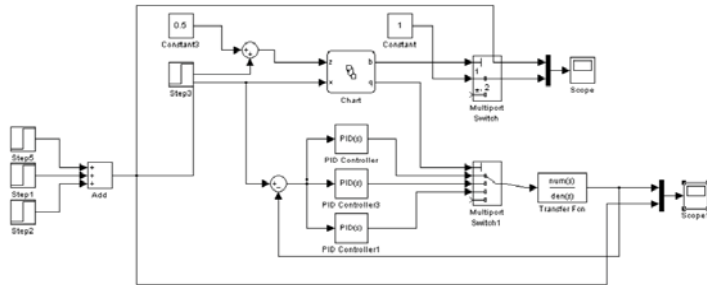


Fig.5 Control simulation model for pitch channel

## ANALYSIS OF SIMULATION RESULTS

Simulation process (1): the AUV dives vertically first and then moves horizontally under the ideal or small interference conditions, as shown in Fig.6. During the period of  $t < 10s$ , the AUV is diving vertically and its depth is less than 10 m. With two periods of 0-5 s and 5-10 s, the input signals of pitch angle are  $1^\circ$  and  $4^\circ$  respectively, and both of them are less than the setting critical value of the diving/rising state. In this process, the diving state is relatively stable, which shows that Ctr1 can meet the control requirements. When  $t = 10 s$ , since the diving depth exceeds 10 m, which is the predetermined depth, the AUV stops diving and begins to move horizontally or approximate horizontally. The input signal of pitch angle is  $9^\circ$ , and smooth controller works. After about 5 s, the AUV reaches a stable moving state. Because of the different controller parameters and real circumstances, the rise time of step response of smooth moving stage is about 2.5 s, while in diving stage it is less than 1s. At the same time, overshoot when it reaches steady state of the diving stage are smaller than that of the smooth moving stage. When diving or rising vertically, the AUV must keep an approximately horizontal attitude with a small pitch angle ( $\theta < 5^\circ$ ), which requires better rapidity and higher accuracy. However, when moving horizontally or approximately horizontally, the AUV will adjust its pitch angle in a larger scope ( $5^\circ < \theta < 30^\circ$ ) to meet the requirements of changing the moving velocity.

Simulation process (2): the AUV is moving horizontally, and when  $t = 15 s$ , it encounters strong currents, which cause that the instantaneous pitch angle is greater than  $30^\circ$ , as shown in Fig.7. The stability controller generates augmentation stimulus, meanwhile, augmentation controller will be started so that it can adjust the attitude angle quickly to avoid being out of control.

As shown in Fig.8, the control error of Ctr1 is less than  $2^\circ$ , which of Ctr2 is less than  $5^\circ$ . In almost all actual cases, the attitude angles change continuously. But the simulation input in this paper is a step signal under ideal conditions, which is

more rigorous. So the stability controller can meet the control requirements.

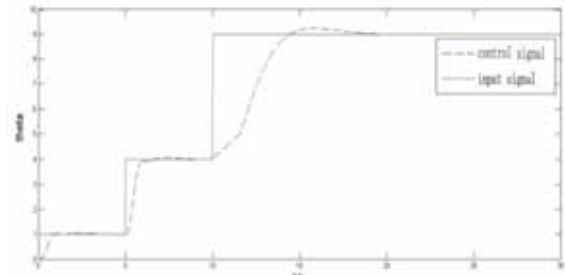


Fig.6 Control process of pitch angle

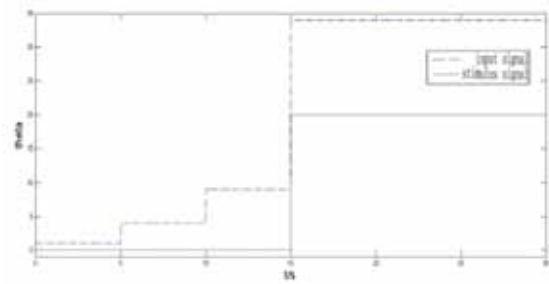


Fig.7 Stability stimulus

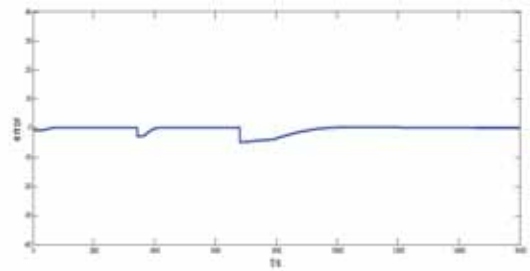


Fig.8 Error curve

## CONCLUSIONS

1. Learning from the motion principle of quadrotor, a symmetric propeller AUV, which has small size and low velocity, is designed. Compared with the AUV equipped with rudders, it can dive, hover, rise, go forward and backward or turn around by adjusting the rotate speed of four propellers fixed on the rigid cross structure, which has better maneuverability and flexibility. The linear models of depth, pitch angle and roll angle are obtained.
2. Based on the thoughts of combined sections method, a stability controller is designed. It is composed of 3 PID controllers, which switch each other by triggering critical state value, and each of them is corresponding to a certain motion stage, improving the stability of the propeller AUV under the disturbance of complex ocean currents. The simulation results demonstrate the effectiveness of the stability controller.

## REFERENCE

1. Forrest A L, Laval B, Doble M J, et al. AUV measurements of under ice thermal structure[C]//Proceedings of MTS/IEEE OCEANS 2008. Quebec City: IEEE Press, 2008:1-10.
2. Jun B H, Park J Y, Lee F Y, et al. Development of the AUV 'ISiMI' and a free running test in an ocean engineering basin [J]. Ocean Engineering, 2009, 36(1): 2-14.
3. PETRCH J, WOOLSEY C A, STILWELL D J. Planar flow model identification for improved navigation of small AUVs [J]. Ocean Engineering, 2009, 36(1): 119-131.
4. JIANG Jun, SONG Baowei, PAN Guang, et al. Study on design of shape and hydrodynamic layout for ultra-low-speed AUV [J]. TORPEDO TECHNOLOGY, 2011, 19(5): 321-324.
5. JIA Heming. Study of spatial target tracking nonlinear control of underactuated UUV based on backstepping [D]. Harbin: Harbin Engineering University, 2012.
6. DU Bing. Dynamic behavior and control strategy of a landing AUV [D]. Tianjin: Tianjin University, 2012.
7. YAN Weisheng. Torpedo sailing mechanics[M]. Xi'an: Northwestern Polytechnical University Press, 2005
8. Do K D, Pan J. Robust and adaptive path following for underactuated autonomous underwater vehicles. Proceedings of the American Control Conference, Denver, CO, USA, 2003,3:1994-1999
9. Roberts A, Tayebi A. Adaptive position tracking of VTOL UAVs [J]. IEEE Transactions on Robotics, 2011, 27(1):129-142
10. Sarath B S, Kumar C S, Faruqi M A. A neural network online controller for autonomous underwater vehicle. Industrial Technology,2006:2320-2324
11. CONG Shuang, SONG Ruixiang, Qian Zhen, et al. Improved B-spline fuzzy neural networks [J]. Control Theory and applications, 2001, 18(2): 277-280.
12. ZHAO Jing. AUV fuzzy neural network hybrid learning algorithm control [D]. Harbin: Harbin Engineering University, 2007.
13. ZHANG Bo. Research on fuzzy PID controller [J]. Journal of Software Guide, 2010, 9(1):22-25.
14. SUN Wei. Research on low cost flight control and application of UAV [D]. Nanjing: Nanjing University of Aeronautics and Astronautics. College of Aerospace Engineering, 2011
15. LI Guodong, SONG Zili, WU Hua, et al. Design of stability augmentation hybrid controller for a quadrotor unmanned air vehicle [J]. JOURNAL OF HARBIN INSTITUTE OF TECHNOLOGY, 2013,45(5):86-90.

## CONTACT WITH THE AUTHOR

QI Duo, FENG Jinfu, LIU An, HU Junhua, XU Hu

Aeronautics and Astronautics Engineering College  
Air Force Engineering University  
Xi'an 710038

**CHINA**

LI Yongli

Engineering University of CAPF  
Xi'an 710086

**CHINA**

Muhammad Aqeel Ashraf

Department of Geology, Faculty of Science  
University Of Malaya  
50603 Kuala Lumpur  
**MALAYSIA**

## TWO-STAGE CLASSIFICATION APPROACH FOR HUMAN DETECTION IN CAMERA VIDEO IN BULK PORTS

Chao MI<sup>a</sup>

Zhiwei ZHANG<sup>b</sup>

Xin HE<sup>b</sup>

Youfang HUANG<sup>a</sup>

Weijian MI<sup>a</sup>

<sup>a</sup>)Container Supply Chain Tech. Engineering Research Center, Shanghai Maritime University, No.1550  
Haigang Ave, Shanghai 201306, China

<sup>b</sup>)Logistics Engineering College, Shanghai Maritime University, No.1550 Haigang Ave, Shanghai  
201306, China

### ABSTRACT

*With the development of automation in ports, the video surveillance systems with automated human detection begun to be applied in open-air handling operation areas for safety and security. The accuracy of traditional human detection based on the video camera is not high enough to meet the requirements of operation surveillance. One of the key reasons is that Histograms of Oriented Gradients (HOG) features of the human body will show great different between front & back standing (F&B) and side standing (Side) human body. Therefore, the final training for classifier will only gain a few useful specific features which have contribution to classification and are insufficient to support effective classification, while using the HOG features directly extracted by the samples from different human postures. This paper proposes a two-stage classification method to improve the accuracy of human detection. In the first stage, during preprocessing classification, images is mainly divided into possible F&B human body and not F&B human body, and then they were put into the second-stage classification among side human and non-human recognition. The experimental results in Tianjin port show that the two-stage classifier can improve the classification accuracy of human detection obviously.*

**Keywords:** Human Detection, Histograms of Oriented Gradients, Support Vector Machine, Classification

### INTRODUCTION

According to the safety and security requirements of open-air unmanned handling operation areas of bulk ports, the pedestrians without permission are forbidden entering those areas because of the high risk in the port handling process. Recently, the machine vision technology begun to be applied in some areas with high security and efficiency requirements such as the automated handling fields of bulk terminals [1][2]. Comparing to the large quantity of researches on port handling technology, the research of machine vision technology in automatic port is only just the beginning [3][4]. Although we have done some research on human detection algorithm, the detection accuracy is not enough to meet the practical necessity, which are in need of further research.

At the earliest, template matching was the popular approach to recognize the human in the images. Template matching is to match the feature of detection image and the template of human contour to conduct human detection [5]. Songmin Jia et al. proposed varying scale template matching (VSTM) to detect human from disparity image based on head-shoulder method [6]. But the diversity of human postures and clothing caused problems in template matching and led to a large amount of calculation.

After that, because of the low accuracy and high calculation consumption, the template matching has been eliminated. The research on human detection is now categorized under 2 steps – feature extracting and classifier designing. Navneet Dalal and Bill Triggs firstly proposed Histograms of Oriented

Gradients (HOG) approach in 2005[7]. Since geometric and optical deformation affects a little on the features and some subtle body actions can be ignored, HOG is suitable for human detection. It relies on contrast between human contour and background. Thus, Hong Tian et al. proposed a multiplex cascade classifier which can filter out most of irrelevant background [8]. Hai-Miao Hu et al. applied a joint global-local information algorithm to suppress the background interference and enrich the description of pedestrian [9]. To a great extent, these researches reduced the influence of background and improved the detection accuracy.

However, 3780 HOG features needs to be extracted in each sub-image with the consideration of the impact of each possible factor and then Support Vector Machine (SVM) classifier is used to make a binary decision, which results in low efficiency. A year after the proposition of the above method, Qiang Zhu et al. introduced integral image into the calculation of HOG features to solve huge computation of HOG feature extraction [10]. Variable-size blocks were used to replace the multi-scale detection in traditional method and the cascade classifier was used to select a small subset of HOG features. Compared with Navneet Dalal's method, its accuracy is lower than Navneet Dalal's algorithm in most cases because integral histograms of orientated gradients abandons the original Gaussian weighted tri-linear interpolation and cannot avoid the influence of overlapping. Moreover, the considered feature set is not abundant enough. In our previous research, we presented an improved HOG algorithm with a combined classifier to reduce the calculation consumption [1]. Human detection efficiency is improved, but the accuracy is still equal to the traditional ways, which cannot meet the precision requirements in practical application.

Currently, most scholars study on the human detection mainly based on HOG proposed by Navneet Dalal [11]. Marco Pedersoli et al. proposed presents a multiresolution cascade of HOG that can highly reduce the computational cost without affecting accuracy [12]. HOG can obtain abundant feature sets by extracting shape and motion information of human body, which can entirely describe the contour features with a strong robustness [13]. HOG feature has been widely used in human detection, as a feature based on edge and shape of object, which is a kind of fuzzy edge direction oriented feature. Therefore, HOG feature can ignore some subtle changes of human body to get a better robustness than other methods such as template matching. But the large difference between human standing postures, such as front & back standing posture or side standing posture, will lead to the final HOG features for classifiers are less specific.

At present, the classifiers widely used in human detection are the Adaptive Boosting (Adaboost) cascade classifier and SVM classifier. The traditional single classifier is trained by HOG features combined of different human body postures can only screen a few effective features. For most classifiers, they are usually used to find those specific features among the whole features from samples. SVM is a machine learning method based on Vapnik-Chervonenk is dimension and Structural Risk Minimization of statistical learning theory [14] [15].

SVM can classify the samples by the specific features with classification ability. Less sample training can obtain a SVM classifier with preferable performance. In terms of Adaboost classifier, this classifier selects some important specific feature vectors as weak classifiers to train a strong classifier [16] [17]. Then it establishes a statistical method for human body so that it can detect human body from candidate targets. Some researchers tried to combine the single classifiers to classify the human body based on HOG. In our previously researches and Lie Guo's researches, Adaboost and SVM were combined to classify the human body, the performances were better than the traditional single classifier, but these combined classifiers did not consider the human postures [1][18]. Therefore, there will be room for improvement.

The major work of this paper is that a two-stage SVM classifier is chosen to replace traditional SVM classifier to improve the detection accuracy. As the research proposed by Huimin Qian, humans have a variety of postures in images [19]. Front or back standing (F&B) humans with relatively large effective areas have rich contour features and are easy to be classified, while side standing (Side) humans have less features and are more complex, comparatively. If the classifier is trained like the traditional method using mixed samples, it may cause classification conflict which will lead to unsatisfactory effects. Therefore, at the beginning of classification, detection images should be divided into three categories, front and back standing posture, side standing posture and non-human. In the first stage, the samples are mainly divided into possible F&B human body and not F&B human body, and then they were put into the second-stage classification among Side human and non-human recognition. Finally the detection results are merged together.

## **TWO-STAGE HUMAN CLASSIFICATION ALGORITHM**

### **HOG FEATURE EXTRACTION ALGORITHM**

In fact, it has been found that HOG descriptor has many advantages compared with other feature description methods. 1) HOG represents the structural feature of edge, so that it can describe local shape information and depict contour feature of human body to a great extent [20]; 2) Quantization of position and direction in the space can suppressed the influence of translation and rotation to some extent; 3) Since HOG is operated on the local cell unit of images, it can maintain good invariance on geometric and photometric deformation[21]. The main idea of HOG is to calculate the statistics data of local gradient direction in the images proposed by Navneet Dalal and Bill Triggs [7]. The whole image is divided into small areas (called cells), and histograms are created for each cell according to gradient direction. The combination of these histograms shows the detected object's feature. In order to improve accuracy, local histogram can combine small cells into a large area (called block), and then normalize in block units to ensure better illumination or shadow invariance [22].

The HOG feature is extracted by the following steps:

1. Standardization of color space is needed for images because the environment of open-air handling operation is complex and the illumination is strong. Image noise can be suppressed using square root compression gamma correction operations. The standardized pixel values of three channels,  $R_{x,y}$ ,  $G_{x,y}$  and  $B_{x,y}$ , can be obtained by Eq.1;

$$\begin{cases} R_{x,y} = \sqrt{r_{x,y}} \\ G_{x,y} = \sqrt{g_{x,y}} \\ B_{x,y} = \sqrt{b_{x,y}} \end{cases} \quad (1)$$

Where,  $r_{xy}$ ,  $g_{xy}$  and  $b_{xy}$  are the pixel original values of red channel, green channel and blue channel, respectively, where  $(x, y)$  is the pixel coordinates.

2. The intensity and direction of gradient for each point need to be calculated after standardized gradation; One-dimensional discrete template  $[-1, 0, 1]$  and  $[-1, 0, 1]^T$  are used both in the horizontal and vertical directions, the gradient magnitude  $G_{x,y}$  and gradient direction  $\theta_{x,y}$  of the pixel point  $(x, y)$  are calculated according to the following Eq.2 and Eq.3:

$$G_{x,y} = \sqrt{G_x^2(x, y) + G_y^2(x, y)} \quad (2)$$

$$\theta_{x,y} = \tan^{-1} (G_y(x, y) / G_x(x, y)) \quad (3)$$

Where,  $G_x(x, y)$  and  $G_y(x, y)$  are the gradient magnitude of pixel point  $(x, y)$  in the x axis (horizontal direction) and y axis (vertical direction), which can be calculated by Eq.4:

$$\begin{cases} G_x(x, y) = f_{x+1,y} - f_{x-1,y} \\ G_y(x, y) = f_{x,y+1} - f_{x,y-1} \end{cases} \quad (4)$$

Where,  $f_{x,y}$  is the value of pixel point  $(x, y)$ .

3. According to Fig.1, the whole image is scanned by a block, which is divided into 4 cells.  $[0^\circ, 180^\circ]$  is divided into 9 bins as shown in Fig.2. And then the gradient direction of each point in the unit is discretized into the 9 bins. The gradient direction of each pixel is assigned to the neighboring bins by a certain ratio using a tri-linear interpolation method [23]. 36 dimensional HOG feature vector can be extracted from each block.

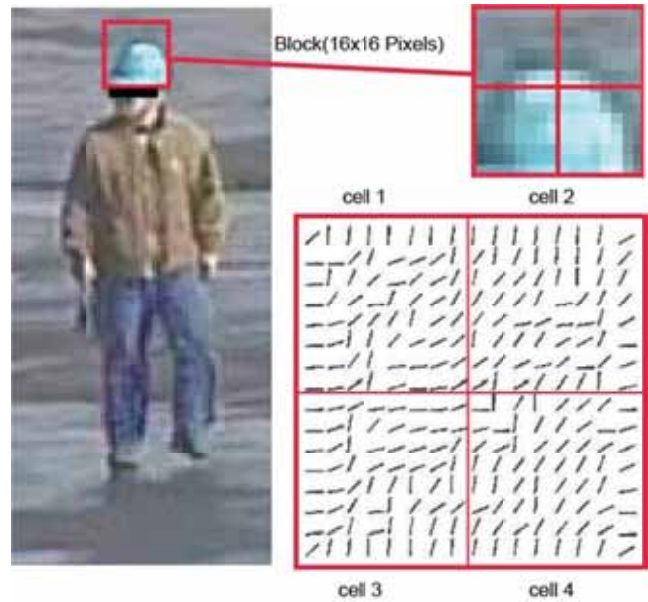


Fig. 1 HOG descriptors schematic.

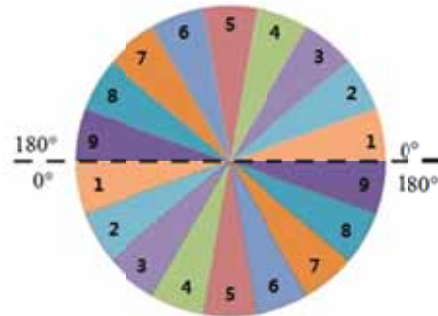


Fig. 2 Bin's schematic diagram.

4. L2-Norm is used in each block for normalization to reduce the effect of illumination and shape variation of edges.
5. Finally, the entire 105 blocks are connected in series to form a 3780 dimensional feature vectors for each detection window.

In the above steps, HOG feature extraction of each block is the foundation to extract the HOG feature of the whole image. Here, tri-linear interpolation is usually adopted to process the local block image. For analyzing its principle, it can be easy to know that HOG feature is a feature based on edge direction and shape feature of human body.

(a)



(b)

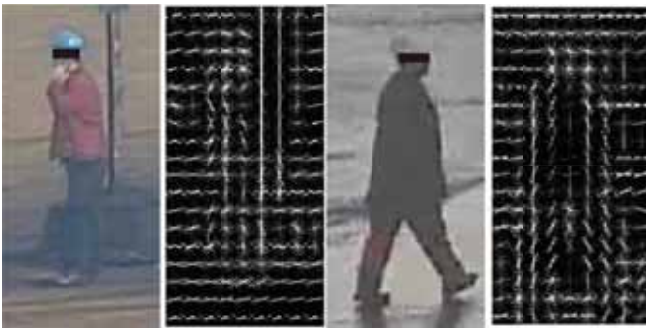


Fig. 3 HOG features of human

However, HOG feature based on edge direction information limits the performance of traditional classifier for human detection. As shown in Fig.3, in the case of different posture, effective features from human body also show different specific characteristics. As shown in Fig.3 (a), the head and shoulders of F&B human body basically keeps invariant geometric features, including relative position, angle and size. When standing or walking, F&B human bodies are basically not cross their legs. HOG features extracted by F&B samples are nearly symmetrical with more obvious specific characteristics. For side human samples as shown in Fig.3 (b), the shoulders overlap each other and the legs also overlap or cross, which means that the effective features from side humans are more confusion and lack symmetry. Obviously, as described in the above HOG extraction process, HOG features can obtain the specific characteristics of human body based on contour features and shape features of human. Thus, under this situation, it is necessary to add one-stage classifier for distinguishing different postures of the human.

## TWO-STAGE CLASSIFICATION APPROACH

High-dimensional feature vectors in detection window have been calculated in previous section. The next step is to make judgment according to the particularity of human contour.

Over the past ten years, SVM has been widely used for human detection because of its generality and good performance [24]. On the other hand, the selection of classification feature has a great impact on SVM classification effect. However, as mentioned in previous section, HOG feature will represent

large different specific characteristics when extracted by different human body postures. Hence, a novel classification needs to be applied to improve SVM classification accuracy on the basis of assuring classification efficiency.

Within the scope of the detection, human body will not always show F&B postures in cameras. Due to the effect of many factors, such as dust, illumination, color change and body postures, it is very difficult to design classifier to obtain an ideal detection result by using single classifier. One of the reasons is the long training time and the poor detection performance of SVM algorithm for various human postures. The major purpose of this paper is to improve the traditional classification method by replacing single classifier with a two-stage classifier based on classifiers fusion using the idea of SVM classifier. The detailed concept is shown as follows:



Fig. 5 The sample sets of F&B and side postures.

Two-stage classifier firstly processes human contour samples and divides targets into three types: possible F&B and side and non-human as shown in Fig.4. Firstly, the pre-classified images of each posture should concurrently be made a binary decision: F&B human or not F&B human by F&B classifiers. Then, the second classifier can make the rest image divided into two types: side human or non-human. Finally, the detection results of F&B and side human body are merged to generate candidate areas with people inside. The sample sets of F&B and side postures are shown in Fig.5.

SVM is a supervised learning algorithm, which you need to import the training sample sets with a label. Here, the calculated HOG features set will be the initial 3780 dimensional feature vector space. The detailed training process of classifiers is shown as follows:

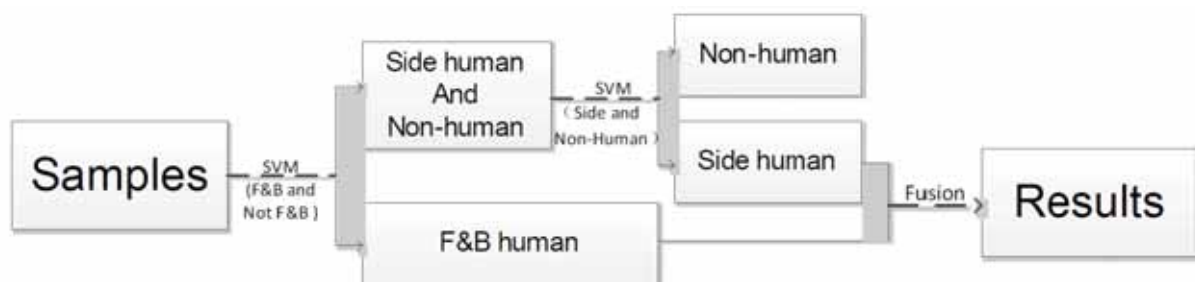


Fig. 4 Two-stage classification approach flowchart.

### 1. Preprocessing of samples

First, the samples are divided into three types: F&B, side and non-human. Using radial basis function (RBF) as Eq.5, the 3780 dimensional feature space of samples will be mapped to a higher-dimensional feature space, which is linearly separable.

$$K(x, x_c) = e^{-\frac{\|x-x_c\|^2}{(2\sigma^2)}} \quad (5)$$

Where,  $\mathbf{x}$  is a feature vector in the feature space and  $\mathbf{x}_c$  is the position of the center of kernel function. The width parameter  $\sigma$  of function can control the radial scope of impact from kernel function. Thus, when  $\mathbf{x}$  far away from  $\mathbf{x}_c$ , the function value will be very small.

In order to find the two hyper planes in the labeled sample feature space, objective function and constraint function of the two-stage classifier is shown in Eq.6.

$$\begin{cases} \min \frac{1}{2} \|\mathbf{w}\|^2, \min \frac{1}{2} \|\mathbf{w}'\|^2 \\ s. t : y_i \cdot (\mathbf{w}^T \mathbf{x}_i + b) - 1 \geq 0 \quad (i = 1, 2, \dots, l) \\ (\mathbf{w}'^T \mathbf{x}'_i + b') - 1 \geq 0 \quad (i = 1, 2, \dots, l') \end{cases} \quad (6)$$

$\mathbf{x}_i$  ( $\mathbf{x}'_i$ ) and  $\mathbf{w}$  ( $\mathbf{w}'$ ) represent the feature vector and a combination of feature vectors when training F&B (side) classifier.  $l$  ( $l'$ ) means the number of samples. By given samples and labels,  $\mathbf{w}$  ( $\mathbf{w}'$ ) can be calculated by Eq.7:

$$\mathbf{w} = \alpha_1 \mathbf{x}_1 y_1 + \alpha_2 \mathbf{x}_2 y_2 + \dots + \alpha_n \mathbf{x}_n y_n \quad (7)$$

In Eq.7,  $\mathbf{x}$  represents the HOG feature vector and  $y$  means the label value of  $\mathbf{x}$ .  $\alpha$  and  $n$  are Lagrange multipliers and the size of sample sets. To avoid that the results might be controlled by several points of samples space, slack variables  $\zeta$  and punishment factor  $c$  need to be imported to increase fault tolerance of the two-stage classifier.

$$\begin{cases} \min \frac{1}{2} \|\mathbf{w}\|^2 + c \sum_{i=1}^l \zeta_i, \min \frac{1}{2} \|\mathbf{w}'\|^2 + c' \sum_{i=1}^{l'} \zeta'_i \\ s. t : y_i \cdot (\mathbf{w}^T \mathbf{x}_i + b) - 1 \geq 0 \quad (i = 1, 2, \dots, l) \\ (\mathbf{w}'^T \mathbf{x}'_i + b') - 1 \geq 0 \quad (i = 1, 2, \dots, l') \end{cases} \quad (10)$$

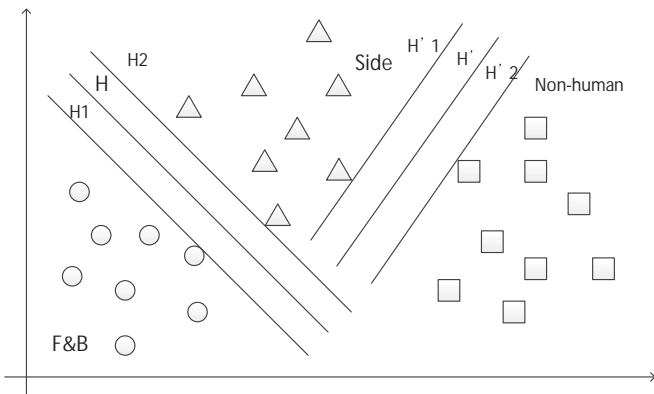


Fig. 6 Two-stage classifier.

Therefore, as shown in Fig.6, the objective functions of the

two-stage classifier will be used to find the two hyper planes  $H$  and  $H'$  for training F&B classifier and side classifier.

### 2. Training F&B classifier and side classifier

For F&B classifier, the sample feature  $\mathbf{x}_i$  will be labeled as  $y_i = +1$ , which belongs to F&B sample features, otherwise  $y_i = -1$ . For side classifier, if the sample feature  $\mathbf{x}'_i$  belongs to the side sample features, it will be labeled as  $y'_i = +1$ , otherwise  $y'_i = -1$ .

Then, SVM parameters needs to be determined, such as, the type of SVM classifier, kernel function type, punishment factor and the other main parameters.

After that, using these HOG feature vectors with labels respectively, SVM classifier is trained to get the first-stage and second-stage initial classifiers. As shown in Fig.6, through F&B as positive samples and the others as negative samples, the support vectors and hyper plane  $H$  will be got by training the first-stage classifier, which can separate two features spaces. In the same way, the hyper plane  $H'$  will be obtained by training side as positive samples and non-human as negative samples..

### 3. Training final two-stage classifier

Trying to detect human in the negative samples through initial classifiers, there will be many erroneous detection results, which can be termed "hard example". In order to improving detection accuracy, HOG feature from these hard examples will be combined with the original negative samples as new negative samples.

Based on the new samples space, new two-stage classifier with a higher accuracy can be trained. Repeating the step 3), the final two-stage classifier with appropriate detection accuracy will be trained.

## EXPERIMENTAL RESULTS AND ANALYSIS

The system has conducted several field tests in operation field in terminals of Tianjin Port. Fig.7 shows the video captures of field tests.

Representative images are selected to build 3 image sets of different types and complexity to perform evaluation for the proposed human detection system. The main characteristics of the 3 test sets are shown in table 3, which are F&B test set and side test set and various mixed postures test set including F&B, side etc.

Table 1 The testing sample sets.

Test set	Sample size	Number of person	Posture
1	453	453	F&B
2	365	365	Side
3	398	866	Mixed



Fig. 7 The experimental results of grain terminal.

The experimental results are shown in the table 2 below, among which the two-stage classifier is the novel method introduced in Section 2.2. “FDR” means “false detection rate”.

Table 2 The experimental results.

Test set	Classifier	True	Undetected	False	FDR	Accuracy
F&B 1	F&B (first-stage SVM)	448	0	5	1.10%	98.90%
	Side (second-stage SVM)	214	223	16	3.53%	47.24%
	Two-stage SVM	447	0	6	1.32%	98.68%
	SVM	426	9	18	3.97%	94.03%
Side 2	F&B (first-stage SVM)	186	164	15	4.11%	50.96%
	Side (second-stage SVM)	334	14	17	4.66%	91.51%
	Two-stage SVM	341	12	12	3.29%	93.42%
	SVM	335	13	19	5.21%	91.78%
Mixed 3	F&B (first-stage SVM)	653	174	39	4.50%	75.40%
	Side (second-stage SVM)	346	477	43	4.97%	39.95%
	Two-stage SVM	842	6	18	2.07%	97.23%
	SVM	789	28	49	5.70%	91.11%

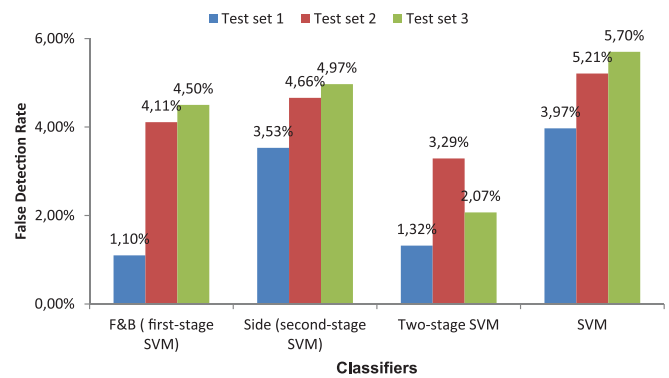


Fig. 8 Comparison of five classifiers about false detection rate.

The false detection rate of the two-stage classifier to the 3 test sets are 1.32%, 3.29 % and 2.07%, has been a lot lower than single SVM classifier. It is because that the classification method in this paper is the results of the combination of single classifiers.

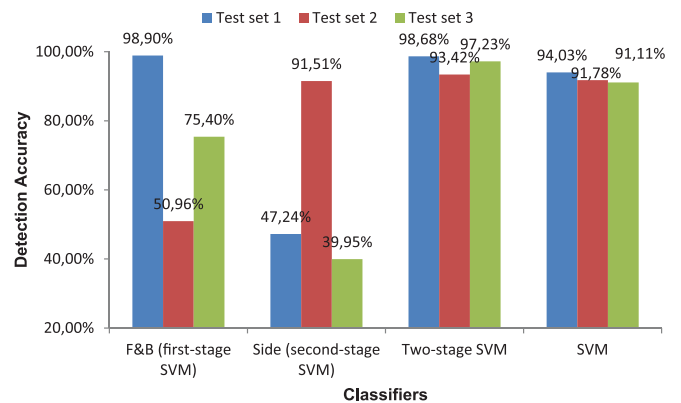


Fig. 9 Comparison of five classifiers about detection accuracy.

The F&B (first-stage) classifier has very good detection results for F&B images and its detection accuracy reached 98.90% while the side classifier it correctly detect the test set 2 at a rate of 91.51%. From the data above, it is found that the effect of F&B detection is better than side detection mainly because the HOG features of F&B posture in the images are

more specific to detect and easier to classify so that a better F&B classifier can be trained easier. As for side posture, there are large variation and great difference between these training sets, thus it is difficult to obtain a high-performance universal classifier for side-posture human.

According to the traditional classification method, we can get a SVM classifier trained with the mixed human postures. As shown in Fig.8 and Fig.9, the two-stage classifier based on SVM algorithm has a greater improvement of adaptive capacity for human postures. Comparing to our previous studies, the sample sets are all collected in the same background, but this paper improved the detection accuracy of nearly 3% due to the preprocessing of building different sample sets for different human postures.

This paper proposes a novel two-stage classifier which is made up of two single SVM classifiers for two types human postures. It can improve the detection accuracy of F&B posture significantly and make the detection accuracy of side postures flat with traditional approach. Its accuracy for the three test sets reaches 98.68%, 93.42% and 97.23%, which has a great progress compared to traditional SVM classifier.

## CONCLUSION

According to the existing problems of traditional HOG based classification method, a novel two-stage classification approach is proposed. Two-stage SVM is selected to replace traditional classifier to improve classification accuracy. At the first stage of classification, the samples are mainly divided into possible F&B human body and not F&B human body, and then they were put into the second-stage classification among side human and non-human to detect human. Finally the detection result is integrated with the use of disjoint sets.

The experimental tests of operation field in bulk terminal of Tianjin Port show that single traditional SVM algorithm has a large limitation for F&B, side and complicated posture human body test sets. And it lacks adaptability to human postures. The first-stage classification has a greater detection accuracy than the second-stage classification, which means F&B posture human has more specific HOG features than side human. The two-stage classification method proposed in this paper has a detection accuracy of more than 97%, which is higher than using traditional SVM. In conclusion, the improved classification approach purposed in this paper is more feasible and advanced.

## ACKNOWLEDGEMENT

This research was supported by “Scientific Research Innovation Project” of Shanghai Municipal Education Commission (No. 14ZZ140), the “Ph.D. Innovation Program” of Shanghai Maritime University (No. 2014ycx040), and the “Yang Fan Plan for Shanghai Youth Science and Technology Talent” of the Science and Technology Commission of Shanghai Municipality (No.15YF1404900).

## CONFLICT OF INTERESTS

The authors declare that there is no conflict of interests regarding the publication of this paper.

## REFERENCES

1. Mi, Chao; He, Xin; Liu, Haiwei; Huang, Youfang; Mi, Weijian, “Research on a Fast Human-Detection Algorithm for Unmanned Surveillance Area in Bulk Ports”, *Mathematical Problems in Engineering*, 2014, DOI: 10.1155/2014/386764
2. Mi C, Shen Y, Mi W, et al. “Ship Identification Algorithm Based on 3D Point Cloud for Automated Ship Loaders”. *Journal of Coastal Research*, 2015, 73(sp1): 28-34, DOI: 10.2112/SI73-006.1
3. Bian Zhicheng, Yang Yongsheng, Mi Weijian, Mi Chao. “Dispatching electric AGVs in Automated Container Terminals with long travel distance”. *Journal of Coastal Research*, 2015, 73(sp1): 75-81, DOI: 10.2112/SI73-014.1
4. Xiaoming Yang, Ning Zhao, Zhicheng Bian, Jiaqi Chai, and Chao Mi. “An intelligent storage determining method for inbound containers in container terminals”. *Journal of Coastal Research*, 2015, 73(sp1): 197-204, DOI: 10.2112/SI73-035.1
5. Yung-Chi Lo; Po-Yen Lee ;Shyi-Chyi Cheng. “Space-time template matching for human action detection using volume-based Generalized Hough transform”. *Image Processing (ICIP), 2011 18th IEEE International Conference on*. pp.2097 – 2100(2011), DOI: 10.1109/ICIP.2011.6116021
6. SongminJia; ShuangWang ;Lijia Wang et al. “Robust human detecting and tracking using varying scale template matching”. *Information and Automation (ICIA), 2012 International Conference on*. pp. 25 – 30(2012), DOI: 10.1109/ICInfA.2012.6246776
7. Navneet Dalal and Bill Triggs, 2005. “Histograms of oriented gradients for human detection”.. *Computer Vision and Pattern Recognition, 2005. CVPR 2005. IEEE Computer Society Conference on*, pp.886- 893(2005), DOI: 10.1109/CVPR.2005.177
8. Hong Tian, Zhu Duan, Ajith Abraham, Hongbo Liu.” A novel multiplex cascade classifier for pedestrian detection”. *Pattern Recognition Letters*, Volume 34, Issue 14, 15 October 2013, Pages 1687-1693, DOI: 10.1016/j.patrec.2013.04.015
9. Hai-Miao Hu, Xiaowei Zhang, Wan Zhang, Bo Li.” Joint global-local information pedestrian detection algorithm for outdoor video surveillance”. *Journal of Visual Communication and Image Representation*, Volume 26, January 2015, Pages 168-181, DOI: 10.1016/j.jvcir.2014.11.009

10. Qiang Zhu; Yeh, M.-C. ; Kwang-Ting Cheng, et al. "Fast Human Detection Using a Cascade of Histograms of Oriented Gradients". *Computer Vision and Pattern Recognition, 2006 IEEE Computer Society Conference on. Vol.2*, pp.1491 – 1498(2006), DOI: 10.1109/CVPR.2006.119
11. Cristina Conde, Daniela Moctezuma, et.al."HoGG: Gabor and HoG-based human detection for surveillance in non-controlled environments" *Neurocomputing*, Volume 100, 16 January 2013, Pages 19-30, DOI: 10.1016/j.neucom.2011.12.037
12. Marco Pedersoli, Jordi González, Andrew D. Bagdanov, Xavier Roca. "Efficient discriminative multiresolution cascade for real-time human detection applications". *Pattern Recognition Letters*, Volume 32, Issue 13, 1 October 2011, Pages 1581-1587, DOI: 10.1016/j.patrec.2011.06.019
13. Ninomiya, H; Ohki, H.; Gyohten, K. et al. "An evaluation on robustness and brittleness of HOG features of human detection". *Frontiers of Computer Vision (FCV), 2011 17th Korea-Japan Joint Workshop on*. pp. 1 – 5( 2011), DOI: 10.1109/FCV.2011.5739746
14. Ying Tan; Jun Wang. "A support vector machine with a hybrid kernel and minimal Vapnik-Chervonenkis dimension". *Knowledge and Data Engineering, IEEE Transactions on. Vol.16*, pp 385 – 395(2004), DOI: 10.1109/TKDE.2004.1269664
15. QiuXintao; Fu Dongmei ; Yang Tao. "A novel approach to optimize the objective function based on VC dimension and structural risk minimization". *Control Conference (CCC), 2011 30th Chinese*. pp. 3226 – 3230(2011)
16. Ando, H. Fujiyoshi, H. "Human-Area Segmentation by Selecting Similar Silhouette Images Based on Weak-Classifer Response". *Pattern Recognition (ICPR), 2010 20th International Conference on*. pp. 3444 – 3447(2010). DOI: 10.1109/ICPR.2010.841
17. Jiayuan Yu. "The application of BP-Adaboost strong classifier to acquire knowledge of student creativity". *Computer Science and Service System (CSSS), 2011 International Conference on*. pp.669 – 2672(2011). DOI: 10.1109/CSSS.2011.5974999
18. Lie Guo, Ping-Shu Ge, Ming-Heng Zhang, Lin-Hui Li, Yi-Bing Zhao." Pedestrian detection for intelligent transportation systems combining AdaBoost algorithm and support vector machine" *Expert Systems with Applications*, Volume 39, Issue 4, March 2012, Pages 4274-4286, DOI: 10.1016/j.eswa.2011.09.106
19. Huimin Qian, Yaobin Mao, Wenbo Xiang, Zhiquan Wang." Recognition of human activities using SVM multi-class classifier". *Pattern Recognition Letters*, Volume 31, Issue 2, 15 January 2010, Pages 100-111, DOI: 10.1016/j.patrec.2009.09.019
20. Kanitkar, A. Bharti, B. ;Hivarkar, U.N. "Vision based preceding vehicle detection using self shadows and structural edge features". *Image Information Processing (ICIIP), 2011 International Conference on*. pp.1 – 6(2011), DOI: 10.1109/ICIIP.2011.6108922
21. Man Zhang; Zhenan Sun ;Tieniu Tan. "Deformed iris recognition using bandpass geometric features and lowpass ordinal features". *Biometrics (ICB), 2013 International Conference on*. pp.1 – 6(2013), DOI: 10.1109/ICIIP.2011.6108922
22. Yu Cheng; ZhigangJin; CunmingHao. "Illumination normalization based on 2D Gaussian illumination model". *Advanced Computer Theory and Engineering (ICACTE), 2010 3rd International Conference on. Vol.3*, pp.V3-451 - V3-455(2010). DOI: 10.1109/ICACTE.2010.5579870
23. Ying Bai; Dali Wang. "On the Comparison of Trilinear, Cubic Spline, and Fuzzy Interpolation Methods in the High-Accuracy Measurements". *Fuzzy Systems, IEEE Transactions on. Vol.8*, pp. 1016 – 1022(2010), DOI: 10.1109/TFUZZ.2010.2064170
24. Corinna Cortes; Vladimir Vapnik. "Support-vector networks". *Machine Learning. Vol.20, Issue 3*, pp 273-297(1995), DOI: 10.1007/BF00994018

#### CONTACT WITH THE AUTHORS

Chao MI  
 Youfang HUANG  
 Weijian MI  
 e-mail: kingdows@gmail.com

Container Supply Chain Tech. Engineering Research  
 Center  
 Shanghai Maritime University, No.1550 Haigang Ave,  
 Shanghai 201306  
**CHINA**

Zhiwei ZHANGb  
 Xin HEB

Logistics Engineering College  
 Shanghai Maritime University, No.1550 Haigang Ave,  
 Shanghai 201306  
**CHINA**